Streptavidin-Based Nanostructures: From Bulk to Surface-Confined Assembly Studies

Inauguraldissertation

zur
Erlangung der Würde eines Doktors der Philosophie
vorgelegt der
Philosophisch-Naturwissenschaftlichen Fakultät
der Universität Basel

von

Sabina Burazerovic
aus Kanada

Basel, 2013

Genehmigt von der Philosophisch-Naturwissenschaftlichen Fakultät auf Antrag

Von:

Prof. Dr. Thomas R. Ward Prof. Dr. Wolfgang Meier

Basel, den 11 Dezember 2012

Prof. Dr. Jörg Schibler

Dekan der Philosophisch-

Naturewissenchaftliche Fakultät

creative commons

Attribution-Noncommercial-No Derivative Works 2.5 Switzerland

---

You are free:

to Share — to copy, distribute and transmit the work

Under the following conditions:

Attribution. You must attribute the work in the manner specified by the author or licensor (but not in any way that suggests that they endorse you or your use of the work).

Noncommercial. You may not use this work for commercial purposes.

No Derivative Works. You may not alter, transform, or build upon this work.

- For any reuse or distribution, you must make clear to others the license terms of this work. The best way to do this is with a link to this web page.
- Any of the above conditions can be waived if you get permission from the copyright holder.
- Nothing in this license impairs or restricts the author's moral rights.

Your fair dealing and other rights are in no way affected by the above.

This is a human-readable summary of the Legal Code (the full license) available in German:
http://creativecommons.org/licenses/by-nc-nd/2.5/ch/legalcode.de

Disclaimer:
The Commons Deed is not a license. It is simply a handy reference for understanding the Legal Code (the full license) — it is a human-readable expression of some of its key terms. Think of it as the user-friendly interface to the Legal Code beneath. This Deed itself has no legal value, and its contents do not appear in the actual license. Creative Commons is not a law firm and does not provide legal services. Distributing of, displaying of, or linking to this Commons Deed does not create an attorney-client relationship.

Quelle: http://creativecommons.org/licenses/by-nc-nd/2.5/ch/deed.en Datum: 3.4.2009

List of Abbreviations

AFM: atomic force microscopy

Au NPs: gold nanoparticles

BBA: bis-biotin anchor

Biot-SH: biotin-terminated tri(ethylene glycol)hexanethiol

CDMT: 2-chloro-4,6-bis[3-(perfluorohexyl)propyloxy]-1,3,5-triazine

DACA: *p*-dimethylaminocinnamaldehyde

DCC: *N*,*N*'-dicyclohexylcarbodiimide

DIEA: *N*,*N*-diisopropylethylamine

DNA: deoxyribonucleic acid

DX: double crossover

EDC: *N*-(3-dimethylaminopropyl)-*N'*-ethylcarbodiimide

EEDQ: 2-ethoxy-1-ethoxycarbonyl-1,2-dihydroquinoline

ESI-MS: electrospray ionization mass spectrometry

HABA: 2-(4'-hydroxyazobenzene)benzoic acid

HOBt: 1-hydroxybenzotriazole

HOPG: highly ordered pyrolytic graphite

MOPF: metalorganic protein framework

NMM: *N*-methylmorpholine

NMR: nuclear magnetic resonance

OEG: oligo(ethylene glycol)

OEG-SH: (1-mercapto-11-undecyl) tetra(ethylene glycol)

PFP: pentafluorophenol

QCM(-D): quartz crystal microbalance (with dissipation monitoring)

RP-HPLC: reversed-phase high pressure liquid chromatography

SAM: self-assembled monolayer

SAv: streptavidin

SDS-PAGE: sodium dodecyl sulfate polyacrylamide gel electrophoresis

SEM: scanning electron microscopy

S-layer: surface layer

SPR: surface plasmon resonance

ssDNA: single-stranded deoxyribonucleic acid

TBTU: *O*-benzotriazol-1-yl-*N*,*N*,*N*',*N*'- tetramethyluronium tetrafluoroborat

TEM: transmission electron microscopy

TFA: trifluoroacetic acid

TIR: total internal reflection

TLC: thin layer chomatography

TMVP: tobacco mosaic virus protein

XPS: x-ray photoelectron spectroscopy

Abstract

Self-assembly, the ability of disordered units to spontaneously organize themselves into high-order structures via non covalent bonds, is a physical principle allowing nanostructures to be created from the bottom-up, extending nano-order to macroscales. In that spirit, this thesis was dedicated to program the self-organization of mature wild-type streptavidin by using linear tetrabiotinylated and trifurcated hexabiotinylated connectors.

Self-organization studies in bulk solution demonstrated that streptavidin combined with a linear tetrabiotinylated connector spontaneously assembled into a one-dimensional streptavidin-based block copolymer. In the presence of calcium ions, the fibrils formed bundles that served as a template for the nucleation, the growth and the assembling of calcite microcrystals. This hierarchical self-assembly process yielded millimeter-sized one-dimensional mineralized protein matrices. Both mineralized and naked one-dimensional streptavidin-based block copolymers were imaged by electron microscopy.

With the aim of obtaining well-defined and monodisperse nanostructures, a step-by-step assembly approach was investigated. Designed mixed bis-biotinylated monolayers on gold were used to anchor streptavidin, which was successively exposed to linear tetrabiotinylated or trifurcated hexabiotinylated connectors and streptavidin. The stepwise elongation process was followed *in situ* by surface plasmon resonance and quartz crystal microbalance with dissipation monitoring. The size-controlled immobilized streptavidin-based fibrils were scrutinized by atomic force microscopy in the hydrated state.

Keywords:

protein structure, nanotechnology, self-assembly, biotin/streptavidin recognition, calcite mineralization, SAMs, QCM, SPR, protein immobilization.

Table of Contents

Chapter I

Introduction

I General Introduction

Protein and nucleic acid biopolymers are well appreciated for their high-performance capabilities for molecular recognition, catalysis and information storage.[1] In recent years, both have become important building blocks for assembling larger structures from the bottom up. Although different systems incorporating proteins and/or nucleic acids were reported to self-assemble into larger nanostructures,[2-7] one of the key challenge is to organize them to a scale large enough for nanotechnological application. The following section highlight recent advances in the use of protein- and nucleic acid-related materials as smart building blocks in nanotechnology.

1.1 Proteins and DNA in Bionanotechnology

Seeman proposed the use of DNA as a scaffold for protein organization at the beginning of the 1980s.[8] Since then, DNA has become one of the most promising materials for nanobiotechnology. One of the advantage of DNA over proteins resides in his predictable self-assembly due to the high fidelity association according to simple base-pairing rules.[9] DNA gives researchers a precise assembly code to define which strands will pair, and results in double helices presenting a width of 2 nm and a 3.4 nm length for a 10-base helical pitch (B-form). In addition, automated methods enable the synthesis and amplification of virtually any DNA sequence. The availability of highly specific enzymes, such as endonucleases and polymerases, provides a toolbox to process DNA material with atomic precision.[10]

The first DNA-based 2D lattice was presented by Seeman and coworkers 15 years ago.[11] Double-crossover (DX) motifs presenting proper sticky ends self-assembled into 2D arrays extending to the micrometer scale (Fig. 1a). Fully addressable DNA tiles were later reported by the groups of Yan and LaBean.[12] Both used finite-size nanoarrays assembled from unique tiles. LaBean used a 4×4 array with 16 unique addresses used to display the letters “D”, “N” and “A” by precise arrangement of SAv (Fig. 1b). The same year, Rothemund introduced a new ap-

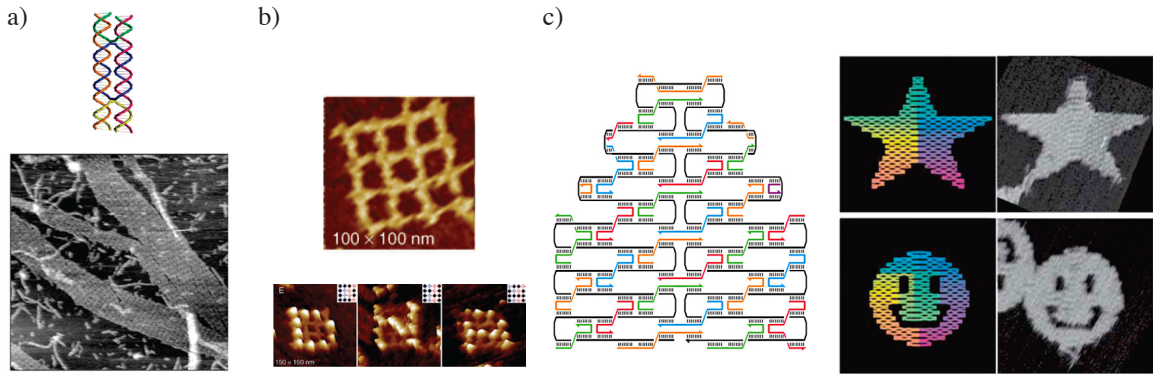

Figure 1 Models of some representative DNA tiles and their assemblies into periodic 2D arrays. (a) Double-helix (DX) tile formed through strand exchange between two DNA duplexes with representative AFM image (1.5 μm × 1.5 μm) of the 2D network. (b) Finite-sized DNA arrays used to attach SAv units to diplay the letters "D", "N" and "A". (c) DNA origami: principle of DNA origami, folding long ssDNA into shapes by multiple helper strands; star and smiley face DNA origami tiles self-assembled by folding a 7 kb ssDNA with more than 200 helper strands (AFM images : 165 nm × 165 nm). Adapted from ref. [11-14].

proach to create fully addressable molecular pegboards by introducing the DNA origami.[13] Upon addition of 226 short helper ssDNA, a viral circular ssDNA scaffold folded into different shapes presenting 226 addressable positions (Fig 1c).

In the past decade, numerous examples outlining the precise patterning of different entities, such as gold nanoparticles (Au NPs), were reported. A two-tile system, with one of the tiles being biotinylated, was used to create density-controlled streptavidin (SAv) arrays

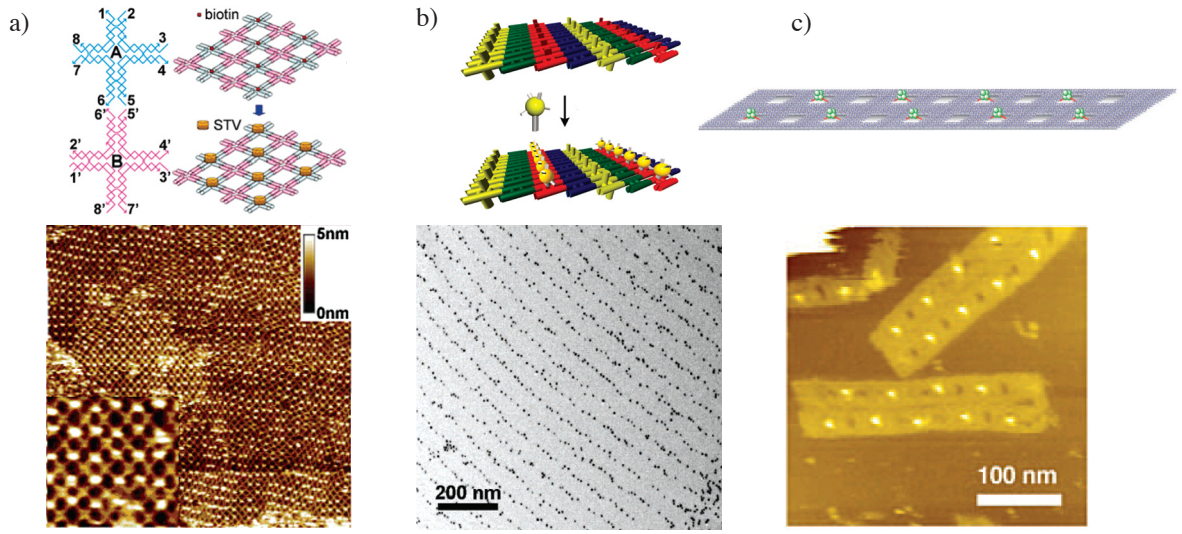

Figure 2 DNA-directed assembly of multicomponents nanoarrays. a) Programmable streptavidin 2D arrays formed on biotinylated DNA lattices and corresponding AFM image (1 μm × 1 μm; inset 150 nm × 150 nm). b) Organization of 5 nm AuNPs on DNA DX lattices with TEM image of the nanocomponent array. c) 2D SAv nanoarray assembled from two rectangular origami subunits where SAv was selectively positionned in zigzag arrangement. Adapted from ref. [15, 16, 18].

(Fig. 2a).[15] Au NPs modified with thiolated single stranded DNA were assembled on a 2D DNA scaffold via hybridization to form an ordered Au NPs array.[16] TEM images revealed periodic rows of Au NPs separated by a distance of ~60 nm. Taking advantage of the origami structure, fluorophores were positioned to generate a nanoscopic ruler for super resolution microscopy.[17] A rectangular origami scaffold was also involved in the creation of nanowells selectively modified with biotin to generate a zigzag arrangement of SAv (Fig. 2c).[18]

All structures discussed so far have been exclusively assembled from oligonucleotides of various lengths. However, by synthesizing artificial junctions, Sleiman and co-workers introduced an alternative method to construct DNA nanostructures. Combining various "vertex organic molecules" with ssDNA, they created a library of DNA polygons (triangles, square, pentagon and hexagon), which were readily assembled into various 3D nano-objects (Fig. 3a).[19] This was done by connecting the DNA polygons top and bottom, using linking strands, in quantitative yields. By assembling these polygons longitudinally, they created some DNA nanotubes[20] which were able to encapsulate and selectively release Au NPs (Fig. 3b).[15] These materials are promising for drug delivery and nanowire growth.

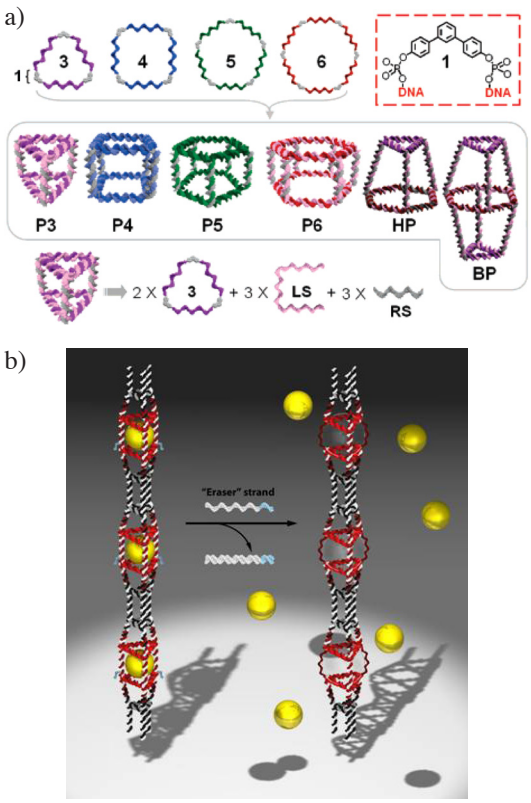

Figure 3 Dynamic DNA cycles allow the preparation of a) 3D prisms and b) nanotubes that can be used for nanoscale organization. Adapted from ref. [9]

Taking a step towards soft attachment methodology, Börjesson *et al*. tethered a DNA hexagon to a lipid membrane using three porphyrins modifications (Fig. 4).[22] The weak an-

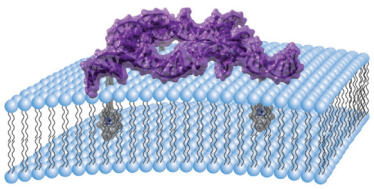

Figure 4 Scheme of a DNA network anchored to a lipid membrane using three porphyrins. Adapted from ref. [22]

choring allows DNA components to migrate and adjust to their environment without leaving the membrane surface. This dynamic yet surface bounded assembly could open the way to self-repairing material.

Although proteins do not have the versatile base-pair rule to program DNA assemblies, they present superior specificity for target binding with complex molecular recognition mechanism.[23] Using recognition functions, assembly into specific shapes extending to the micrometer scale is achievable as observed in the crystalline cell surface layers (S-layers). S-layers consist of a single protein, which spontaneously forms highly regular two-dimensional lattices of varying symmetry (Fig. 5). The regular pores within the S-layer have been used to template regular arrangements of monodisperse cadmium sulfide and gold nanoparticles.[24,25]

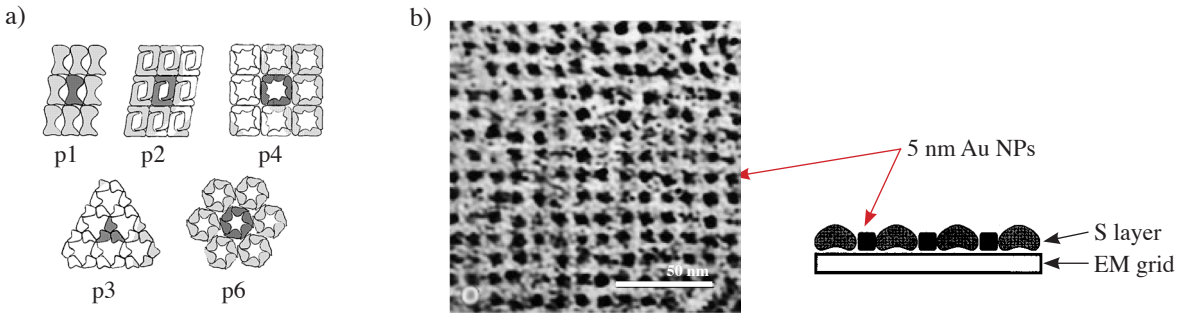

Figure 5 Bacterial S-layers a) Schematic drawing of different S-layer lattice types with a diagonal (p1, p2), square (p4), or hexagonal (p3, p6) symmetry. b) Electron micrograph of a gold superlattice prepared by using a square S-layer lattice. Adapted from ref. [25]

Exploiting the SAv-biotin interaction, different protein-based nanostructures were created. Schulz and coworkers produced protein nanostructures based on the ligand-directed assembly of a biotin tagged tetrameric aldolase and SAv.[26] Biotin and bis-biotin mediated connections between the subunits directed their assembly into two-dimensional network sizes extending to 50 by 50 nm, and varied cruciform discrete nanoassemblies. Although the networks were improved by anchoring the system on a planar monolayer, irregularities in the lattice structure persisted. We showed that metalorganic protein frameworks (MOPFs) were assembled into one-dimensional protein bundles, which mimics collagen assembly in biomineralization processes, by using the strong interaction between SAv and bis-biotinylated organometallic linear

connectors.[27] Recently, the SAv-biotin interaction was also exploited to obtain large-scale 3D peptide scaffolds where SAv-functionalized Au NPs were incorporated in the cage-like unit cells made from biotinylated peptides.[28]

Traditionally considered as infectious agents, viruses offer many exciting opportunities for creating new materials with advanced properties. They present a highly symmetrical and monodisperse structure, and can assemble on multiple length scales. Different studies have highlighted the utility of viral capsids to template the mineralization of different inorganic material,[29] and for encapsulation.[30] Viruses were more recently exploited as targeted imaging agents[31] and energy-converting materials.[32] For example, tobacco mosaic virus proteins (TMVP) bearing chromophores were reported to self-assemble into a synthetic light harvesting system (Fig. 6a).[33] Belcher and coworkers successfully fabricated virus-templated Co_3O_4 nanowires as anode materials for lithium ion batteries (Fig. 6b).[34] They further exploited the toolkits of genetic engineering, multilayer assembly methods, and soft lithography to stamp microbattery electrodes on platinum microbands.[35] These developments demonstrate the potential of protein-based materials towards the creation of light, environmentally benign and flexible batteries for use in electronic equipment.

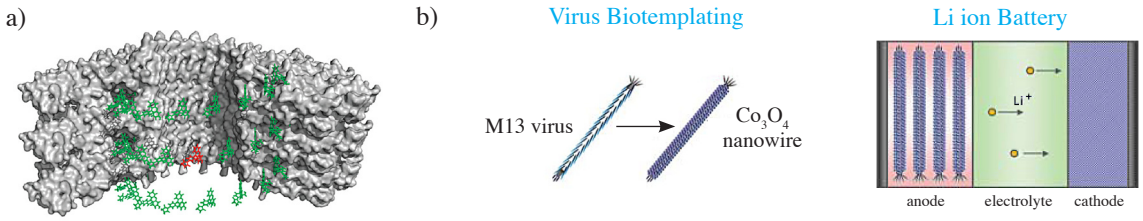

Figure 6 Viruses in nanotechnological application. a) Model of TMVP labeled with chromophores for energy transfer in light harvesting systems. b) Schematic diagram of the virus-enabled synthesis and assembly of nanowires as negative electrode materials for Li ion batteries. Adapted from ref. [32, 34]

1.2 Self-Assembled Monolayers

With the aim of developing biosensors for bioanalytical and biomedical applications, different stategies to immobilize biomolecules on modified surfaces have been exploited.[36] Self-assembly is one of the most popular bottom-up approaches to modify surfaces and intro-

duce anchoring elements: it is easy to apply and allows end groups modifications to confer specific functionality. Among various self-assembly processes, the formation of a self-assembled monolayer is one of the most elegant ways for making an organic film with specific functional properties.[37, 38]

Back in the 80s, Nuzzo and coworkers were the first to show that dialkyl disulfides form oriented monolayers on gold, which are nowadays commonly referred to as self-assembled monolayers (SAMs).[39] Whitesides pioneering work in using SAMs for biological applications was a driving force in the development of the current biosensors based on this technology.[40, 41] Even though monolayers formation have been studied on different type of metals, the most widely applied class of SAMs derives from the adsorption of alkane thiol on gold. The latter is a relatively inert metal, and is easy to pattern by a combination of lithographic tools and chemical etchants. Moreover, gold binds to thiols with a high affinity, and does not undergo any unusual reaction with them.[38]

As effective platforms to study biomolecules, SAMs should prevent nonspecific adsorption, and should present the probes of interest in a well-defined manner ensuring accessibility to the biomolecules. The best protein-resistant surfaces presently known are the ones composed of oligo- or poly(ethylene glycol) (OEG). Alkanethiols terminated with an OEG_n (n = 3, 4, 6) group form a dense, ordered monolayer with the same molecular conformation found for n-alkanethiols, *i.e.* all-trans chains tilted by 30° from the surface normal. The terminal OEG end-group adopts either a helical conformation aligned perpendicular to the surface or an amorphous conformation.[42] Both the hydration and the conformational flexibility of the ethylene glycol chains are responsible for their resistance to protein adsorption.[43]

Considering the above discussion, one approach to immobilize biomolecules on a surface resistant towards nonspecific adsorption consist of assembling mixed monolayers composed of two different alkanethiols - one reactive towards the biomolecule of interest and the other inert, as OEG_n terminated thiols. The presence of biotinylated probes into a mixed monolayer enables the strong noncovalent interaction with SAv to be exploited for oriented immobi-

lization of biotinylated biomolecules. For these reasons, mixed SAMs of alkanethiols bearing OEG_4 and biotin terminal groups on gold were used during this thesis (chap. 2.4). An overview of the published work using this immobilization platform is given in the next section.

1.2.1 Biotinylated mixed Self-Assembled Monolayers

Ringsdorf and Knoll were the first to show that the specific recognition between SAv and biotin could be observed on biotinylated SAMs by surface plasmon resonance (SPR), suggesting potential application as biosensors.[44] Using mixed SAMs prepared by coadsorption method from solutions of biotinylated thiol and mercaptoundecanol (ratio 1:9), they generated a multilayer system of biotinylated antibody Fab fragments/SAv/Biot-SH to detect a protein probe, human chorionic gonadotropin (HCG).[45] Although the binding was highly specific, the detection platform was not sensitive enough to be used as commercial pregnancy test. Stayton and co-workers took advantage of the SPR sensing technique to study the binding and dissociation of wild-type and mutant SAv on biotinylated mixed SAMs.[46] They proposed that at low (<10%) and high (>60%) biotin surface coverage, SAv was bounded via a single biotin binding site. They reported optimum SAv immobilization with SAMs composed of 5 to 10% of biotinylated thiols. Their studies also showed that dilution of the monolayer with OEG_4-terminated alkane thiols gave superior results than alcohol-terminated alkane thiol towards nonspecific adsorption of SAv. Knoll and coworkers reported the adsorption of SAv onto SAMs bearing 10% of biotinylated thiols monitored by QCM-D.[47] Referring to previous results on SAv immobilization onto biotin-doped lipid films,[48] they explained the drop of dissipation observed upon SAv adlayer formation being due to SAv rearrangement into a more rigid layer.

In order to obtain a surface presenting well-distanced immobilized SAv units, biotin probe density controlled by using a labile dendron spacer was demonstrated.[49] In this process, anchor molecules with attached dendron modifiers were first adsorbed onto the surface; steric interactions of the bulky dendrons controlled the density of anchor molecules bound to the surface. The dendron branches were subsequently detached from the anchor molecules, enabling the attachment of biotin. Although the binding of the immobilized SAv towards biotinylated

biomolecules was not tested, it produced a surface with controlled spacing among probe molecules.

More recently, Svedhem and coworkers used monolayers prepared from OEG_n (n = 7-9) disulfide and various mole fraction (0.01% to 10%) of biotinylated disulfide to study the immobilization sequence SAv/biotinylated BSA by QCM-D.[50] Monolayers containing 1% of the biotin disulfide were concluded to be the most performent and were tested for the immobilization sequence SAv/biotinylated Protein A/antigen BSA/BSA. In addition, the antibody/antigen complex was repeatedly removed by basic treatment and, again immobilized. The biotinylated sensors proved to be stable and showed the possibility of protein interaction studies by QCM-D.

1.3 Methodology

Analytical tools used to gain insight in the studied system are briefly described in this section.

1.3.1 Atomic Force and Electron Microscopy

The atomic force microscopy (AFM) is a technique widely used to characterize self-assembled biomaterials. It is based on interaction forces occuring between a very sharp probe and the scanned surface. The probe is generally made of silicon or silicon nitride, and has a diameter smaller than 50 nm. The scanning mechanism relies upon piezoelectric transducers; by adjusting the voltage through a piezo, the probe can be move a few Ångström in every step. The detection mechanism consists of an optical lever system, where a laser beam focuses onto the end of the cantilever and then reflects off onto a photo diode.[51] As the probe moves due to alteration of the surface during scanning, the cantilever bends, and changes in the laser's deflection enable height data to be recorded. A combination of the lines scanned profile yields three-dimensional topographic data of the samples. There are different imaging modes available; one can operate in tapping mode, which oscillate the probe over the surface of the sample or, in contact mode, which bends the probe in direct contact with the sample's surface and a constant force

is applied while scanning.[52] Both modes can be operated in air or liquid. The tapping mode is the most popular to observe biological samples since deformation the latter is minimized. The scanned area are smaller then 100 μm x 100 μm, and magnifications of the images captured by AFM range between 10^2 to 10^9 times.[53] However, the atomic resolution obtained for hard surfaces has not been reached for biological samples.[54] For example, the highest resolution achieved on membrane proteins is ~ 0.1 nm vertically and ~ 0.5 nm laterally, which nonetheless allowed the observation of substructural details of single membrane proteins.[55]

In transmission electron microscopy (TEM), an electron beam is emitted from a cathode at high voltage. The wavelength of this electron beam depends on the applied potential that accelerates the electrons in the direction of the anode. Powerful electromagnets act on the electron beam as lenses. On passage of electrons through the sample, which must be kept very thin, inelastic and elastic scattering occur at the sample atoms.[56] The enlarged image of the sample, which is generated by interaction of the incident electron beam with sample atoms, is presented on a fluorescent screen and can be recorded on a photographic negative or a CCD camera. Since the observed contrast depends on the average atomic number of the atom, biological sample are usually stained with material exhibiting pronounced electron-scattering properties (*e.g.* uranyl acetate).

In scanning electron microscopy (SEM), a beam of electrons is rastered over the sample, while the signals emitted from the sample, secondary electron (SE) and backscattered electron (BSE), are collected by the detectors. The detected signals reveal information about the topography (SE) and the chemical composition (BSE). For traditional SEM experiment, the sample has to be conducting and is usually imaged under high vacuum. Insulating specimens are usually coated with a thin layer of conducting material (*e.g,* carbon, gold, platinum) to avoid charging of the sample.[57]

1.3.2 Biosensing Techniques

a) Surface Plasmon Resonance (SPR)

Surface plasmon resonance (SPR) is based on the total internal reflection (TIR) optical phenomenon. When the incident light travels from the higher refractive index medium 1 to the lower refractive index medium 2, the TIR can take place within medium 1 as long as the incident angle, θ_1, is greater than the critical angle, θ_c, where $\sin(\theta_c) = n_2/n_1$ (Fig. 1).

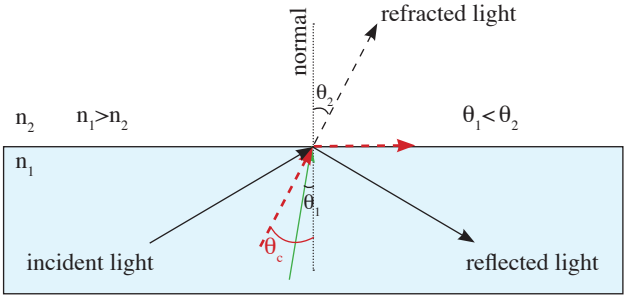

Figure 1 Total internal reflection (TIR) of light.

Under conditions of TIR, exponentially decaying evanescent waves are formed in the lower refractive index medium. Surface plasmons, a surface electromagnetic wave whose propagation is confined to the metal-dielectric interface, can be excited by evanescent wave. When a thin gold layer is placed at the interface, the evanescent wave is enhanced, penetrating the gold film and existing in the medium 2 (Fig. 2).

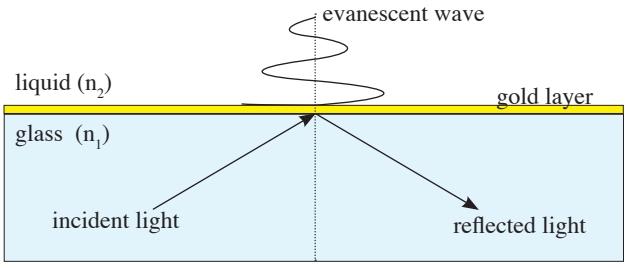

Figure 2 Evanescent field.

When this happens, the resonance energy transfer from evanescent wave to surface plasmons induces a sharp decrease of the intensity of the reflected light. This specific incident angle

required for the resonance, θ_{SPR}, depends on the refractive index of media 2 at the vicinity of the metal surface. Adsorption and desorption of biomolecules on the gold surface are translated into changes in refractive index of the media 2 near the metal-dielectric interface. Since variation in refractive index can be related to the adsorbed mass using a linear relationship,[58] monitoring of the θ_{SPR} changes can be used to track adsorption-desorption processes occuring at the liquid-solid interface.

In the BIAcore system, the changes in θ_{SPR} are expressed as SPR responses measured in resonance units (RU), where 1 RU = 0.0001°. A SPR shift of 1000 RU corresponds to approximately 100 ng/cm^2 in surface protein concentration.[59]

b) Quartz Crystal Microbalance with Dissipation Monitoring (QCM-D)

In the QCM technique, a quartz crystal is set to oscillate at its resonant frequency. As first recognized by Sauerbrey in 1959, the resonnance frequency of the crystal is extremely sensitive to mass changes.[60] Sauerbrey equation, valid for thin and rigid film, describes the linear relationship between the resonant frequency decrease and the added mass:

$$\Delta f_n = -\frac{2nf_0^2}{\sqrt{\rho_q \mu_q}} \Delta m = -\frac{n}{c_{QCM}} \Delta m \qquad (1)$$

where Δf is the observed frequency shift, n is the overtone number and Δm denotes the mass change per unit area. The mass sensitivity constant, c_{QCM}, depends on the resonant frequency, f_0, the density, ρ_q, and the shear modulus, μ_q, of the quartz crystal. For a f_0 = 5 MHz quartz crystal, c_{QCM} is 17.7 ng·Hz^{-1}·cm^{-2}. In contrast to SPR, the QCM is sensitive to the total mass coupled to the sensor oscillation, *i.e.* both the mass of biomolecules and the solvent bound or hydrodynamically coupled to the layer.[61] For that reason, the mass provided by Sauerbrey relation overestimates the amount of biomolecules immobilized onto the sensor. The second physical value detected by QCM-D, the energy dissipation (ΔD), corresponds to the energy loss related

to the viscoelastic properties of the adlayer. In combination with monitoring of Δf at several overtones, quantities such as shear modulus, viscosity, density and thickness can be extracted from the data.[62] This so-called Voigt-based model is used to analyze and characterizes dissipative layers. A layer is considered dissipative when $\Delta D > 1 \cdot 10^{-6}$ or $\Delta D/\Delta f > 1 \cdot 10^{-8}$ Hz^{-1}.[63]

1.4 Scope of the Thesis

The aim of this thesis was to organize streptavidin (SAv) units into well-defined one-dimensional and dendritic nanoarchitectures.

The first part of this thesis was dedicated to the synthesis and characterization of different BBA-based connectors. Based on the work previously accomplished by Stayton and Wilbur, BBA moiety **1** (scheme 1) was the first key intermediate to be synthesized.[64, 65] Followed the synthesis of compounds **2**, **3** and disulfide **4**. The synthesis of a trifurcated ligand analog to compound **3** accomplished by Dr Koji Oohora is also presented.

In the second part, the self-organization of SAv combined with linear and trifurcated BBA-based connectors was studied in bulk solution. The resulting nanostrucures were analyzed by gel electrophoresis, electron and probe microscopy.

The third part covers the ability of the SAv-based linear polymers to form bundles when exposed to calcium ions, and template the mineralization of calcite.

Finally, we immobilized the system via a mixed biotinylated SAM on gold and studied the step-by-step assembly of SAv. Sequential additions of SAv and BBA-based connectors was followed *in situ* by QCM-D and SPR. The resulting structures were scrutinized by atomic force microscopy (AFM).

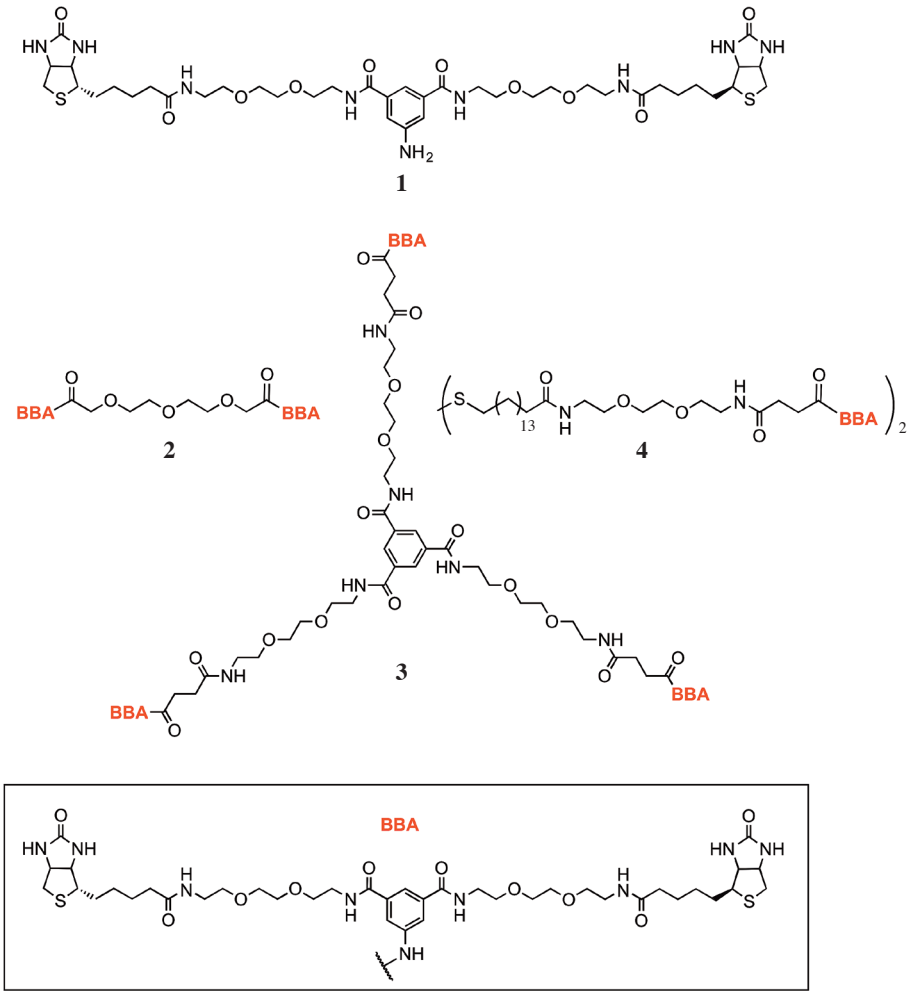

Scheme 1 Chemical structure of the bis-biotin anchor (BBA) moiety and BBA-based connectors.

1.5 References

1. Payne, G. F., *Curr. Opin. Chem. Biol.* **2007**, *11* (2), 214.; Thomas, C. M.; Ward, T. R., *Chem. Soc. Rev.* **2005**, *34* (4), 337.; Steinreiber, J.; Ward, T. R., *Coord. Chem. Rev.* **2008**, *252* (5-7), 751.; Zimbron, J. M.; Sardo, A.; Heinisch, T.; Wohlschlager, T.; Gradinaru, J.; Massa, C.; Schirmer, T.; Creus, M.; Ward, T. R., *Chem. Eur. J.* **2010**, *16* (43), 12883.

2. Niemeyer, C. M.; Adler, M.; Pignataro, B.; Lenhert, S.; Gao, S.; Chi, L.; Fuchs, H.; Blohm, D., *Nucleic Acids Res.* **199**9, *27* (23), 4553.

3. Niemeyer, C. M.; Adler, M.; Gao, S.; Chi, L., *J. Biomol. Struct. Dyn.* **2002**, *20* (2), 223.

4. Carlson, J. C. T.; Jena, S. S.; Flenniken, M.; Chou, T.-F.; Siegel, R. A.; Wagner, C. R., *J. Am. Chem. Soc.* **2006**, *128* (23), 7630.

5. Kitagishi, H.; Oohora, K.; Yamaguchi, H.; Sato, H.; Matsuo, T.; Harada, A.; Hayashi, T., *J. Am. Chem. Soc.* **2007**, *129* (34), 10326.; Kitagishi, H.; Kakikura, Y.; Yamaguchi, H.; Oohora, K.; Harada, A.; Hayashi, T., *Angew. Chem., Int. Ed.* **2009**, *48* (7), 1271.

6. Pires, M. M.; Chmielewski, J., *J. Am. Chem. Soc.* **2009**, *131* (7), 2706.

7. Bastings, M. M. C.; de Greef, T. F. A.; van Dongen, J. L. J.; Merkx, M.; Meijer, E. W., *Chem. Sci.* **2010**, *1* (1), 79.

8. Seeman, N. C., *J. Theor. Biol.* **1982**, *99* (2), 237; Kallenbach, N. R.; Ma, R. I.; Seeman, N. C., *Nature* **1983**, *305* (5937), 829.

9. McLaughlin, C. K.; Hamblin, G. D.; Sleiman, H. F., *Chem. Soc. Rev.* **2011**, *40* (12), 5647.

10. Niemeyer, C. M., *Curr. Opin. Chem. Biol.* **2000**, *4* (6), 609.

11. Winfree, E.; Liu, F.; Wenzler, L. A.; Seeman, N. C., *Nature* **1998**, *394* (6693), 539.

12. Lund, K.; Liu, Y.; Lindsay, S.; Yan, H., *J. Am. Chem. Soc.* **2005**, *127* (50), 17606; Park, S. H.; Pistol, C.; Ahn, S. J.; Reif, J. H.; Lebeck, A. R.; Dwyer, C.; LaBean, T. H., *Angew. Chem., Int. Ed.* **2006**, *45* (5), 735.

13. Rothemund, P. W. K., *Nature* **2006**, 440 (7082), 297.

14. Lin, C.; Liu, Y.; Yan, H., *Biochemistry* **2009**, *48* (8), 1663.

15. Park, S. H.; Yin, P.; Liu, Y.; Reif, J. H.; LaBean, T. H.; Yan, H., *Nano Lett.* **2005**, *5* (4), 729.

16. Le, J. D.; Pinto, Y.; Seeman, N. C.; Musier-Forsyth, K.; Taton, T. A.; Kiehl, R. A., *Nano Lett.* **2004**, *4* (12), 2343.

17. Steinhauer, C.; Jungmann, R.; Sobey, T. L.; Simmel, F. C.; Tinnefeld, P., *Angew. Chem., Int. Ed.* **2009**, *48* (47), 8870.

18. Kuzuya, A.; Kimura, M.; Numajiri, K.; Koshi, N.; Ohnishi, T.; Okada, F.; Komiyama, M., *ChemBioChem* **2009**, *10* (11), 1811.

19. Aldaye, F. A.; Sleiman, H. F., *J. Am. Chem. Soc.* **2007**, *129* (44), 13376.

20. Aldaye, F. A.; Lo, P. K.; Karam, P.; McLaughlin, C. K.; Cosa, G.; Sleiman, H. F., *Nat. Nanotechnol.* **2009**, *4* (6), 349.

21. Lo, P. K.; Karam, P.; Aldaye, F. A.; McLaughlin, C. K.; Hamblin, G. D.; Cosa, G.; Sleiman, H. F., *Nat. Chem.* **2010**, *2* (4), 319.

22. Boerjesson, K.; Lundberg, E. P.; Woller, J. G.; Norden, B.; Albinsson, B., *Angew. Chem., Int. Ed.* **2011**, *50* (36), 8312.

23. de la Rica, R.; Matsui, H., *Chem. Soc. Rev.* **2010**, *39* (9), 3499.

24. Shenton, W.; Pum, D.; Sleytr, U. B.; Mann, S., *Nature* **1997**, *389* (6651), 585.

25. Sleytr, U. B.; Messner, P.; Pum, D.; Sara, M., *Angew. Chem., Int. Ed.* **1999**, *38* (8), 1034.

26. Ringler, P.; Schulz, G. E., *Science* **2003**, *302* (5642), 106.

27. Burazerovic, S.; Gradinaru, J.; Pierron, J.; Ward, T. R., *Angew. Chem., Int. Ed.* **2007**, *46* (29), 5510.

28. Kaur, P.; Maeda, Y.; Mutter, A. C.; Matsunaga, T.; Xu, Y.; Matsui, H., *Angew. Chem., Int. Ed.* **2010**, *49* (45), 8375.

29. Douglas, T.; Young, M., *Nature* **1998**, *393* (6681), 152; Shenton, W.; Mann, S.; Colfen, H.; Bacher, A.; Fischer, M., *Angew. Chem., Int. Ed.* **2001**, *40* (2), 442; Douglas, T.; Young, M., S*cience* **2006**, *312* (5775), 873.

30. Uchida, M.; Klem, M. T.; Allen, M.; Suci, P.; Flenniken, M.; Gillitzer, E.; Varpness, Z.; Liepold, L. O.; Young, M.; Douglas, T., *Adv. Mater.* **2007**, *19* (8), 1025.

31. Ghosh, D.; Lee, Y.; Thomas, S.; Kohli, A. G.; Yun, D. S.; Belcher, A. M.; Kelly, K. A., *Nat. Nanotechnol.* **2012**, *7* (10), 677.

32. Witus, L. S.; Francis, M. B., *Acc. Chem. Res.* **2011**, *44* (9), 774.

33. Miller, R. A.; Presley, A. D.; Francis, M. B., *J. Am. Chem. Soc.* **2007**, *129* (11), 3104.

34. Nam, K. T.; Kim, D.-W.; Yoo, P. J.; Chiang, C.-Y.; Meethong, N.; Hammond, P. T.; Chiang, Y.-M.; Belcher, A. M., *Science* **2006**, *312* (5775), 885.

35. Nam, K. T.; Wartena, R.; Yoo, P. J.; Liau, F. W.; Lee, Y. J.; Chiang, Y.-M.; Hammond, P. T.; Belcher, A. M., *Proc. Natl. Acad. Sci.* **2008,** *105* (45), 17227.

36. Jonkheijm, P.; Weinrich, D.; Schroeder, H.; Niemeyer, C. M.; Waldmann, H., *Angew. Chem., Int. Ed.* **2008**, *47* (50), 9618.

37. Ulman, A., *Chem. Rev.* **1996**, *96* (4), 1533.

38. Love, J. C.; Estroff, L. A.; Kriebel, J. K.; Nuzzo, R. G.; Whitesides, G. M., *Chem. Rev.* **2005**, *105* (4), 1103.

39. Nuzzo, R. G.; Allara, D. L., *J. Am. Chem. Soc.* **1983**, *105* (13), 4481.

40. Lahiri, J.; Ostuni, E.; Whitesides, G. M., *Langmuir* **1999**, *15* (6), 2055; Bain, C. D.; Whitesides, G. M., *Science* **1988**, *240* (4848), 62; Bain, C. D.; Troughton, E. B.; Tao, Y. T.; Evall, J.; Whitesides, G. M.; Nuzzo, R. G., *J. Am. Chem. Soc.* **1989**, *111* (1), 321; Pale-Grosdemange, C.; Simon, E. S.; Prime, K. L.; Whitesides, G. M., *J. Am. Chem. Soc.* **1991**, 113 (1), 12; Prime, K. L.; Whitesides, G. M., *Science* **1991**, *252* (5009), 1164; Prime, K. L.; Whitesides, G. M., *J. Am. Chem. Soc.* **1993**, *115* (23), 10714; Sigal, G. B.; Bamdad, C.; Barberis, A.; Strominger, J.; Whitesides, G. M., *Anal. Chem.* **1996**, *68* (3), 490; Sigal, G. B.; Mrksich, M.; Whitesides, G. M., *J. Am. Chem. Soc.* **1998**, *120* (14), 3464; Xia, Y.; Whitesides, G. M., *Angew. Chem., Int. Ed.* **1998**, *37* (5), 550; Lahiri, J.; Isaacs, L.; Grzybowski, B.; Carbeck, J. D.; Whitesides, G. M., *Langmuir* **1999**, *15* (21), 7186.

41. Harder, P.; Grunze, M.; Dahint, R.; Whitesides, G. M.; Laibinis, P. E., *J. Phys. Chem. B* **1998**, *102* (2), 426.

42. Zolk, M.; Eisert, F.; Pipper, J.; Herrwerth, S.; Eck, W.; Buck, M.; Grunze, M., *Langmuir* **2000**, *16* (14), 5849.

43. Li, L.; Chen, S.; Zheng, J.; Ratner, B. D.; Jiang, S., *J. Phys. Chem. B* **2005**, *109* (7), 2934.

44. Haeussling, L.; Ringsdorf, H.; Schmitt, F. J.; Knoll, W., *Langmuir* **1991**, *7* (9), 1837.

45. Spinke, J.; Liley, M.; Guder, H. J.; Angermaier, L.; Knoll, W., *Langmuir* **1993**, *9* (7), 1821.

46. Perez-Luna, V. H.; O'Brien, M. J.; Opperman, K. A.; Hampton, P. D.; Lopez, G. P.; Klumb, L. A.; Stayton, P. S., *J. Am. Chem. Soc.* **1999**, *121* (27), 6469; Jung, L. S.; Nelson, K. E.; Stayton, P. S.; Campbell, C. T., *Langmuir* **2000**, *16* (24), 9421.

47. Azzaroni, O.; Mir, M.; Knoll, W., *J. Phys. Chem. B* **2007**, *111* (48), 13499.

48. Hoeoek, F.; Ray, A.; Norden, B.; Kasemo, B., *Langmuir* **2001**, 17 (26), 8305.

49. Tokuhisa, H.; Liu, J. a.; Omori, K.; Kanesato, M.; Hiratani, K.; Baker, L. A., *Langmuir* **2009**, *25* (3), 1633.

50. Nilebaeck, E.; Feuz, L.; Uddenberg, H.; Valiokas, R.; Svedhem, S., B*iosens. Bioelectron.* **2011**, *28* (1), 407.

51. Morris, V. J.; Kirby, A. R.; Gunning, A. P., *Atomic Force Microscopy for Biologists*. Imperial College Press: London **1999** p332.

52. Binnig, g.; Quate, C. F.; Gerber, C., *Phys. Rev. Lett.* **1986**, *56* (9), 930.

53. Young, R.; Ward, J.; Scire, F., *Rev. Sci. Inst.* **1972**, *43* (7), 999.

54. Bippes, C. A.; Muller, D. J., *Rep. Prog. Phys.* **2011**, *74* (8), 086601/1.

55. Muller, D. J.; Sass, H.-J.; Muller, S. A.; Buldt, G.; Engel, A., *J. Mol. Biol.* **1999**, *285* (5), 1903.

56. Williams, D. B.; Carter, C. B., *Transmission Electron Microscopy*. Springer ed., **1996**, p 760.

57. McMullan, D.; Pawley, J. B.; Joy, D. C.; Schatten, H.; Albrecht, R.; Meyer, D.; Boyde, A.; Erlandsen, S. L.; Cox, G.; Vesk, P.; Dibbayawan, T.; Baskin, T. I.; Vesk, M.; Walther, P.; Newbury, D. E., *Biological Low-Voltage Scanning Elecron Microscopy*. Springer ed.; **2008**; p 318.

58. De Feijter, J. A.; Benjamins, J.; Veer, F. A., *Biopolymers* **1978**, *17* (7), 1759.

59. Liedberg, B.; Lundstroem, I.; Stenberg, E., *Sens. Actuators, B* **1993**, *B11* (1-3), 63.

60. Sauerbrey, *G., Z. Phys.* **1959**, *155*, 206.

61. Reimhult, E.; Larsson, C.; Kasemo, B.; Hook, F., *Anal Chem* **2004**, *76* (24), 7211.

62. Rodahl, M.; Hook, F.; Fredriksson, C.; Keller, C. A.; Krozer, A.; Brzezinski, P.; Voino va, M.; Kasemo, B., *Faraday Discuss.* **1997**, *107*, 229.

63. Wang, G.; Rodahl, M.; Edvardsson, M.; Svedhem, S.; Ohlsson, G.; Hook, F.; Kasemo, B., *Rev. Sci. Instrum.* **2008**, *79* (7), 075107/1; Cho, N.-J.; Frank, C. W.; Kasemo, B.; Hook, F., *Nat. Protoc.* **2010**, *5* (6), 1096.

64. Rodahl, M.; Hook, F.; Krozer, A.; Brzezinski, P.; Kasemo, B., *Rev. Sci. Instrum.* **1995**, *66* (7), 3924.

65. Wilbur, D. S.; Pathare, P. M.; Hamlin, D. K.; Weerawarna, S. A., *Bioconjugate Chem.* **1997**, *8* (6), 819.

66. Hamblett, K. J.; Kegley, B. B.; Hamlin, D. K.; Chyan, M.-K.; Hyre, D. E.; Press, O. W.; Wilbur, D. S.; Stayton, P. S., *Bioconjugate Chem.* **2002**, *13* (3), 588.

Chapter II

Results and Discussion

2 Results and Discussion

2.1 Synthesis of BBA-Based Connectors

2.1.1 Bis-Biotin Anchor (BBA)

The biotin dimer **1** was readily synthesized (Scheme 1), according to the published experimental procedures.[1] Even though Stayton and Wilbur used tetrafluorophenol to activate biotin and diacid **7**, we used pentafluorophenol (PFP) for cost reasons, and good yields were obtained.

Biotin-PFP **5** was prepared via the formation of an O-acylisourea intermediate using DCC and purification was performed by recrystallization in MeOH. An excess of dioxadiamine was acylated with biotin-PFP **5** to afford compound **6** with 61% yield. Alternatively, the reac-

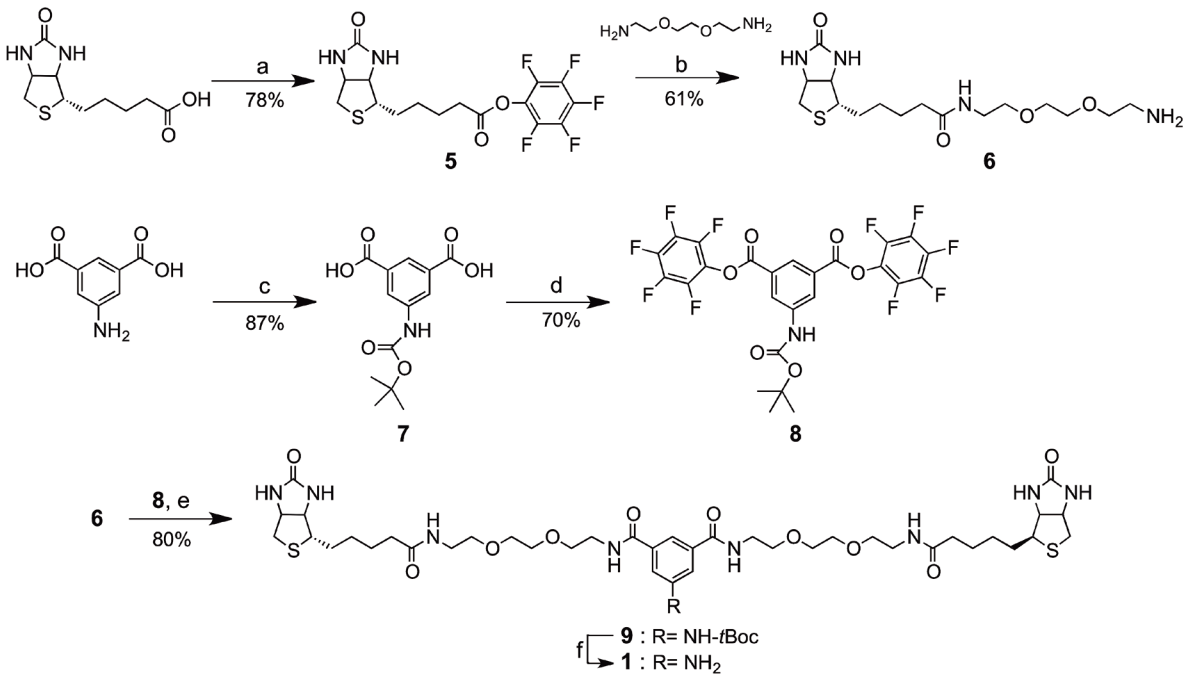

Scheme 1 a) DCC, PFP, DMF, 60°C, 4h. b) Dioxadiamine, Et_3N, DMF, RT, 5h. c) DMF/H_2O 1:1, NaOH, Boc_2O, 0°C→RT, 1h. d) PFP, DCC, DMF, 4h. e) **8**, Et_3N, DMF, 5h. f) TFA, 30 min., RT, quantitative.

tion was carried out with crude compound **5**; the dicyclohexylurea (DCU) was filtered off from the reaction mixture and crude compound **5** was directly reacted with an excess of dioxadiamine to afford **6** with an overall yield of 49% (see Experimental section). dicarbonate to afford the Boc-protected amine **7**, which was further reacted with PFP, using DCC, to afford the activated PFP-diester in 70% yield. The coupling of **8** with an excess of biotin derivative **6** provided Boc-protected BBA **9**.

Compound **9** was initially purified by column chromatography on silica gel, which was a lenghty procedure. Therefore, a new purification method using preparative reversed-phase HPLC was developped. That enabled us to reduce the time required to purify compound **9** - from 6 h down to 20 minutes - and to increase the reaction yield - from 71 up to 80%. A representative RP-HPLC chromatogram from the reaction mixture and a HPLC / ESI-MS analysis of purified compound **9** are annexed in Appendix 1. BBA (**1**) was finally liberated by the treatment of compound **9** with TFA. With BBA (**1**) in hand, attention turned to the synthesis of linear ligand BBA_2 (**2**).

2.1.2 Linear Connector - BBA_2

The synthesis of compound **12** was first studied as a model reaction (Sheme 2). Based on a published procedure,[2] activation of 3,6,9-trioxaundecanedioic acid with PFP, using EDC,

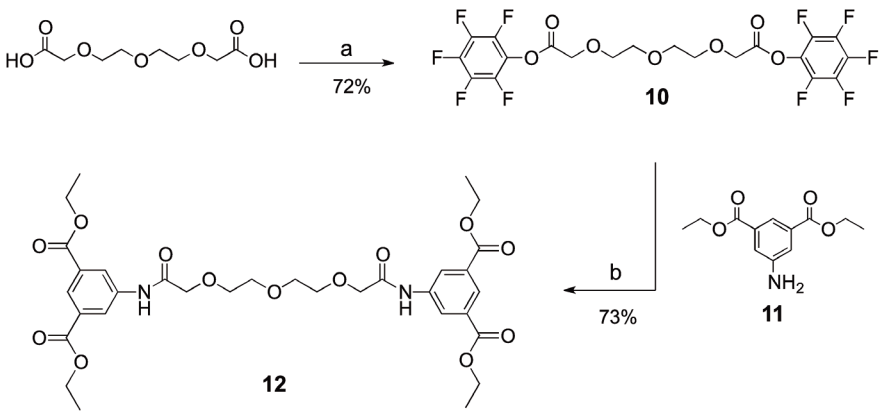

Scheme 2 Linear connector model reaction a) EDC, PFP, CH_2Cl_2, RT, 14h. b) Et_3N, **11**, DMF, RT, 6h

afforded PFP-activated diester **10** in good yields. After acid catalyzed esterification of 5-aminoisophtalic acid in EtOH, the aromatic amine **11** was coupled to PFP-activated diester **10** to produce model compound **12,** which was purified by precipitation from ethyl acetate into hexane. Three *in situ* activation-coupling methods were then tested to synthesize compound **12** (Scheme 3). The reactions were only tested on small amount of starting materials and qualitatively analyzed by TLC. When isobutylchloroformate and HOBt-TBTU were used as activating agent, the desired product formed in minority compared to side-products. However,

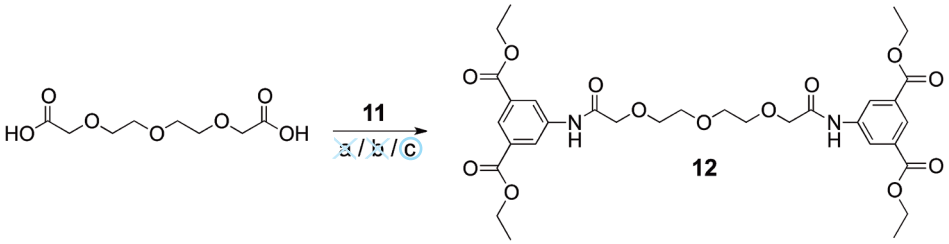

Scheme 3 Linear connector model reaction a) Bu_3N, isobutylchloroformate, **12**, DMF, 0°C (1h), RT (12h). b) TBTU, HOBt, DIEA, **12**, DMF, 0°C (1h), RT (12h). c) CDMT, NMM, **12**, RT, 12h.

when CDMT-NMM was used, the TLC showed that all diacid was consumed to form the coupling product **12**. This successful coupling reaction condition was therefore also applied to synthesize target linear connector BBA_2 (**2**). The coupling reaction of BBA (**1**) with PFP-activated diester **10** afforded target compound BBA_2 (**2**) in slightly better yields than the method

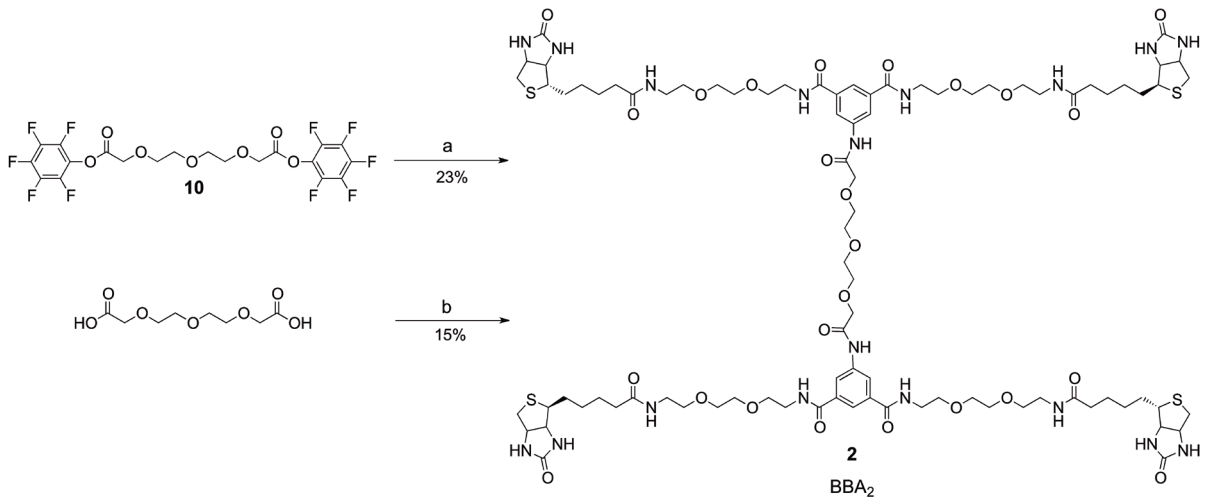

Scheme 4 BBA_2 (**2**) synthesis a) Et_3N, **1**, DMF, 60°C, 24h. b) CDMT, NMM, **1**, DMF, 60°C, 24h.

using CDMT/NMM as coupling agent (Scheme 4). Even though the yields obtained were quite low, compound **2** was isolated in analytically pure form.

The ESI mass spectrum (Fig.1) presented a charged ion peak at 1996.9 mass units with 100% intensity, which corresponds to the sodium adduct $[1974+Na]^+$ of BBA_2 (**2**).

The ^{1}H-NMR spectrum of compound **2** is displayed in Fig.2. The signals from the two aromatic protons of the BBA unit (the doublet at 8.25 ppm and the triplet at 8.05 ppm), and those from biotin were clearly identified and assigned (see Experimental section for hydrogens numbering system and detailed signals attribution). All the signals from 3.80 ppm to 3.33 ppm were assigned to the ethylene glycol methylene protons. The sharp singlet at 4.22 ppm was assigned to the methylene protons alpha to the carbonyl (synthon **10**). The integration ratio of this singlet to the aromatic and biotin protons confirmed the molecular structure of BBA_2 (**2**).

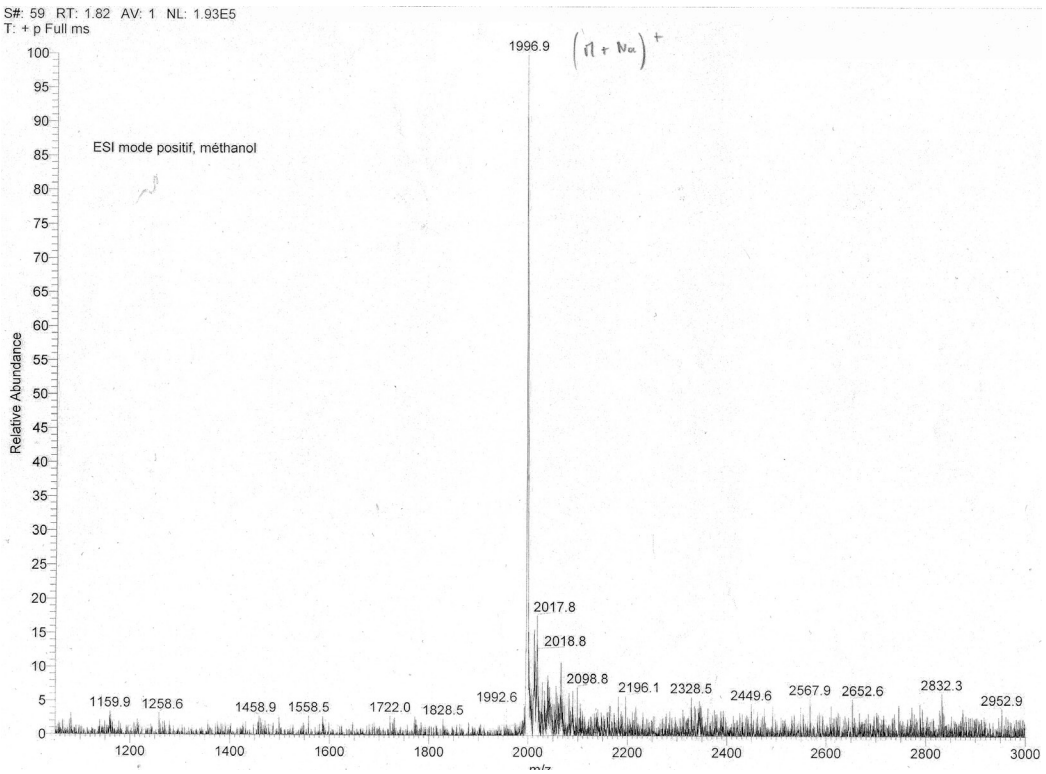

Figure 1 ESI mass spectrum of BBA_2 (**2**).

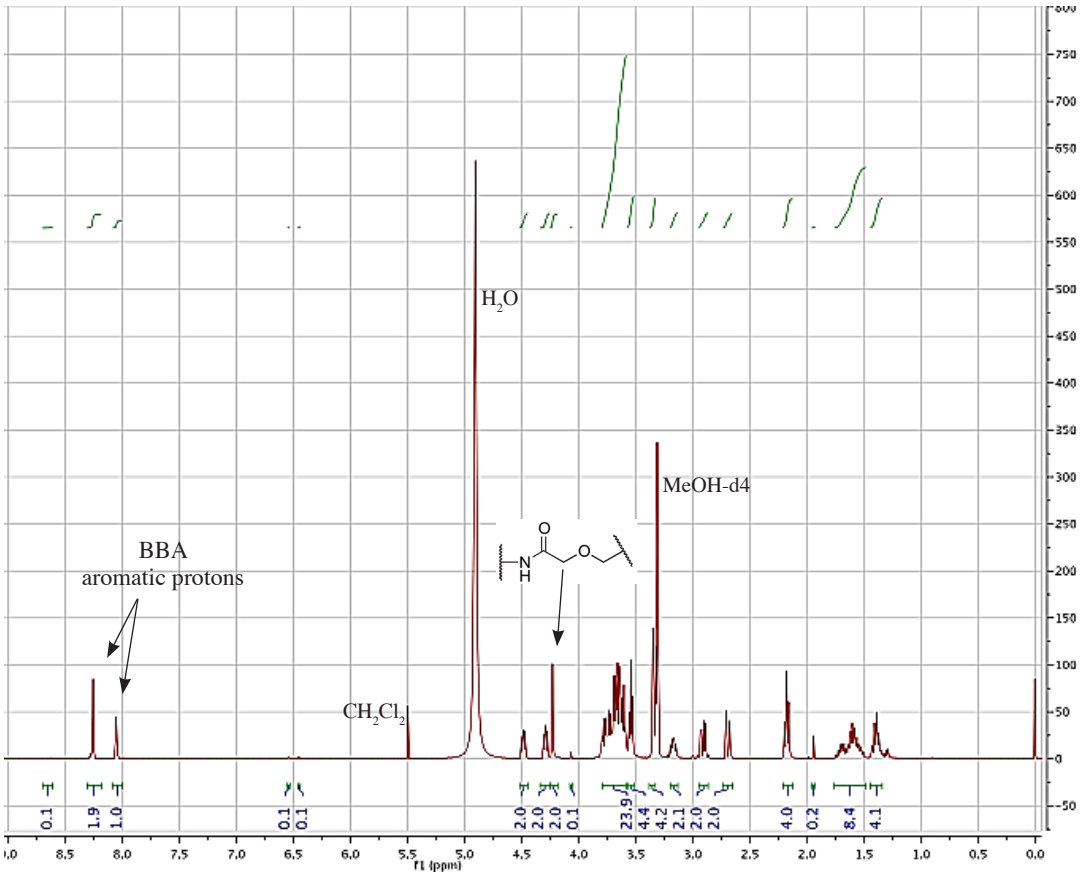

Figure 2 ^{1}H-NMR spectrum of BBA_2 (**2**).

2.1.3 Trifurcated Connector - BBA_3

A lot of efforts were invested in the synthesis and purification of trifurcated BBA-based connectors. Two different synthetic routes using peptide coupling chemistry were used to obtain BBA_3-1 (**3**) (Scheme 5). Dr Koji Oohora (Osaka University, Japan), who worked in our lab during six months, synthesized analogue BBA_3-2 (**13**) by means of click chemistry. Even though the synthetic approach of Dr Oohora has shown to be superior in terms of reaction yields, both approaches are discussed in this section.

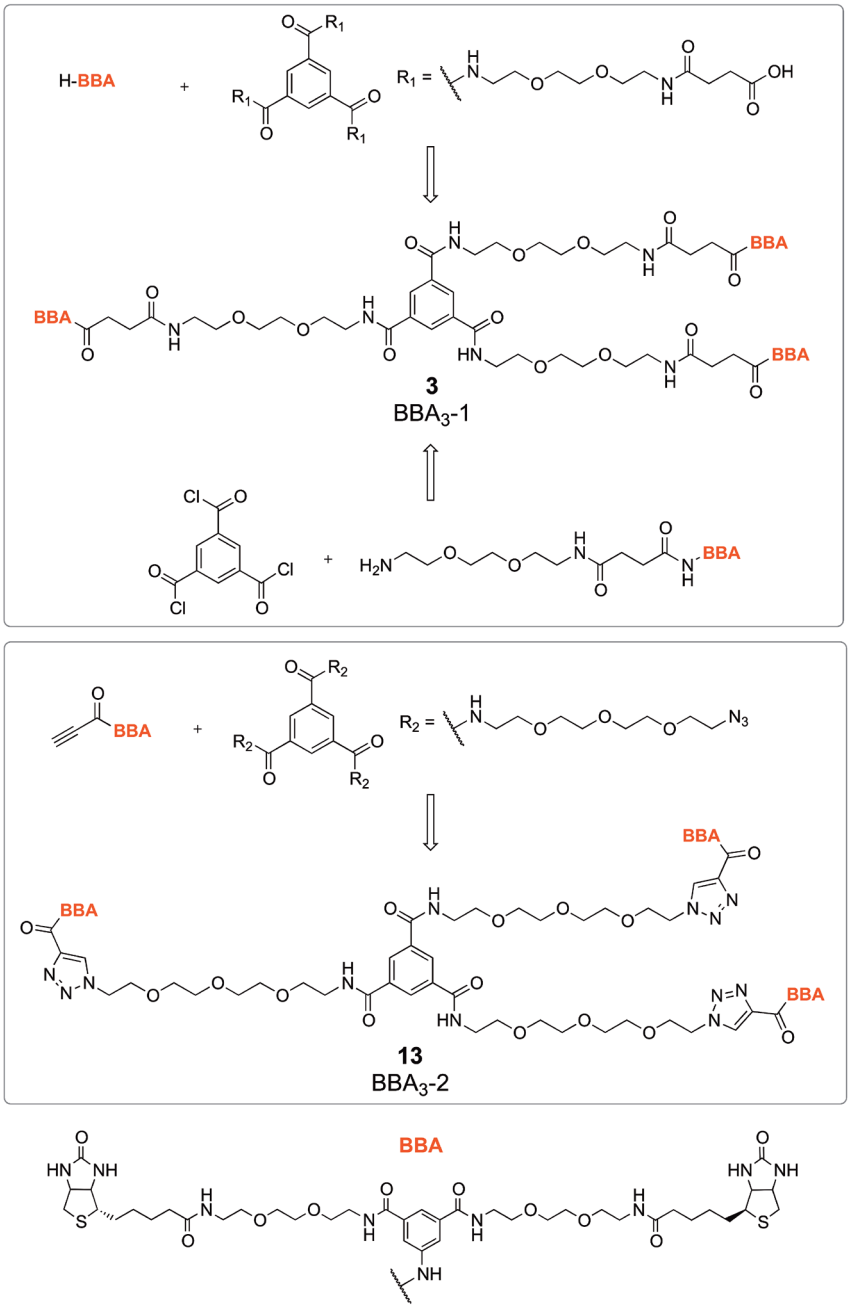

Scheme 5 Synthetic overview of trifurcated connectors BBA_3-1 (**3**) and BBA_3-2 (**13**).

The first synthetic route leading to BBA_3-1 (**3**) began with the formation of compound **16** (scheme 6). Following a published procedure,[3] dioxadiamine was reacted with di-tert-butyl dicarbonate to give the monoprotected diamine **14** in 42% yield. A three-fold excess of monoamine **14** was then reacted with trimesoyl chloride, to afford the tris Boc-protected amine derivative **15** in 55% yield. The Boc groups were removed with TFA and

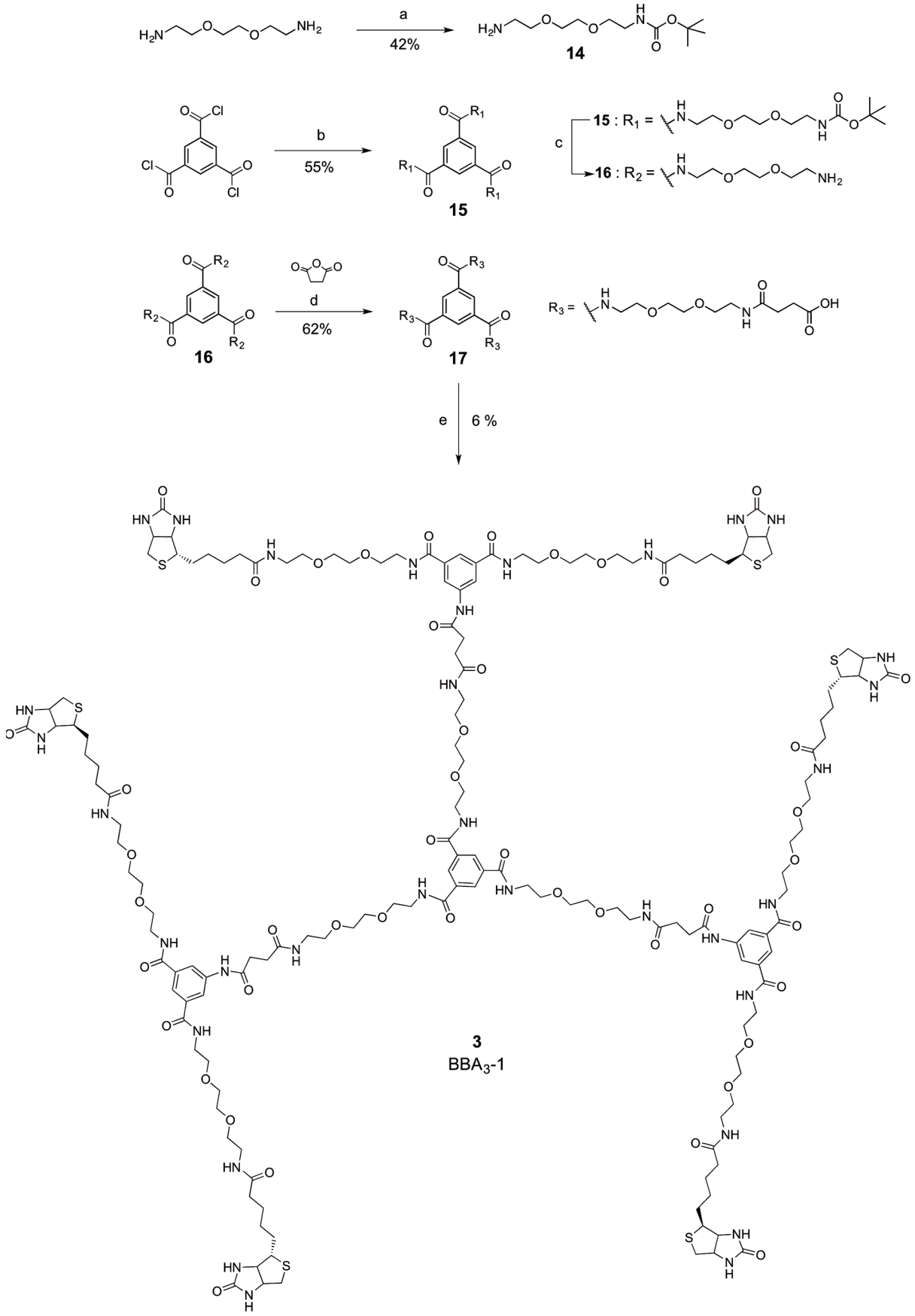

Scheme 6 Diverging synthetic route to BBA_3-1 (**3**). Reagents and conditions: a) Boc_2O, DIEA, CH_2Cl_2, RT, 3h. b) **14**, Et_3N, CH_2Cl_2, 0°C→25°C, 12h. c) TFA, CH_2Cl_2, 1h. d) Succinic anhydride, CH_3CN/DMF, 40ºC, 10h. e) CDMT/NMM, **1**, DMF, 60°C, 30h.

the liberated triamine was converted to the corresponding triacid **17**, using succinic acid anhydride,[4] in 62% yield. The peptide coupling reaction of amino compound **1** with triacid **19**, using CDMT and NMM, afforded BBA_3-1 (**3**). The reaction proceeded in very poor yield (6%). Besides the expected mono- and bis-coupled side products, LC-MS analysis from the crude reaction mixture of BBA_3-1 (**3**) (see Appendix 1) revealed that cyclisation of the amic acid moieties occured, leading to the formation of the corresponding imide rings (scheme 7) as the remaining side products.

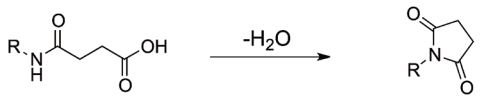

Scheme 7 Amic acid undergoing cyclisation with the elimination of water and formation of imide ring.[5]

The purification of BBA_3-1 (**3**) by chromatography on silica gel and by reversed-phase was attempted but the biscoupled side-product persistently contaminated BBA_3-1 (**3**). In view of the difficulties met in the synthesis and purification of BBA_3-1 (**3**), an alternative convergent synthetic route was investigated.

Monoprotected amine **14** was reacted with excess succinic anhydride in acetonitrile to generate the hemisuccinamide **18** (Scheme 8). The coupling of **18** with aromatic amine **1**, using CDMT and NMM, produced the Boc-protected amine derivative **19** in 71% yield. The Boc group was removed by treatment with TFA, and the liberated amine was coupled in a three-fold excess to trimesoyl chloride to afford target compound BBA_3-1 (**3**) in 12% yield. That reaction path produced fewer side products than the previous approach (see HPLC-ESI-MS spectra annexed in Appendix 1), and analytically pure material was obtained after purification by chromatography on silica gel.

The ESI mass spectrum of BBA_3-1 (**3**) displayed the triply and quadruply charged ion peaks at m/z: 1199.2 assigned as $[M+3Na]^{3+}$, and m/z: 905.2 assigned as $[M+4Na]^{4+}$ (Fig. 3).

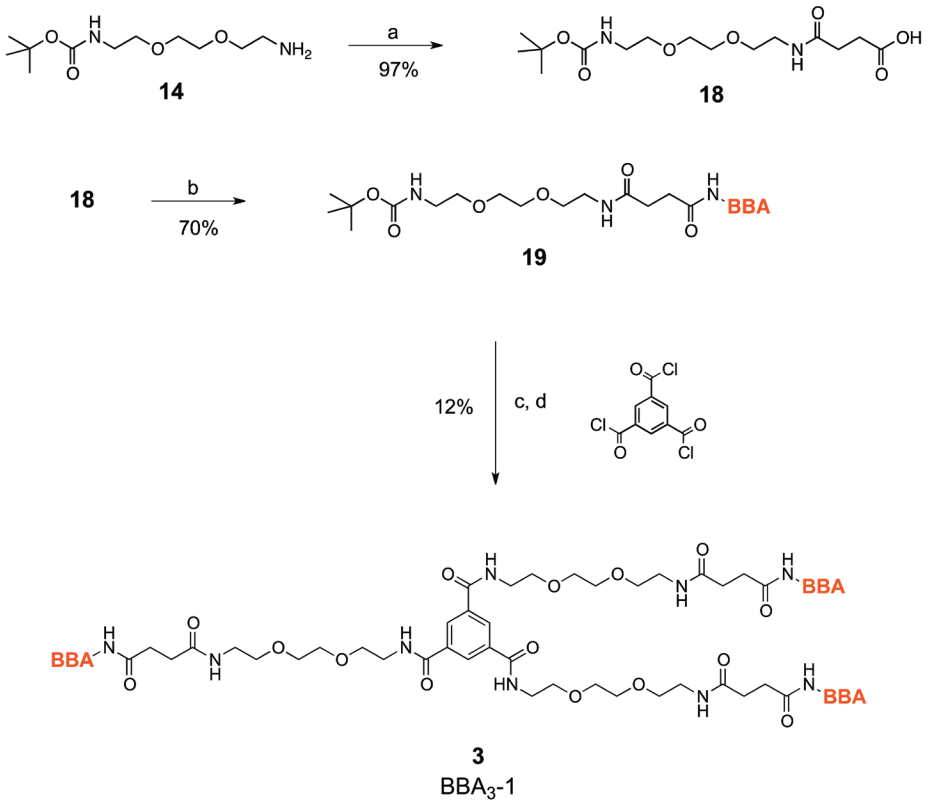

Scheme 8 Convergent synthetic route to BBA_3-1 (**3**). Reagents and conditions: a) Succinic anhydride, CH_3CN, 40ºC, 12h. b) CDMT/NMM, **1**, DMF, 50°C, 10h. c) TFA, CH_2Cl_2. d) Trimesoyl chloride, Et_3N, CH_3Cl/DMF, 0°C→25°C, 30h.

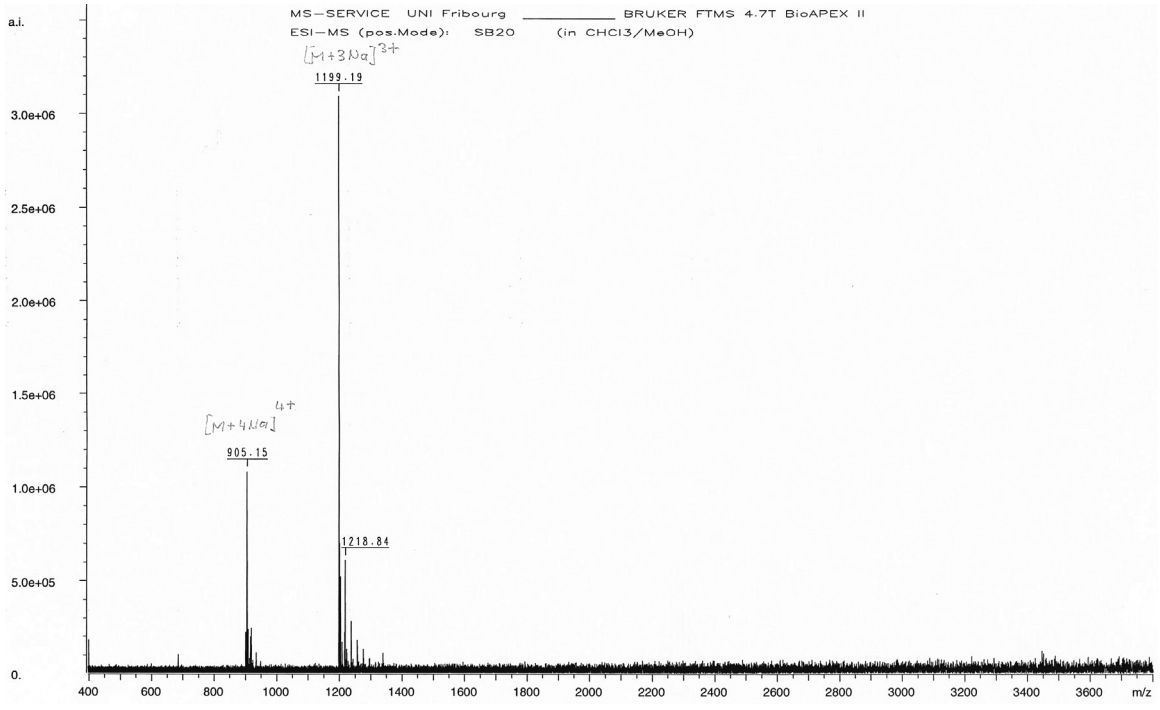

Figure 3 ESI mass spectrum of BBA_3-1 (**3**).

Due to the low solubility of BBA_3-1 (**3**) in the usual volatiles NMR solvents, the ^{1}H-NMR spectrum was recorded in a mixture of $CDCl_3$ and MeOH-d_4 (Fig. 4). The singlet at 8.39 ppm, the least shielded of the aromatic protons, was assigned to the aromatic proton of the trimesate core. It was followed by the aromatic protons of the BBA unit, the doublet at 8.10 ppm and the triplet at 7.94 ppm. All the biotin protons were clearly identified and assigned (see Experimental section for hydrogens numbering system and detailed signals attribution). The integration ratio of the trimesate core proton to the BBA unit, and biotin protons confirmed the molecular structure of BBA_3-1 (**3**).

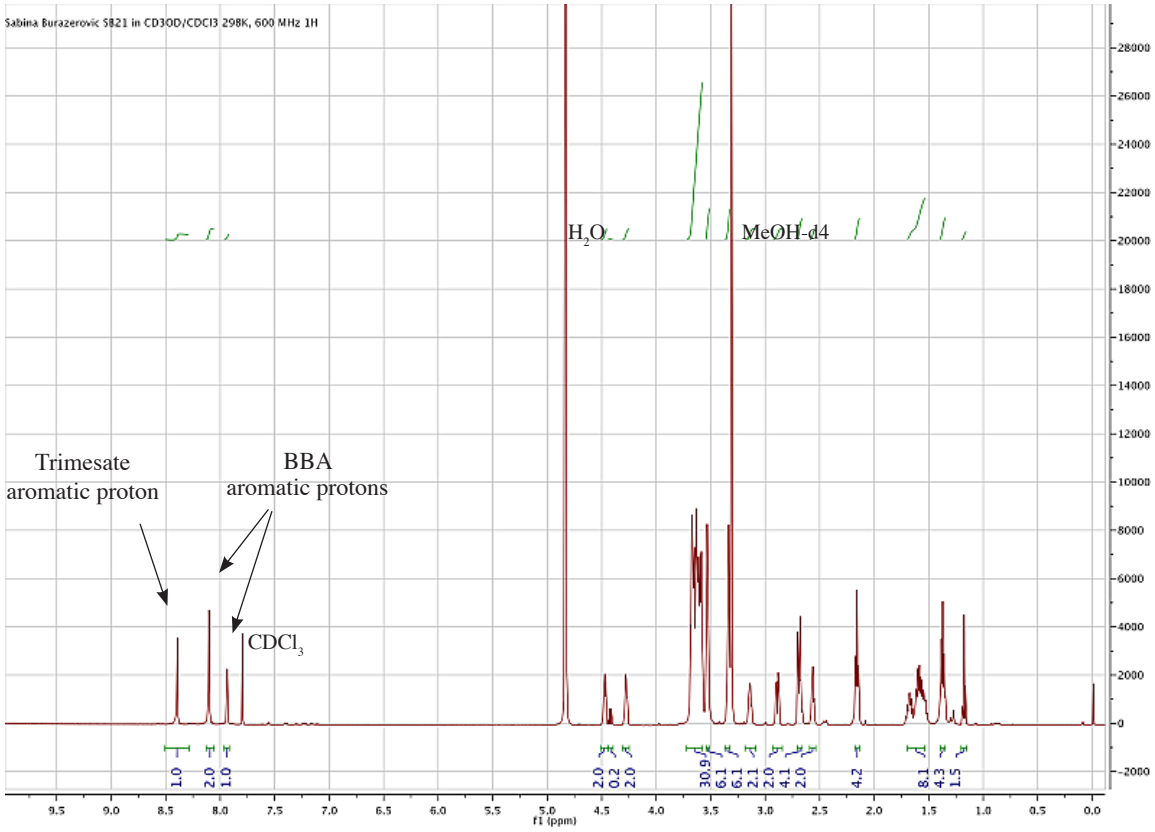

Figure 4 ^{1}H-NMR spectrum of BBA_3-1 (**3**).

A BBA-based tripod analog was synthesized using the Cu(I)-catalyzed Huisgen cycloaddition (click reaction).[6] The synthetic strategy involved 1,3-diplolar cycloaddition of triazido compound **20** to BBA-propiolamide **21** to produce trifurcated ligand BBA_3-2 (**13**) (Scheme 9). Accordingly, the first task was to prepare the triazido derivative. A three-fold excess of 11-azide-

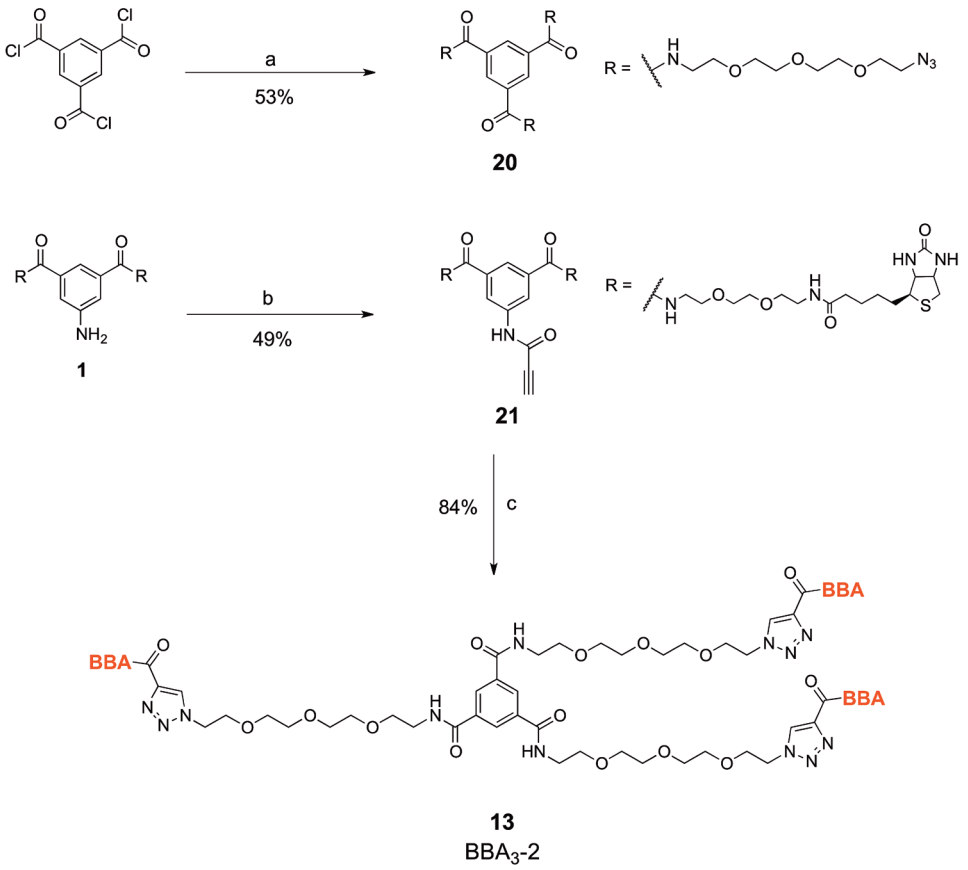

Scheme 9 "Click chemistry" synthesis of BBA_3-2 (**13**). Reagents and conditions: a) 11-azide-3,6,9-trioxaundecan-1-amine, DIPEA, CH_2Cl_2, 0°C→25°C, 12h. b) Propiolic acid, EEDQ, DMF, RT, 48h. d) **20**, DIPEA, $CuSO_4$, sodium ascorbate, DMF/H_2O 5:1, RT, 14h.

3,6,9-trioxaundecan-1-amine in the presence of diisopropylethylamine (DIPEA) was reacted with trimesoyl chloride, to afford the triazido compound **20** in 53% yield. The preparation of compound **21** demanded some efforts. The coupling of propiolic acid with aromatic amine **1** was attempted using usual coupling agents (*e.g.* DCC, EDC and CDMT); however, no coupling product was observed. Propiolamide **21** was successfully synthesized in 49 % yield by reacting aromatic amine **1** with propiolic acid in the presence of 2-ethoxy-1-ethoxycarbonyl-1,2-dihydroquinoline (EEDQ) as coupling agent.

With the triazide **20** and the BBA-propiolamide **21** in hand, synthesis of BBA_3-2 (**13**) via "click chemistry" was attempted. The reaction between triazide **20** and BBA-propiolamide **21** in the presence of 5 mol% of sodium ascorbate and 1 mol% of copper (II) sulfate in a mixture of

5:1 of DMF and water generated tris 1,4-disubstituted triazole product almost quantitatively. Purification by chromatography on silica gel afforded analitically pure BBA_3-2 (**13**) in 84% yield.

ESI mass spectrum of BBA_3-2 (1**3**) displayed the triply and doubly charged ion peaks at m/z:1239.2, assigned as $[M+3Na]^{3+}$, and m/z:1874.3 assigned as $[M+2Na]^{2+}$ (Fig. 5).

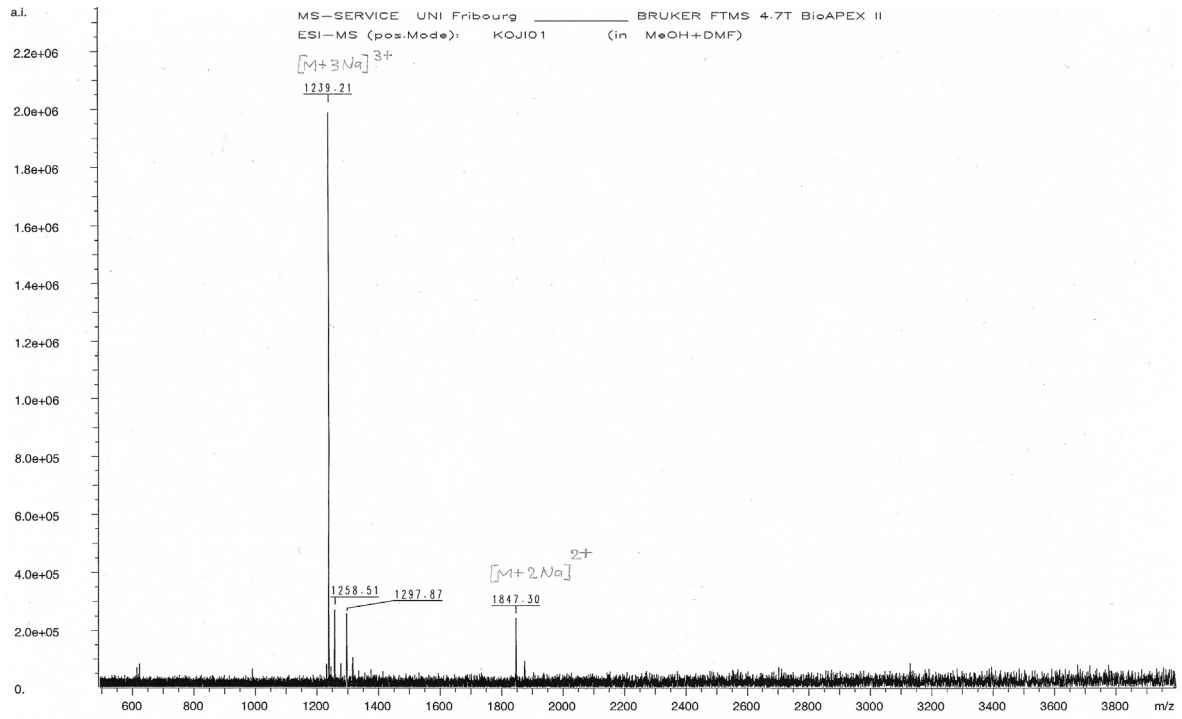

Figure 5 ESI mass spectrum of BBA_3-2 (**13**).

As for BBA_3-1 (**3**), the ^{1}H-NMR spectrum of BBA_3-2 (**13**) was recorded in a mixture of $CDCl_3$ and MeOH-d_4 (Fig. 6). The spectrum is, as expected, very similar to the one from BBA_3-1 (**3**). The singlet at 8.39 ppm was assigned to the aromatic proton of the trimesate core, the least shielded of the aromatic protons. The following signal, a singlet at 8.24 ppm, corresponded to the triazole ring proton. It was followed by the aromatic protons of the BBA unit, the doublet at 8.10 ppm and the triplet at 7.94 ppm. All the biotin protons were clearly identified and assigned (see Experimental section for hydrogens numbering system and detailed signals attribution). The integration ratio of the trimesate core proton to the triazole

ring-, the BBA unit- and biotin protons confirmed the molecular structure of BBA_3-2 (**13**).

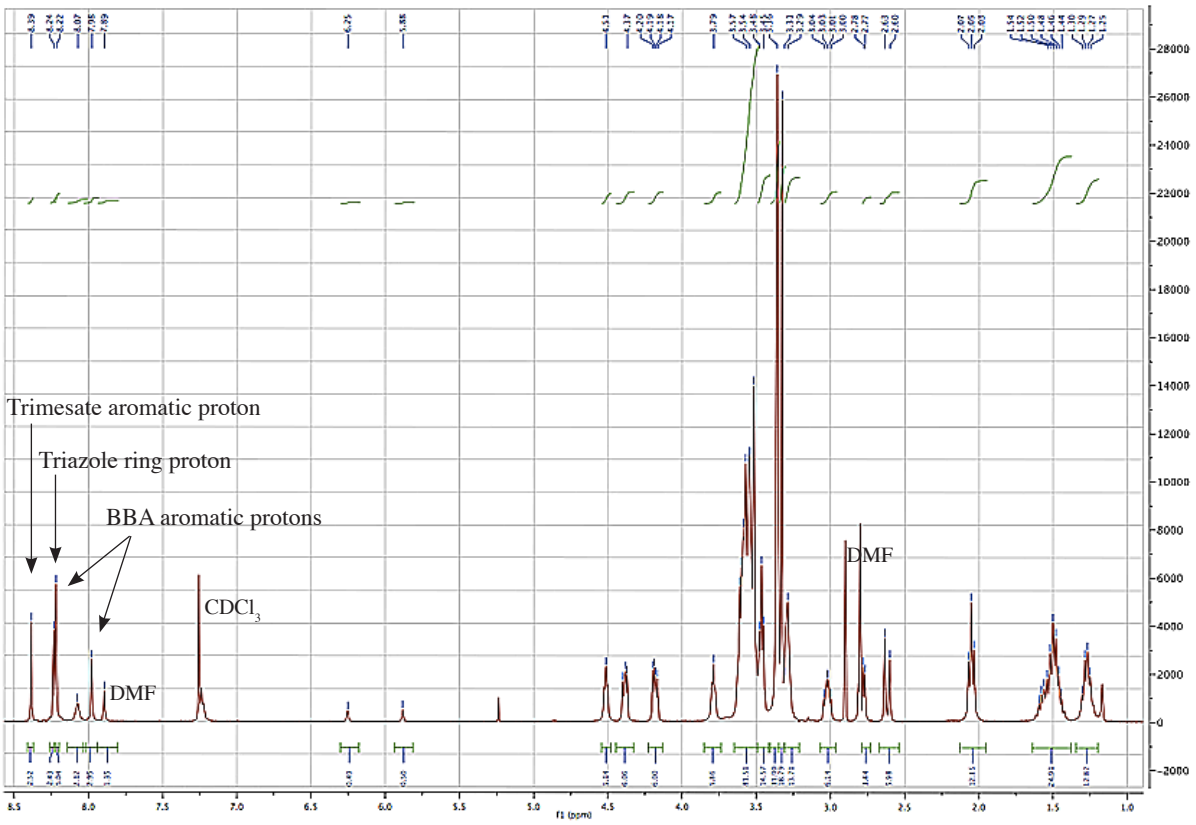

Figure 6 ^{1}H-NMR spectrum of BBA_3-2 (**13**).

2.1.4 Thioalkane BBA-Based Ligand - BBA-S-S-BBA

Compound **4** was obtained in one step by using the previously synthesized compound **19** (Scheme 10). The Boc-group was first removed by treatment with

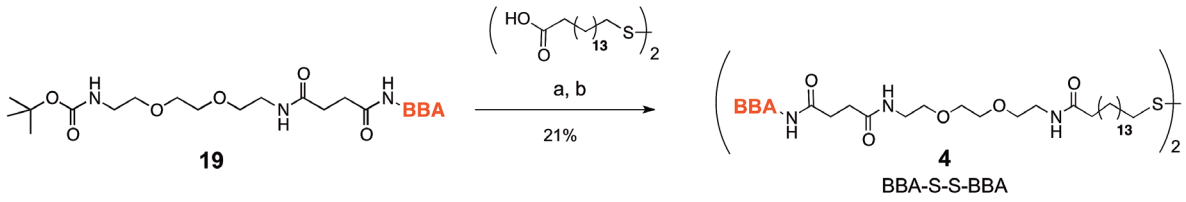

Scheme 10 Synthesis of BBA-S-S-BBA (4). Reagents and conditions: a) TFA, CH_2Cl_2, 1h. b) 16-carboxyhexadecyl disulfide, CDMT/NMM, DMF, 60°C, 15h.

TFA, and a three-fold excess of the liberated amine was acylated with 16-carboxyhexadecyl disulfide, using CDMT/NMM, to produce BBA-S-S-BBA (**4**) in 21% yield.

The ESI mass spectrum of BBA-S-S-BBA (**4**) displayed the doubly, triply and quadruply charged ion peaks at m/z:1416.2 $[M+2Na]^{2+}$, m/z:951.8 $[M+3Na]^{3+}$ and m/z:719.8 assigned as $[M+4Na]^{4+}$ (Fig. 7).

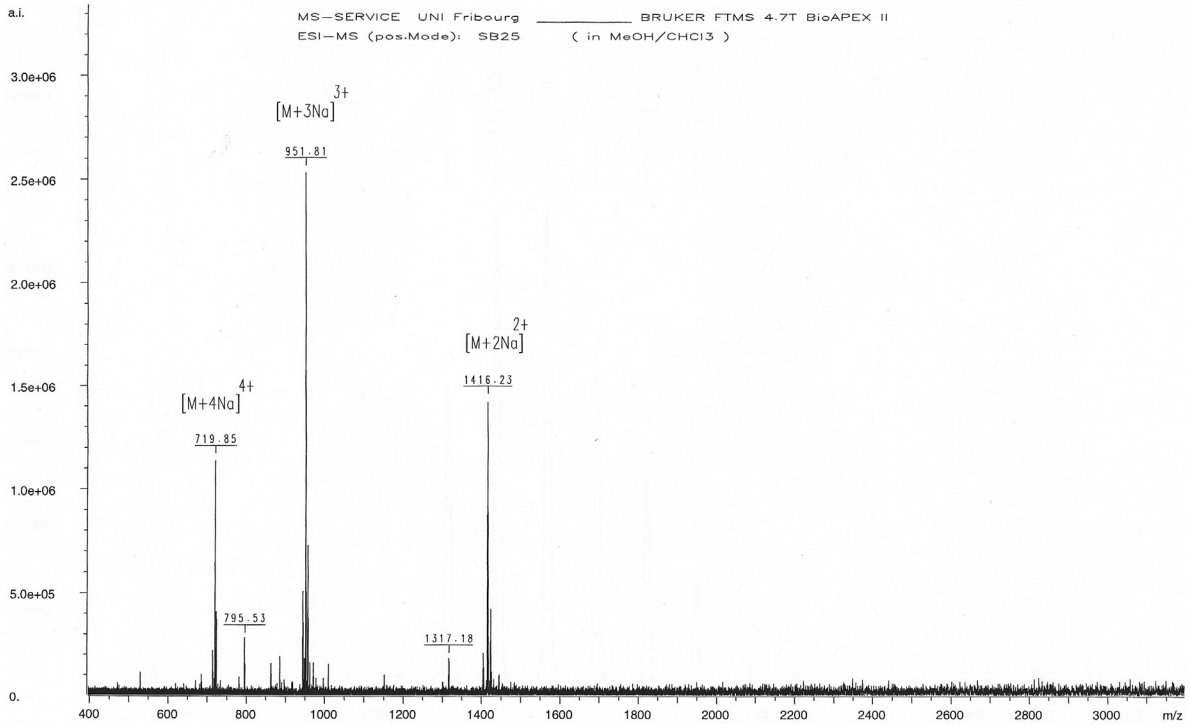

Figure 7 ESI mass spectrum of BBA-S-S-BBA (**4**).

Due to solubility issues, the characterization of BBA-S-S-BBA (**4**) by NMR spectroscopy revealed to be difficult. An NMR experiment in DMF-d_7 was attempted but all the resonance signals were broad and unresolved. Even though the sample was sparingly soluble in $CHCl_3$/MeOH 3:1, the data aquired in this solvent system are presented here.

The ^1H NMR spectrum, recorded in a mixture of $CDCl_3$ and MeOH-d_4 (Fig. 18), presented some overlapping signals, which were assigned by using ^1H-^1H COSY, ^1H-^{13}C HMQC and HMBC experiments (see Appendix 1). The aromatic protons of the BBA unit, the doublet at 8.11 ppm and the triplet at 7.98 ppm, presented an integration ratio differing from the

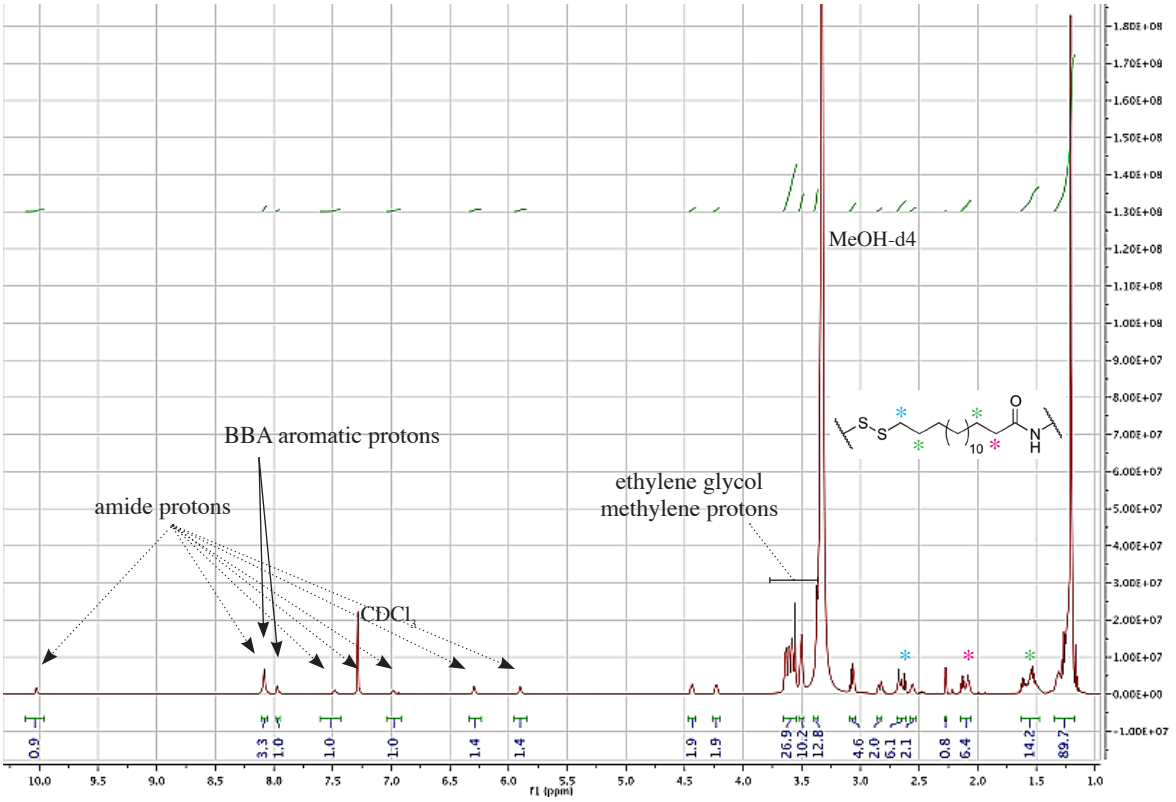

Figure 18 ^{1}H-NMR spectrum of BBA-S-S-BBA (**4**).

expected value (2:1). The 2D NMR experiments revealed the presence of an overlapping signal at 8.10 ppm corresponding to an amide proton. All the signals corresponding to methylene protons from the disulfide diacid synthon were overlapping the biotin protons signals, which complicated the assignment of the resonance signals. The integration of the resonance signals indicated a large excess of protons in the aliphatic region. This was partially explained by the presence of Et_3NH^+ in the sample - a multiplet at 3.05 ppm and a triplet at 1.15 ppm.

Even though all the signals were clearly identified and assigned (see Experimental section for hydrogens numbering system and detailed signals attribution), due to the excess of protons observed in the aliphatic region, the chemical structure of BBA-S-S-BBA (**4**) could not be confirmed by NMR spectroscopy.

With all the BBA-based ligands synthesized and characterized at hand, our focus turned to the study of the self-assembly of SAv with the different BBA-based ligands (Chap. 2.2 - 2.4).

2.1.5 References

1. Hamblett, K. J.; Kegley, B. B.; Hamlin, D. K.; Chyan, M.-K.; Hyre, D. E.; Press, O. W.; Wilbur, D. S.; Stayton, P. S., *Bioconjugate Chem*. **2002**, *13*, 588.

2. Wilbur, D. S.; Pathare, P. M.; Hamlin, D. K.; Weerawarna, S. A., *Bioconjugate Chem*. **1997**, *8* , 819.

3. Mart, R. J.; Liem, K. P.; Wang, X.; Webb, S. J., *J. Am. Chem. Soc*. **2006**, *128*, 14462.

4. Burazerovic, S.; Gradinaru, J.; Pierron, J.; Ward, T. R., *Angew. Chem., Int. Ed*. **2007**, *46*, 5510.

5. Volksen, W., *Adv Pol. Sci*. **1994**, *117*, 111.

6. Rostovtsev, V. V.; Green, L. G.; Fokin, V. V.; Sharpless, K. B., *Angew. Chem., Int. Ed*. **2002**, *41*, 2596.

2.2 Streptavidin Self-Organization from Bulk Solution

Our aim was to program the self-organization of wild-type streptavidin (hereafter referred to as SAv) by using BBA-based ligands (Fig. 1). In the first organization step, the junction

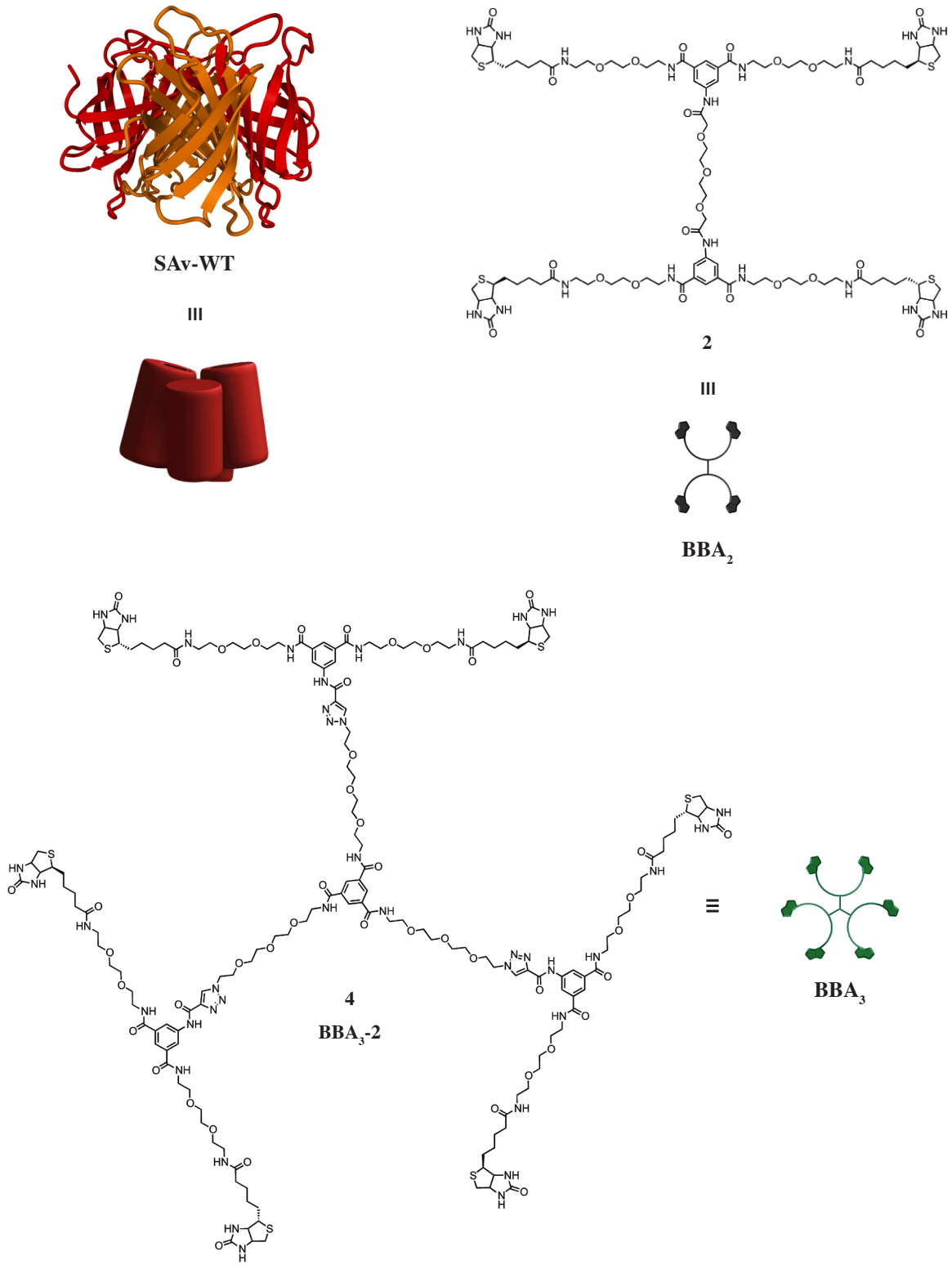

Figure 1 Nanolegos used for the self-organization from bulk solution experiments.

multiplicity between the BBA units contains the intrinsic information about the geometry of the resulting architectures, SAv acting basically as a linear linker in the self-organization process. A one-dimensional linear nano-structure was expected when using a two-way junction such as BBA_2. However, when using a three-way junction

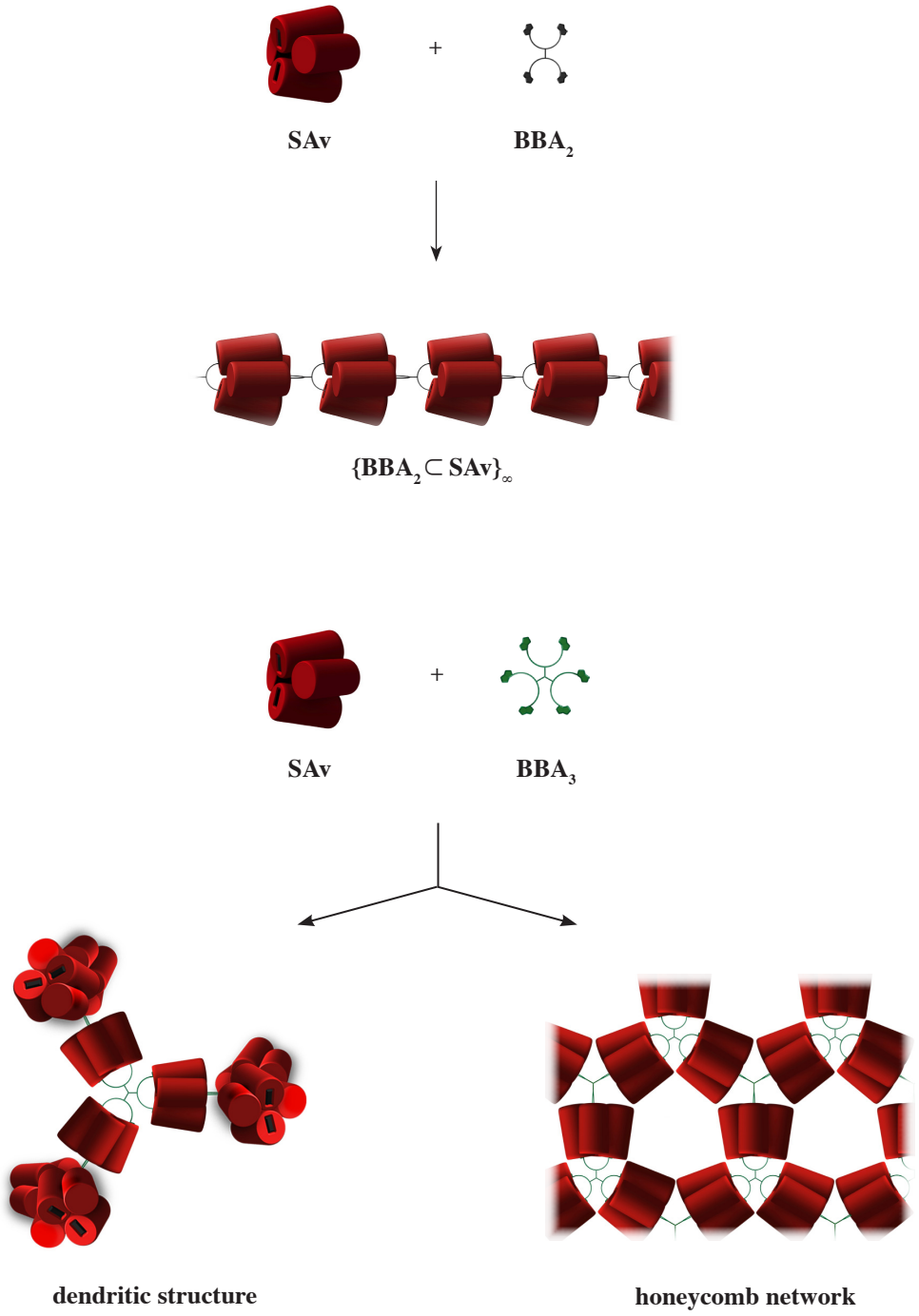

Figure 2 Schematic representation of hypothetical SAv-based nanostructures generated by linear and trifurcated connectors, BBA_2 and BBA_3 respectively.

as BBA_3, two different nano-structures could theoretically be generated; an extended two-dimensional network of honeycombs as basic patterns, or a dendritic structure (Fig. 2). To create a program using BBA-based connectors to organize SAv, polymerization should occur solely along the axial direction of the protein (Fig. 3). This translates into ascertaining the fact that the BBA moiety binds exclusively to two *cis*-related sites in SAv (Fig. 3). The second obvious factor to avoid errors in the programming task is the spacer's length of the molecular junctions; it has to be long enough to circumvent protein-protein repulsion, hence steric hindrance becom-

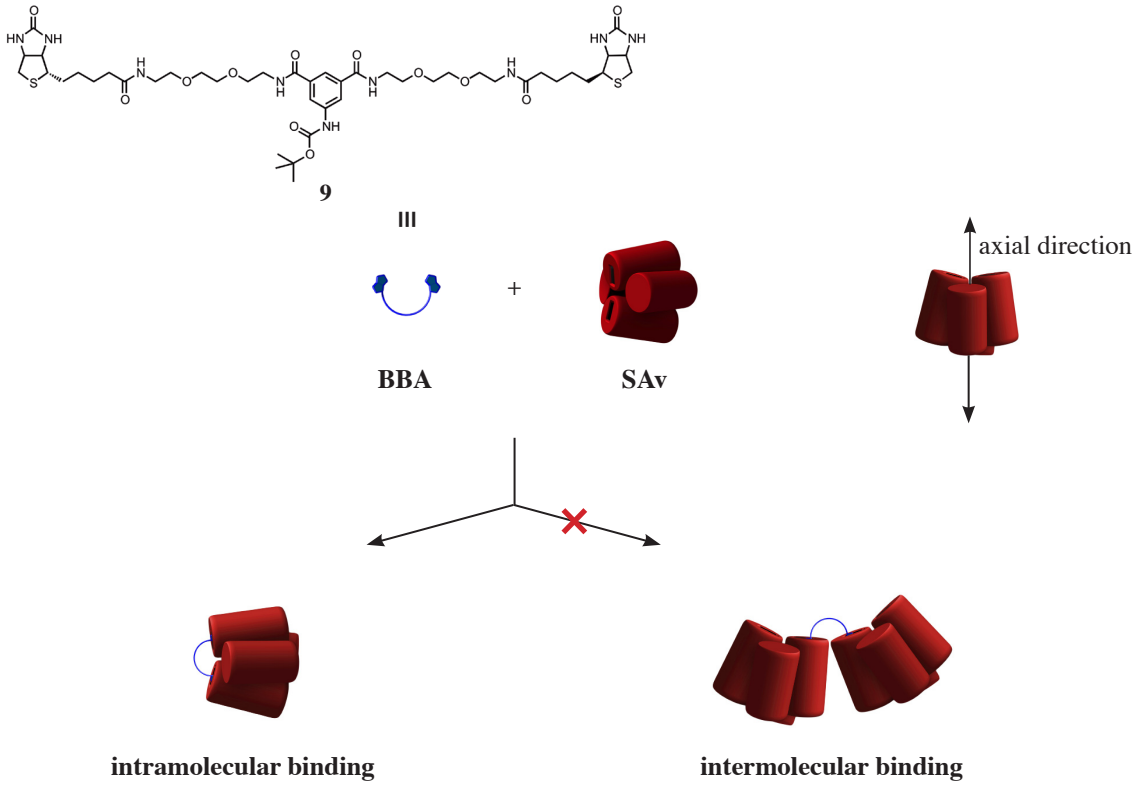

Figure 3 Schematic representation of the two binding possibilities of the **BBA** ligand to SAv. An intramolecular binding where BBA binds to two *cis*-related biotin binding sites, is a prerequisite for successful programmed self-organization.

ing an issue during the self-organization process. If the sources of errors mentioned above are avoided, BBA_2 and BBA_3 should be effective in programming the self-assembly of SAv into a 1D fibril and 2D network or dendritic structure, respectively.

In order to assess the use of BBA-based connectors and SAv as building blocks of a molecular LEGO kit, we proceeded as follow. In a first step, the stoechiometry of binding of each BBA ligands towards SAv was investigated by HABA displacement assays.[1] The binding pattern of

BBA with SAv and the ability of BBA_2 and BBA_3 to polymerize SAv in aqueous solution were then analyzed by SDS-PAGE.[2] Finally, the nanostructures composed of SAv and BBA_2 and/or BBA_3 were scrutinized using electron and probe microscopy.

*N.B.: Both trifurcated **BBA_3-1** and **BBA_3-2** (section 2.1.3) produced the same results for the experiments conducted during this thesis. Since **BBA_3-2** was isolated in bigger amount, all the experiments (in chapter 2.2 and 2.4) could be conducted at least in duplicate with this ligand. Therefore we will present the results obtained with **BBA_3-2** solely, hereafter referred to as **BBA_3**.*

2.2.1 Stoechiometry of Bis-Biotin Ligands Binding

The binding stoechiometry of the different BBA ligands toward SAv was determined by 2-(4'-hydroxyazobenzene)benzoic acid (HABA, a hydrophobic dye weakly bound within the biotin-binding pocket) displacement assays. BBA ligands were titrated into a solution containing HABA-saturated SAv, allowing us to determine the quantity of HABA displaced per quantity of ligand added.[3] The biotin-binding event between the BBA ligands and SAv was

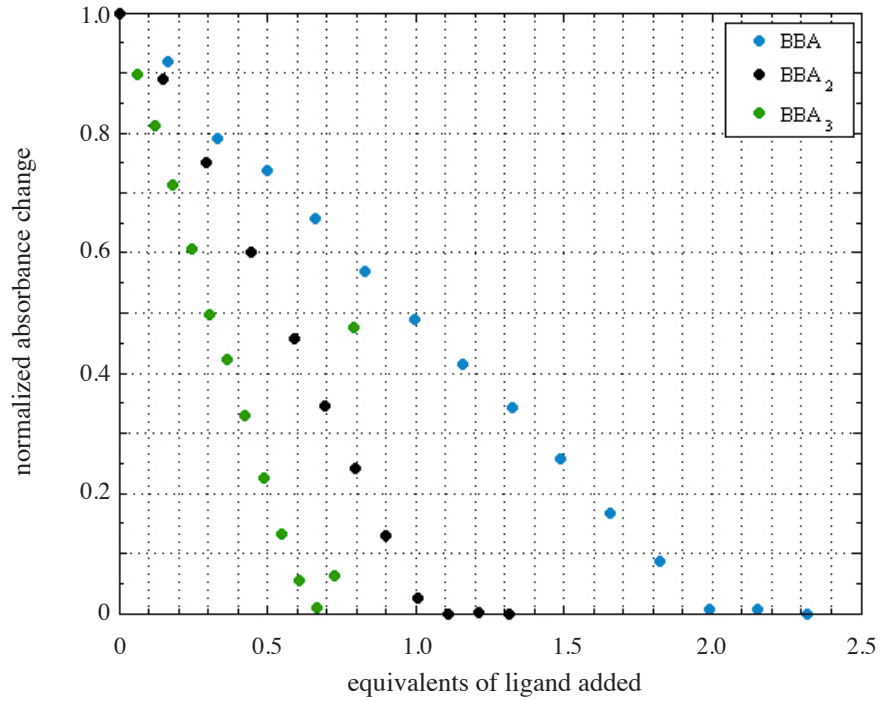

Figure 4 Binding stoechiometry determination; the displacement of HABA ⊂ SAv by BBA, BBA_2 and BBA_3 was followed at 505 nm. The percent change in the OD_{505} is plotted versus the molar equivalent of the competitor added with respect to the concentration of biotin binding sites.

monitored with the disappearance of an induced UV-Vis signal, λ_{max}=505 nm, caused by the displacement of HABA by the BBA ligand. The HABA displacement assays were plotted as the percent change in HABA occupied biotin-binding sites *versus* the ratio of BBA moiety added to the biotin binding-site concentration (Fig. 4). The expected ratio of two BBA molecules per SAv tetramer was observed, confirming the result initially obtained by Hamblett et al.[3] One equivalent (1.03 eq) of BBA_2 per SAv was needed to displace HABA⊂SAv, which corresponds to the molar fraction required to form a 1D co-polymer. As expected, a ratio of 0.67 equivalent of BBA_3 per SAv was observed. When an excess of BBA_3 was added, the solution turned highly turbid. That explains the marked increase in absorbance observed once the equivalence point was exceeded. Nevertheless, these results suggested that BBA_3 has the ability to oligomerize SAv. The binding stoechiometry of each BBA ligands towards SAv being promising, the self-assembly products were then analyzed by SDS-PAGE.

2.2.2 SDS-PAGE Analysis of Streptavidin Self-Assembly from Bulk Solution

Before evaluating the propensity of BBA_2 and BBA_3 to polymerize SAv, we first ascertained the fact that the BBA unit could bind exclusively to two adjacent biotin-binding sites located on one face of a tetrameric SAv. To do so, a SAv solution (PBS 0.1 M, pH 7.4) was mixed with different equivalents of BBA, and incubated for half an hour at room temperature before analysis by SDS-PAGE (8% acrylamide gel).

Although most of the self-assembly experiments throughout this thesis were carried out at concentrations of 1 μM or lower, the standard protocol to analyze SAv by SDS-PAGE in our lab requires a protein concentration of 30 μM.[4] Intermolecular reactions being often favored over intramolecular binding at higher concentration, we performed the experiment at two different SAv concentrations: 30 μM and 0.8 μM. The diluted self-assembly reactions were concentrated using centrifugal filter units (50 KDa cut-off) followed by SDS-PAGE analysis. The results (Fig. 5) suggested that BBA has, to a moderate extent, the ability to bind to two different SAv units. According to the intensity analysis of the different bands, the amount of dimer of tetramer formed in lane 5 can be estimated to 12%. Nevertheless, BBA can unite a

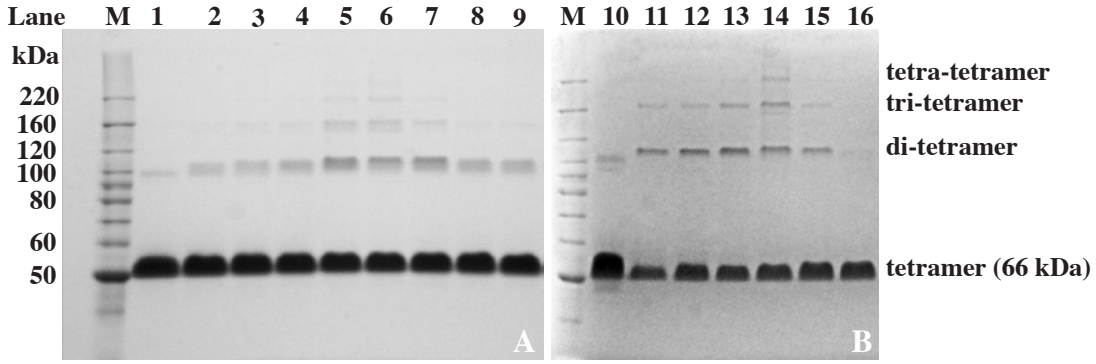

Lane	SAv (eq.)	BBA(eq.)
1 & 10	1	-
2	"	0.25
3 & 11	"	0.5
4	"	0.75
5 & 12	"	1.0
6 & 13	"	1.5
7 & 14	"	1.75
8 & 15	"	2.0
9	"	2.5
16	"	3.0

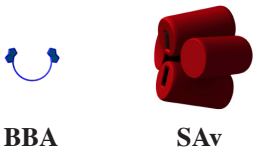

Figure 5 SDS-PAGE (8% acrylamide gel) analysis of BBA ⊂ SAv. The self-assembly experiments were carried out at 30 µM (gel A) and at 0.8 µM (gel B). The molar equivalents of ligand used for each experiment are given in the above table.

maximum of four SAv units and this, only in traces amount. It is to mention that the different samples loaded onto gel B did not have the same concentration. Even though the samples were handled in the same way, the final volume after centrifugation varied. Therefore, the concentration of SAv-based species varied between the samples, and the intensity of the different bands could not be compared. Considering the fluctuating concentration of the samples and the fact that the diluted self-assembly experiments produced essentially the same results as the concentrated ones, the subsequent analysis using BBA_2 and BBA_3 were conducted at a 30 µM concentration of SAv.

To affect polymerization, varying molar quantities of BBA_2 and BBA_3 were added to solutions of SAv (30 µM in PBS 0.1 M, pH 7.4). The solutions were gently stirred at room temperature during half an hour before analysis by SDS-PAGE. Expecting high molecular weight species, 6% acrylamide gels were used for these electrophoretic analysis. Both BBA_2 and BBA_3 dramatically changed the electrophoretic mobility of the species observed by SDS-PAGE. Indeed,

very high molecular weight oligomerized products formed (Fig 6). In some cases, the species were too big to migrate through the gel and almost no SAv-based material was observed. For instance, in lane 3, only traces of SAv oligomers were observed, suggesting that polymerization was most effective with equimolar amounts of SAv and BBA_2. The presence of shorter oligomers, even though in traces amount, suggested that either the molar ratio was not exactly equivalent or that BBA_2 is not long enough to efficiently organize SAv into a one-dimensional fibril. Considering the intensity of the bands from lane 3 to 6, we clearly observed that upon increasing the ratio of BBA_2 with respect to SAv, the yield in shorter SAv oligomers as in tetrameric SAv

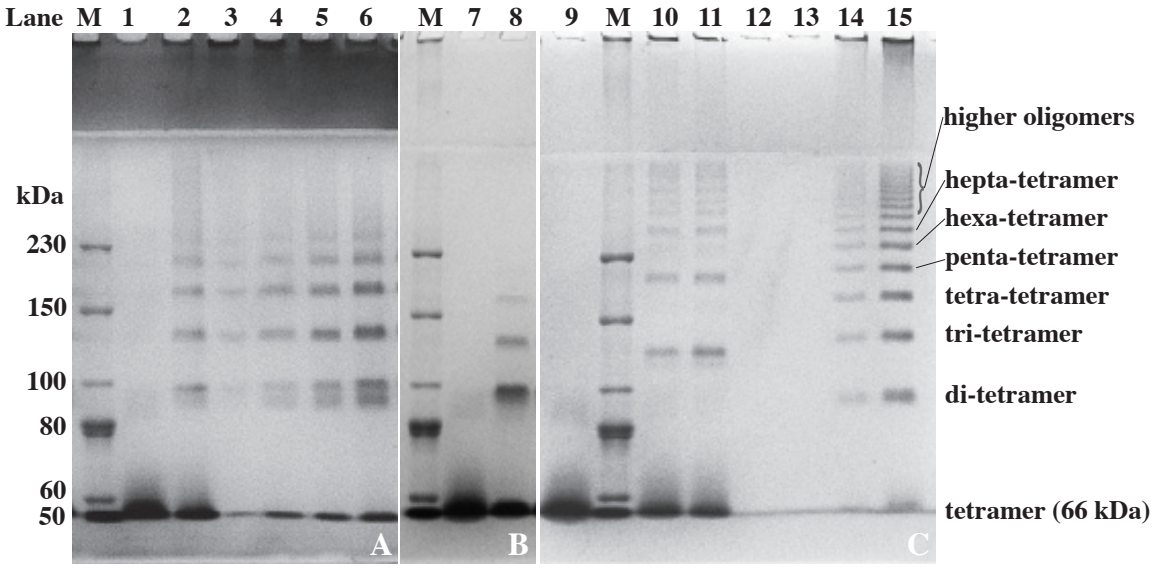

Lane	SAv (eq.)	BBA (eq.)	BBA_2 (eq.)	BBA_3 (eq.)
1,7 & 9	1	-	-	-
2	"	-	0.5	-
3	"	-	1.0	-
4	"	-	1.5	-
5	"	-	2.0	-
6	"	-	4.0	-
8	"	1.5	-	-
10	"	-	-	0.25
11	"	-	-	0.35
12	"	-	-	0.50
13	"	-	-	0.66
14	"	-	-	0.80
15	"	-	-	1.0

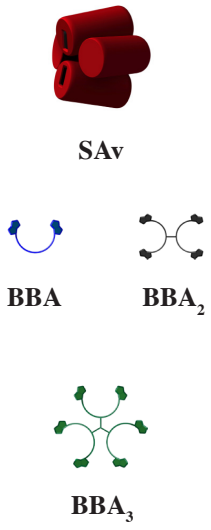

Figure 6 SDS-PAGE (6% acrylamide gel) analysis of the SAv-based assemblies. The molar equivalents used for each experiments using BBA_2 (gel A) and BBA_3 (gel C) are given in the above table. An electrophoretic analysis of BBA ⊂ SAv on a 6% acrylamide gel (gel B) is also shown for comparison.

increased. To produce a dendritic structure or a honeycomb network, the required molar ratio of BBA_3 with respect to SAv should tend to a theoretical value of 0.5 or 0.66 respectively. For both values, the resulting nanostructures were too big to migrate through the gel and no SAv-based material was detected with SDS-PAGE analysis. The electrophoretic mobilities of the different species observed throughout the SDS-PAGE analysis of the self-assembly experiments with the different BBAs ligands was remarkably consistent. Therefore, the number of SAv units present in each band could be attributed. Interestingly, when a molar ratio of $[BBA_3]/[SAv] < 0.5$ was used, odd numbers of SAv-assemblies were solely observed (Fig, 6, lanes 10 & 11). This suggested that BBA_3 binds three SAv units, and hence, is an effective trifurcated connector. When a molar ratio of $[BBA_3]/[SAv] > 0.5$ was used (Fig. 6, lanes 13-15), even numbers of SAv assembly product added up to the previously odd entities.

Having confirmed the ability of BBA_2 and BBA_3 to oligomerize SAv, we investigated the SAv-based nanostructures generated with each ligand. For that purpose, electron and probe microscopy was used.

2.2.3 Microscopic Analysis of the Nanostructure

Although it is a known fact that mature WT-SAv tends to form high order aggregates,[5] no literature on the molecular aspect of those aggregates was found. Since our aim was to control the self-assembly of SAv, we obviously had to identify to which extent those aggregates were organized. Tetrameric SAv and the self-assembled nanostructures with BBA_2 and BBA_3 were first scrutinized by scanning electron microscopy (SEM). We then turned to transmission electron (TEM) and atomic force microscopy (AFM) to obtain higher resolution micrographs of the created nano-objects.

2.2.3.1 Electron Microscopy Experiments

Samples prepared from 8 μM SAv solutions in PBS (0.1 M, pH=7.4) were scrutinized with scanning and transmission electron microscopes (Fig. 7). For the TEM experiments, the samples

were not "electron transparent" due to an excess of material present on the TEM grid, and were therefore diluted 10-fold with PBS. In contrast to the SEM experiments which only revealed the presence of some unstructured aggregates, structured features were observed by TEM. The circular (Fig. 7 c, d) and linear (Fig.7 e, f) structures observed were considered as artifacts in the subsequent self-assembly experiments of SAv with BBA_2 and BBA_3.

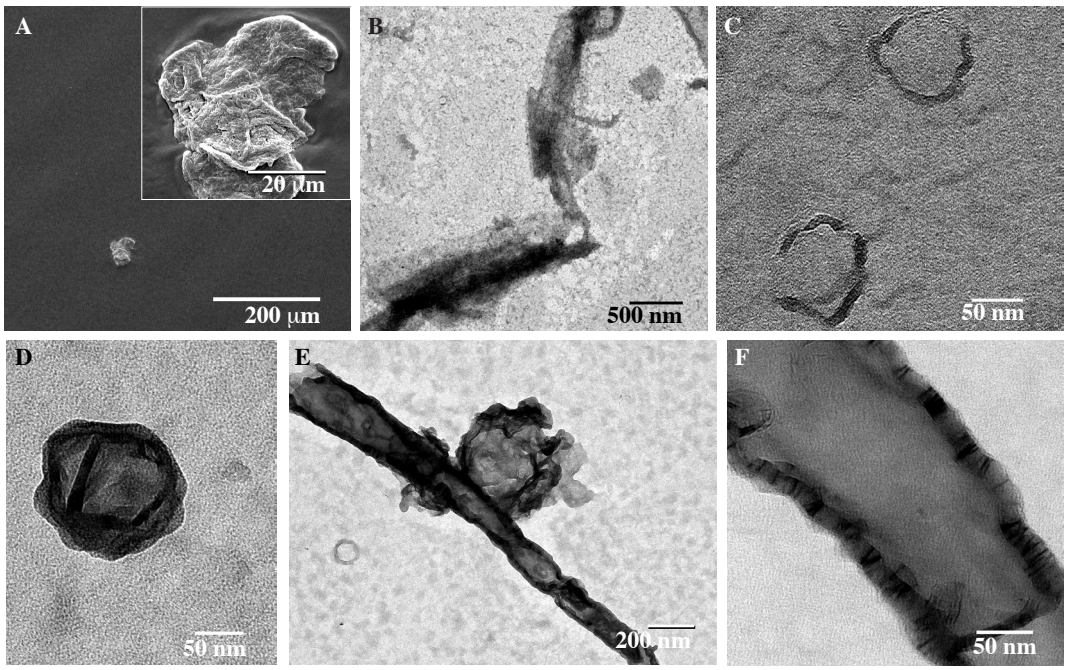

Figure 7 Electron microscopy images of SAv solution. a) Typical SEM image of a solution of 8 μM SAv in PBS (0.1 M, pH=7.4) and b-f) TEM images of 0.8 μM SAv in PBS (0.1 M, pH=7.4) stained with uranyl acetate.

A mixture of equimolar amount of biotin tetramer BBA_2 and SAv in PBS (0.1 M, pH=7.4) was left under magnetic stirring at room temperature during 5 minutes before samples were prepared for SEM experiments. Randomly entangled fibrils several micrometers long and 30 to 100 nm wide were typically observed (Fig. 8a).

A serie of samples with varying equivalents of BBA_2 (0.5, 1 and 5) vs SAv (0.8 μM in PBS 0.1 M, pH= 7.4) were stained for TEM experiments. The TEM micrographs clearly showed fibrillic structures of SAv for all the samples (Fig. 8). When an equimolar amount of BBA_2 and SAv was used (Fig. 8c), fiber bundles reaching micrometers length were observed. In contrast, when an excess of BBA_2 was left to react with SAv, short fibrils reaching a maximum lenght of 100 nm dominated the species observed by TEM (Fig 8c). When a molar ratio of $[BBA_2]/[SAv]$ equals to 0.5 was used, fibers of varying lenghts were observed. In all cases, the

fibers presented a width of 1.9±2 nm, and showed a tendency to aggregate into bundles. Since drying artefacts can cause samples to appear more densely packed or with a completely different structure than that present in the hydrated state,[6] we could not conclude whether the observed bundles of nanofibres exist in the solution state.

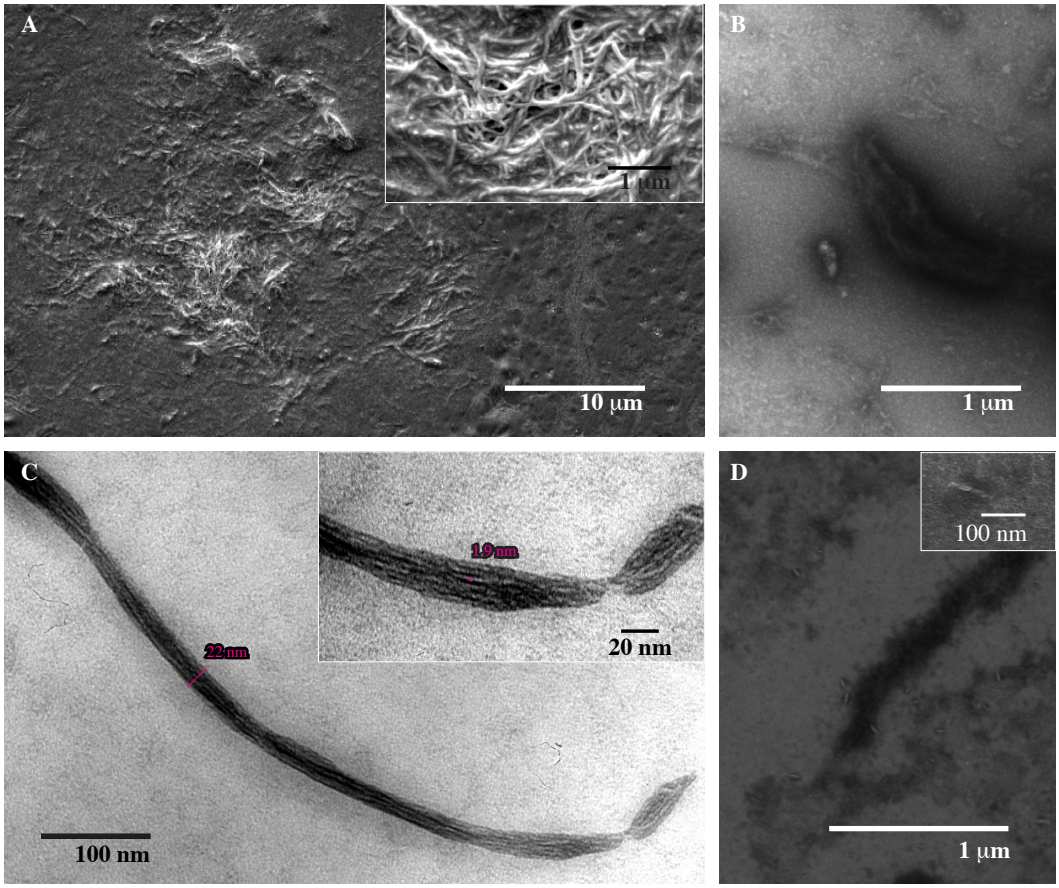

Figure 8 Electron microscopy images of the self-assembly of BBA_2 and SAv showing the formation of fibrillar structure. a) SEM micrograph of fibrils prepared from an equimolar amount of SAv and BBA_2 (8 μM in PBS 0.1 M, pH=7.4). Negatively stained TEM images of the structures generated by 0.8 μM SAv in PBS (0.1 M, pH=7.4) in the presence of b) 0.5, c) 1 and d) 5 equivalents of BBA_2.

The nanostructures generated by SAv (8 μM in PBS 0.1 M, pH= 7.4) in the presence of varying molar equivalents of BBA_3 (0.5, 0.66 and 2 eq.) were then investigated by SEM (Fig. 9). In all cases, except an apparent network pattern also observed for samples of SAv in the presence of $CaCl_2$, no defined structure was observed. A typical SEM micrograph of the samples is shown in Figure 9a. The TEM experiments (Fig. 9a, b) revealed flower like structure reaching a diameter equals to 1 μm. When a molar ratio equals to 0.66/1/1 of BBA_3/BBA_2/SAv was used, a structure suggesting the formation of a 2D network was observed (Fig.9d) by SEM. The acquisition of a better resolution image was attempted but the heat generated inside the specimen melted the

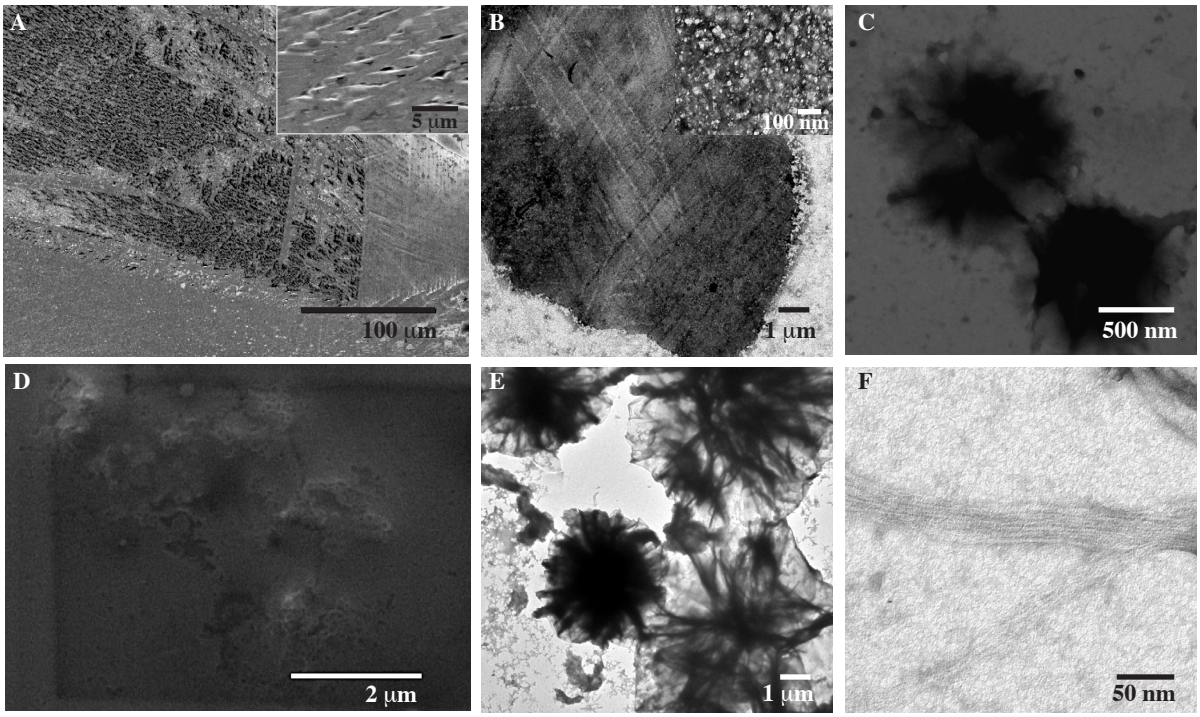

Figure 9 Electron microscopy images of the self-assembly product of BBA_3 and SAv. Typical SEM micrograph of samples prepared from a molar ratio equals to a) 0.66 and 0.5 of BBA_3 with respect to SAv (8 μM in PBS 0.1 M pH= 7.4) and to d) 0.66 : 1 : 1 of BBA_3, BBA_2 and SAv, respectively. Negatively stained TEM images of the structures generated by 0.8 μM SAv in PBS (0.1 M, pH= 7.4) in the presence of b) 0.66, c) 0.5 equivalents of BBA_3 and e,f) 0.66 and 1 equivalents of BBA_3 and BBA_2 , respectively.

structure as evidenced on the micrograph. Similar samples (diluted 10-fold) were then stained with uranyl acetate and scrutinized by TEM. Flower like structures were again observed, this time reaching a diameter up to 7 μm (Fig. 9e), as well as fibrillic assemblies (Fig. 9f). The 2D network of honeycombs structure observed by SEM could not be confirmed by the TEM experiments of the stained samples.

2.2.3.2 AFM Experiments

The samples were also analyzed by atomic force microscopy (AFM) in air by tapping mode, using highly oriented pyrolitic graphite (HOPG) as a solid support.

Images of the freshly cleaved HOPG surface were initially acquired (Fig. 10) and showed features typical of an HOPG surface. The images contained domains of smooth surface demarcated by step features that correspond either to cleavage edges or microcrystallite

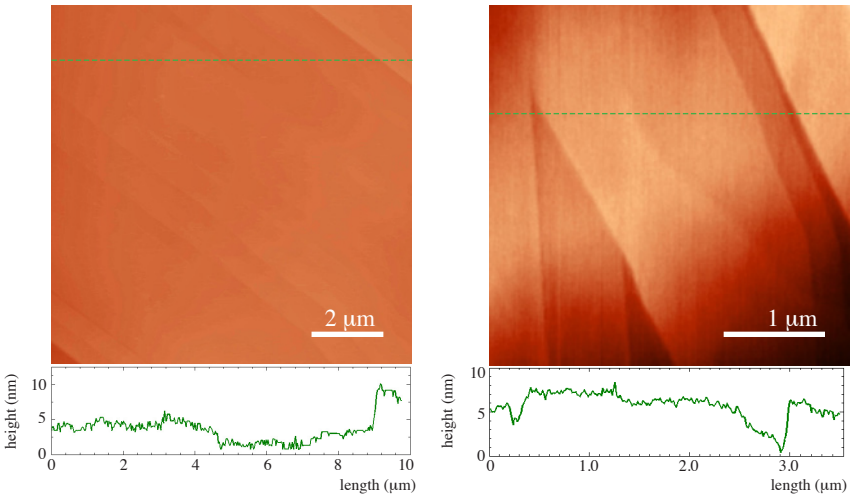

Figure 10 AFM images and height profiles of HOPG.

boundaries.[7] Dry samples were prepared from a 0.8 µM solution of SAv in PBS (0.1 M, pH=7.4), and the AFM micrographs of the samples showed that the protein adsorbed evenly onto the sub-

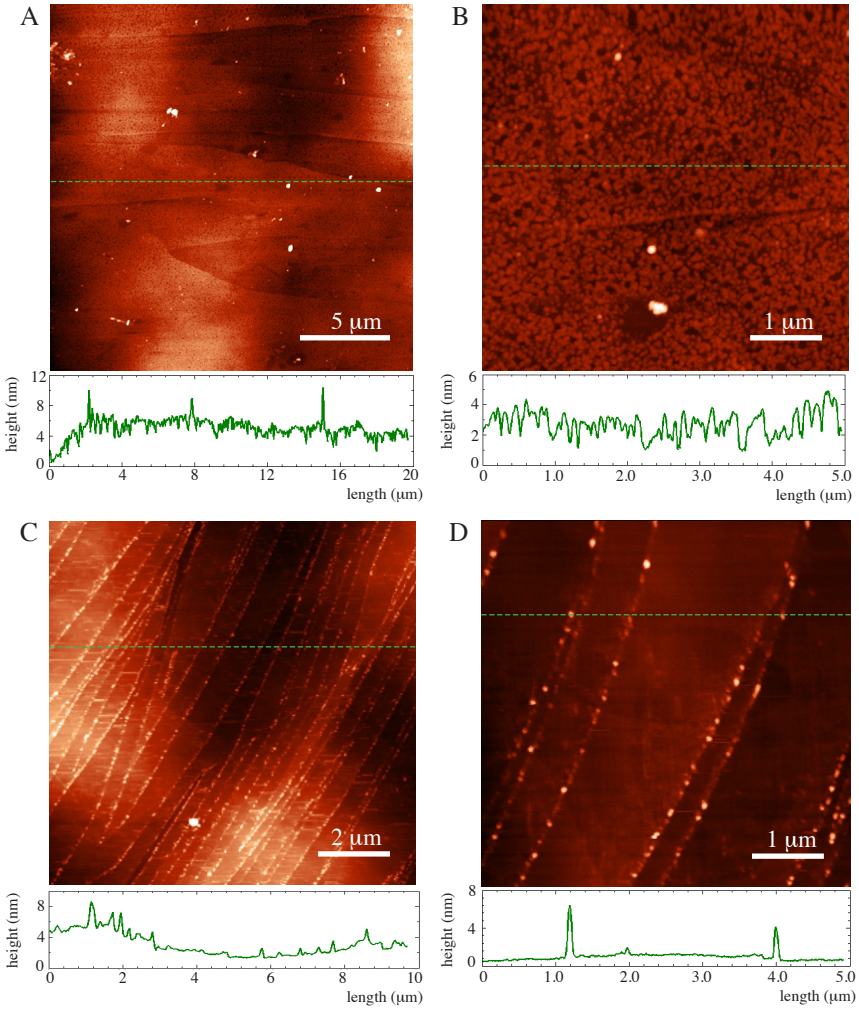

Figure 11 AFM images and height profiles of SAv adsorbed on HOPG in the dry state. Samples were prepared from a; a, b) 0.8 µM and c, d) 80 nM SAv solution in PBS (0.1 M, pH= 7.4)

strate (Fig. 11a, b).11a, b). The SAv units typically presented a height equals to 2.1 nm ± 0.2 nm (n = 15). Dry samples were also prepared from a 80 nM solution of SAv and in that case, the SAv units resolved by AFM were mainly present at the step feature of the HOPG surface. The proteins adsorbed onto the flat domains were displaced by the scanning tip and could not be resolved.

A serie of samples with varying ratios of BBA_2 (0.5, 1 and 5) with respect to SAv (0.8 μM in PBS 0.1 M pH= 7.4) were then imaged by AFM (Fig. 12). When an equimolar amount of BBA_2 and SAv was used, disrupted fibrillic structures, mainly located at the step features of the HOPG, were observed (Fig 12c-d). Disrupted fibrils located on flat areas (Fig 12e) presented a height equals to 4.8 nm ± 0.4 nm (n = 15). Aggregated structures appearing to be circular were also observed on the flat domains of the HOPG. Their measured height, 6.0 nm ± 0.5 nm (n = 15), was higher than the disrupted fibrils. The sample prepared with a molar ratio equals to 0.5 of BBA_2 with respect to SAv, presented a ramified network with a height equals to 6.5 nm ± 0.5 nm (n = 15), most probably a drying artifact. When an excess of BBA_2 with respect to SAv was used, short fibers were observed on the 10 μm scan window (Fig. 12f), but only isolated SAv units presenting a height equals to 2.4 nm ± 0.5 nm (n = 15) and aggregates were resolved at higher magnification (Fig. 12g).

The nanostructures generated by SAv in the presence of varying molar equivalents of BBA_3 (0.25, 0.66 and 2 eq.) were then analyzed by AFM (Fig.13). For all the samples, the micrographs obtained from a scanned area of 10 μm suggested an extended 2D network assembly. Although not perfect, the network presented less defects when a molar equivalent of BBA_3 with respect to SAv equals to 0.66 was used (Fig. 13c, d). The heights from the networks measured on the samples prepared from 0.25 and 0.66 equivalents of BBA_3 with respect to SAv were respectively 2.9 nm ± 0.3 nm (n = 17) and 3.4 nm ± 0.4 nm (n = 15). When an excess of BBA_3 was used, the micrograph obtained from a 2μm scanned area (Fig. 13f) showed that the network was disrupted, the partially connected network presented a height of 3.0 nm ± 0.5 nm (n = 17).

Although a 2D-network structure was observed for the self-assembly experiments of

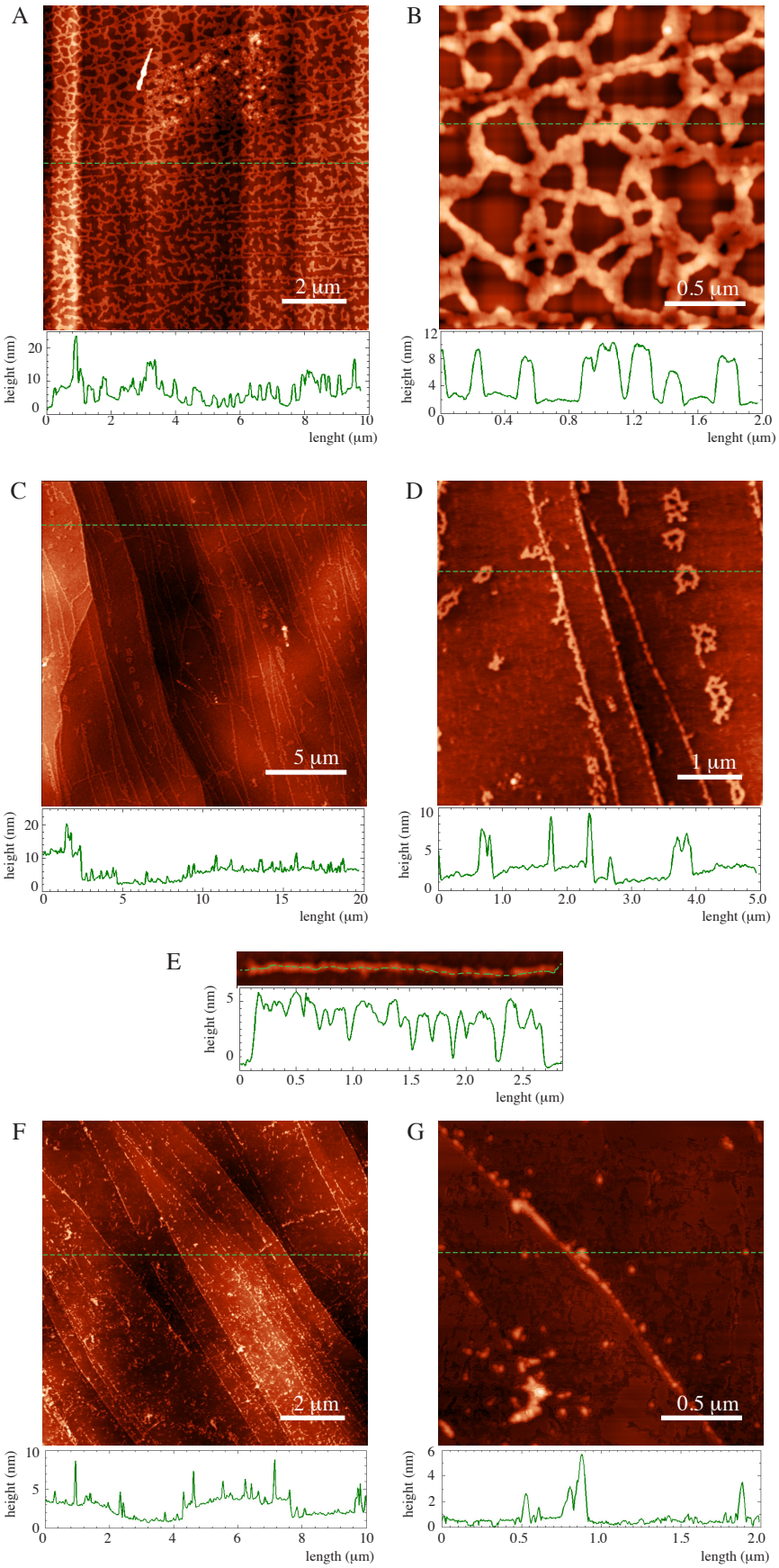

Figure 12 AFM images and height profiles of SAv-based self-assembled fibrils on HOPG in the dry state. AFM images of the structures generated by 0.8 µM SAv in PBS (0.1 M, pH=7.4) in the presence of a, b) 0.5; c, d, e) 1 and f, g) 5 equivalents of BBA_2.

SAv with BBA_3, the fibrillic structures generated by BBA_2 were not clearly confirmed by the AFM experiments. As hydrophobic surfaces have been reported to denature water-soluble pro

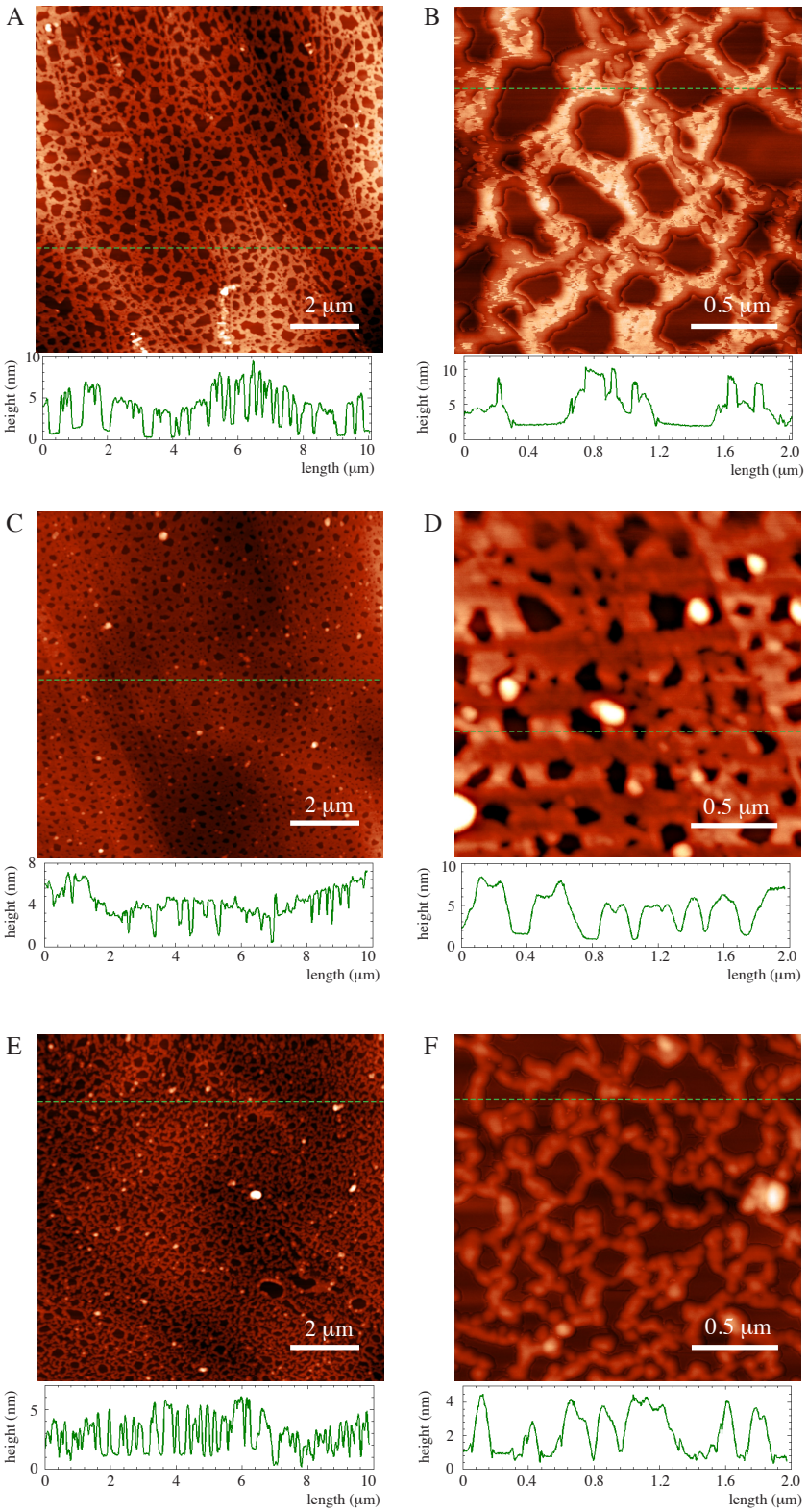

Figure 13 AFM images and height profiles of the self-assembly product of BBA_3 and SAv on HOPG in the dry state. AFM images of the structures generated by 0.8 µM SAv in PBS (0.1 M, pH=7.4) in the presence of a, b) 0.25, c, d) 0.66 and e, f) 2 equivalents of BBA_3.

teins,[7-9] it may be speculated that the hydrophobic interactions with the HOPG[8] can destabilize the formed fibrils. In order to assess the influence of HOPG on the sample conformation, control experiments consisting in imaging the samples on mica were attempted. Unfortunately, no adsorption of SAv was observed in the conditions used (0.8 μM in PBS 0.1 M pH = 7.4).

Even though the stoechiometry of binding of the BBAs ligands (HABA-displacement assays) and the SDS-PAGE analysis of the self-assembled species gave promising results, the microscopic analysis of the self-assembly products revealed to be non-trivial. Overall, there was a lack of consistency observed throughout the micrographs acquired with the different microscopes, namely the SEM, TEM and AFM. Although the SEM and TEM images from the self-assembly products of SAv and BBA_2 suggested the formation of nanofibers, the AFM micrographs showed mainly disrupted or agglomerated fibers (excluding the aligned SAv at the HOPG steps). For the self-assembly experiments conducted with BBA_3, a 2D network formation was suggested by the SEM and the AFM micrographs but it was not observed by TEM.

Since drying artifacts can cause samples to appear more densely packed or with a completely different structure than in the hydrated state,[6] the images obtained might not reflect the nanostructures present in solution. In addition, the use of a highly hydrophobic surface for the AFM experiments added another level of uncertaintity in ascertaining the existence of the observed nanostructures in solution. For theses reasons, we considered the microscopic results with caution. We believe the presence of nanofibres or 2D networks in the solution can only be proved by imaging the system in a hydrated environment.[6] If the microscopic analysis of the self-assembly of SAv and the BBAs ligands were to be followed, images should be acquired in the hydrated state, by Cryo TEM or AFM in liquid for instance. Even though we didn't observe any adsorbed SAv on mica, different parameters like buffer composition, pH or ionic strength of the protein solution[10, 11] could be tuned to favor the adsorption process. This way, the influence of hydrophobic surfaces on the formation of the nanostructures observed during this work could be assessed.

Following this, we shifted our efforts in the two following directions; for one part, we studied the ability of the one-dimensional polymer to template the mineralization of calcium carbonate (Chap. 2.3). The second and most exciting part was dedicated to further investigate the structures generated by BBA_2 and BBA_3 with SAv. To achieve this goal, we set out to immobilize SAv on gold via biotinylated mixed SAMs, to follow the growth of the SAv-based material step-by-step by QCM and SPR, and finally to image the resulting nanostructures by AFM in aqueous environment (Chap. 2.4).

2.2.4 References

1. Green, N. M. *Biochem. J.* **1965**, *94*, 23c.
2. Bayer, E. A.; Ehrligh-Rogozinski, S.; Wilchek, M. *Electrophoresis* **1996**, *17*, 1319.
3. Hamblett, K. J.; Kegley, B. B.; Hamlin, D. K.; Chyan, M.-K.; Hyre, D. E.; Press, O. W.; Wilbur, D. S.; Stayton, P. S.*Bioconjugate Chem.* **2002**, *13*, 588.
4. Humbert, N.; Zocchi, A.; Ward, T. R. *Electrophoresis* **2005**, *26*, 47.
5. Sano, T.; Pandori, M. W.; Chen, X.; Smith, C. L.; Cantor, C. R. *J. Biol. Chem.* **1995**, *270*, 28204.
6. O'Leary, L. E. R.; Fallas, J. A.; Bakota, E. L.; Kang, M. K.; Hartgerink, J. D. *Nat. Chem.* **2011**, *3*, 821.
7. Cullen, D. C.; Lowe, C. R., *J. Colloid Interface Sci.* **1994**, *166*, 102.
8. Bippes, C. A.; Muller, D. J. *Rep. Prog. Phys.* **2011**, *74*, 086601/1.
9. Svaldo-Lanero, T.; Penco, A.; Prato, M.; Canepa, M.; Rolandi, R.; Cavalleri, O. *Soft Matter* **2008**, *4*, 965.
10. Nakanishi, K.; Sakiyama, T.; Imamura, K. *J. Biosci. Bioeng.* **2001**, *91*, 233.
11. Rabe, M.; Verdes, D.; Seeger, S. *Adv. Colloid Interface Sci.* **2011**, *162*, 87.

2.3 One-Dimensional Streptavidin-Based Block Copolymer as a Matrix for Calcium Carbonate Mineralization

This section focuses on the ability of one-dimensional SAv-based block copolymer to self-assemble in bundles when exposed to calcium ions solution. In the presence of carbon dioxide vapors, these bundles template the nucleation, the growth, and the assembling of calcite microcrystals.

Although the organometallic complex $[Fe(BBA\text{-}terpy)_2]^{2+}$ was presented as linear junction in the published results, the organic analog BBA_2 was initially used, and produced the same results. Thus, the following article, reprinted with permission from the publisher, condenses the calcium carbonate mineralization experiments conducted during this thesis.

Hierarchical Self-Assembly of One Dimensional Streptavidin
Bundles as Collagen Mimetic for the Biomineralization of Calcite

Sabina Burazerovic, Julieta Gadinaru, Julien Pierron and Thomas R. Ward. *Angew. Chem. Int. Ed. Engl.* **2007**, *46*, 5510 (selected as "hot paper")

Coordination Polymers

DOI: 10.1002/anie.200701080

Hierarchical Self-Assembly of One-Dimensional Streptavidin Bundles as a Collagen Mimetic for the Biomineralization of Calcite**

*Sabina Burazerovic, Julieta Gradinaru, Julien Pierron, and Thomas R. Ward**

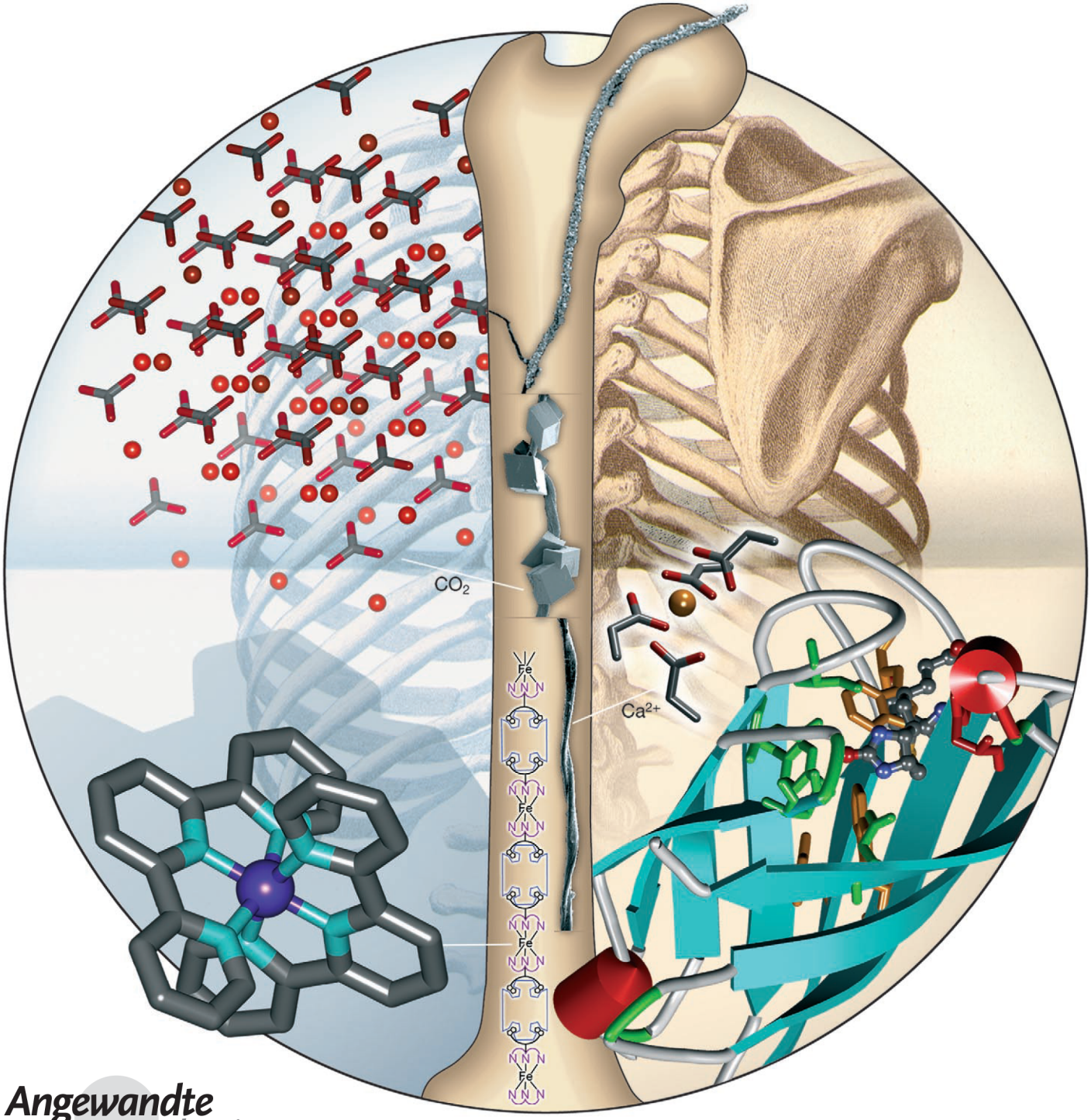

Over the past two decades, major effort has been dedicated to the metal-directed self-assembly of discrete one-, two-, or three-dimensional frameworks. In addition to their appealing architecture, these coordination polymers (also coined metal–organic frameworks) possess cavities that can accommodate various guest molecules. Such guest⊂host complexes often display unusual properties such as chemical reactivity, energy or electron transfer, second harmonic generation materials, high-capacity gas storage, catalysis, etc.[1–6]

In parallel to these developments, surfaces and cavities spanned by protein higher-order aggregates have been exploited for molecular encapsulation and for templating nanoparticle synthesis. Typical examples include protein fibrils,[7,8] ferritin,[9,10] S-layers,[11–13] antibodies,[14] peptide amphiphiles,[15] capsids,[16–19] leucine zippers,[20] etc.[21–26]

Controlled protein aggregation is a critical process in many areas, ranging from biomineralization[27] to neurodegenerative diseases.[28] In contrast with molecular tectonics, however,[5,29] the de novo design of higher-order architectures by using proteins as building blocks (e.g. protein tectonics) remains challenging.[21–24,30–34]

In the spirit of coordination polymers, we reasoned that one may exploit the versatility of transition-metal connectors in conjunction with proteins bearing tethered ligands to create discrete one-, two-, or three-dimensional metal–organic protein frameworks (MOPF; Figure 1). For this proof-of-principle study, we used a linear Fe(terpy)$_2$ moiety (terpy = terpyridine) bearing four biotin anchors, [Fe(Biot$_2$-terpy)$_2$]$^{2+}$ complex (the connector), in conjunction with streptavidin (hereafter referred to as Sav, the linker) to afford a one-dimensional MOPF. We show that in the presence of calcium ions and CO_2-rich vapors, these MOPF aggregates form bundles that template the biomineralization of calcite.

Based on our previous experience with the compatibility between organometallic moieties and proteins, we selected a noncovalent approach based on the biotin–streptavidin technology to assemble MOPFs.[35–41] Streptavidin is a slightly acidic (isoelectric point, pI = 6.3) homotetrameric protein that bears four biotin binding sites.[42,43] For this proof-of-principle study, we selected a preorganized bis-biotinylated terpyridine ligand Biot$_2$-terpy that binds to two *cis*-related sites in streptavidin.[44–47] A ferrous ion was chosen as terpyridine binds in a cooperative fashion ($K_1 = 1.26 \times 10^7\,\text{M}^{-1}$, $K_2 = 6.31 \times 10^{13}\,\text{M}^{-1}$),[48] thus ensuring the exclusive formation of a linear connector bearing four biotin anchors (Figure 2). Experimental details for the synthesis and the characterization of the [Fe(Biot$_2$-terpy)$_2$]$^{2+}$ complex are described in the Supporting Information.

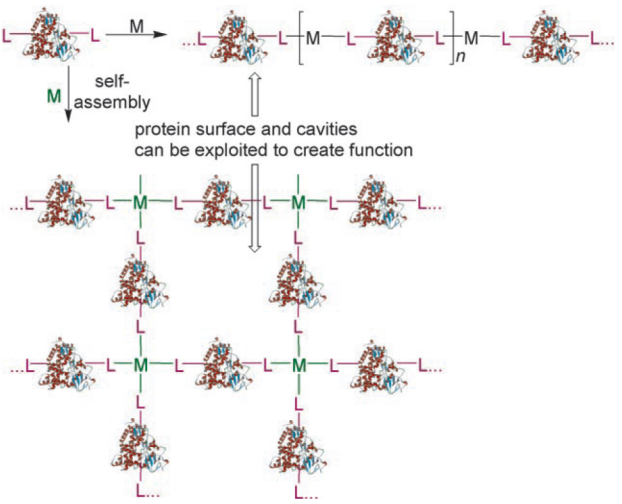

Figure 1. Extending the concept of coordination polymers to MOPFs. The nature of the metal M and the denticity of the ligand L determines the topology of the self-assembled MOPF.

Despite the presence of many potentially coordinating functionalities on the streptavidin surface, the selected metal + ligand + protein triad ensures the exclusive formation of a one-dimensional noncovalent MOPF upon addition of streptavidin to afford ([Fe(Biot$_2$-terpy)$_2$]$^{2+}$⊂Sav)$_\infty$. The characteristic [Fe(terpy)$_2$]$^{2+}$ complex absorption band ($\varepsilon_{557\,\text{nm}} = 9237\ \text{cm}^{-1}\text{M}^{-1}$) allows one to assess the integrity of the linear connector throughout the hierarchical self-assembly process. The biotin-binding event between the [Fe(Biot$_2$-terpy)$_2$]$^{2+}$ ion and Sav can be conveniently monitored with the disappearance of an induced CD signal, $\lambda_{max} = 505$ nm, caused by the displacement of 2-(4′-hydroxyazobenzene)benzoic acid (HABA, a hydrophobic dye weakly bound within the biotin-binding pocket) by the [Fe(Biot$_2$-terpy)$_2$]$^{2+}$ ion (see the Supporting Information).[37,49]

Upon standing at room temperature, the dilute purple solution containing the metal + ligand + protein triad slowly becomes turbid, suggesting the formation of polymeric material {[Fe(Biot$_2$-terpy)$_2$]$^{2+}$⊂Sav}$_\infty$. In the presence of calcium ions (0.05 M), threads appear within minutes and can be visualized by scanning electron microscopy (SEM, Figure 3a,b). We speculate that the presence of aspartate and glutamate side chains (48 in total for the Sav tetramer)[50] on streptavidin's surface favors the chelation of calcium, eventually resulting in the cross-linking of MOPF to form bundles with a micrometer diameter and a millimeter length (Figure 3a,b). Calcium-induced bundle formation of polyacrylate fibers on carboxylate-terminated SAMs was reported by Tremel and co-workers.[51]

In the presence of carbon dioxide vapors, the MOPF bundles template the nucleation, the growth, and the assembling of calcite microcrystals (Figure 3). The biomineralization experiments were carried out by using the diffusion method in a closed dessicator.[52,53] A solution of ammonium

[*] S. Burazerovic, Dr. J. Gradinaru, J. Pierron, Prof. T. R. Ward
Institute of Chemistry
University of Neuchâtel
Av. Bellevaux 51, CP 158, 2009 Neuchâtel (Switzerland)
Fax: (+41) 327-182-516
E-mail: thomas.ward@unine.ch
Homepage: http://www.unine.ch/chw

[**] This work was supported by the Canton of Neuchâtel and the Swiss National Science Foundation (Grants FN 200021-105192 and 200020-113348). We thank Prof. C. R. Cantor for providing us with the streptavidin gene, A. Ivanova for producing streptavidin, and L. Addadi, F. Seebeck, and E. Verrechia for insightful comments.

Supporting information for this article is available on the WWW under http://www.angewandte.org or from the author.

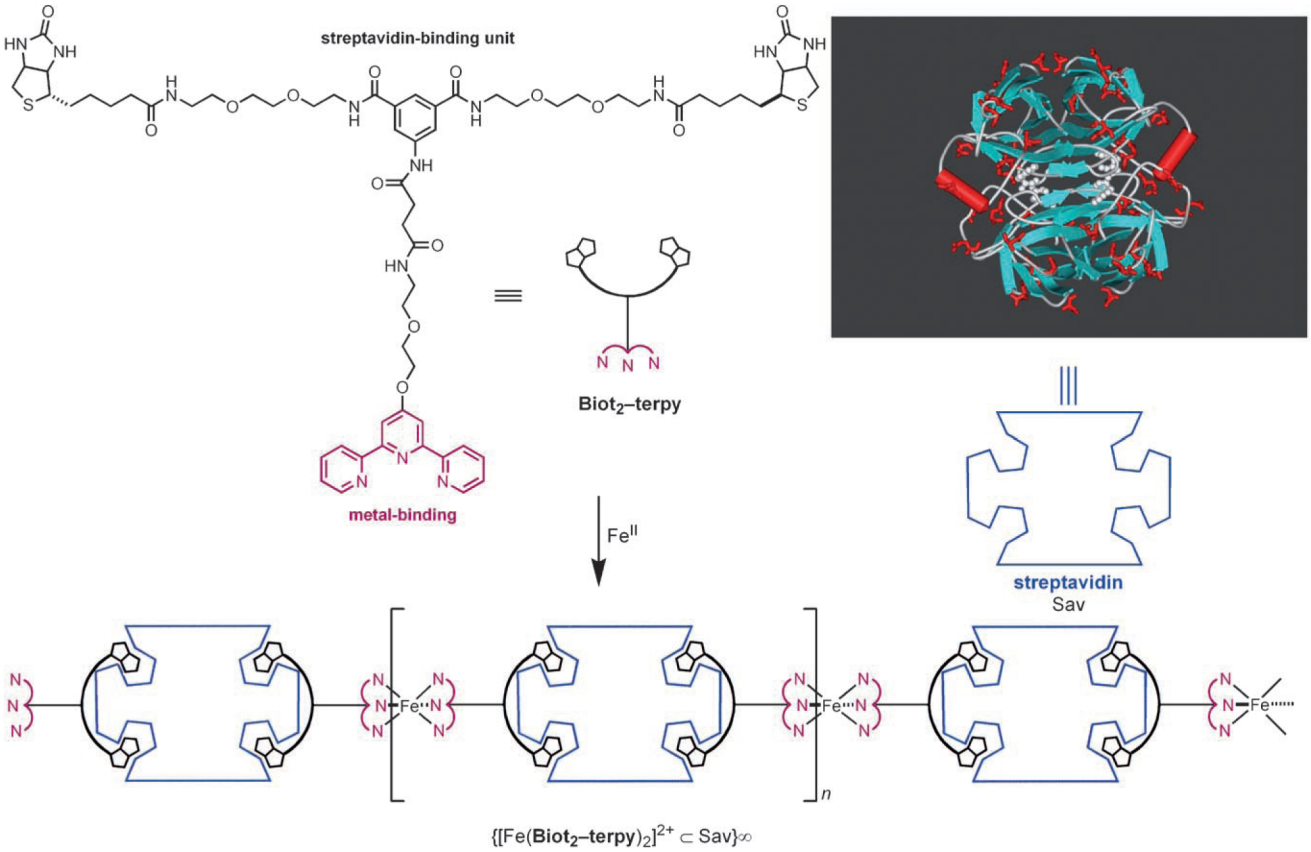

Figure 2. Structure of the bis-biotinylated (black) terpyridine (violet) $Biot_2$-terpy, which, upon reaction with Fe^{II}, forms a linear tetrabiotinylated connector, the $[Fe(Biot_2\text{-terpy})_2]^{2+}$ complex. In the presence of streptavidin (right insert emphasizing the 48 acidic side chains and the stick representation shown in red),[50] linear coordination polymers, $\{[Fe(Biot_2\text{-terpy})_2]^{2+}\subset Sav\}_\infty$, are formed.

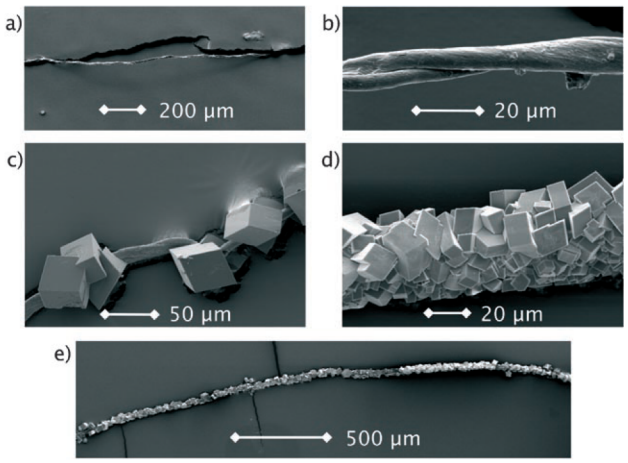

Figure 3. Scanning electron micrographs (gold-coated): a) MOPF bundles obtained from $\{[Fe(Biot_2\text{-terpy})_2]^{2+}\subset Sav\}_\infty$ solutions (8×10^{-7} M) containing $CaCl_2$ (0.05 M) after 5 min at room temperature and b) the close-up view. c–e) Biomineralized $\{[Fe(Biot_2\text{-terpy})_2]^{2+}\subset Sav\}_\infty$ bundles: c) 8×10^{-6} M, $[CaCl_2]=0.01$ M, 12 h; d, e) 8×10^{-6} M, $[CaCl_2]=0.05$ M, 12 h.

carbonate served as a CO_2 source that diffused in $CaCl_2$ solutions ($c=0.01$–0.05 M) containing the MOPF building blocks ($c=8\times10^{-6}$ M). Manipulations were carried out in a laminar flow hood in a clean room by using six-well plates, and each experiment was performed in triplicate. The CO_2 atmosphere was maintained over 12 h at room temperature after which each sample was scrutinized under a polarized-light optical microscope (see the Supporting Information). Control experiments revealed that the presence of calcite crystal wires only occurred in the wells containing both the $[Fe(Biot_2\text{-terpy})_2]^{2+}$ complex and Sav building blocks.

Calcite microcrystals have been grown on a wide variety of templates, including Kevlar,[54–56] nylon,[57] self-assembled monolayers, proteins, etc.[51,58–68] Reminiscent of collagen processing,[69] the approach delineated herein represents an example of hierarchical self-assembly in which each stage involves building blocks of increasing size such that the resulting supramolecular structure spans over six orders of magnitude, from nanometer-sized covalent building blocks to millimeter calcite wires.[70]

We have demonstrated that streptavidin (the linker) combined with a linear tetrabiotinylated connector, the $[Fe(Biot_2\text{-terpy})_2]^{2+}$ complex, spontaneously self-assemble into a one-dimensional metal–organic protein framework. In the presence of calcium ions, these MOPFs form bundles that serve as a template for the biomineralization of calcite. This hierarchical self-assembly process relies on noncovalent interactions that are typical of both coordination polymers (dative M–L bonds) and of higher-order protein aggregates

(protein–protein interactions) to yield millimeter-sized one-dimensional biomineralized protein matrices.

Current efforts in the group include a) the characterization of the hierarchical self-assembly process by using light-scattering experiments, b) the generation of two- and three-dimensional MOPFs by using polytopic connectors, and c) the exploitation of these frameworks for templating the growth of various nanoparticles.

Received: March 12, 2007
Published online: May 24, 2007

Keywords: biomineralization · calcite · coordination polymers · metal–organic protein frameworks · protein structures

[1] O. R. Evans, W. Lin, *Acc. Chem. Res.* **2002**, *35*, 511.
[2] S. Kitagawa, R. Kitaura, S. Noro, *Angew. Chem.* **2004**, *116*, 2388; *Angew. Chem. Int. Ed.* **2004**, *43*, 2334.
[3] N. W. Ockwig, O. Delgado-Friedrichs, M. O'Keeffe, O. M. Yaghi, *Acc. Chem. Res.* **2005**, *38*, 176.
[4] M. Fujita, M. Tominaga, A. Hori, B. Therrien, *Acc. Chem. Res.* **2005**, *38*, 369.
[5] M. W. Hosseini, *Acc. Chem. Res.* **2005**, *38*, 313.
[6] M. H. Bartl, S. W. Boettcher, K. L. Frindell, G. D. Stucky, *Acc. Chem. Res.* **2005**, *38*, 263.
[7] T. Scheibel, R. Parthasarathy, G. Sawicki, X. M. Lin, H. Jaeger, S. L. Lindquist, *Proc. Natl. Acad. Sci. USA* **2003**, *100*, 4527.
[8] T. Scheibel, *Curr. Opin. Biotechnol.* **2005**, *16*, 427.
[9] T. Douglas, M. Young, *Science* **2006**, *312*, 873.
[10] T. Ueno, M. Suzuki, T. Goto, T. Matsumoto, K. Nagayama, Y. Watanabe, *Angew. Chem.* **2004**, *116*, 2581; *Angew. Chem. Int. Ed.* **2004**, *43*, 2527.
[11] D. Moll, C. Huber, B. Schlegel, D. Pum, U. B. Sleytr, M. Sara, *Proc. Natl. Acad. Sci. USA* **2002**, *99*, 14646.
[12] W. Shenton, D. Pum, U. B. Sleytr, S. Mann, *Nature* **1997**, *389*, 585.
[13] U. B. Sleytr, P. Messner, D. Pum, M. Sara, *Angew. Chem.* **1999**, *111*, 1098; *Angew. Chem. Int. Ed.* **1999**, *38*, 1034.
[14] J. Yang, M. Mayer, J. K. Kriebel, P. Garstecki, G. M. Whitesides, *Angew. Chem.* **2004**, *116*, 1581; *Angew. Chem. Int. Ed.* **2004**, *43*, 1555.
[15] B. M. Rabatic, R. C. Claussen, S. I. Stupp, *Chem. Mater.* **2005**, *17*, 5877.
[16] Q. Wang, T. Lin, L. Tang, J. E. Johnson, M. G. Finn, *Angew. Chem.* **2002**, *114*, 477; *Angew. Chem. Int. Ed.* **2002**, *41*, 459.
[17] R. M. Kramer, C. Li, D. C. Carter, M. O. Stone, R. R. Naik, *J. Am. Chem. Soc.* **2004**, *126*, 13282.
[18] F. P. Seebeck, K. J. Woycechowsky, W. Zhuang, J. P. Rabe, D. Hilvert, *J. Am. Chem. Soc.* **2006**, *128*, 4516.
[19] W. Shenton, S. Mann, H. Colfen, A. Bacher, M. Fischer, *Angew. Chem.* **2001**, *113*, 456; *Angew. Chem. Int. Ed. Engl.* **2001**, *40*, 442.
[20] M. G. Ryadnov, *Angew. Chem.* **2007**, *119*, 987; *Angew. Chem. Int. Ed.* **2007**, *46*, 969.
[21] J. E. Padilla, C. Colovos, T. O. Yeates, *Proc. Natl. Acad. Sci. USA* **2001**, *98*, 2217.
[22] K. Matsuura, K. Murasato, N. Kimizuka, *J. Am. Chem. Soc.* **2005**, *127*, 10148.
[23] J. C. T. Carlson, S. S. Jena, M. Flenniken, T.-f. Chou, R. A. Siegel, C. R. Wagner, *J. Am. Chem. Soc.* **2006**, *128*, 7630.
[24] P. Ringler, G. E. Schulz, *Science* **2003**, *302*, 106.
[25] X. Gao, H. Matsui, *Adv. Mater.* **2005**, *17*, 2037.
[26] C. Mao, D. J. Solis, B. D. Reiss, S. T. Kottmann, R. Y. Sweeney, A. Hayhurst, G. Georgiou, B. Iverson, A. M. Belcher, *Science* **2004**, *303*, 213.
[27] S. Mann, J. Webb, R. J. P. Williams in *Biomineralization. Chemical and Biochemical Perspectives*, Wiley-VCH, New York, **1989**, p. 541.
[28] J. Shorter, S. Lindquist, *Nat. Rev. Genet.* **2005**, *6*, 435.
[29] S. Mann, *Nature* **1993**, *365*, 499.
[30] J. D. Hartgerink, E. Beniash, S. I. Stupp, *Proc. Natl. Acad. Sci. USA* **2002**, *99*, 5133.
[31] M. Ahlers, R. Blankenburg, D. W. Grainger, P. Meller, H. Ringsdorf, C. Salesse, *Thin Solid Films* **1989**, *180*, 93.
[32] W. Müller, H. Ringsdorf, E. Rump, X. Zhang, L. Angermaier, W. Knoll, J. Spinke, *J. Biomater. Sci. Polym. Ed.* **1994**, *6*, 481.
[33] H. Fukushima, D. M. Taylor, H. Morgan, H. Ringsdorf, E. Rump, *Thin Solid Films* **1995**, *266*, 289.
[34] A. M. Smith, S. F. A. Acquah, N. Bone, H. W. Kroto, M. G. Ryadnov, M. S. P. Stevens, D. R. M. Walton, D. N. Woolfson, *Angew. Chem.* **2005**, *117*, 329; *Angew. Chem. Int. Ed.* **2005**, *44*, 325.
[35] G. Klein, N. Humbert, J. Gradinaru, A. Ivanova, F. Gilardoni, U. E. Rusbandi, T. R. Ward, *Angew. Chem.* **2005**, *117*, 7942; *Angew. Chem. Int. Ed.* **2005**, *44*, 7764.
[36] J. Collot, J. Gradinaru, N. Humbert, M. Skander, A. Zocchi, T. R. Ward, *J. Am. Chem. Soc.* **2003**, *125*, 9030.
[37] M. Skander, N. Humbert, J. Collot, J. Gradinaru, G. Klein, A. Loosli, J. Sauser, A. Zocchi, F. Gilardoni, T. R. Ward, *J. Am. Chem. Soc.* **2004**, *126*, 14411.
[38] M. Skander, C. Malan, A. Ivanova, T. R. Ward, *Chem. Commun.* **2005**, 4815.
[39] C. Letondor, N. Humbert, T. R. Ward, *Proc. Natl. Acad. Sci. USA* **2005**, *102*, 4683.
[40] C. Letondor, A. Pordea, N. Humbert, A. Ivanova, S. Mazurek, M. Novic, T. R. Ward, *J. Am. Chem. Soc.* **2006**, *128*, 8320.
[41] C. M. Thomas, C. Letondor, N. Humbert, T. R. Ward, *J. Organomet. Chem.* **2005**, *690*, 4488.
[42] M. Wilchek, E. A. Bayer, *Methods in Enzymology, Vol. 184*, Academic Press, San Diego, **1990**.
[43] T. Sano, C. R. Cantor, *Proc. Natl. Acad. Sci. USA* **1990**, *87*, 142.
[44] D. S. Wilbur, P. M. Pathare, D. K. Hamlin, S. A. Weerawarna, *Bioconjugate Chem.* **1997**, *8*, 819.
[45] K. J. Hamblett, B. B. Kegley, D. K. Hamlin, M.-K. Chyan, D. E. Hyre, O. W. Press, D. S. Wilbur, P. S. Stayton, *Bioconjugate Chem.* **2002**, *13*, 588.
[46] H. Hofmeier, J. Pahnke, C. H. Weidl, U. S. Schubert, *Biomacromolecules* **2004**, *5*, 2055.
[47] H. Hofmeier, U. S. Schubert, *Chem. Soc. Rev.* **2005**, *34*, 2423.
[48] R. H. Holyer, C. D. Hubbard, S. F. A. Kettle, R. G. Wilkins, *Inorg. Chem.* **1966**, *5*, 622.
[49] N. M. Green, *Methods Enzymol.* **1970**, *18*, 418.
[50] I. LeTrong, N. Humbert, T. R. Ward, R. E. Stenkamp, *J. Mol. Biol.* **2006**, *356*, 738.
[51] M. Balz, H. A. Therese, J. Li, J. S. Gutmann, M. Kappl, L. Nasdala, W. Hofmeister, H.-J. Butt, W. Tremel, *Adv. Funct. Mater.* **2005**, *15*, 683.
[52] S. Albeck, J. Aizenberg, L. Addadi, S. Weiner, *J. Am. Chem. Soc.* **1993**, *115*, 11691.
[53] Y. Levi, S. Albeck, A. Brack, S. Weiner, L. Addadi, *Chem. Eur. J.* **1998**, *4*, 389.
[54] G. Fu, S. Valiyaveettil, B. Wopenka, D. E. Morse, *Biomacromolecules* **2005**, *6*, 1289.
[55] I. W. Kim, E. DiMasi, J. S. Evans, *Cryst. Growth Des.* **2004**, *4*, 1113.
[56] R. Lakshminarayanan, S. Valiyaveettil, G. L. Loy, *Cryst. Growth Des.* **2003**, *3*, 953.
[57] P. K. Ajikumar, R. Lakshminarayanan, S. Valiyaveettil, *Cryst. Growth Des.* **2004**, *4*, 331.
[58] L. Addadi, S. Weiner, *Proc. Natl. Acad. Sci. USA* **1985**, *82*, 4110.
[59] L. Addadi, S. Raz, S. Weiner, *Adv. Mater.* **2003**, *15*, 959.

[60] J. Aizenberg, D. A. Muller, J. L. Grazul, D. R. Hamann, *Science* **2003**, *299*, 1205.
[61] M. F. Butler, N. Glaser, A. C. Weaver, M. Kirkland, M. Heppenstall-Butler, *Cryst. Growth Des.* **2006**, *6*, 781.
[62] Y. J. Han, J. Aizenberg, *Angew. Chem.* **2003**, *115*, 3796; *Angew. Chem. Int. Ed.* **2003**, *42*, 3668.
[63] W.-T. Hou, Q.-L. Feng, *Cryst. Growth Des.* **2006**, *6*, 1086.
[64] K. Subburaman, N. Pernodet, S. Y. Kwak, E. DiMasi, S. Ge, V. Zaitsev, X. Ba, N. L. Yang, M. Rafailovich, *Proc. Natl. Acad. Sci. USA* **2006**, *103*, 14672.
[65] L. A. Estroff, C. D. Incarvito, A. D. Hamilton, *J. Am. Chem. Soc.* **2004**, *126*, 2.
[66] S. Mann, G. Ozin, *Nature* **1996**, *382*, 313.
[67] G. A. Ozin, *Acc. Chem. Res.* **1997**, *30*, 17.
[68] G. A. Ozin, A. C. Arsenault, *Nanochemistry: A Chemical Approach to Nanomaterials*, RSC Publishing, Cambridge, **2005**.
[69] G. A. Kinberger, J. P. Taulane, M. Goodman, *Inorg. Chem.* **2006**, *45*, 961.
[70] S. Mann, *Biomineralization: Principles and Concepts in Bioinorganic Materials Chemistry*, Oxford University Press, Oxford, **2001**.

"Hierarchical Self-Assembly of One Dimensional Streptavidin Bundles as Collagen Mimetic for the Biomineralization of Calcite"

Sabina Burazerovic, Julieta Gadinaru, Julien Pierron and Thomas R. Ward

Experimental Section

Starting Materials. All chemicals were of reagent grade and used as commercially purchased without further purification. Compound **3** was synthesized according to published procedures.[1]

Analyses and physical measurements. Mass-spectrometric analyses were performed on an Analytical VG 7070 EQ instrument. The relative intensities are given in parenthesis (%). The UV/Vis measurements were recorded in a 1 cm quartz cell using a Lambda 6 Perkin-Elmer spectrophotometer. The CD spectra were measured in a 1 cm quartz cell with a J-910 spectropolarimeter (JASCO). HABA titration was performed according to published procedure.[3] Both ^{1}H (400 MHz) and ^{13}C NMR (100 MHz) measurements were carried out on a Bruker Avance 400 spectrometer. The assignments in the 1D spectra were based on additional DEPT, HETCOR and COSY experiments.

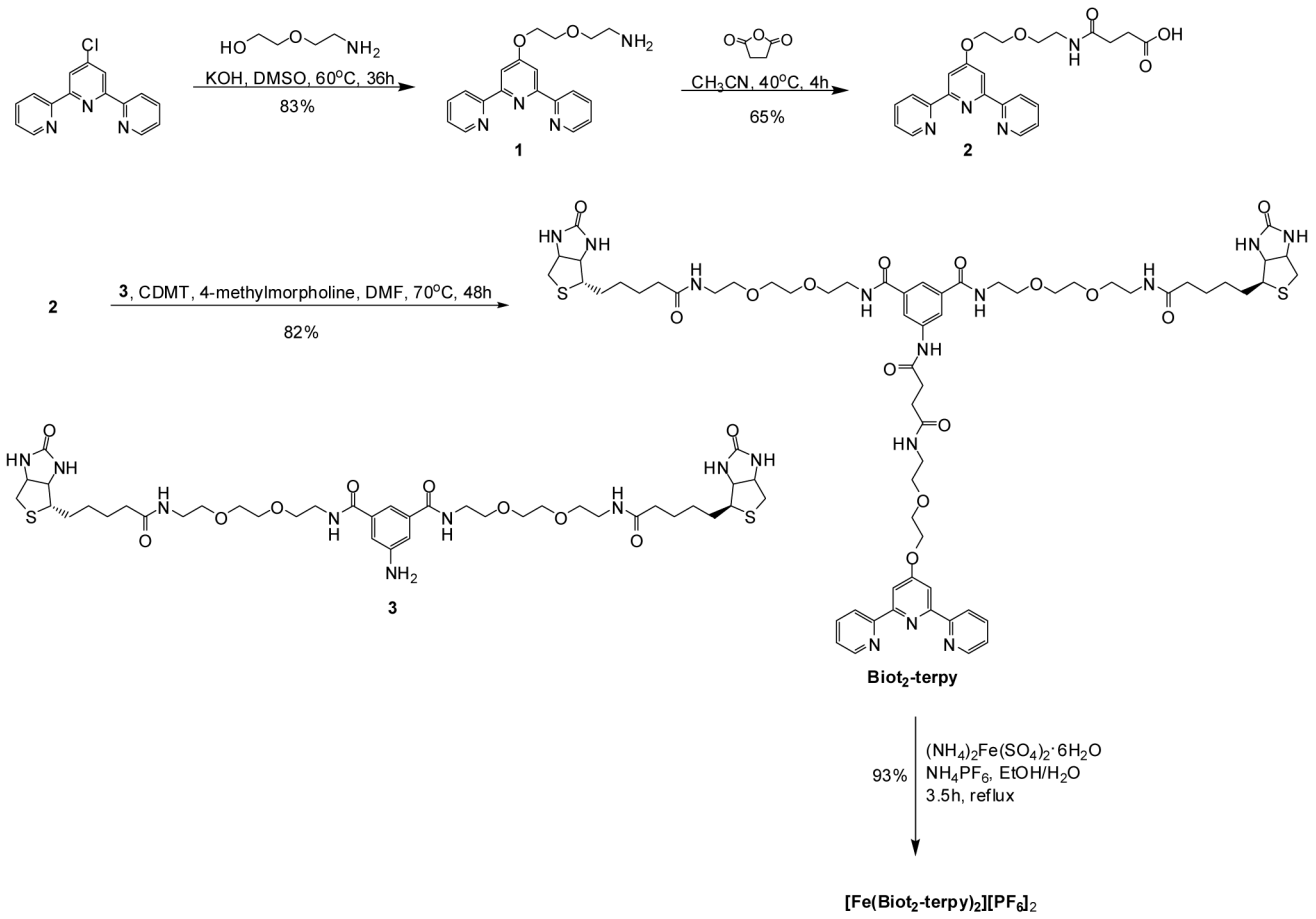

Scheme 1. Synthesis of $[Fe(\mathbf{Biot_2\text{-}terpy})_2]^{2+}$

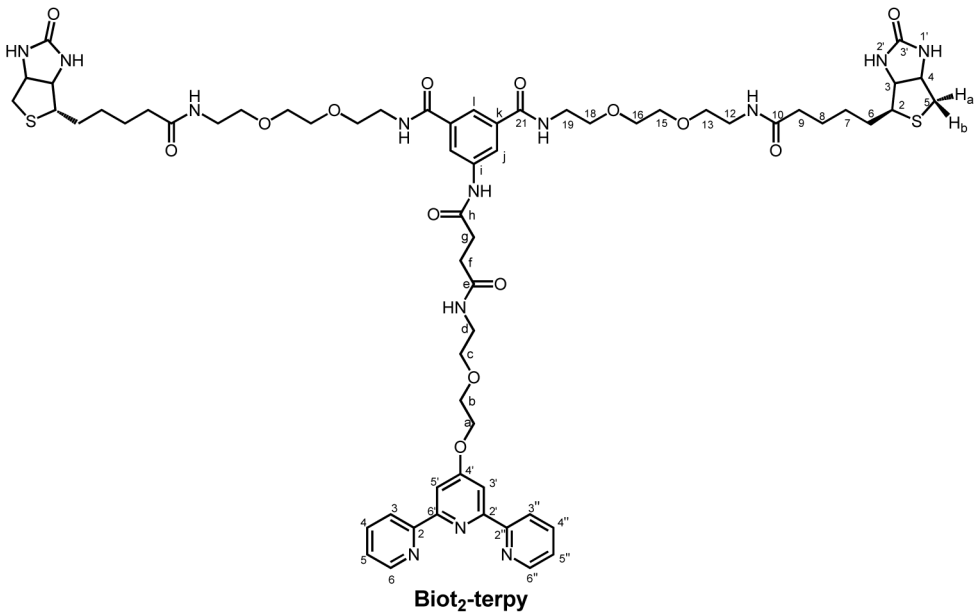

Scheme 2. Numbering scheme used for the NMR assignment

Synthesis of 1[2]: 2-(2-aminoethoxy)ethanol (0.393 g, 3.74 mmol) was added to a suspension of powdered KOH (1.157 g, 20.55 mmol) in dry DMSO (15 mL) under N_2. After 30 min. stirring at 60°C, 4´-Cl-tpy (1.0 g, 3.74 mmol) was added and stirred under heating for an additional 36 h. After cooling to room temperature the mixture was poured onto water (160 mL) and allowed to set for 3 h. The aqueous phase was extracted with CH_2Cl_2 (3x100 mL). The combined organic phases were dried over $MgSO_4$ and evaporated under vacuum to yield 1.041g (83%) of **1** as a yellowish oil. $C_{19}H_{20}N_4O_2$ ESI-MS: 337.1 (100%) ($[M+H]^+$), 694.9 (17%) ($[2M+Na]^+$).

^{1}H NMR (400 MHz, $CDCl_3$): δ 1.70 (s, 2H, NH_2), 2.83 (t, 2H, $^3J_{d-c}$=5.1 Hz, CH_2, H_d), 3.54 (t, 2H, CH_2, H_c), 3.83 (m, 2H, $^3J_{b-a}$=4.6 Hz, CH_2, H_b), 4.33 (t, 2H, CH_2, H_a), 7.24 (ddd, 2H, $^3J_{5-4}$=7.5 Hz, $^3J_{5-6}$=4.8 Hz, $^4J_{5-3}$=1.1 Hz, CH_{terpy}, $H_{5,\ 5''}$), 7.76 (ddd, 2H, $^3J_{4-3}$=7.7 Hz, $^4J_{4-6}$=1.8 Hz, CH_{terpy}, $H_{4,\ 4''}$), 7.98 (s, 2H, CH_{terpy}, $H_{3',\ 5'}$), 8.53 (d, 2H, CH_{terpy}, $H_{3,\ 3''}$), 8.61 (dd, 2H, CH_{terpy}, $H_{6,\ 6''}$).

^{13}C NMR (100 MHz, $CDCl_3$): δ 40.8 (CH_2, C_d), 66.7 (CH_2, C_a), 68.3 (CH_2, C_b), 72.6 (CH_2, C_c), 106.5 (CH_{terpy}, $C_{3',\ 5'}$),

120.3 (CH_{terpy}, $C_{3,\ 3''}$), 122.8 (CH_{terpy}, $C_{5,\ 5''}$), 135.8 (CH_{terpy}, $C_{4,\ 4''}$), 148.0 (CH_{terpy}, $C_{6,\ 6''}$), 155.0 (C_{tert}, $C_{2,\ 2''}$), 156.1 (C_{tert}, $C_{6',\ 2'}$), 166.6 (C_{tert}, $C_{4'}$).

Synthesis of **2**: compound **1** (0.250 g, 0.744 mmol) was dissolved in CH_3CN (10 mL) under heating until complete dissolution occured and then cooled to room temperature. Succinic anhydride (0.147 g, 1.11 mmol) was added, yielding a white precipitate. After one hour stirring at 40° C, the solid was filtered, washed with EtOH and Et_2O, yielding 0.240 g (74%) of **2**. $C_{23}H_{24}O_5N_4$ ESI-MS: 437.2 (100) $[M+H]^+$.

^1H NMR (400 MHz, DMSO-d_6): δ 2.37 (d, 2H, $^3J_{f-g}$=6.4 Hz, CH_2, H_f), 2.46 (d, 2H, CH_2, H_g), 3.30 (td, 2H, $^3J_{d-c}$=5.9 Hz, $^3J_{d-NH}$=5.7 Hz, CH_2, H_d), 3.57 (t, 2H, CH_2, H_c), 3.88 (t, 2H, $^3J_{b-a}$=4.1 Hz, CH_2, H_b), 4.44 (t, 2H, CH_2, H_a), 7.56 (ddd, 2H, $^3J_{5-4}$=7.5 Hz, $^3J_{5-6}$=4.8 Hz, $^4J_{5-3}$=1.2 Hz, CH_{terpy}, $H_{5,\ 5''}$), 8.00 (t, 1H, ^3J=5.7 Hz, NH), 8.04 (s, 2H, CH_{terpy}, $H_{3',\ 5'}$), 8.06 (ddd, 2H, $^3J_{4-3}$=7.7 Hz, $^4J_{4-6}$=1.6 Hz, CH_{terpy}, $H_{4,\ 4''}$), 8.67 (d, 2H, CH_{terpy}, $H_{3,\ 3''}$), 8.77 (dd, 2H, CH_{terpy}, $H_{6,\ 6''}$).

^{13}C NMR (100 MHz, DMSO-d_6): δ 29.1 (CH_2, C_g), 29.9 (CH_2, C_f), 38.5 (CH_2, C_d), 67.6 (CH_2, C_a), 68.4 (CH_2, C_b), 69.3 (CH_2, C_c), 106.7 (CH_{terpy}, $C_{3',\ 5'}$), 120.9 (CH_{terpy}, $C_{3,\ 3''}$), 124.5 (CH_{terpy}, $C_{5,\ 5''}$), 137.3 (CH_{terpy}, $C_{4,\ 4''}$), 149.2 (CH_{terpy}, $C_{6,\ 6''}$),

154.8 (C_{tert}, $C_{2,\ 2''}$), 156.7 (C_{tert}, $C_{6',\ 2'}$), 166.6 (C_{tert}, $C_{4'}$), 171.0 (C_{tert}, C_e), 173.8 (C_{tert}, C_h).

Synthesis of **Biot$_2$-terpy**: To a solution of **2** (0.132 g, 0.302 mmol) in DMF (5 mL), 2-chloro-4,6-dimethoxy-1,3,5-triazine (0.0583 g, 0.332 mmol) and 4-methyl-morpholine (0.1 ml, 0.910 mmol) were added. After 15 min of stirring at room temperature, amino-biotin dimer **3**[1] (0.083 g, 0.0929 mmol) in DMF (5 mL) was added and the solution turned pale pink. The mixture was stirred during 48h at 70°C and the DMF was evaporated under vacuum. The remaining oil was purified by chromatography (Al_2O_3 neutral, $CHCl_3$/MeOH 9:1), to yield 0.163 g (82%) of **Biot$_2$-terpy** as a pale pink foam. $C_{63}H_{86}O_{14}N_{13}S_2$ ESI-MS: 1335.7 (100) $[M+Na]^+$.

^{1}H NMR (400 MHz, CD_3OD-d_4): δ 1.38 (m, 4H, CH_2, H_7), 1.73-1.50 (m, 8H, CH_2, $H_{6,\ 8}$), 2.16 (t, 4H, $^3J_{9-8}$=7.3 Hz, CH_2, H_9), 2.59 (t, 2H, $^3J_{f-g}$=6.6 Hz, CH_2, H_f), 2.69 (d, 2H, $^3J_{5b-5a}$=12.5Hz, CH_2, H_{5b}), 2.71 (t, 2H, CH_2, H_g), 2.90 (dd, 2H, $^3J_{5a-4}$=4.9 Hz, CH_2, H_{5a}), 3.12-3.16 (m, 2H, CH_2, H_2), 3.43-3.70 (m, 28H, CH_2, $H_{12,13,15,16,18,19,c,d}$), 3.93 (t, 2H, $^3J_{b-a}$=4.3 Hz, CH_2, H_b), 4.27 (dd, 2H, $^3J_{3-4}$=7.8 Hz, $^3J_{3-2}$=4.4 Hz, CH_2, H_3), 4.41 (t, 2H, J=4.5 Hz, CH_2, H_a), 4.47 (dd, 2H, CH_2, H_4), 7.47 (ddd, 2H, $^3J_{5-4}$=7.5 Hz, $^3J_{5-6}$=4.8 Hz, $^4J_{5-3}$=1.2 Hz, CH_{terpy}, $H_{5\ ,5''}$), 7.94 (m, 1H, CH_{ar}, H_1), 7.98 (s, 2H, CH_{terpy}, $H_{3',\ 5'}$), 8.00 (m, 2H, $^3J_{4-3}$=7.7 Hz, $^4J_{4-6}$=1.6 Hz, CH_{terpy}, $H_{4,\ 4''}$), 8.14 (d, 2H, $^4J_{g-1}$=1.4 Hz, CH_{ar},

H_g), 8.60 (d, 2H, CH_{terpy}, $H_{3,\ 3''}$), 8.67 (dd, 2H, CH_{terpy}, $H_{6,\ 6''}$).

^{13}C NMR (100 MHz, CD_3OD-$_{d4}$): δ 25.8 (CH_2, C_8), 28.5 (CH_2, C_6), 28.7 (CH_2, C_7), 30.7 (CH_2, C_g), 31.1(CH_2, C_f), 35.7 (CH_2, C_9), 39.3 (CH_2), 39.5 (CH_2), 40.0 (CH_2), 40.1 (CH_2), 56.0 (CH, C_2), 60.6 (CH, C_4), 62.3 (CH, C_3), 68.1 (CH_2), 69.4 (CH_2), 69.5(CH_2), 69.6(CH_2), 69.9(CH_2), 70.3(CH_2), 70.4 (CH_2), 107.5 (CH_{terpy}, $C_{3',\ 5'}$), 121.2 (CH_{ar}, C_1), 121.5 (CH_{ar}, C_j), 122.0 (CH_{terpy}, $C_{3,\ 3''}$), 124.5 (CH_{terpy}, $C_{5,\ 5''}$), 135.8 (C_{tert}, C_k), 137.7 (CH_{terpy}, $C_{4,\ 4''}$), 139.6 (C_{tert}, C_i), 149.1 (CH_{terpy}, $C_{6,\ 6''}$), 156.1 (C_{tert}, $C_{2,\ 2''}$), 157.4 (C_{tert}, $C_{6',2'}$), 165.1(C_{tert}, $C_{4'}$), 167.6 ($C_{tert.biot}$, $C_{5'}$), 168.2 (C_{tert}, C_{21}), 172.2 (C_{tert}, C_{10}), 173.7 (C_{tert}, C_e), 175.1 (C_{tert}, C_h).

Synthesis of [Fe(**Biot$_2$-terpy**)$_2$][(PF_6)$_2$]: The ligand **Biot$_2$-terpy** (0.071 g , 0.0541 mmol) was dissolved in EtOH (4 ml) and an aqueous solution of $(NH_4)_2Fe(SO_4)_2{\cdot}6H_2O$ (Mohr salt, 0.0106g, 0.0270mmol in 1 ml) was added dropwise. The resulting deep violet mixture was refluxed for 3.5h under inert atmosphere. After cooling to 25°C, an excess of NH_4PF_6 (0.176 g, 1.082 mmol in 1 ml of water) was added to the solution and during evaporation under vacuum of the solvent, a dark-violet solid precipitated. The solid was filtered, washed with water. After redissolution in EtOH/CH_2Cl_2 (2:1), the product was precipitated with ether, filtered, and dried in vacuo to give 0.0750 g (93%) of [Fe(**Biot$_2$-terpy**)$_2$](PF_6)$_2$.

$C_{126}H_{172}F_{12}FeN_{26}O_{28}P_2S_4$, ESI-$MS_{(+)}$: 1340.04 (100) $[(M-2PF_6)/2]^+$. ESI-$MS_{(-)}$: 145.1 (100) $[PF_6]^-$.

UV-Vis, $_{max}$ ($M^{-1}cm^{-1}$), c = 5.0135 x10^{-5}M, DMSO: 557 nm (9237), 316 nm (31212), 268 nm (43777), 244 nm (53276).

Bundle formation and biomineralization experiments.

General considerations. Manipulations were carried out in a laminar flow hood in a clean room using six-well-plates (well diameter = 3.5cm) with a low evaporation lid. Each experiment was performed in triplicate.

Bundle formation. A Sav sample ($8\cdot10^{-6}$ M, final concentration) was dissolved in a $CaCl_2$ solution (0.05M). An equimolar amount of $[Fe(\mathbf{Biot_2\text{-}terpy})_2]^{2+}$ (dissolved in dmso, 0.34 mM, 70 μl required for 3 ml of the Sav solution above) was added to the aqueous solution and allowed to stirr at rt for 5 min.

Biomineralization. The biomineralization experiments were carried out in a closed desiccator with vials of $(NH_4)_2CO_3$(s) to provide a CO_2 atmosphere. A solution of $CaCl_2$ (1 ml, 0.05 M) was introduced in each well followed by the addition of $[Fe(\mathbf{Biot_2\text{-}terpy})_2]^{2+} \subset$ Sav (1 ml of a $8\cdot10^{-6}$ M solution). After 15 hours, the plates were removed from the desiccator and the crystals obtained were observed under the optical microscope. The crystal strands were picked with tweezers

and rinsed gently with distilled water before set put aside for SEM experiments.

Optical Microscopy. The crystals obtained during the mineralization experiments were directly observed in the six well plates with a polarizing microscope equipped with a digital camera (Olympus ZSH 10, enlargement: 10 to 100 times).

Electron Microscopy.

$[Fe(Biot_2\text{-terpy})_2]^{2+} \subset$ Sav bundles. A drop of the solution prepared as described above was deposited onto a carbon adhesive tab and allowed to adhere for 1 min. The excess solution was then blotted off and the samples were dried in a desiccator overnight before being gold-coated. The acceleration voltage used for the bundles was typically 5kV.

Biomineralized $[Fe(Biot_2\text{-terpy})_2]^{2+} \subset$ Sav bundles. The crystals strands described above were deposited on carbon adhesive tabs and dried overnight in a desiccator before gold-coating. The acceleration voltage used for observation of the biomineralized bundles was typically 10 kV.

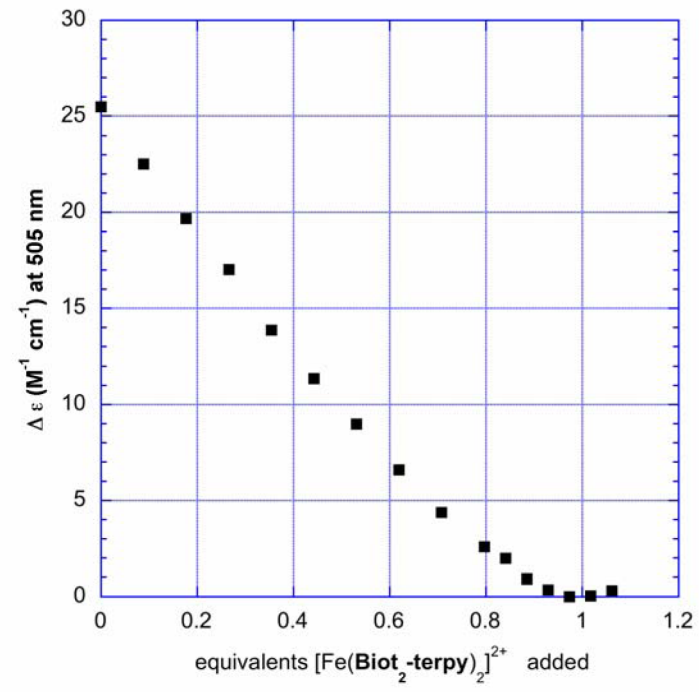

Figure 1. Diplacement of HABA ⊂ Sav by $[Fe(\mathbf{Biot_2\text{-}terpy})_2]^{2+}$ to afford $[Fe(\mathbf{Biot_2\text{-}terpy})_2]^{2+} \subset$ Sav. This reaction is conveniently followed by the disappearance of the induced CD signal at λ_{max}=505 nm. For details, see ref [3].

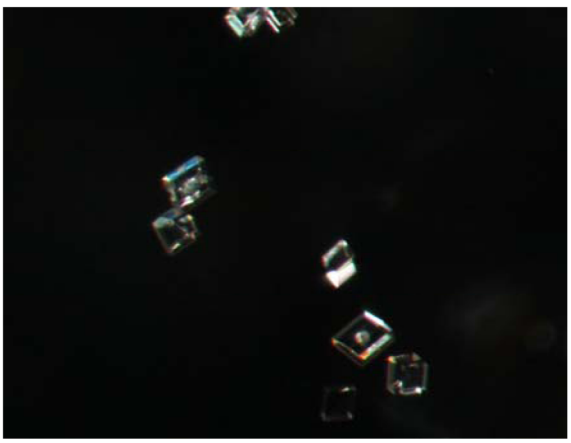

a)

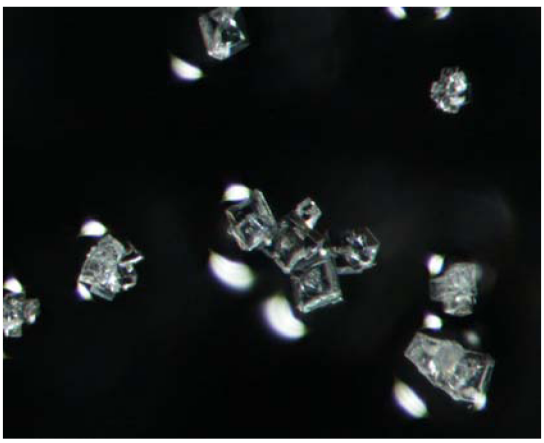

b)

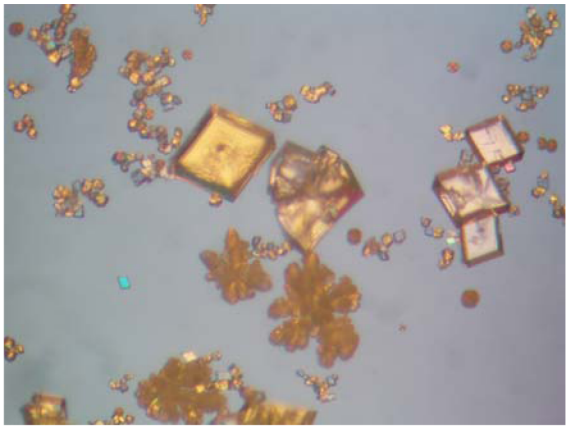

c)

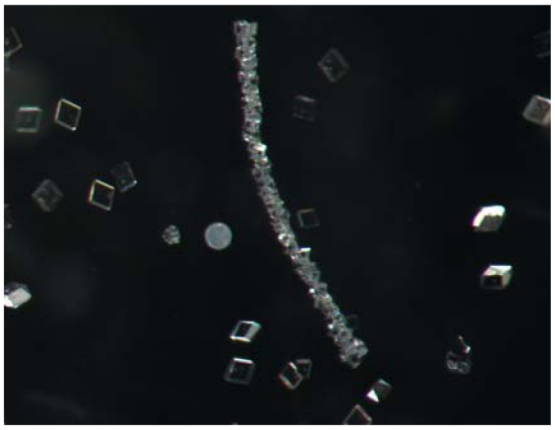

d)

Figure 2. Optical micrographs of calcium carbonate crystals: in the absence of additives a); in the presence of Sav b); Sav + **3** c); and Sav +[Fe(**Biot$_2$-terpy**)$_2$]$^{2+}$ d).

References

[1] K. J. Hamblett, B. B. Kegley, D. K. Hamlin, M.-K. Chyan, D. E. Hyre, O. W. Press, D. S. Wilbur, P. S. Stayton, *Bioconj. Chem.* 2002, **13**, 588.

[2] G.R.Newkome, E.He, *J. Mat. Chem.* 1997, **7**, 1237.

[3] M. Skander, N. Humbert, J. Collot, J. Gradinaru, G. Klein, A. Loosli, J. Sauser, A. Zocchi, F. Gilardoni, T. R. Ward, *J. Am. Chem. Soc.* 2004, **126**, 14411.

2.4 Step-by-Step Assembly of Streptavidin Units

In our efforts to produce well defined protein-based nanostructures, a Step-by-Step (SbS) assembly approach was investigated. Biotinylated self-assembled monolayers (SAMs) on gold were used to anchor SAv, which was successively exposed to BBA-based connectors - BBA_2 or BBA_3 - and SAv (Fig.1).

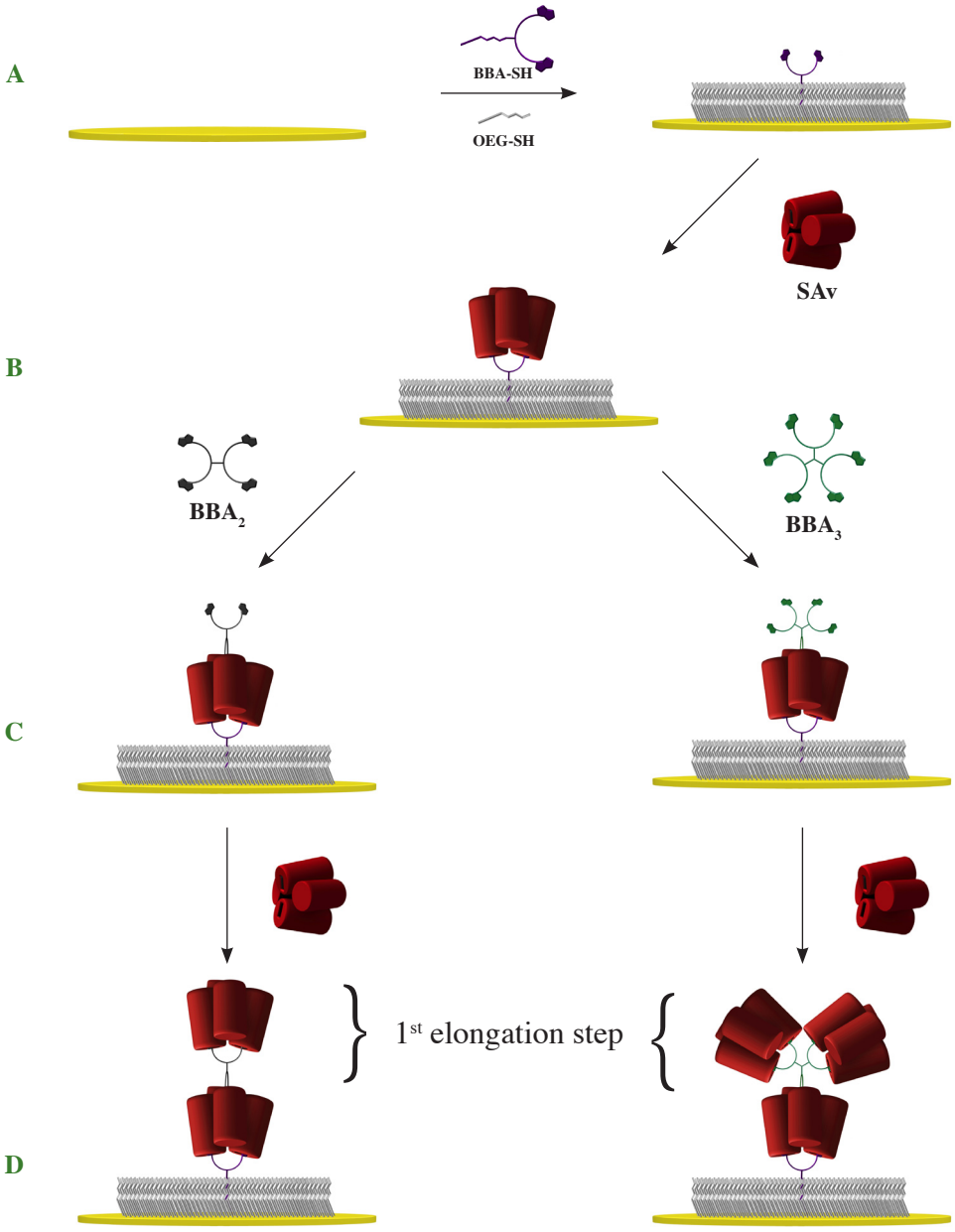

Figure 1 Schematic representation of the SbS assembly of SAv units. a) A bis-biotinylated mixed SAM was formed on gold and b) SAv was anchored onto the functionalized monolayer. c) The latter was exposed to BBA_2 or BBA_3 followed by d) further immobilization of SAv.

In addition, this SbS assembly approach enabled us to produce monodisperse and size-controlled SAv-based nano-objects (Fig. 2).

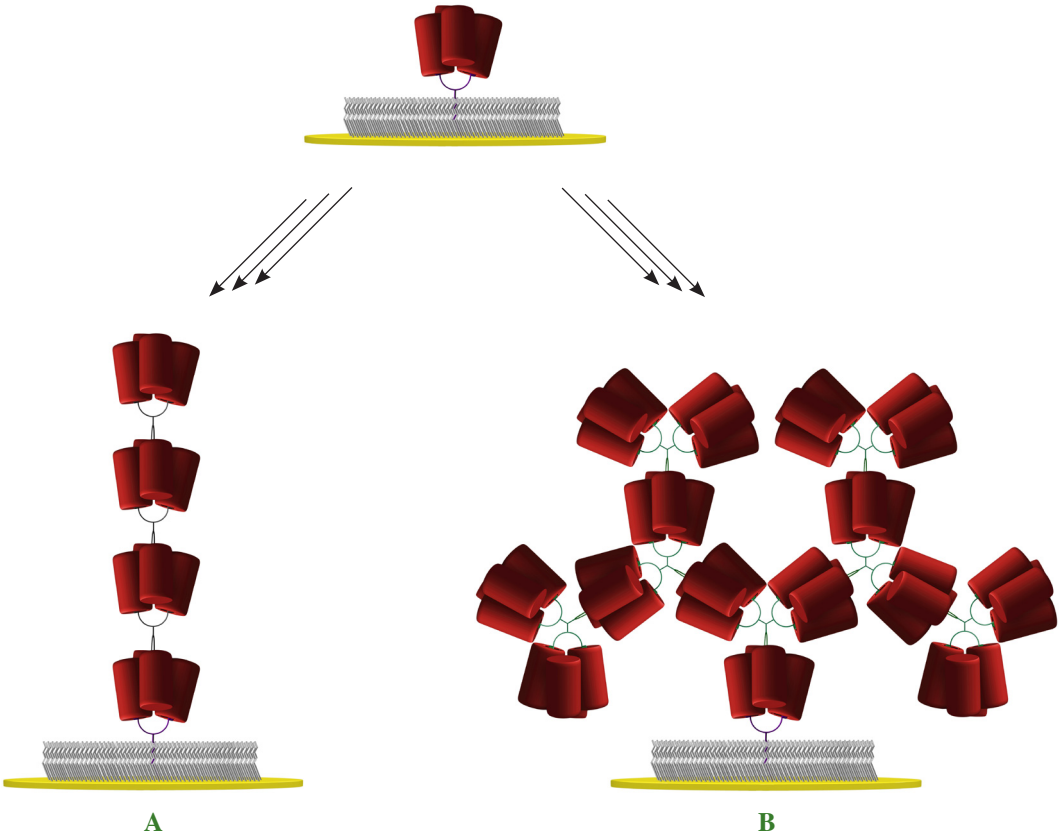

Figure 2 Schematic representation of the discrete nanostructures generated by an immobilized SAv unit being three times successively exposed to a) BBA_2 and SAv; b) BBA_3 and SAv.

The stepwise elongation process was followed *in situ* by SPR and QCM, enabling the estimation of the amount of protein immobilized at each elongation step. These valuable informations were used to probe whether the growth process followed a linear or exponential trend when BBA_2 or BBA_3 was respectively involved in the nanoconstructs.

To obtain an immobilization platform for which non-specific interactions towards SAv were minimized, oligo(ethylene glycol) alkanethiolate (OEG-SH) (Fig. 3) was chosen as a diluting component of the SAMs.[1-4] Monolayers containing 1% of biotin have been extensively studied by different research groups[5-11] and the required thiolated molecules (*e.g*, Biot-SH) are commercially available. Even though this SAM composition was reported to

achieve the immobilization of a full monolayer of SAv,[10] it was used as a starting point to investigate the SbS assembly of SAv with BBA_2 and BBA_3. Indeed, a low-density coverage of SAv was required to record images of the growing immobilized architectures by AFM. We

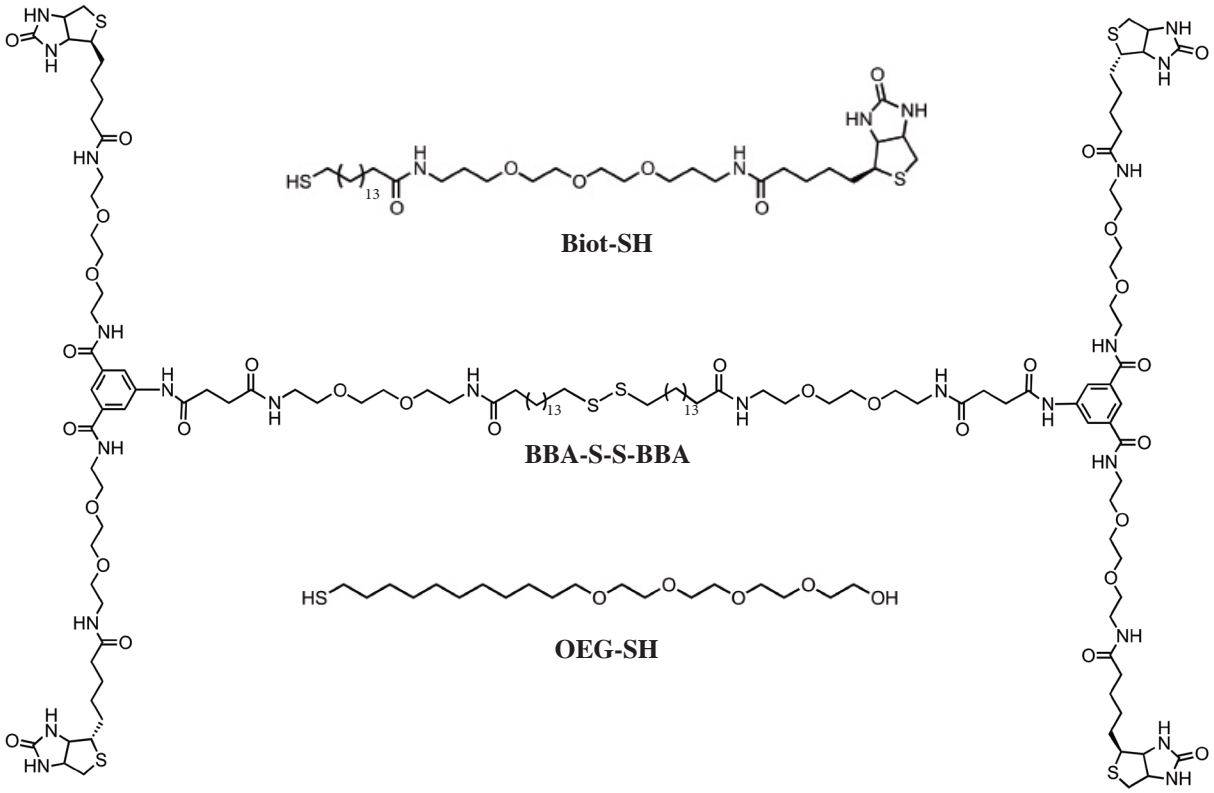

Figure 3 Chemical structure of the alkanethiolates used to form the self-assembled monolayers (SAMs): commercially available Biot-SH and OEG-SH; and synthesized BBA-S-S-BBA.

rationalized that well-distanced SAv-based nanostructures would be easier to identify and scrutinize by AFM compared to a compact multi-layered system. Besides, steric hindrance was to be expected when growing SAv-based architectures onto a high-density adlayer of SAv, especially with BBA_3, considering the increase of the footprint area expected after each extension step. However, sub-monolayer coverages of immobilized SAv were reported to be less stable [5] and to result in substantially less binding of biotinylated molecules.[9,10] This instability has been attributed to the fact that, at low biotin fraction, SAv is bound to the monolayer through one biotin only.[5,7] In addition, full monolayer of SAv are believed to undergo a 2D structural rearrangement leading to a more compact and rigid phase.[12-14]

In the pursuit of our goal to obtain well-distanced SAv units anchored on a SAM, we

speculated that the immobilization of SAv units through two biotin binding-sites would increase the stability of a low-density adlayer. For that purpose, BBA-S-S-BBA (Fig. 3) synthesized beforehand (section 2.1.4), was used to create a new immobilization platform suiting our needs.

To study the SbS growth of SAv-based nanostructures with BBA_2 and BBA_3, we proceeded as follow: in a first round of experiments, we controlled the unspecific adsorption of SAv and BBA-based ligands on OEG SAMs. Published results on 1% biotinylated sensors were reproduced, and the SbS assembly of SAv on Biot-SH/OEG-SH SAMs with $\chi_{Biot\text{-}SH} = 0.01$ and 0.001 was studied by QCM-D and SPR. The immobilization of SAv onto BBA-SH/OEG-SH SAMs with $\chi_{BBA\text{-}SH} = 0.001$ and 0.0001, as the SbS extensions of SAv units with BBA_2 and BBA_3 were then followed by SPR and/or QCM. The resulting immobilized SAv-based nanostructures were finally imaged by AFM in the hydrated state.

NB: A detailed explanation of the QCM-D and SPR data interpretation and analysis is annexed in Appendix 2.

2.4.1 Nonspecific Adsorption of SAv on SAMs Composed of OEG-SH

To study the assembly of SAv SbS, it was of importance to obtain an immobilization platform for which non-specific interactions at the sensor surface were minimized.[10] In that spirit, the non-specific adsorption of SAv and the BBA moiety onto the modified surface was first evaluated. To do so, solutions of SAv (1.0 μM in PBS 0.1 M, pH:7.4) and BBA_2 (6.0 μM in MeOH/HBS-P :1/100) were successively flowed over OEG-SH monolayers and the process was monitored by SPR (Fig. 4). At the end of each injection, the surface was washed three times with running buffer solution (HBS-P) and a stable baseline was acquired for at least 5 min. before proceeding to the next injection.

The sensorgram confirmed that SAv did not bind onto the OEG-SH monolayer (ΔR = 2.0 RU and 0 RU respectively for the two first injections). The injection of BBA_2 induced a relative SPR response shift of 31.0 RU. Since the subsequent exposition of the

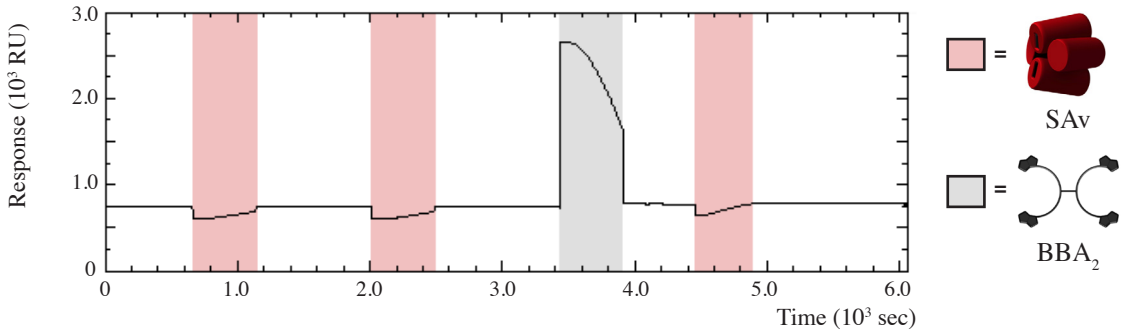

Figure 3 SPR response on the passage of solutions of SAv ($1 \cdot 10^{-6}$ M in PBS) and BBA_2 ($2 \cdot 10^{-6}$ M in HBS-P (1% MeOH)) over a OEG-SH SAM. The surface was washed with HBS-P after each injection of the solution of biomolecules. A flow rate of 5 µl/min was used during the whole procedure. The SAv and BBA_2 injection steps are indicated respectively by the pink and grey colored bands.

sensor to SAv solution did not induce any significant binding of the protein (ΔR = 4.0 RU), the non-specific adsorption of SAv and BBA_2 was considered as being negligible and OEG-SH was used as a diluent component for all the biotinylated mixed SAMs used in this work.

2.4.2 Characterization of SAv Immobilization onto 1% Biot-SH Sensors

Before proceeding to the SbS assembly of SAv experiments, the initial anchoring step of SAv onto modified surfaces containing 1% of biotin (Biot-SH/OEG-SH : 1/99) was first characterized (Table 1). With both sensing techniques, 95% of the saturation value was reached within 120 seconds. A frequency shift of -26 Hz ± 2 Hz with a dissipation shift of $0.2 \pm 0.1 \cdot 10^{-6}$ was recorded at the 3rd overtone by QCM-D. These are in the range of earlier reported values for SAv monolayer formation on biotinylated mixed SAMs.[10, 11, 13] Since the normalized frequency shift observed at different overtones gave essentially the same value, Sauerbrey relation,[15] $\Delta m_{QCM} = -C_{QCM} \Delta f$ (C_{QCM} = 17.7 ng·cm^{-2}·Hz^{-1}), was used to estimate an adsorbed mass for SAv of 469 ± 35 ng/cm^2.

Similar to the results published by Jung *et al.*, a response shift of 1446 ± 53 RU was recorded by SPR.[6] By assuming 1000 RU = 100 ng/cm^2, the observed response shift corresponded to 144 ± 6 ng/cm^2 of immobilized SAv.[17] This is below the value (~230 ng/cm^2) usually associated with the formation of SAv 2D layer on biotinylated surfaces.[6, 13] Even though mature SAv differs from the widely used core SAv by 20 additionnal residues at the C-terminus, we assumed that a 2D "crystalline" monolayer of SAv was not achieved in this case.

The difference observed between Δm_{QCM} and Δm_{SPR} reflects the fact that, in contrast to SPR which measures the "dry" mass, QCM is sensitive to both the adsorbed biomolecules and the coupled solvent. By comparing the optical and hydrated masses, a hydration of 69% was estimated for the immobilized layer of SAv. This result is consistent with results previously reported for SAv monolayer formation onto biotinylated supported lipid bilayers (SLBs).[12, 18, 19] Furthermore, using a molecular weight of 65 700 g/mol^{-1}, the immobilized mass of SAv (144 ng/cm^2) corresponded to an available area of 76 nm^2 per SAv unit. Assuming a footprint area of ~30 nm^2 for SAv, we speculated that the linear SbS assembly of SAv using BBA_2 could potentially be successful.

	1% Biot-SH SAMs
ΔSPR (RU)	1440 ± 58
$\Delta f_3/3$ (Hz)	-26.0 ± 2.1
ΔD_3 (10^{-6})	0.19 ± 0.05
Δm_{SPR} (ng/cm^2)	144 ± 6
Δm_{QCM} (ng/cm^2)	469 ± 35
hydration (%)	69
area per SAv (nm^2/SAv unit)	76

Table 1 Quantification of the immobilized amount of SAv onto 1% Biot-SH sensors. Adsorption values from QCM-D are shown as normalized frequency shifts for the 3rd overtone that was chosen as the most reproducible and stable one. The error indicates the variation between four measurements. The degree of hydration was calculated by comparing Δm_{QCM} (calculated from Δf using Sauerbrey equation) to Δm_{SPR} (calculated by using the assumption 1000 RU = 100 ng/cm^2). The occupied area per SAv unit was estimated by using Δm_{SPR} and a molecular weight of 65 700 g·mol^{-1} for SAv.

2.4.3 Step-by-Step Assembly of SAv on SAMs Composed of Biot-SH and OEG-SH

The SbS assembly of SAv using BBA_2 and BBA_3 was attempted on 1% Biot-SH sensors. Two extension steps using BBA_2 (Fig.4) and four steps using BBA_3 (Fig. 5) were followed by QCM-D. Throughout both experiments, the frequency decreased (mass uptake due to adsorption) at each injection step without any increase at the rinsing step (ΔD and Δf values recorded at the 3rd overtone for each injection step were annexed in Appendix 2). Since the normalized frequency shifts observed at different overtones did not differ much and $\Delta D/\Delta f < 1 \cdot 10^{-8}$ Hz,[20] Sauerbrey relation was used to translate the recorded Δf into mass uptake.

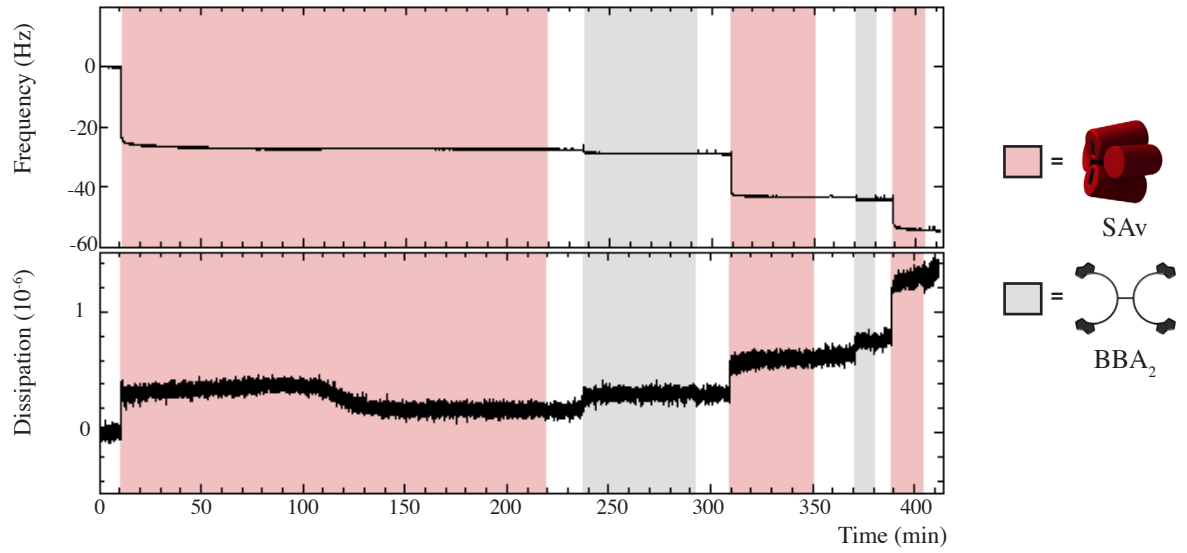

Figure 4 QCM-D measurements for the SbS assembly of SAv using BBA_2 on a 1% Biot-SH sensor. Δf and ΔD vs time traces (3rd overtone) recorded upon successive exposure of the biotinylated surface to SAv ($1{\cdot}10^{-6}$ M in HBS-P) and BBA_2 ($2{\cdot}10^{-6}$ M in HBS-P (1% MeOH)) solutions. The surface was rinsed three times with running buffer (HBS-P) at the end of each injection. The SAv and BBA_2 injection steps are indicated respectively by the pink and grey colored bands.

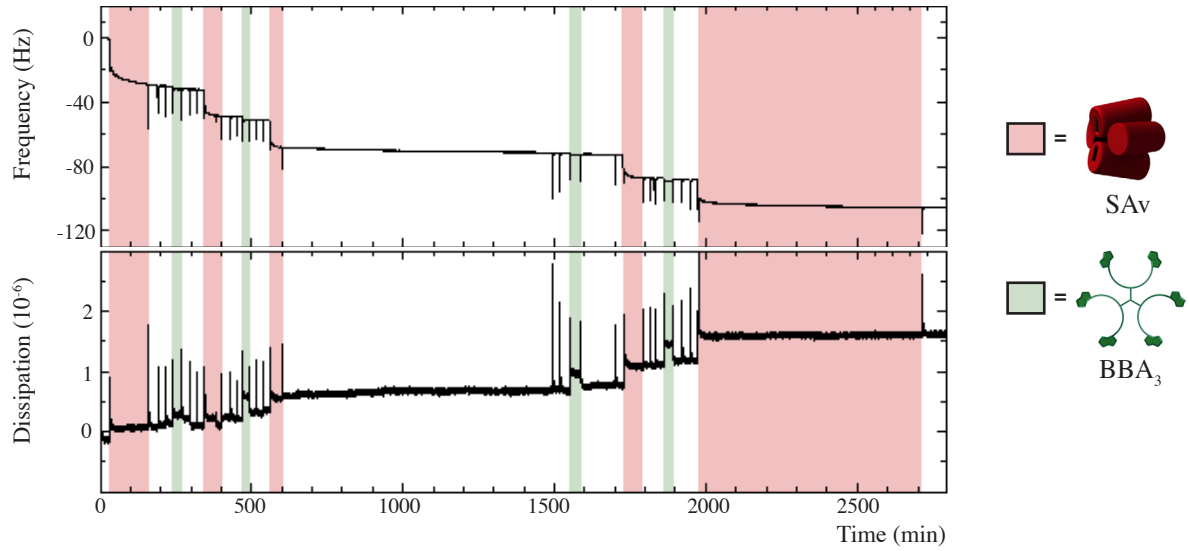

Figure 5 QCM-D measurements for the SbS assembly of SAv using BBA_3 on a 1% Biot-SH sensor. Δf and ΔD vs time traces (3rd overtone) recorded upon successive exposure of the biotinylated surface to SAv ($1{\cdot}10^{-6}$ M in HBS-P) and BBA_3 ($2{\cdot}10^{-6}$ M in HBS-P (1% MeOH)) solutions. The surface was rinsed three times with running buffer (HBS-P) at the end of each injection. The SAv and BBA_3 injection steps are indicated respectively by the pink and green colored bands.

In parallel to the QCM experiments, ten extension steps of SAv using BBA_2 (Fig.6) and five steps using BBA_3 (Fig. 7) were followed by SPR. The sensorgrams climbed (mass up-take due to adsorption) at each SAv injection step without any decrease at the washing step (Δ*R* values recorded for each injection step were annexed in Appendix 2).

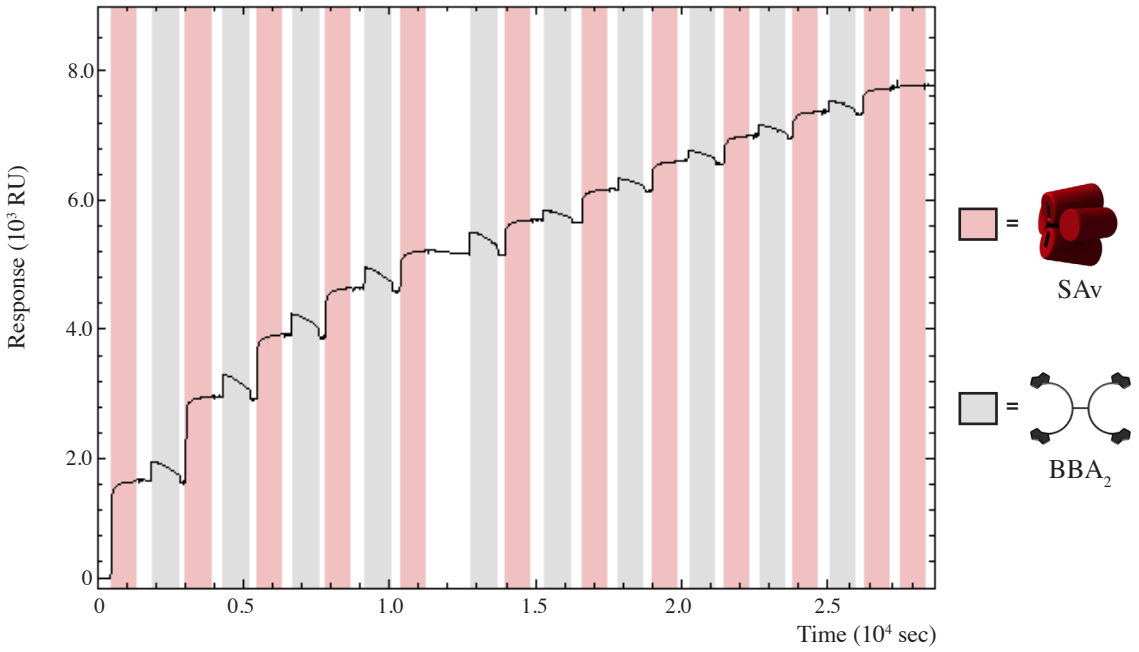

Figure 6 SPR sensogram for a ten-steps elongation of SAv using BBA_2 on a 1% Biot-SH sensor. A flow rate of 5 µl/min was used during the whole procedure; 80 µl of SAv ($1 \cdot 10^{-6}$ M in PBS) and BBA_2 ($2 \cdot 10^{-6}$ M in HBS (1% MeOH)) were flowed over the sensor at each injection step. The surface was washed three times with running buffer (HBS-P) at the end of each injection. The SAv and BBA_2 injection steps are indicated respectively by the pink and grey colored bands. After the 10th SAv elongation step and the subsequent washing step, SAv was flown over the surface and no adsorption was observed.

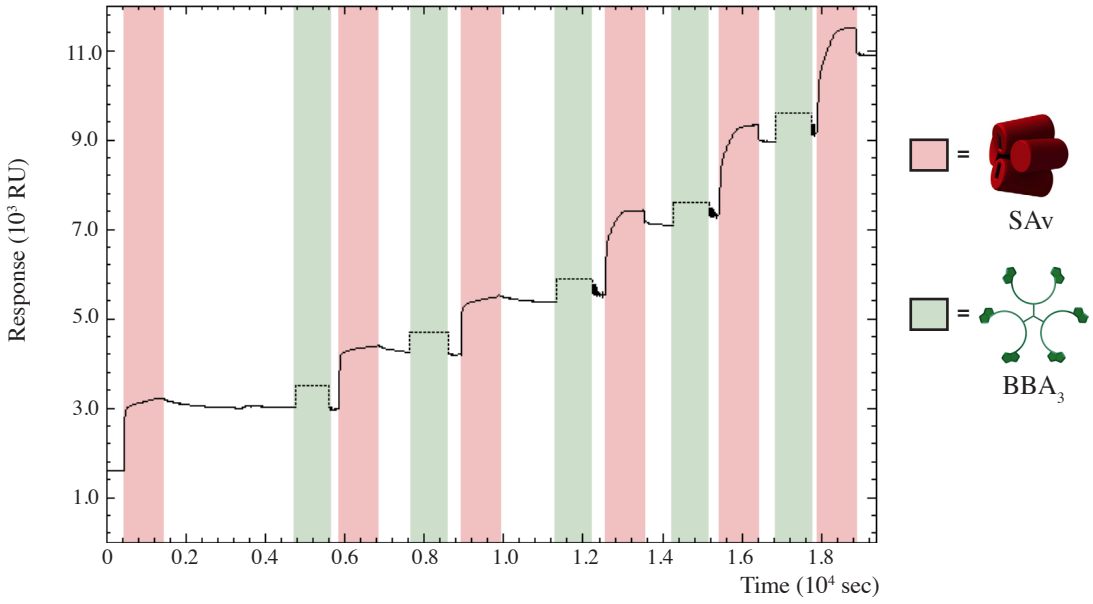

Figure 7 SPR sensogram for a five-steps elongation of SAv using BBA_3 on a 1% Biot-SH sensor. A flow rate of 5 µl/min was used during the whole procedure ; 80 µl of SAv ($1 \cdot 10^{-6}$ M in HBS-P) and BBA_3 ($2 \cdot 10^{-6}$ M in HBS-P (0.5% DMF) solutions were flowed over the biotinylated SAM each injection step. The SAv and BBA_3 injection steps are indicated respectively by the pink and green colored bands.

The resulting Δm_{QCM} and Δm_{SPR} obtained for the successive elongation steps of SAv using BBA_2 and BBA_3 (Fig. 8), as the corresponding extension efficiencies (Table 2), defined as $Eff = \Delta m_n / \Delta m_{n-1}$ were determined.

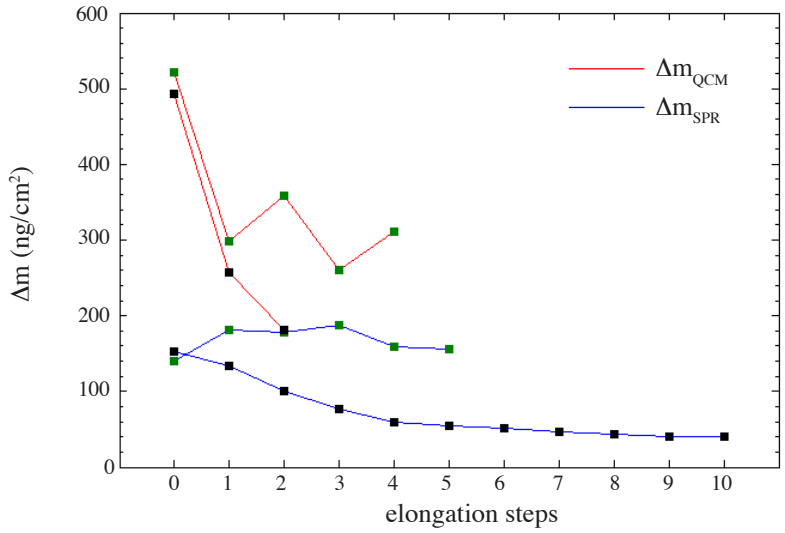

Figure 8 Variation of the adsorbed mass of SAv at each elongation step using BBA_2 (black squares) and BBA_3 (green squares) on 1% Biot-SH SAMs. For consistency of terminology, the initial immobilization step of SAv onto the biotinylated SAMs was denoted as the elongation step "0".

	Elongation step									
	1	2	3	4	5	6	7	8	9	10
Eff using: BBA_2 (QCM)	0.52	0.70	-	-	-	-	-	-	-	-
" (SPR)	0.87	0.76	0.76	0.78	0.91	0.96	0.90	0.93	0.94	1.0
BBA_3 (QCM)	0.57	1.2	0.72	1.2	-	-	-	-	-	-
" (SPR)	0.92	0.91	1.35	1.04	1.06	-	-	-	-	-

Table 2 Extension efficiency (*Eff*) of each elongation step of SAv using BBA_2 and BBA_3 for the SbS assembly experiment on 1% Biot-SH SAMs followed by QCM-D and SPR.

The SbS assembly of SAv onto 1% Biot-SH SAMs did not proceed quantitatively; the *Eff* values obtained were below 1.0 and 2.0 for the successive extension steps using BBA_2 and BBA_3, respectively (Table 2). The results suggested that, onto 1% Biot-SH sensors, BBA_3 behaved more or less as a linear junction in the SbS assembly of SAv. Also, the *Eff* value of 0.96 obtained at the sixth extension step using BBA_2 approached the ideal value expected for an effective linear junction. The Δm_{SPR} for this elongation step corresponded to ~50 ng/cm²; about 1/3 of the amount of SAv immobilized at the initial anchoring step. We concluded that the Biot-SH SAMs needed to be further diluted with OEG-SH to avoid steric hindrance during

the SbS assembly of SAv.

The SbS elongation of SAv using BBA_3 onto a 0.1% Biot-SH SAM was followed by QCM (Fig. 9). The initial exposure of the modified surface to a SAv solution (t ~ 35 min) resulted in a drop of the frequency ($\Delta f_{n=3}$ = -4.9 Hz) and an increase in dissipation ($\Delta D_{n=3} = 0.15 \cdot 10^{-6}$). However, an increase of the frequency was observed during the buffer rinsing step (t ~ 85 min)

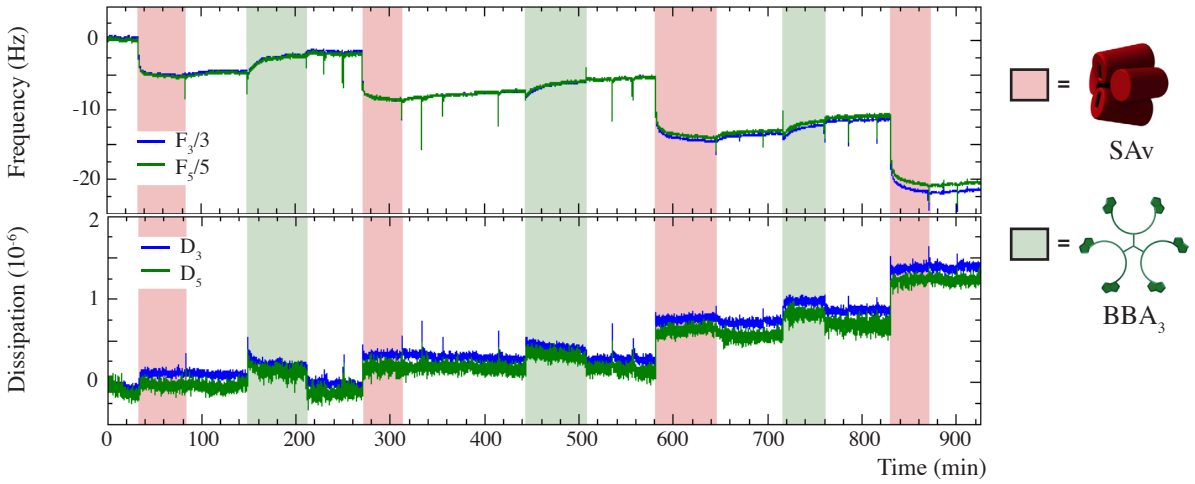

Figure 9 QCM-D measurements for the SbS assembly of SAv using BBA_3 on a 0.1% Biot-SH sensor. Δf and ΔD vs time traces (3rd and 5th overtone) recorded upon successive exposure of the biotinylated surface to SAv ($1 \cdot 10^{-6}$ M in HBS-P) and BBA_3 ($2 \cdot 10^{-6}$ M in HBS-P (1% MeOH)) solutions. The surface was rinsed three times with running buffer (HBS-P) at the end of each injection. The SAv and BBA_3 injection steps are indicated respectively by the pink and green colored bands.

and, more importantly, when the immoblized SAv units were exposed to a BBA_3 solution (t ~ 150 min), stabilizing at $\Delta f_{n=3}$ = 2.8 Hz. This behavior was observed throughout the experiment; exposure of the immobilized SAv to a BBA_3 solution induced a decrease of the frequency (mass loss due to desorption). Taking into account the mass loss recorded after the BBA_3 injection steps (see Appendix 2 for detailed Δf and ΔD values), elongation efficiency values of 2.7, 2.2 and 1.7 were respectively obtained for three successive elongation steps of SAv. The fact that the first two extension steps exceed the theoretical value of 2.0 can be explained by rearrangement events taking place; desorption followed by rebinding to another anchored SAv at the sensor surface.

Considering the lack of stability observed for the 0.1% Biot-SH monolayer towards the

SbS growth of SAv nanostructures using BBA-based ligands, the next step consisted of testing our tailor-made immobilization platform, the BBA-SH/OEG-SH SAMs.

2.4.4 Preparation of SAMs Composed of BBA-SH and OEG-SH

Considering the solubility issues encountered during the purification process of BBA-S-S-BBA (section 2.1.4), mixed SAMs composed of BBA-SH and OEG-SH prepared by two different adsorption methods were qualitatively analyzed by. The coadsorption method consisted of immersing the gold substrate in a solution of OEG-SH and BBA-S-S-BBA in EtOH for a period of 15 h. In the sequential adsorption, the gold substrate was first exposed to a solution of BBA-S-S-BBA for 30 min and then immersed into an ethanolic solution of OEG-SH during a period of 15h. The XPS analysis results are presented below (Table 3). For the coadsorption method, no nitrogen was detected in the elemental analysis of the monolayer composition. This suggested that BBA-S-S-BBA, the only thiolated component bearing nitrogen atoms, was not incorporated into the SAM or, at least, not in

Method	% C	% N	% O	% S
coadsorption	73.9	-	23.3	2.8
sequential adsorption	72.2	2.7	21.2	3.9

Table 3 XPS data of surface elemental percentages of 1% BBA-SH SAMs prepared by coadsorption and stepwise procedures.

detectable amounts. The mixed SAMs prepared by the stepwise procedure presented 2.7% of nitrogen in the monolayer composition, confirming the presence of biotin in the monolayer. Moreover, angle-resolved XPS (ARXPS) experiments were carried out to characterize the depth profile composition of the monolayer (see Appendix 2). The results suggested that the biotin moieties were on average more abundant at the surface of the monolayer than at the SAM-gold substrate interface.

In the light of the XPS experiments, BBA-SH/OEG-SH SAMs used as immobilization platforms for the SbS assembly of SAv were all prepared by sequential adsorption.

2.4.5 Step-by-Step Assembly of SAv on SAMs Composed of BBA-SH and OEG-SH

The SbS extension of SAv using BBA_2 and BBA_3 was attempted on 0.1‰ BBA-SH SAMs. With this SAM composition, no stable baseline could be recorded for the frequency signal at the begining of the QCM experiments. Although the SbS assembly of SAv using BBA_2 was attempted, a persistent drift interfered with the data acquisition. Nevertheless, six extension steps of SAv using BBA_3 were monitored by QCM (Fig 10). The monitored frequency signal

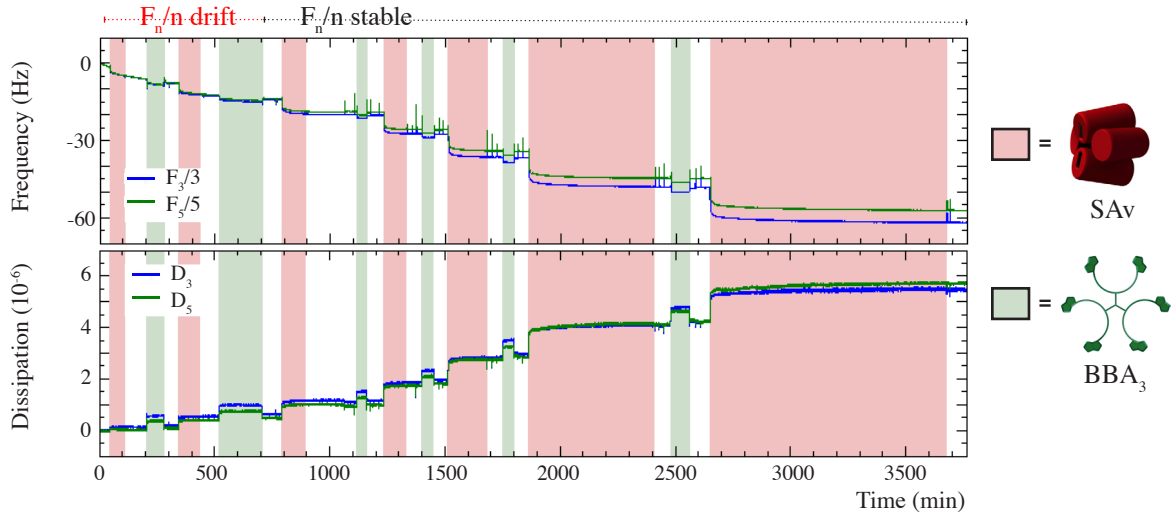

Figure 10 QCM-D measurements for the SbS assembly of SAv using BBA_3 on a 0.1‰ BBA-SH sensor. Δf and ΔD vs time traces (3rd (blue) and 5th (green) overtone) recorded upon successive exposure of the biotinylated surface to SAv ($1 \cdot 10^{-7}$ M in HBS-P) and BBA_3 ($4 \cdot 10^{-7}$ M in HBS-P (1% MeOH)) solutions. The surface was rinsed three times with running buffer (HBS-P) at the end of each injection. Eventhough the frequency signal drifted until t~700 min, the whole frequency vs time trace is shown. The SAv and BBA_3 injection steps are indicated respectively by the pink and green colored bands.

stabilized from t ~ 700 min and the frequency shifts, Δf, were analyzed from then on.

In contrast to the Biot-SH sensors, our tailor-made BBA-SH monolayer revealed to be more stable towards desorption of SAv at low biotin fraction; the frequency decreased at each extension steps and no increase was observed for both BBA_3 and buffer rinsing steps (see Appendix 2 for detailed Δf and ΔD values). The third SAv immobilization step (injected at t ~ 780 min) saturated at a frequency shift of -5.8 Hz with a dissipation shift of $0.6 \cdot 10^{-6}$ (3rd overtone). Although the frequency and dissipation responses displayed overtone dependencies and $\Delta D/\Delta f > 1 \cdot 10^{-8}$ Hz^{-1},[20] the frequency shifts were translated to mass uptake using Sauerbrey relation. The calculated masses might not truly reflect the reality but the *Eff* values obtained for the

successive elongation steps followed a similar trend to the results obtained by SPR (see below). For that reason, we did not analyze the QCM-D data using a viscoelastic model.

In parallel to the QCM-D experiments, six elongation steps of SAv using BBA_2 (Fig.11) and BBA_3 (Fig. 12) were followed by SPR. The sensorgrams climbed at each SAv injection step without any decrease recorded at the washing steps (see Appendix 2 for detailed ΔR values). The

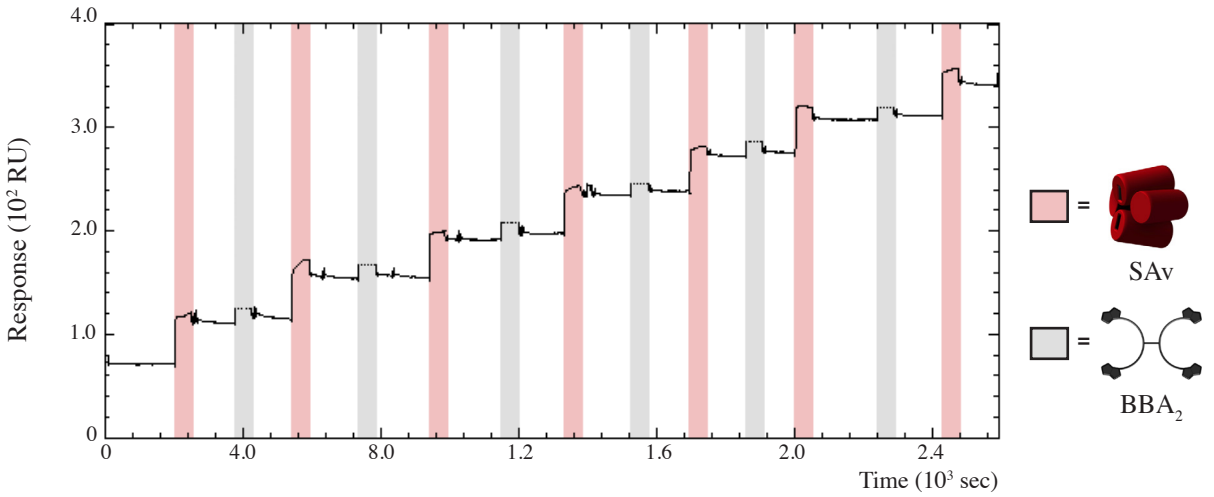

Figure 11 SPR sensogram showing the six-steps elongation of SAv using BBA_2 on a 0.1‰ BBA-SH sensor. A flow rate of 5 µl/min was used during the whole procedure; 40 µl of SAv ($1{\cdot}10^{-7}$ M in HBS-P) and BBA_2 ($4{\cdot}10^{-7}$ M in HBS-P (0.2% MeOH)) were flowed over the sensor at each step. The surface was washed three times with running buffer (HBS-P) at the end of each injection. The SAv and BBA_2 injection steps are indicated respectively by the pink and grey colored bands. A drift of -0.003 RU/sec was corrected on the presented sensorgram.

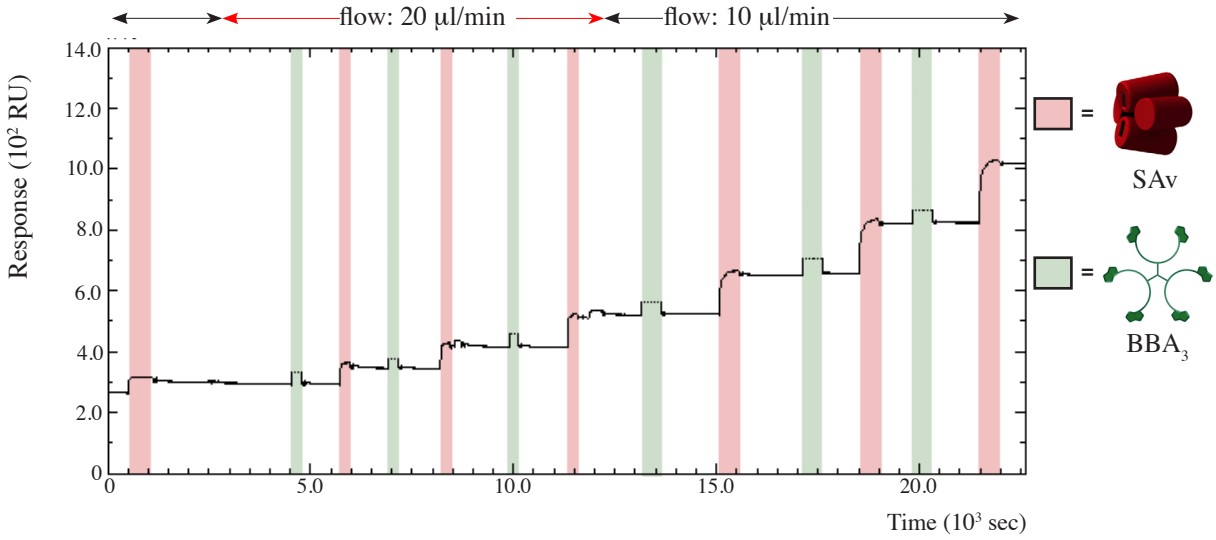

Figure 12 SPR sensogram showing the 6-steps elongation of SAv using BBA_3 on a 0.1‰ BBA-SH sensor. To correct the baseline drift, the initial flow rate of 10 µl/min was increase to 20 µl/min from t ~ 2500 sec to t ~ 12200 sec. When the baseline stabilized, the flow rate was brought back to 10 µl/min. 80 µl of SAv ($1{\cdot}10^{-7}$ M in HBS-P) and BBA_3 ($3{\cdot}10^{-7}$ M in HBS-P (0.2% DMF)) were flowed over the sensor at each step. The surface was washed three times with running buffer (HBS-P) at the end of each injection. The SAv and BBA_3 injection steps are indicated respectively by the pink and green colored bands. A drift of -0.004 RU/sec was corrected on the presented sensorgram.

SPR experiments revealed that only 4.9 ± 0.8 ng/cm^2 of SAv were immobilized at the initial anchoring step. This value being essentially the detection limit of the QCM device used throughout this work explained the baseline drift problems encountered during the QCM experiments. An immobilized mass of ~5 ng/cm^2 corresponded to an available area of ~2 μm^2 per SAv unit, which was well enough space to accomodate both linear and dendritic growth processes.

The Δm_{QCM} and Δm_{SPR} (Fig. 13), as the corresponding extension efficiency values (Table 4) obtained at each elongation step of SAv onto 0.1‰ BBA-SH SAMs, are presented below.

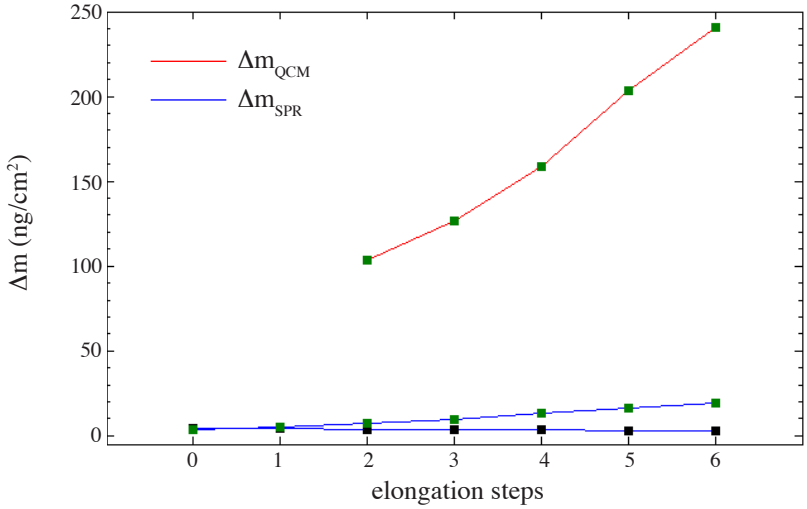

Figure 13 Variation of the adsorbed mass of SAv at each elongation step using BBA_2 (black squares) and BBA_3 (green squares) onto 0.1‰ BBA-SH SAMs. For consistency of terminology, the initial immobilization step of SAv onto the biotinylated SAMs was denoted as the elongation step "0".

	Elongation step					
	1	2	3	4	5	6
Eff using: BBA_3 (QCM)	-	-	1.22	1.25	1.28	1.18
" (SPR)	1.60	1.38	1.29	1.35	1.25	1.19
BBA_2 (SPR)	0.99	0.93	0.99	0.93	0.93	0.94

Table 4 Extension efficiency (*Eff*) values obtained for each elongation step of SAv using BBA_2 and BBA_3 during the SbS assembly experiments on 0.1‰ BBA-SH SAMs followed by QCM-D and/or SPR.

According to the SPR results, the SbS assembly of SAv using BBA_2 was close to a quantitative linear elongation construct; *Eff* values from 0.93 to 0.99 were recorded for the successive elongation steps of SAv. However, the results obtained for the SbS assembly of SAv using BBA_3 were difficult to rationalize. Since the *Eff* values did not approach the value of 2.0, as expected for a dendritic growth process, different growth cases scenario were envisioned. In the first case

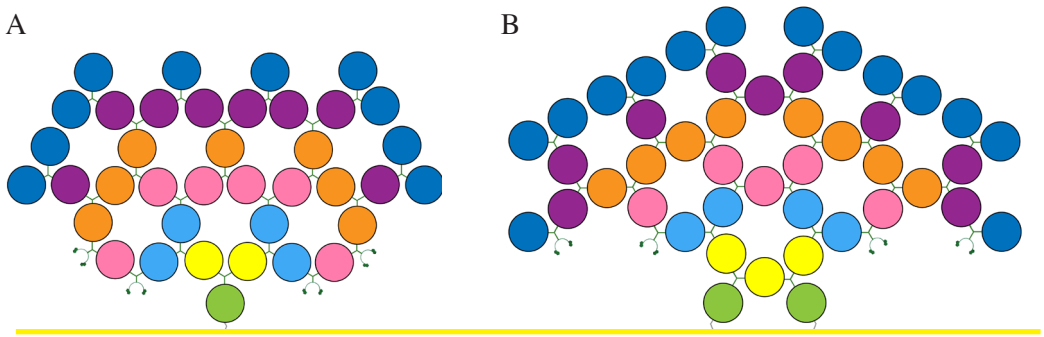

		Elongation step					
		1	2	3	4	5	6
Eff :	scenario a	2	2	3/2	7/6	8/7	5/4
	scenario b	3/2	4/3	5/4	8/5	9/8	14/9

Figure 14 Schematic representation of growth cases scenario for the SbS assembly of SAv using BBA_3 onto 0.1‰ BBA-SH SAMs. Honeycomb-based network formation onto a BBA-SH/OEG-SH SAM where a) the thiolated BBA molecules are well distanced from one another; b) two thiolated BBA molecules are in the vicinity of one another. SAv was represented as spheres for convenience purposes. Each elongation step of SAv was colored differently and the *Eff* values expected at each step appear in the above table.

scenario (Fig. 18a), a honeycomb-based network growing from an isolated anchorage point was considered. The second case scenario reflected the fact that bis-biotinylated disulfide molecules were used to prepare the immobilization platform: a honeycomb-based network growing from two neighboring anchorage points. The *Eff* values for each elongation step were calculated for both growth cases scenario. Even though one can argue about where to stop the growth process, *i.e.* when steric hindrance comes into play, the *Eff* values for the second case scenario are closer to our experimental results.

In order to gain additional information, the SbS assembly of SAv where BBA_2 and BBA_3 were successively alternated was studied. A six-steps elongation of SAv for the alternating construct onto 0.1‰ BBA-SH SAMs was monitored by QCM (Fig. 15) and SPR (Fig. 16). Due to strong drift issues, the first three injections, namely the initial immobilization step of SAv followed by the injections of BBA_2 and SAv, could not be analysed and therefore were omitted. Thus, the frequency and dissipation traces presented below (Fig. 15) start at the fourth injection (BBA_3 immobilization step). The ΔR , Δf and ΔD recorded for each injection was annexed in Appendix 2.

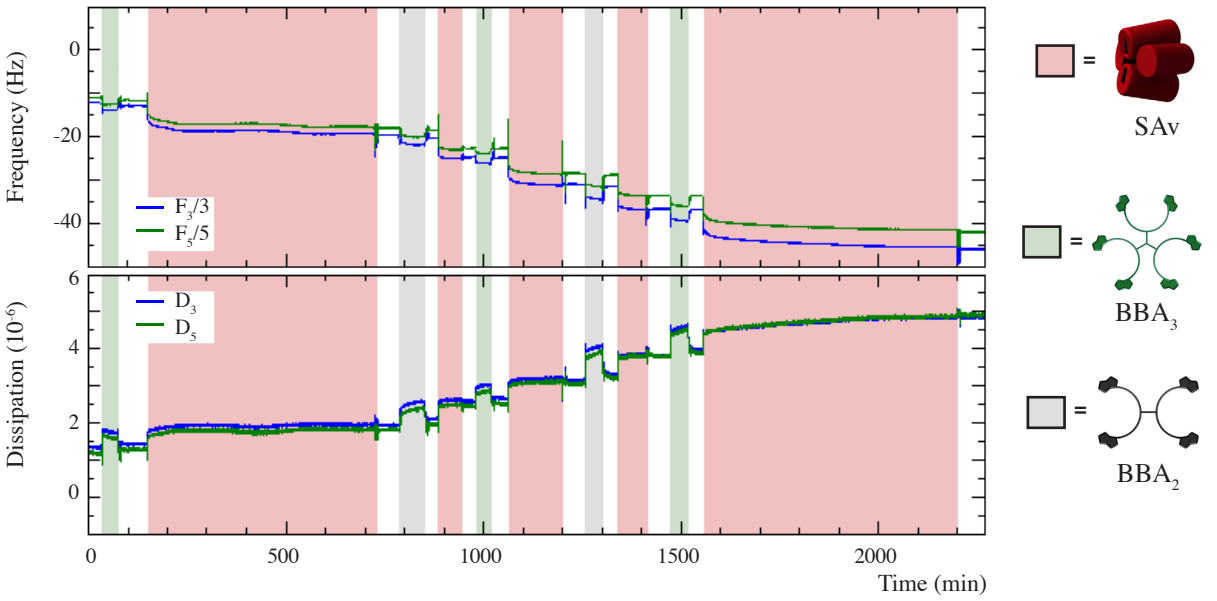

Figure 15 QCM-D measurements for the SbS assembly of SAv using BBA_2 and BBA_3 on a 0.1‰ BBA-SH sensor. Δf and ΔD vs time traces (3rd (blue) and 5th (green) overtone) recorded upon successive exposure of the biotinylated surface to SAv ($1{\cdot}10^{-7}$ M in HBS-P) with alternating BBA_2 ($4{\cdot}10^{-7}$ M in HBS-P (0.2% DMF) and BBA_3 ($4{\cdot}10^{-7}$ M in HBS-P (1% MeOH)) solutions. Due to strong drift issues, the first 3 injection steps (1.SAv ; 2.BBA_2 ; 3.SAv) are not shown. The surface was rinsed three times with running buffer (HBS-P) at the end of each injection. The SAv, BBA_2 and BBA_3 injection steps are indicated respectively by the pink, grey and green colored bands.

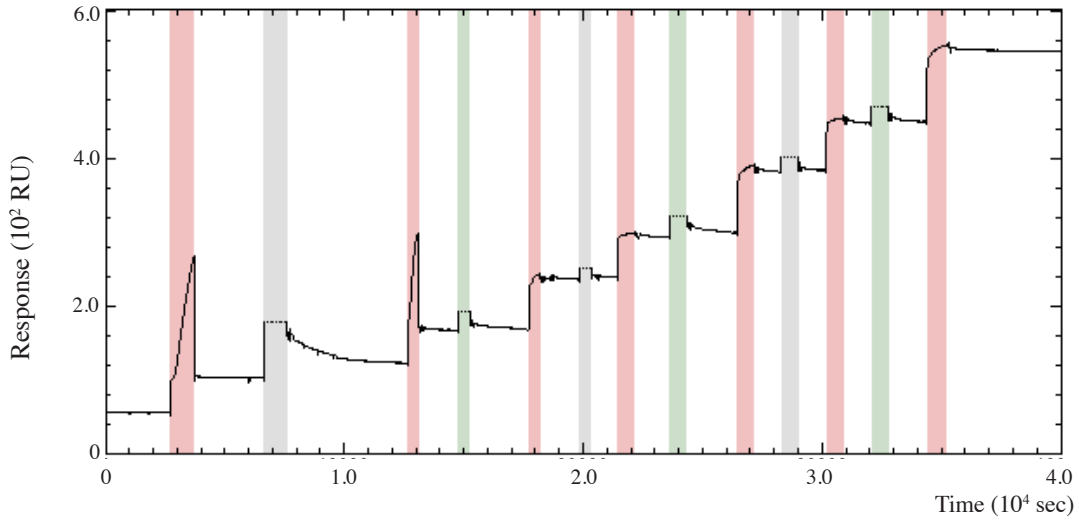

Figure 16 SPR sensogram showing the six-steps extension assembly of SAv by alternating BBA_2 and BBA_3 on a 0.1‰ BBA-SH sensor. A flow rate of 5 µl/min was used during the whole procedure except from t~7650 sec to t~9650 sec where a flow rate of 50 µl/min was used for washing purposes; 80 µl of SAv ($1{\cdot}10^{-6}$ M in HBS-P) and BBA_2 ($4{\cdot}10^{-7}$ M in HBS-P (0.2% DMF) was used for the first two injections. However, four washing steps using a flow rate of 50 µl/min was needed to recovered a stable baseline. For that reason, a volume of 40 µl for SAv, BBA_2 and BBA_3 ($3{\cdot}10^{-7}$ M in HBS-P (0.2% DMF)) was used for injections 3, 4, 5 and 6. A volume of 60 µl was used for injections 7 to 13. Except for injection 2 which was followed by four washing steps, the surface was washed three times with running buffer (HBS-P) at the end of each injection. The SAv, BBA_2 and BBA_3 injection steps are indicated respectively by the pink, grey and green colored bands. A drift of -0.001 RU/sec was corrected on the presented sensorgram.

The Δm_{QCM} and Δm_{SPR} translated from the ΔR and Δf recorded at each extension step of SAv are presented below (Fig. 17). An interesting trend emerges from the corresponding *Eff* values (table 5), especially for the SPR measurements since all elongation steps were monitored.

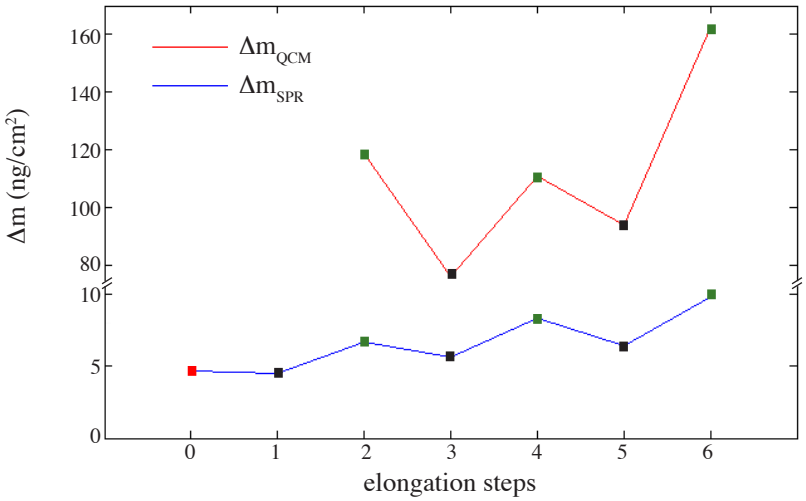

Figure 17 Variation of the adsorbed mass of SAv at each elongation step by alternate use of BBA_2 (black squares) and BBA_3 (green squares) on 0.1‰ BBA-SH SAMs. For consistency of terminology, the initial immobilization step of SAv onto the biotinylated SAMs was denoted as the elongation step "0".

	Elongation step					
	1	2	3	4	5	6
Eff (QCM)	-	-	0.64	1.48	0.84	1.74
(SPR)	0.95	1.49	0.83	1.50	0.76	1.52

Table 5 Extension efficiency (*Eff*) of each elongation step of SAv by alternate use of BBA_2 (*Eff* values in black) and BBA_3 (*Eff* values in green) for the SbS assembly experiment on 0.1‰ BBA-SH SAMs followed by QCM-D and/or SPR.

An *Eff* value close to 1.0 was obtained for the first extension step using BBA_2. For the subsequent extension steps, *Eff* values around 1.5 and 0.8 were obtained when BBA_3 and BBA_2 were used, respectively. To rationalize these results, a growth case scenario for the SbS assembly of SAv with alternating ligand construct was envisioned (Fig. 18). Using a "two anchorage points localized in the vicinity of one another" model, theoretical *Eff* values similar to the ones recorded experimentally by SPR are obtained; 3/2 and 2/3 for SAv elongation steps involving BBA_3 and BBA_2, respectively.

These results suggested that the SbS assembly process onto 0.1‰ SAMs is well described by a situation approaching the model where two BBA anchorage points are localized in the vicinity of one another.

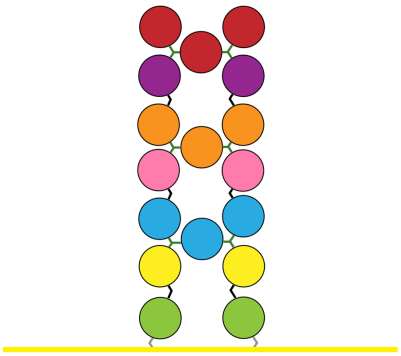

Elongation step	*Eff*
1	1
2	3/2
3	2/3
4	3/2
5	2/3
6	3/2

Figure 18 Schematic representation of a growth scenario for the SbS assembly of SAv with alternating ligand construct. SAv was represented as spheres for convenience purposes. Each elongation step of SAv was colored differently and the *Eff* values expected for each step appear in the above table.

To circumvent the problems related to the QCM detection limit, mixed SAM containing 0.1% of BBA-SH were prepared. Three extension steps of SAv using BBA_2 were monitored by QCM (Fig 19). With this SAM composition, a stable baseline could be recorded. The first immobilization step of SAv on 0.1% BBA-SH monolayer saturated at a frequency shift of -13 ± 1 Hz with a dissipation shift of 0.3 ± 0.1 $\cdot 10^{-6}$ (3rd overtone) (see Appendix 2 for Δf and ΔD values). Eff values for each elongation step were determined (Table 6). Although the first elongation step of SAv corresponded to an

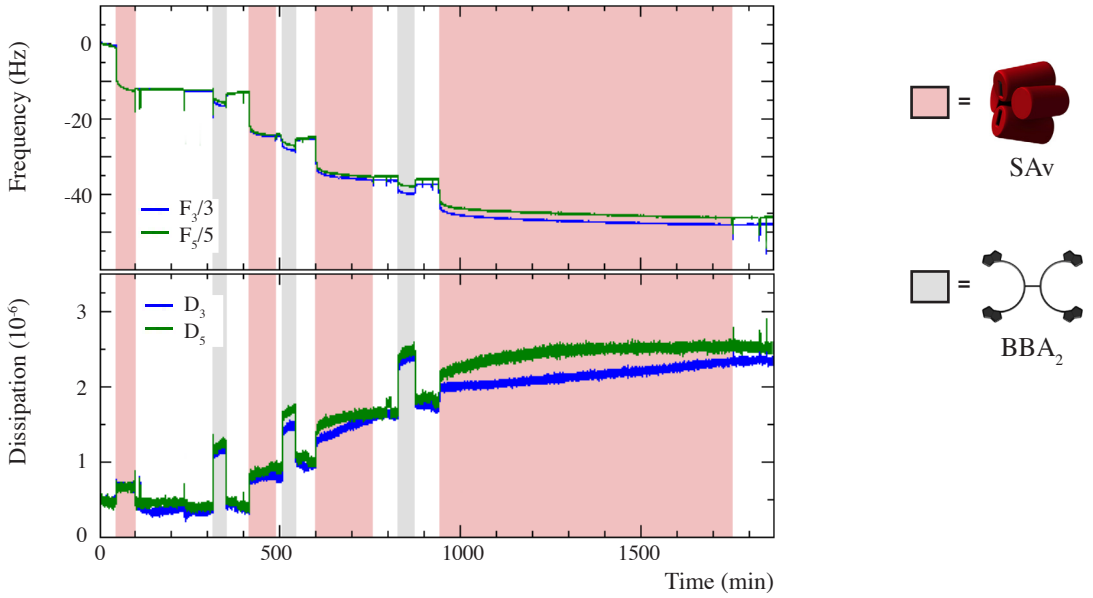

Figure 19 QCM-D measurements for the SbS assembly of SAv using BBA_2 on a 0.1% BBA-SH sensor. Δf and ΔD vs time (3rd and 5th harmonic) recorded upon successive exposure of the biotinylated surface to SAv ($1 \cdot 10^{-6}$ M in HBS-P) and BBA_3 ($2 \cdot 10^{-6}$ M in HBS-P (1% MeOH)) solutions. The surface was rinsed three times with running buffer (HBS-P) at the end of each injection. The SAv and BBA_2 injection steps are indicated respectively by the pink and grey colored bands. Signals recorded at the 3rd (blue) and 5th (green) overtone are presented

extension efficiency of 0.92, the following ones - *Eff* = 0.94 and 0.98, respectively - tended towards the value expected for a linear growth process.

The SbS assembly of SAv using BBA_3 on a 0.1% BBA-SH was also attempted . However, following the initial immobilization of SAv, the available biotin binding sites were partially blocked. To do so, a solution of BBA-S-S-BBA and BBA in a ratio of 1:4 was flowed over the sensor: BBA acted as a blocking agent while BBA-S-S-BBA enabled further extension of SAv. Moreover, by introducing a disulfide bridge in the nanostructure, the latter could, at a later stage, be cleaved off from the sensor. Counting in the blocking step, four elongation steps of SAv were followed by QCM (Fig. 20). The extension efficiencies obtained for each elongation

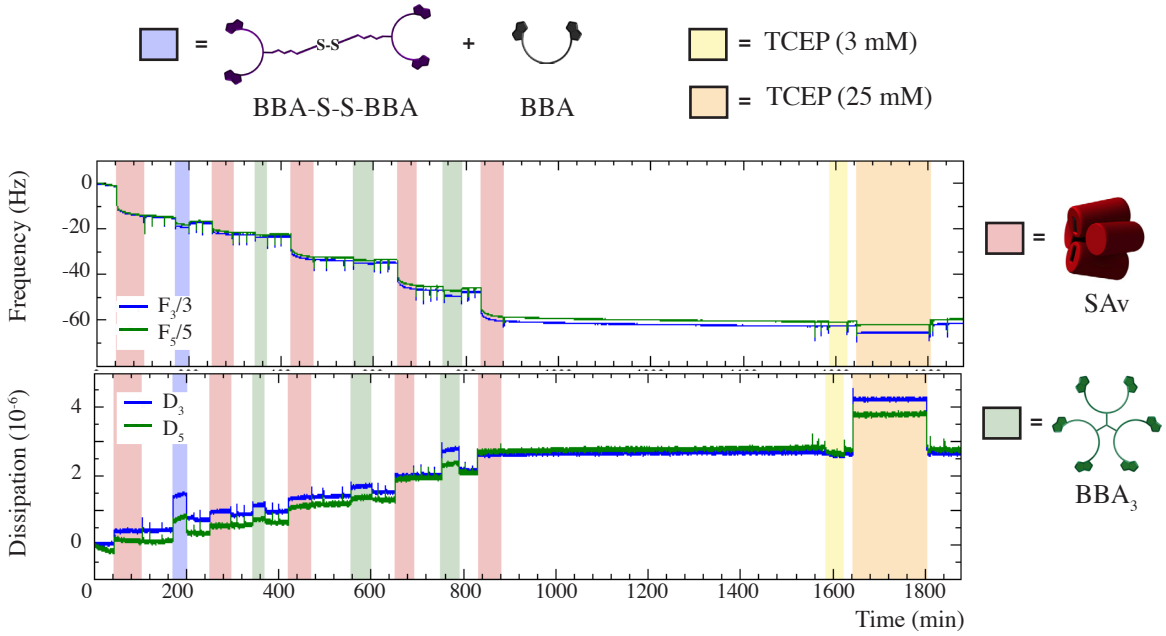

Figure 20 QCM-D measurements for the SbS assembly of SAv using BBA_3 on a 0.1% BBA-SH sensor where a mixture . Δf and ΔD vs time (3rd and 5th harmonic) recorded upon successive exposure of the biotinylated surface to SAv ($1 \cdot 10^{-6}$ M in HBS-P) and BBA_3 ($2 \cdot 10^{-6}$ M in HBS-P (1% MeOH)) solutions. The surface was rinsed three times with running buffer (HBS-P) at the end of each injection. The SAv and BBA_2 injection steps are indicated respectively by the pink and grey colored bands. Signals recorded at the 3rd (blue) and 5th (green) overtone are presented

step of SAv are listed in table 6. A *Eff* value of 0.36 was recorded for the first elongation step, suggesting that ~2/3 of the bioting binding sites got effectively blocked. The following elongation step of SAv using BBA_3 resulted in an *Eff* of 2.0, the expected value when using an effective three-way junction. The subsequent elongation steps gave *Eff* values tending towards 1.0, suggesting steric hindrance and hence BBA_3 behaving as a linear junction. However, when a

		Elongation step			
		1	2	3	4
Eff	BBA_2 (QCM)	0.92	0.94	0.98	-
	BBA_3 (QCM)	0.36 [a]	2.02	1.14	1.00

Table 6 Extension efficiency (*Eff*) for each elongation step of SAv using BBA_2 and BBA_3 on 0.1% BBA-SH SAMs followed by QCM-D. a) Partial blocking of the biotin binding sites was performed for the first extension step.

solution of reducing agent - TCEP (3 mM and 25 mM in HBS) - was flowed over the sensor, no significant frequency nor dissipation shifts were recorded suggesting that cleavage of the introduced disulfide bond did not occur.

A last observation is that the results obtained onto 0.1% BBA-SH sensors were very consistent; the Δf recorded for the elongation steps where BBA_3 acted as a linear junction ($\Delta f \sim$ -12 Hz) were very similar to the values recorded using BBA_2 ($\Delta f \sim$ -11 Hz) (c.f Appendix 2).

Considering the knowledge accumulated for the SbS assembly of SAv through the QCM and SPR experiments, the 0.1‰ BBA-SH monolayer was chosen as immobilization platform for AFM image acquisition of the linear SAv nanostructures in liquid.

2.4.6 AFM Experiments in Liquid

Ultraflat template-stripped gold (TSG) surfaces were used for the AFM experiments. Using the sequential adsorption method, 0.1‰ BBA-SH monolayers were prepared and AFM topographs were acquired in imaging buffer (Fig. 21a, b). The monolayer assembled on TSG appeared as an homogeneous featureless surface and presented a roughness of 0.17 nm (RMS). From the recorded AFM images where defects appeared in the monolayer, a height of 1.1 ± 0.1 nm (n = 4) was measured. It is in accordance with the 1.13 ± 0.05 nm height value recorded for OEG-SH SAMs on gold by Vanderah et al.[21]

After exposure of the biotinylated SAMs to a SAv solution, the samples were imaged again. The micrograph obtained from a 5 μm scanned area (Fig. 21c) showed what appeared as well-distanced immobilized SAv units. From the 1 μm scanned areas, protusions corresponding

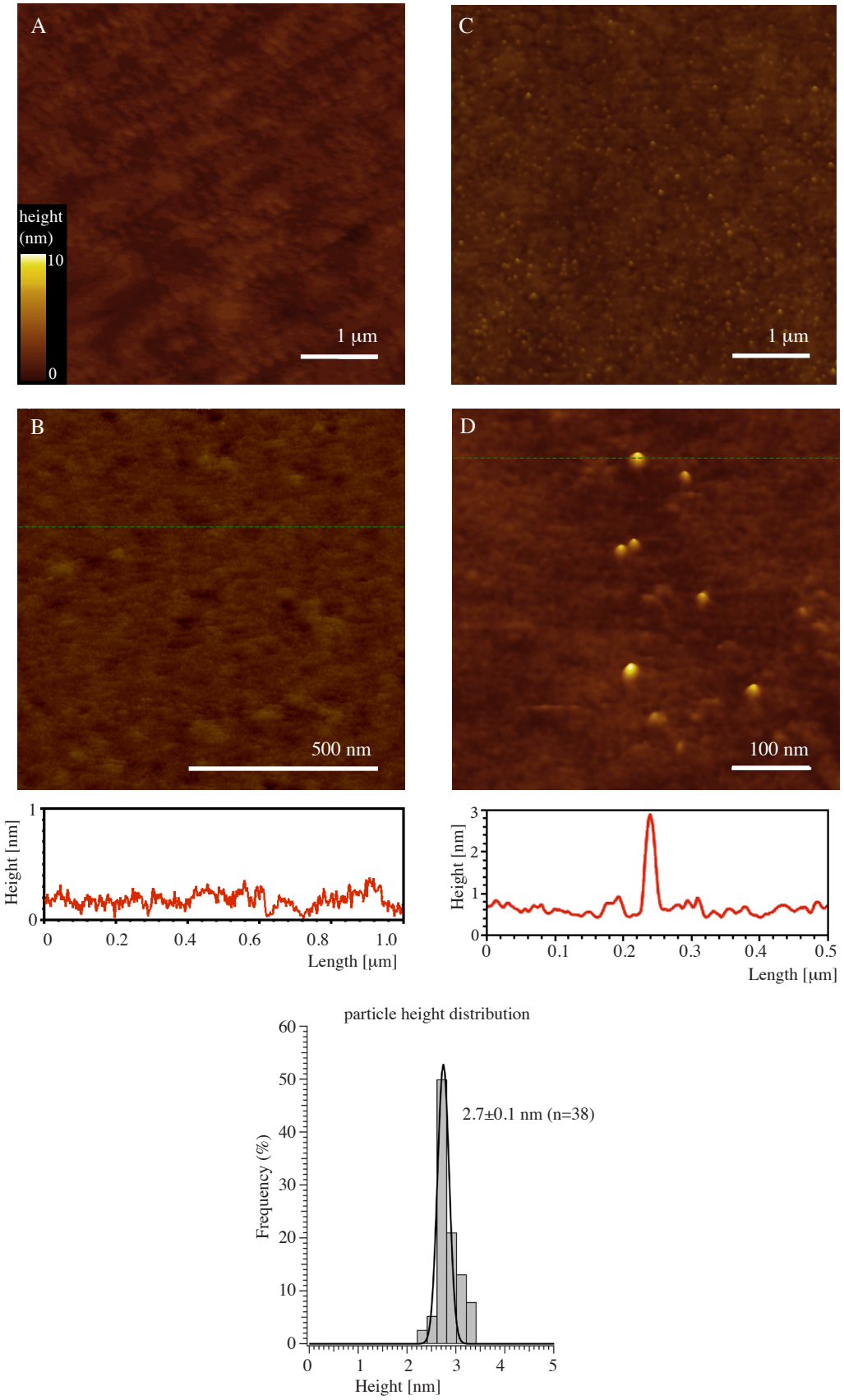

Figure 21 Typical AFM topographs of 0.1‰ BBA-SH SAMs before (a, b) and after (c, d and e) being exposed to a SAv solution ($1 \cdot 10^{-6}$ M in HBS-P). The AFM topographs were recorded in PBS buffer and exhibit a full color range that corresponds to the vertical scale of a, c) 10 nm and b, d) 5 nm. Height distribution of the immobilized SAv units calculated from 38 measurements revealed an height of 2.7 ± 0.1 nm.

to SAv presented an height of 2.7 ± 0.1 nm (n=38). A similar value (3.1 ± 0.1 nm) was recorded for 2D crystals of SAv on biotinylated SLBs.[22]

Although height measurements can be acquired with a resolution of ~ 0.1 - 0.5 nm, the diameter observed by AFM depends on the stylus shape and diameter.[23] Since the latter varies even for tip of the same kind, the observed diameter is not a reliable measurement.[24] For that reason, we could not conclude whether the protrusions observed on the micrographs corresponded to one or two SAv units. Nevertheless, the amount of SAv observed on the AFM micrographs was higher by at least a factor of ~7 than what was detected by SPR.

The SbS assembly using BBA_2 was performed onto the anchored SAv; the substrate was successively exposed to BBA_2 and SAv solutions until four elongation steps of SAv was

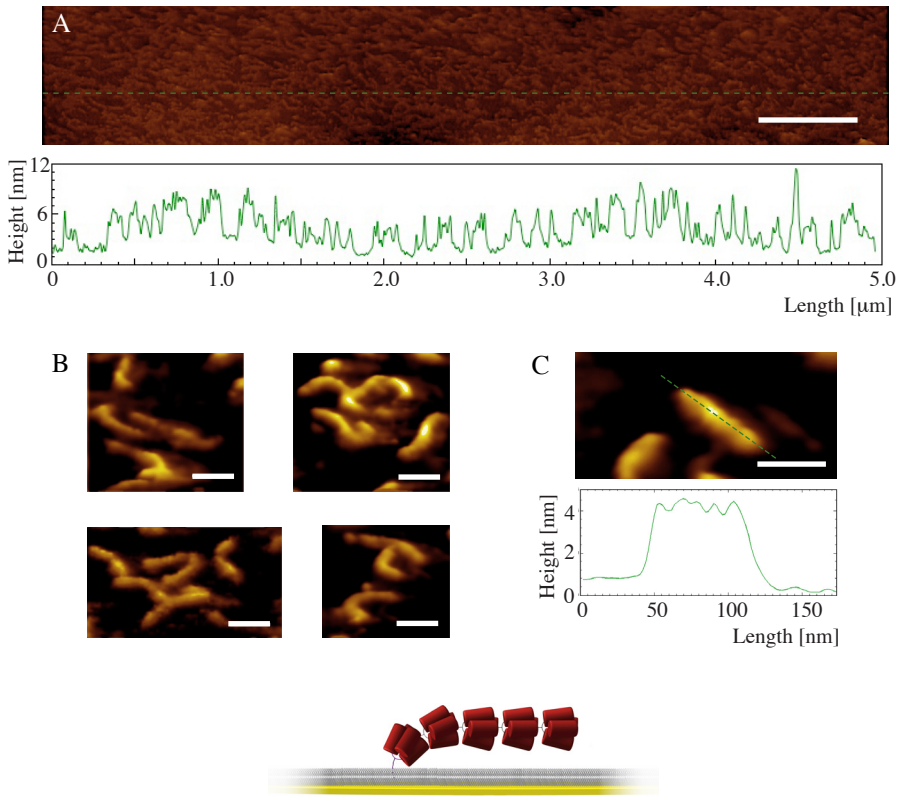

Figure 22 Typical AFM topographs of 4 elongation steps of SAv on 0.1‰ BBA-SH SAMs. The AFM topographs were recorded in PBS buffer and exhibit a full color range that corresponds to the vertical scale of a) 10 nm and b, c) 5 nm . a) Large scan area showing the homogeneous population of SAv fibrils.b) Gallery of AFM images of protein fibrils for which the constituting SAv unit were resolved. c) Height profile showing the height variation between the connecting junction and the SAv units. The length of the scale bars corresponds to a) 500nm and b, c) 50 nm.

reached. The resulting immobilized nanotructures were scrutinize by AFM (Fig. 21). The AFM topographs acquired in liquid revealed the presence of fibrilic structures over a wide range of the surface (Fig. 21 a). Even though the sample got damaged upon scanning (see Appendix 2), fibrils presenting an height of 3.6 ± 0.3 nm (n=15) were observed. Moreover, protrusions corresponding to SAv were resolved along the fibers. Although fibers anchored next to each other were observed, some isolated ones were also present (Fig. 21b).

The SbS assembly of SAv using BBA_3 could not be recorded in liquid. Still, AFM images of the dried 0.01% BBA-SH functionalized QCM sensor onto which six elongation steps of SAv were recorded (experiment presented in Fig. 10) can be found in Appendix 2.

In conclusion, QCM and SPR were appropriate tools to monitor the SbS assembly of SAv. Through those experiments, the SAM composition permitting unhindered SbS growth of SAv-based nanostructures was determined. Compared to the widely used Biot-SH/PEG-SH SAMs, our tailor-made immobilization platform enabled a much lower surface coverage of SAv to be achieved. However, according to the QCM and SPR results, the BBA-SH/OEG-SH SAMs failed in anchoring well-distanced SAv units. This is most probably due to the fact that the disulfide form of thiolated BBA was used to prepare the monolayers. Although both QCM and SPR experiments revealed a linear growth process for the stepwise assembly of SAv involving BBA_2, a growth process more complex than expected was observed when BBA_3 was involved.

AFM image acquisition in buffer of the SbS assembled nanostructures revealed to be a very challenging task. The fibrils tended to slip around the AFM tip and, when the imaging force was increased, disruption of the fibrils occured. The anchored SAv units as the immobilized linear nanoconstructs were successfully imaged but, due to the fragility of the latter, 2 μm or smaller scanned area images presented a mixed population of intact and disrupted fibrils. For that reason, we could not fully prove, through AFM imaging, that monodisperse and size-controlled SAv-based fibrils were created.

2.4.7 References

1. Prime, K. L.; Whitesides, G. M., *Science* **1991**, *252* (5009), 1164.

2. Prime, K. L.; Whitesides, G. M., *J. Am. Chem. Soc.* **1993**, *115* (23), 10714.

3. Harder, P.; Grunze, M.; Dahint, R.; Whitesides, G. M.; Laibinis, P. E., *J. Phys. Chem. B* **1998**, 102 (2), 426.

4. Li, L.; Chen, S.; Zheng, J.; Ratner, B. D.; Jiang, S., *J. Phys. Chem. B* **2005**, *109* (7), 2934.

5. Perez-Luna, V. H.; O'Brien, M. J.; Opperman, K. A.; Hampton, P. D.; Lopez, G. P.; Klumb, L. A.; Stayton, P. S., *J. Am. Chem. Soc.* **1999**, *121* (27), 6469.

6. Jung, L. S.; Nelson, K. E.; Campbell, C. T.; Stayton, P. S.; Yee, S. S.; Perez-Luna, V.; Lopez, G. P., *Sens. Actuators, B* **1999**, B54 (1-2), 137.

7. Jung, L. S.; Nelson, K. E.; Stayton, P. S.; Campbell, C. T., *Langmuir* **2000**, *16* (24), 9421.

8. Nelson, K. E.; Gamble, L.; Jung, L. S.; Boeckl, M. S.; Naeemi, E.; Golledge, S. L.; Sasaki, T.; Castner, D. G.; Campbell, C. T.; Stayton, P. S., *Langmuir* **2001**, *17* (9), 2807.

9. Vareiro, M. M. L. M.; Liu, J.; Knoll, W.; Zak, K.; Williams, D.; Jenkins, A. T. A., *Anal. Chem.* **2005**, *77* (8), 2426.

10. Nilebaeck, E.; Feuz, L.; Uddenberg, H.; Valiokas, R.; Svedhem, S., *Biosens. Bioelectron.* **2011**, *28* (1), 407.

11. Seifert, M.; Rinke, M. T.; Galla, H.-J., *Langmuir* **2010**, *26* (9), 6386.

12. Larsson, C.; Rodahl, M.; Hoeoek, F., *Anal. Chem.* **2003**, *75* (19), 5080.

13. Azzaroni, O.; Mir, M.; Knoll, W., *J. Phys. Chem. B* **2007**, *111* (48), 13499.

14. Edvardsson, M.; Svedhem, S.; Wang, G.; Richter, R.; Rodahl, M.; Kasemo, B., *Anal. Chem.* (Washington, DC, U. S.) **2009**, *81* (1), 349.

15. Sauerbrey, G., *Z. Phys.* **1959**, *155*, 206.

16. Hoeoek, F.; Ray, A.; Norden, B.; Kasemo, B., *Langmuir* **2001**, *17* (26), 8305.

17. Liedberg, B.; Lundstroem, I.; Stenberg, E., *Sens. Actuators, B* **1993**, B11 (1-3), 63.

18. Reimhult, E.; Larsson, C.; Kasemo, B.; Hoeoek, F., *Anal. Chem.* **2004**, *76* (24), 7211.

19. Bingen, P.; Wang, G.; Steinmetz, N. F.; Rodahl, M.; Richter, R. P., *Anal. Chem.* **2008**, *80* (23), 8880.

20. Cho, N.-J.; Frank, C. W.; Kasemo, B.; Hook, F., *Nat. Protoc.* **2010**, 5 (6), 1096.

21. Vanderah, D. J.; Arsenault, J.; La, H.; Gates, R. S.; Silin, V.; Meuse, C. W.; Valincius, G., *Langmuir* **2003**, *19* (9), 3752.

22. Reviakine, I.; Brisson, A., *Langmuir* **2001**, *17* (26), 8293.

23. Allen, M. J.; Hud, N. V.; Balooch, M.; Tench, R. J.; Siekhaus, W. J.; Balhorn, R., *Ultramicroscopy* **1992**, 42-44, 1095.

24. Wegmann, S.; Jung, Y.-J.; Chinnathambi, S.; Mandelkow, E.-M.; Mandelkow, E.; Muller, D. J., *J. Biol. Chem.* **2010**, *285* (35), 27302.

Chapter III

Conclusions and Perspectives

3. Conclusions and Perspectives

The organization of mature WT-SAv into well-defined nanostructures extending to the macroscales is a very challenging task.

From a self-assembly point of view, the high affinity of biotin for SAv ($K_d \sim 10^{-14}$ M) prevents self-healing of the nanostructures once they are created.[1] To devise a nanolego set composed of SAv (linear junction), a careful design implies biotinylated units (connectors) presenting a precise positioning of the biotin moities. In addition, the symmetry of the connector defines the multiplicity of the designed contact,[2] and therefore the first level of organization of the nanolegos. All the data gathered during this work suggest that 1) BBA binds to two cis-related sites in SAv, hence fulfills the prerequisite for a carefully designed connector. 2) BBA_2 and BBA_3 are both efficient linear and trifurcated junction, respectively, in directing the organization of SAv. Through the self-organization experiments in bulk solution, we have demonstrated that SAv combined with a linear connector, BBA_2 or the analog $[Fe(BBA\text{-}terpy)_2]^{2+}$, spontaneously assembled into a one-dimensional SAv-based polymer. In the presence of calcium ions, these SAv fibrils form bundles that serve as a template for the biomineralization of calcite.

Although the stoechiometry of binding of BBA_3 to SAv (HABA-displacement assays), and the SDS-PAGE analysis of the self-organized species in bulk solution proved BBA_3 to be an effective three-way junction, the higher-order nanostructures generated by SAv in the presence of BBA_3 remains unresolved.

The fact that each monomeric mature WT-SAv presents a hydrophobic tail at the C-terminus, brings the play of self-assembly on a higher level. If further self-assembly experiments using BBA_3 were to be conducted, the widely used core WT-SAv could be a better candidate to identify the nanostructures co-existing in solution. Moreover, the use of imaging technique enabling the observation of the nanostructures in the hydrated state, AFM or cryo-TEM, should be emphasized.

The SbS assembly of SAv units monitored by SPR and QCM proved that the creation of well-defined and monodisperse SAv-based nanostructures is achievable. The collected data suggest that on monolayers prepared from solutions of Biot-SH and OEG-SH with $\chi_{Biot\text{-}SH} = 0.01$, the immobilized layer of SAv is too dense to enable a regular elongation process of SAv using BBA_2; 2) $\chi_{Biot\text{-}SH} = 0.001$, displacement of the immobilized SAv by BBA_3 occurs. On monolayers prepared by sequential exposition to solutions of BBA-SS-BBA and OEG-SH with 3) $\chi_{BBA\text{-}SH} = 0.001$, a near to linear SbS elongation of SAv using BBA_2 is achieve; 4) with $\chi_{Biot\text{-}SH} = 0.0001$, less than 5 ng/cm^2 of SAv, a near to linear elongation process of SAv using BBA_2 is achieved, and the thiolated BBA probes are paired on the monolayer. Moreover, this monolayer composition allows AFM imaging in liquid of anchored SAv units and SAv-based fibrils.

Further experiments should be conducted on the BBA-SH/OEG-SH SAMs. First, the SAMs should be systematically characterized. SAMs prepared from concentrations spanning from 0.001% to 1% of BBA-S-S-BBA should be analyzed by contact angle measurements, ellipsometry and XPS.

For applications that require highly sensitive biosensing or arrayed interface, an optimal probe is one allowing control over the space around each probe individually to both reduce probe-probe interactions and maximize the density of probe molecule.[3] With the aim of achieving well-distanced BBA probe units on the SAM, BBA-S-S-BBA could be reduced prior to the SAM preparation. In most biosensing applications taking advantage of the biotin-SAv technology via biotinylated SAMs on gold, a full monolayer of SAv is used to immobilize the biomolecules of interest. However, the results obtained on 1% Biot-SH sensors during this work showed that steric hindrance was an issue until at least five linear elongation steps. As demonstrated by Georgiadis and co-workers, probe-target binding at highly packed probe arrays can significantly differ from the same binding occurring in a biological setting.[4] Even though our results suggest that the probes, the thiolated BBA, are on average paired on the monolayer, we showed that, combined with the use of SPR and QCM, the SbS assembly of the SAv using

BBA_2 and BBA_3 onto BBA-SH/OEG-SH SAMs is a reliable way to "feel" the available volume surrounding the probes. In that spirit, the nanolegos could find applications as a calibrating tool, *i.e.* each BBA-SH/OEG-SH SAM exposing a known amount of BBA moieties or hence SAv per surface unit, would be tailor-made to immobilize biomolecules of know volume. The biomoloecule of interest could then be screened against protein/protein or drug/protein interactions for instance, without steric issues blurring the acquired data.

Another possible avenue to investigate would consist in conferring some functionality to the system. Once a low concentration of well-distanced SAv would be immobilized, BBA-S-S-BBA could be introduced in the SbS assembly. A reducing agent would then act as a trigger to liberate the size controlled and monodisperse nanostructures.

References

1. Ringler, P.; Schulz, G. E., *Science (Washington, DC, U. S.)* **2003**, *302* (5642), 106.

2. Grueninger, D.; Treiber, N.; Ziegler, M. O. P.; Koetter, J. W. A.; Schulze, M.-S.; Schulz, G. E., *Science* **2008**, *319* (5860), 206.

3. Frasconi, M.; Mazzei, F.; Ferri, T., *Anal. Bioanal. Chem.* **2010**, *398* (4), 1545.

4. Wolf, L. K.; Gao, Y.; Georgiadis, R. M., *J. Am. Chem. Soc.* **2007**, *129* (34), 10503.

Chapter IV

Materials and Methods

4 Materials and Methods

4.1 Materials and Reagents

Solvents and reagents were of analytical grade and were purchased from Aldrich, Fluka or Acros and used without further purification. The thiols used for the SAMs formation experiments were purchased from Asemblon Inc. (USA) or Aldrich. Water was purified to milliQ degree of purity. Streptavidin wild-type was prepared by the team of biologists in our laboratory according to published results.

4.2 Instruments and Methods

Nuclear Magnetic Resonance (NMR)

^{1}H, ^{13}C and ^{31}F spectra were acquired on a Bruker DPX-NMR, Bruker DRX-500 or a Bruker DRX-600 spectrometer using deuterated chloroform (99.8% D), methanol (99.8% D) or dimethyl sulfoxide (99.5%) from Cambridge Isotope Laboratories. All spectra were recorded at 298 K.

Liquid chromatography (RP-HPLC)

HPLC separation of biotin derivatives were obtained on a Waters Analytic RP-HPLC chromatograms were acquired and analyzed on an Agilent® 1100 Series HPLC system equipped with a UV-visible diode-array detector. Biotin derivatives **9**, BBA_2 (**2**) and BBA_3-1 (**3**) were analyzed on a reversed-phase C18 columns (4 mm x 250 mm and 3 mm x 150 mm, 10 μm; μ-Bondapak) eluting with a gradient elution at a flow rate of 0.8 mL/min or 0.5 mL/min. Preparative RP-HPLC was performed on a Waters PreP LC 4000 system with a variable UV detector (254 nm) on a reversed-phase C18 column (40 mm x 150 mm, 10 μm; μ-Bondapak) with a gradient elution at a flow rate of 80 mL/min. The solvents (ACN, MeOH, H_2O) and additives (TFA) utilized were of HPLC-grade.

Electron Spray Ionization Mass Spectrometry (ESI-MS)

Mass spectra were recorded using a LCQ-IT (Finningan) and an Esquire 3000 plus (Bruker). For LC-MS measurements, the conditions were set to: nebulizer pressure 40 psi; dry gas flow 9 $L \cdot min^{-1}$ and drying gas temperature 365°C. ChemStation software was used for data acquisition and treatment.

Self-Assembly from Bulk Solution Experiments

A Sav sample ($8 \cdot 10^{-6}$ M to $1 \cdot 10^{-8}$ M, final concentration) was dissolved in a PBS buffer (0.1 M, pH = 7.4). Various molar equivalents of BBA-based ligand were added to the aqueous solution and allowed to stirr at rt for 5 min to 2h.

SDS-PAGE Electrophoresis

Each running gel was prepared by mixing a 30% acrylamide/bisacrylamide solution with a 1.5M Tris (pH 8.8) solution and the 20% SDS solution in milliQ water. After the addition of a 15% ammonium persulfate (APS) solution and TEMED, the solution was briefly mixed before being poured (~7mL) between two glass plates secured in a casting frame. The gel mixture was overlayed with EtOH. Once the gel was set (~50 min), the top of the gel was rinsed with distilled water and a 5% stacking gel was added at the top.

Solutions for preparing the running gels (for two gels Vtot = 15 mL)

	Volume [mL] added for gel composition of	
Solution components	6% Acrylamide	8% Acrylamide
H_2O	7.9	6.9
30% Acrylamide solution	3.0	4.0
1.5 M Tris (pH 8.8)	3.8	3.8
20% SDS	0.075	0.075
15% APS	0.1	0.1
TEMED	0.012	0.009

The stacking gel (5% acrylamide, for two gels V_{tot} = 6 mL) was prepared by mixing a 0.5M Tris (pH 6.8) solution (1.5 mL) with the 30% acrylamide/bisacrylamide solution (1.0 mL) and the

20% SDS (30 µl) in milliQ H_2O (3.4 mL). The 15% APS solution (40 µl) and the TEMED (6 µl) were added last. The solution was briefly mixed before being poured (~3mL) over the running gel. Sample loading wells were made into the stacking gel by inserting a multi well comb. After complete polymerization of the gel (~ 45 min), the comb was removed and the gels were placed into a tank filled with the running buffer (25 mM Tris pH 8.3; 0.192 M Glycine; 0.1% w/v SDS).

Sample Loading and Gel Analysis

20 µL of each sample (containing 19.7 µg, $3.0 \cdot 10^{-10}$ mol of Sav) were mixed with 10 µL of loading buffer (240 mM Tris-HCl pH 6.8; 6% SDS; 30% glycerol; 0.06% Bromophenol-Blue) and 1 µL of 0.6 mM B4F solution in an eppendorf tube. The solution was gently mixed with the pipette before 10 µL (~10-15 µg of Sav) were loaded on the gel. Prestained Protein Marker, Broad Range (New England Biolabs Inc.) and a positive control (SAv saturated with B4F) were also loaded. The gel was then allowed to run at 120 V using the powerpac HC TM (Biorad) until bromophenol blue present in the loading buffer reached the end of the gel. To reveal the bands containing B4F ⊂ Sav, the gel was imaged with UV light with Molecular Image Gel Doc™ XR (Bio-Rad, Switzerland). The gel was then stained with a coomassie blue solution (0.025 % w/v coomassie blue; 50 % v/v MeOH; 10 % v/v acetic acid) overnight and destained (5 % v/v MeOH; 7 % v/v acetic acid) over a period of 48h. The gels were finally imaged with Molecular Image Gel Doc™ XR (Bio-Rad, Switzerland). The relative densitometry of each band was determined after subtracting the background noise with Quantity One Analysis Software (BioRad, Switzerland).

Scanning Electron Microscopy (SEM) Experiments

A drop (50 µL) of the solution prepared as described above was deposited onto a carbon adhesive tab and allowed to adhere for 1 min. The excess solution was then blotted off and samples were dried in a dessicator overnight before being gold-coated. The SEM images were aquired on a Philips ESEM-FEG XL30 at an acceleration voltage of 5 or 10 kV.

Transmisson Electron Microscopy (TEM) Experiments

A drop (5 μL) of the solution prepared as described above was placed on 300 mesh carbon-coated copper grids and allowed to adhere for 1 to 5 min. The excess solution was then blotted off and the grids were washed twice with H_2O. The samples were finally stained with uranyl acetate (2%) during 1 min (for positive staining the grids were subsequently washed 3 times with H_2O; for negative staining the grids were allowed to dry after blotting off the excess of staining solution). The TEM images were aquired on a Philips CM-200 operated at 80 keV.

Atomic Force Microscopy (AFM) Experiments

Self-assembly from bulk solution; 10 μL of the solution as described above was deposited onto freshly cleaved HOPG surfaces, allowed to adsorb during 1 min. followed by rinsing with water. The samples were dried overnight at room temperature before imaging in oscillation mode using a NTegra Prima system (NT-MDT, Moscow, Russia) equipped with a silicon rectangular cantilever (NSG10, NT-MDT) with a diameter ~10 nm and exhibiting spring constant of 3-15 N/m at resonance frequency in air of ~260 kHz. An amplitude ~5 nA was used to record images at a scan rate of 1 Hz.

Step-by-Step assembly of SAv: the samples as described below were immersed in imaging buffer (10 mM PBS (pH:7.4), 30 mM KCl). AFM imaging was performed in oscillation mode using a Nanoscope III (Di-Veeco, Santa Barbara, CA) and Si3N4 cantilevers (NPS series, Di-Veeco) exhibiting spring constants of ~0.32 N/m at resonance frequencies in buffer of 8.5 to 10 kHz. To achieve minimal imaging forces between AFM stylus and sample, the drive amplitude was set between 0.5 and 1.0 V, and images were acquired at a scan rate of 1-2 Hz.

Surface Functionalisation

For the XPS experiments, gold surfaces (Arrandee, Germany) were flame annealed before incubation in thiol solutions. To prepare 1% BBA-SH SAMs by coadsorption method we proceeded as follow: the gold surfaces were immersed in a freshly prepared and degassed ethanolic solution (8 mL) of BBA-SS-BBA (87 μL of a $4.6 \cdot 10^{-5}$ M solution in DMF) and OEG-SH (0.8 mL of a 1 mM stock solution in EtOH) during 15h. Alternatively, the gold surface was sequentially

exposed to the two compounds; it was first immersed in a BBA-S-S-BBA solution (8 mL) during 30 min. The surface was then rinsed with EtOH before immersion in a OEG-SH solution (8 mL). After 15h the surface was rinsed again with EtOH before being blown dried with nitrogen before proceeding to the XPS experiments.

Gold-coated QCM-D (QSense AB, Sweden) and SPR (SIA Kit Au, GE Healthcare, Germany) sensors were cleaned in a 5:1:1 solution of water, 25% ammonia and 30% hydrogen peroxide during 10 min at 60°C followed by extensive washing with water. After being blown dried under a flow of nitrogen, the sensors were placed in 8 mL of a freshly prepared and degassed ethanolic solution of: A) OEG-SH with 0.1% or 1% mole fraction of Bio-SH (total concentration of thiols was 0.1 mM) for a period of 15 h; B) BBA-S-S-BBA (87 or 8.7 μL of a $4.6 \cdot 10^{-6}$ M solution in DMF) during 15 minutes followed by incubation in a degassed ethanolic solution (8 mL) of OEG-SH (0.8 mL of a 1 mM stock solution in EtOH) for a period of 15h. The sensors were rinsed in ethanol and blown dried with nitrogen before proceeding to the SPR and QCM-C experiments.

The mica-gold interfaces (used for the AFM experiments in liquid) were cleaved manually and immediately immersed in a BBA-S-S-BBA solution (8.7 μL of a $4.6 \cdot 10^{-6}$ M solution in DMF diluted with 7.2 mL of degassed EtOH) during 15 minutes followed by incubation in 8 mL of a degassed ethanolic solution of OEG-SH (0.8 mL of a 1 mM stock solution in EtOH) for a period of 15h. The surface was then rinsed with ethanol before being blown dried with nitrogen.

X-ray photoelectron spectroscopy (XPS) Analysis (performed by Dr Laurent Marot)

The XPS measurements were performed in UHV (ultrahigh vacuum) conditions with a VG ESCALAB 210 spectrometer using monochromatized Al Kα radiation (hυ=1486.6 eV) with an energy resolution better than 0.5 eV. The base pressure in the chamber was around $1 \cdot 10^{-7}$ Pa during acquisition. The binding energy scale was calibrated using the Au 4f7/2 line of a cleaned gold sample at 84.0 eV. Moreover, large scale XPS-spectra from 0 to 1200 eV were perfomed to identified all elements.The acquisition mode was set to CAE (constant analyser energy) with 20 eV pass energy (0.025 eV step size) and normal electron escape angle. Fitting of the core level lines was performed using Doniach-Sunjic functions, after a Shirley background subtrac-

tion, using UNIFIT for Windows (Version 2011) software. A convolution of Lorentzian and Gaussian line shapes was used to fit the individual peaks. After this, the intensities were estimated by calculating the integral of each peak; the atomic concentrations were then derived using Scofield sensitivity factors.

Step-by-Step assembly of SAv

The samples for the AFM measurements in liquid were prepared as follow: a drop (100 μL) of Sav 8 μM in HBS (100 mM, pH=7.4, 0.15 M NaCl) was deposited onto the freshly prepared 0.01% BBA-SH SAM and allowed to adsorb for 1h. After washing (1 x HBS 0.05% TWEEN 20 and 5 x 100 μL HBS), a drop (100 μL) of BBA_2 2 μM in HBS (100 μM, pH=7.4, 0.15 M NaCl) was deposited onto the sample and left to adsorb for 0.5h. After washing (HBS 5 x 100μL HBS) the substrate was introduced in a SAv solution as described above, and the procedure was repeated to obtain four elongation steps.

QCM-D Measurements

QCM-D measurements were performed using the Q-Sense D300 system. Non flowing conditions were used and the measurement chamber was temperature-stabilized to 22 ± 0.05 °C. The injection volume was always 3 mL, from which 2 mL were used to rinse the injection loop and 1mL was flown in the measurement chamber.The surface was rinced three times with running buffer between each injection. Substrates (gold-coated AT-cut quartz crystals, f_0 = 5 MHz) were from Q-Sense AB. HBS-P (0.01 M HEPES pH 7.4, 0.15 M NaCl, 0.005% v/v surfactant P20) purchased from GE Healthcare was used as running buffer and to prepare the SAv and ligands solutions.

SPR Measurements

SPR measurements were performed using a BIAcore X system (Biacore AB, Uppsala, Sweden). The experiments were conducted at 22°C using a flow rate of 5 μL/min (stated if otherwise). The injected volume was 80 μL (mentioned if otherwise). Substrates (SIA Kit Au) were from GE Healthcare. HBS-P (0.01 M HEPES pH 7.4, 0.15 M NaCl, 0.005% v/v surfactant P20) was used as running buffer and to prepare the SAv and ligands solutions.

4.3 Synthesis

4.3.1 *N*-(8-Amino-3,6-dioxaoctanyl)biotinamide (**6**)

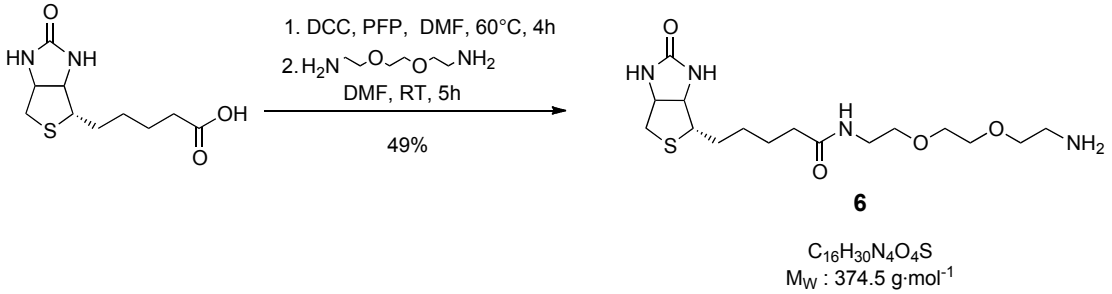

Biotin (3.0 g, $12.3 \cdot 10^{-3}$ mol, 1 eq.) was dissolved in hot dry DMF (75 mL) and the solution was cooled to room temperature. PFP (2.9 g, $16.0 \cdot 10^{-3}$ mol, 1.3 eq.) and DCC (3.7 g, $17.8 \cdot 10^{-3}$ mol, 1.5 eq.) were then added, and the mixture was stirred at 60ºC during 1 hour and at room temperature for 3 more hours. The DCU that precipitated was filtered off. The next reaction step was carried on without further purification of the PFP ester. The biotin-PFP solution was added drop by drop to a solution of 2,2-ethylenedioxy)diethylamine (19.2 g, 0.13 mol, 10 eq.) and Et_3N (2.9 ml, $0.02 \cdot 10^{-3}$ mol) dissolved in 200 mL of DMF. The reaction mixture was stirred at room temperature during 5 hours, and the solvent was removed under reduced pressure. The resulting oil was triturated in 450 mL of Et_2O and filtered to give a white solid. The crude product was purified on a silica gel column, eluting with MeOH/ EtOAc (8/2) to give 2.26 g (49%) of **6** as a beige waxy solid.

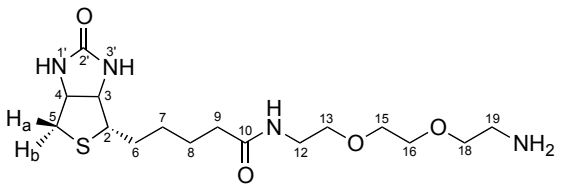

***R*$_f$** (MeOH/AcEt 6:1) = 0.15

^{1}H-RMN (400 MHz, CD_3OD) δ_H (ppm): 4.50 (ddd, ^3J(4-3)=7.9 Hz, ^3J(4-5$_A$)=5.0 Hz, 1H, H_4), 4.31 (dd, ^3J(3-4)=7.9 Hz, ^3J(3-2)=5.0 Hz, 1H, H_3), 3.63 (m, 4H, $CH_{2\ PEG}$, H_{15} & H_{16}), 3.60-3.51 (m, 4H, $CH_{2\ PEG}$, H_{13} & H_{18}), 3.36 (t, 2H, H_{12}), 3.21 (ddd, ^3J(2-

3)=4.4 Hz, $^3J(2\text{-}6_b)$=5.8 Hz, $^3J(2\text{-}6_a)$=9.0 Hz, 1H, H_2), 2.93 (dd, $^3J(5_A\text{-}5_B)$=12.8, $^3J(5_A\text{-}4)$=5.0, 1H, H_{5_A}), 2.79 (t, 2H, H_{19}), 2.71 (d, $^3J(5_A\text{-}5_B)$=12.8 Hz, 1H, H_{5_B}), 2.22 (t, $^3J(9\text{-}8)$=7.4 Hz, 2H, H_9), 1.67 (m, 4H, H_8 & H_6), 1.44 (m, 2H, H_7).

^{13}C-RMN (100 MHz, CD_3OD) δ_C (ppm): 176.1 (C_{10}), 166.1 ($C_{2'}$), 73.4 (C_{EG}, C_{17}), 71.3 (C_{EG}, C_{15} & C_{16}), 70.6 (C_{EG}, C_{13}), 63.4 (C_3), 61.6 (C_4), 57.0 (C_2), 42.0 (C_{19}), 41.1 (C_{12}), 40.3 (C_5), 36.7 (C_9), 29.8 (C_7), 29.5 (C_6), 26.9 (C_8).

MS (ESI): m/z (I %): 375.3 $[M+H]^+$ (100%).

4.3.2 5-(*tert*-Butoxycarbonylamino)isophthalic acid (**7**)

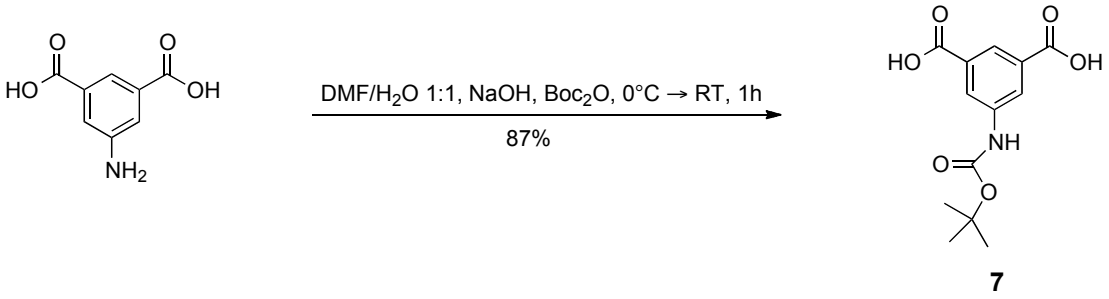

7

$C_{13}H_{15}NO_6$
M_W : 281.3 g·mol^{-1}

To a solution of **3** (25.3 g, 0.14 mol, 1 eq.) and NaOH (12.3 g, 0.30 mol, 2.1 eq.) in DMF/H_2O 1:1 at 0°C, di-*tert*-butyl dicarbonate (32.1 g, 0.15 mol, 1.1 eq) was added. The reaction was allowed to come to room temperature and was stirred for 20 h before HCl 3M (110 mL) was added. The solution was diluted with water (110 mL) and the resulting precipitate was collected, washed with water and dried to yield 34.3 g (87%) of **7** as a white solid.

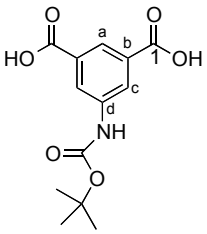

$\boldsymbol{R_f}$ (Hex/EtOAc 5:1) = 0.3

^{1}H-RMN (400 MHz, DMSO) δ_H (ppm): 8.65 (t, 1H, ^{m}J=1.5 Hz, H_a), 8.54 (d, 2H, ^{m}J=1.5 Hz, H_c), 6.91 (s, 1H, N-*H*), 1.55 (s, 9H, *t*-But.)

^{13}C-NMR (400 MHz, DMSO) δ_C (ppm): 167.4 (C_1), 153.6 (C_e), 141.1 (C_d) , 132.5 (C_b), 124.4 (C_a) , 123.4 (C_c), 50.6 ($C_{quat.}$, *t*-But), 28.9 (CH_3, *t*-But).

MS (ESI): m/z (I %): 561.3 $[2M-H]^-$ (100%), 280.5 $[M-H]^-$ (11%)

4.3.3. *N*-(tert-Butyloxycarbonyl)-5-aminoisophtalate bis-pentaflurophenyl Ester (**8**)

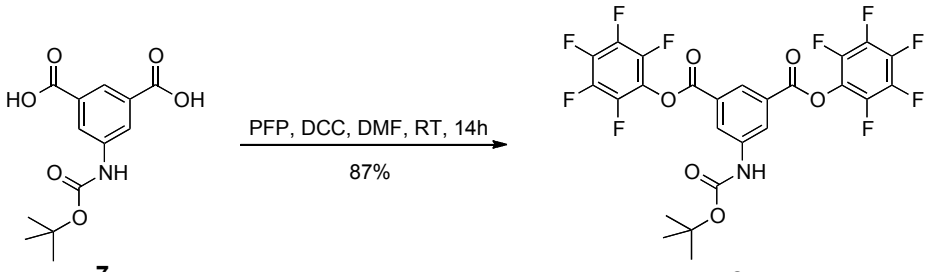

7 **8**

$C_{25}H_{13}F_{10}NO_6$
M_W: 613.4 g·mol^{-1}

To a solution of **7** (2.0 g, $7.1\cdot10^{-3}$ mol, 1 eq.) in dry DMF (80 mL), PFP (2.84 g, $15.4\cdot10^{-3}$ mol, 2.2) and DCC (2.2 g, $15.6\cdot10^{-3}$ mol, 2.2) were added. The reaction was stirred at ambient temperature for 14h and the DMF was removed under vacuum. The crude product was purified by chromatography on silica gel eluting with CH_2Cl_2 to provide 3.79 g (87%) of **8** as a white solid.

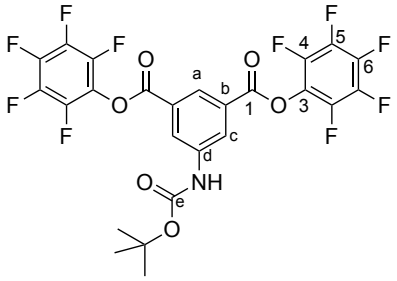

***R*$_f$** (CH_2Cl_2/AcOEt 1:1) = 0.25

^{1}H-NMR (400 MHz, $CDCl_3$) δ_H (ppm): 8.65 (t, 1H, ^{m}J=1.5 Hz, H_a), 8.54 (d, 2H, ^{m}J=1.5 Hz, H_c), 6.91 (s, 1H, N-*H*), 1.55 (s, 9H, *t*-But.).

^{13}C-NMR (400 MHz, $CDCl_3$, 298 K) δ_C (ppm): 161.7 (C_1), 152.4 (C_e), 140.4 (C_d), 129.0 (C_b), 126.9 (C_a), 125.54 (C_c), 77.43 ($C_{quat.}$, *t*-But), 28.5 (CH_3, *t*-But).

^{19}F-NMR (376 MHz, $CDCl_3$) δ_F (ppm): -153.34 (d, ^{3}J = 17.2 Hz, 2F, F_4), -158.26 (t,

^3J = 21.7 Hz, 1F, F_6), -162.97 (dd, ^3J =21.7 Hz, ^3J =17.3 Hz, 2F, F_5).

MS (APCI): m/z (I %): 648 $[M\text{-}H+2H_2O]^-$ (100%)

4.3.4. BBA (**9**)

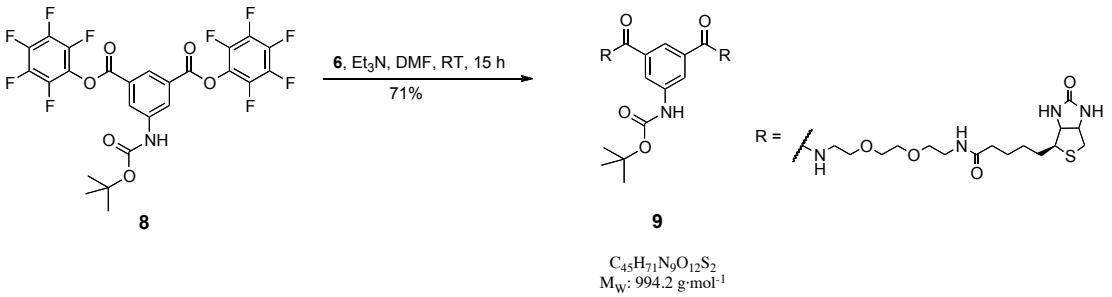

8 **9**

$C_{45}H_{71}N_9O_{12}S_2$
M_W: 994.2 g·mol^{-1}

To a solution of **6** (2.15 g, $5.7\cdot10^{-3}$ mol, 8 eq.) and Et_3N (0.5 mL, $3.6\cdot10^{-3}$ mol, 5 eq.) in DMF (15 mL), a solution of **8** (0.44 g, $0.72\cdot10^{-3}$ mol, 1 eq.) in DMF* (20 mL) was added drop by drop over a 1h period. The mixture was stirred at ambient temperature overnight and the volatiles were removed under vacuum. The remaining solid was purified: a) by chromatography on silica gel with a gradient elution (MeOH/EtOAc 0:100→40:60), to yield 4.02 g (71%) of **9** as a white hygroscopic solid; b) by preparative RP-HPLC on a C_{18} column (40 mm x 150 mm, 10 µm; µ-Bondapak) with a gradient elution (CH_3CN/H_2O 25:75→55:45 in 18 min) at a flow rate of 80 mL/min to afford compound **9** in 80% yield.

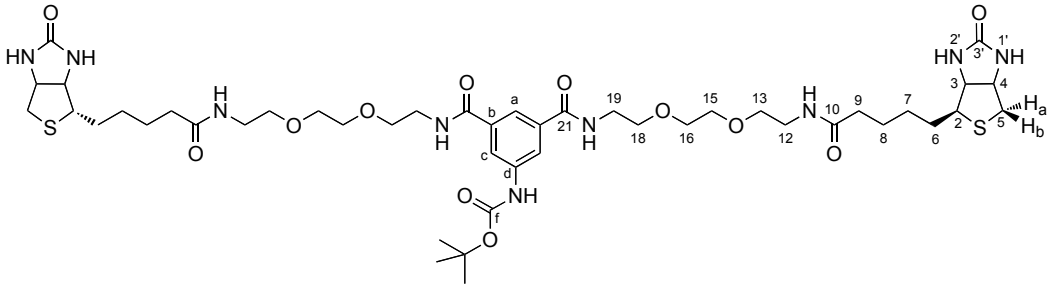

***R*$_f$** (MeOH/AcEt 1:1) = 0.25

^{1}H-RMN (400 MHz, CD_3OD) δ_C (ppm): 8.05 (d, $^m J$=1.5 Hz, 2H, H_c), 7.92 (t, $^m J$=1.5 Hz, 1H, H_a), 4.50 (dd, ^3J(4-3)=7.9 Hz, ^3J(4-5$_A$)=5.0 Hz, 2H, H_4), 4.30 (dd, ^3J(3-4)=7.9

Hz, ^{3}J(3-2)= 4.4Hz, 2H, H_3), 3.71-3.62 (m, 12H, C$H_{2(EG)}$, H_{18} & H_{15} & H_{16}), 3.60 (t,^{3}J=5.4, 8H, C$H_{2(EG)}$, H_{19}), 3.56 (t, ^{3}J=5.5, 4H, C$H_{2(EG)}$, H_{13}), 3.36 (t, 4H,^{3}J=5.4 Hz, C$H_{2(EG)}$, H_{12}), 3.19 (m, ^{3}J(2-3)=4.4 Hz, 2H, H_2), 2.93 (dd, $^{3}J(5_A\text{-}5_B)$=12.7, $^{3}J(5_A\text{-}4)$=5.0, 2H, H_{5_A}), 2.71 (d, $^{3}J(5_A\text{-}5_B)$=12.7 Hz, 2H, H_{5_B}), 2.19 (t, ^{3}J(9-8)=7.4 Hz, 4H, H_9), 1.67 (m, 8H, H_8 & H_6), 1.55 (s, 9H, *t*-But), 1.42 (m, 4H, H_7).

^{13}C-RMN (100 MHz, CD_3OD) δ_C (ppm): 175.1 (C_{10}), 168.5 (C_{21}), 165.1 ($C_{3'}$), 154.0 ($C_{carbonyl}$ *t*-But), 140.5 (C_d), 135.9 (C_b), 120.2 ($CH_{aromatic}$), 120.0 ($CH_{aromatic}$), 80.1 ($C_{quat.}$ *t*-But), 70.4 (C_{EG}, C_{15} & C_{16}), 69.6 (C_{EG}, C_{13}), 69.5 (C_{EG}, C_{18}), 62.3 (C_3), 60.6 (C_4), 56.0 (C_2), 40.1 (C_5), 40.0 (C_{19}), 39.3 (C_{12}), 35.8 (C_9), 28.7 (C_7), 28.5 (C_6), 27.7 (CH_3 *t*-But), 25.8 (C_8).

MS (ESI): m/z (I %): 1016.5 $[M+Na]^+$ (100%)

HPLC-ESI-MS (µ-Bondapak, 4x250 mm, CH_3CN:H_2O (0.1% TFA) 20:80→35:65 in 20 min, flow 0.4 mL/min, DAD (225 and 254 nm), T=25°C) R_t= 20.5 min; m/z 994.9 ($[M+H^+]^+$), 1016.7 ($[M+Na^+]^+$).

4.3.5 3,6,9-Trioxaundecanedioate bis-pentafluorophenyl ester (**10**)

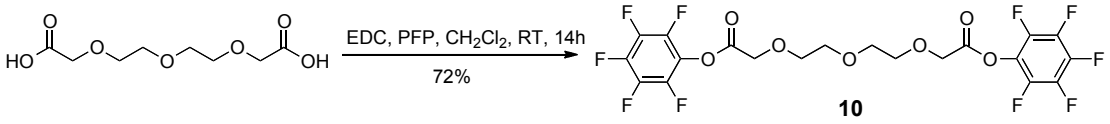

$C_{20}H_{12}F_{10}O_7$
M_W: 554.3 g·mol^{-1}

To a solution of 3,6,9-trioxaundecanedioic acid (5.0 g, $23\cdot10^{-3}$ mol, 1 eq.) in CH_2Cl_2 (75 mL), PFP (9.5 g, $52\cdot10^{-3}$ mol, 2.3 eq) was added followed by EDC (10.5 g, $54\cdot10^{-3}$ mol, 2.2 eq.). The reaction was stirred overnight at room temperature and the solvent was removed under vacuum. The thick oily mass was extracted with Et_2O (3x50 mL), the combined Et_2O fractions were washed with $NaHCO_{3(sat.)}$ solution (3x15 mL) and water (2x10 mL) before being dried over Na_2SO_4. The volatiles were removed under reduced pressure and the residual oil was purified by chromatography on silica gel with a gradient elution (Et_2O/Hex 9:1→ 4:1) to afford 9.17 g (72%) of **10** as a colorless oil.

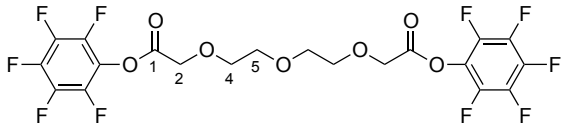

$\boldsymbol{R_f}$ (Et_2O/Hex. 1:1) = 0.23

^{1}H-RMN (400 MHz, DMSO-d_6) δ_H (ppm): 4.66 (s, 4H, H_2), 3.73-3.57 (m, 8H, H_3 & H_4).

^{13}C-NMR (101 MHz, DMSO-d_6) δ_F (ppm): 167.9 (C_1), 142-137 (C_a, C_b, C_c, C), 126.9 (C_a), 125.5 (C_c), 71.1 ($CH_{2\ EG}$, C_3 or C_4), 71.2 ($CH_{2\ EG}$, C_3 or C_4), 61.8 (C_2).

^{19}F-RMN (376 MHz, DMSO-d_6) δ_F (ppm): -153.0 (d, ^3J = 19.0 Hz, 2F, F_4), -157.8 (t, ^3J = 23.0 Hz, 1F, F_6), -162.4 (dd, ^3J =23.0 Hz, ^3J =19.0 Hz, 2F, F_5)

4.3.6 5-Aminoisophthalate bis-ethyl ester (**11**)

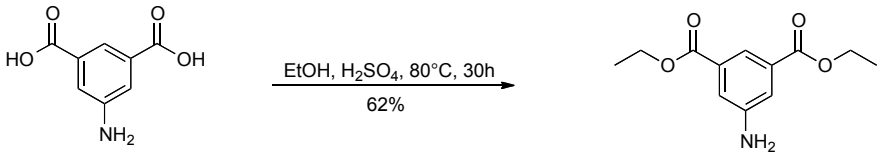

11

$C_{12}H_{15}NO_4$
M_W: 237.3 g·mol^{-1}

A solution of 5-amino isophthalic acid (1.25 g, 6.9·10^{-3} mol) in EtOH (15 mL) was refluxed in the presence of 0,5 mL of concentrated H_2SO_4 during 20h. The solution was poured in an excess of bicarbonate solution, and the product was extracted with Et_2O (3×10 mL). The organic layer was washed with water (10 mL) and dried over Na_2SO_4 before Et_2O was removed under vacuum. The obtained white solid was recrystallized from EtOH to give 1.01 g (62%) of **11** as a white solid.

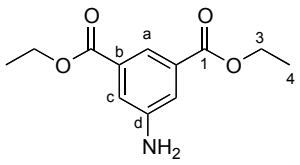

$\boldsymbol{R_f}$ (MeOH/EtOAc 1:1) = 0.65

^{1}H-RMN (400 MHz, $CDCl_3$) δ_H (ppm): 8.05 (t, ^{m}J=1.4 Hz, 1H, H_a), 7.71 (d, ^{m}J=1.4 Hz, 2H, H_c), 4.37 (q, ^{3}J(3-4)=7.1 Hz, 4H, H_3), 1.40 (t, ^{3}J(4-3)=7.1 Hz, 6H, H_4).

^{13}C-RMN (400 MHz, $CDCl_3$, 298 K) δ_H (ppm): 166.5 (C_1), 147.1 (C_d), 132.2 (C_b), 121.0 (C_a), 120.1 (C_c), 61.6 (C_3), 14.7 (C_4).

MS (ESI): m/z (I %): 238.1 $[M+H]^+$ (100%)

4.3.7 *N, N'*-Bis(5-aminoisophthalate bis-ethyl ester)-3,6,9-trioxaundecanediamide (**12**)

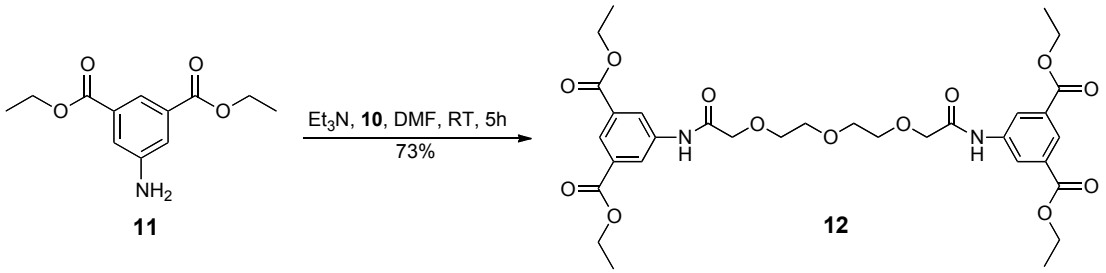

$C_{32}H_{40}N_2O_{13}$
M_W: 660.7 g·mol^{-1}

To a solution **11** (0.27 g, $1.14 \cdot 10^{-3}$ mol, 2.1 eq.) and Et_3N (0.15 mL) in DMF* (25 mL), PFP diester **10** (0.3 g, $0.54 \cdot 10^{-3}$ mol, 1 eq.) was added and the reaction was left under magnetic stirring at room temperature during 6 h before the volatiles were removed under vacuum. The residue was dissolved in a minimal amount of EtOAc followed by the addition of hexane until precipitation of a beige solid which was filtered off and dried under vacuum to afford 0.26 g (73%) of **12**.

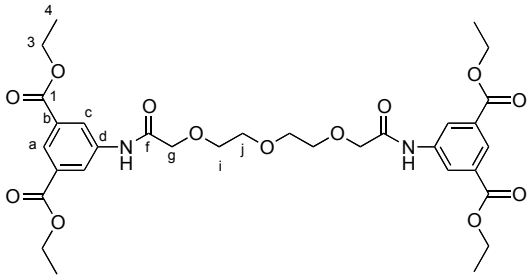

R_f (MeOH/EtOAc (1:1) = 0.33

^{1}H-RMN (400 MHz, $CDCl_3$) δ_H (ppm): 8.94 (s, 2H, N-*H*), 8.37 (t, ^mJ=1.4 Hz, 2H, H_a), 8.35 (^mJ=1.4 Hz, 4H, H_c), 4.39 (q, ^3J(3-4)=7.1 Hz, 8H, H_3), 4.15 (s, 4H, H_g), 3.89 (m, 8H, H_i & H_j), 1.40 (t, ^3J(4-3)=7.1 Hz, 12H, H_4).

^{13}C-RMN (100 MHz, $CDCl_3$) δ_C (ppm): 168.3 (C_f), 166.1 (C_1), 137.7 (C_d), 131.6 (C_b), 126.3 (C_c), 124.6 (C_a), 70.8 (C_{EG}), 70.2 (C_g), 70.1 (C_{EG}), 61.5 (C_3), 14.3 (C_4).

MS (ESI): m/z (I %): 683.3 $[M+Na]^+$ (100%)

4.3.8 BBA_2 (**2**)

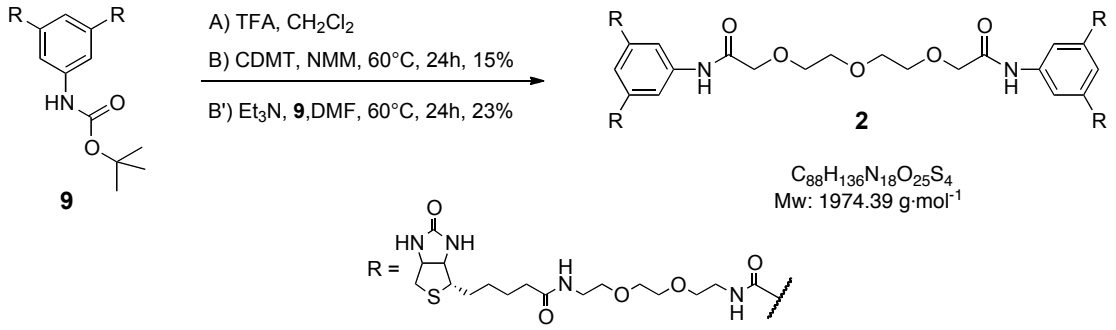

In a 5 mL round-bottom flask, compound **9** (20.6 mg, $0.02\cdot10^{-3}$ mol, 1 eq.) was dissolved in of TFA (0.08 mL, $1.0\cdot10^{-3}$ mol, 50 eq.) and the inner wall of the flask was rinsed with CH_2Cl_2 (1.0 mL). The reaction was allowed to stir for 45 min and the volatiles were removed under reduced pressure. The residue was dissolved in a minimal amount of MeOH, and an excess of Et_3N (0.2 mL, $1.4\cdot10^{-3}$ mol, 70 eq.) was added. The mixture was stirred for 10 min and the excess Et_3N and solvent were removed under vacuum to afford the free amine **1** that was immediately used for peptide coupling.

Method B

To a solution of 3,6,9-trioxaundecanedioic acid (9 mg, 42 μmol, 1 eq.) in DMF* (2.5 mL), CDMT (16 mg, 93 μmol, 2.2 eq.) and *N*-methylmorpholine (23 mg, 232 μmol, 5.4 eq.) were added. The solution was stirred at room temperature during 45 minutes before aromatic amine **1** (83 mg, 93 μmol, 2.2 eq.) was added. The reaction was stirred at 60°C during 24h and the solvent was removed under vacuum. The crude product was purified by chromatography on a silica gel column eluting with MeOH/$CHCl_3$ (4:1) to yield 27 mg (15%) of **2** as a brown solid.

Method B'

Coumpound **1** (83 mg, 83 μmol) was dissolved in dry DMF (6.0 mL) and Et_3N (83 mg, 83 μmol) was added. To this solution, a solution of of PFP diester **10** (22 mg, 40 μmol) in DMF* (3.0 mL) was added dropwise over a period of 15 min and reaction was stirred at 60°C during 24h. Volatiles were removed under vacuum and the crude product was purified by chromatography on silica gel eluting with MeOH/$CHCl_3$, 4:1 to yield 41 mg (23%) of **2** as a brown solid.

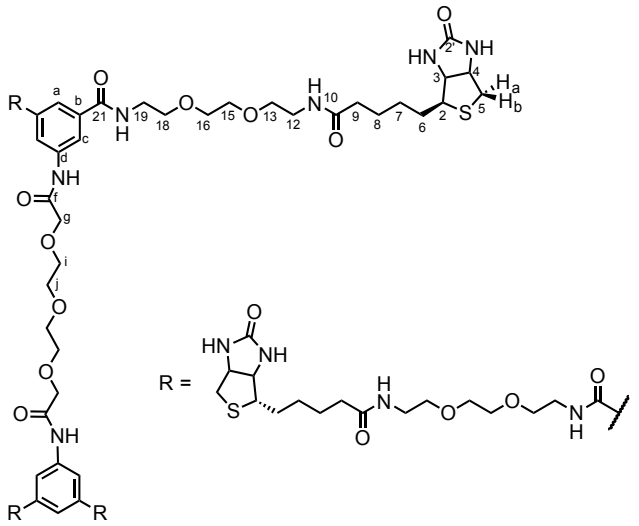

***R*$_f$** (MeOH/$CHCl_3$ 4:1) = 0.23

^{1}H-RMN (400 MHz, MeOH-d4) δ_H (ppm): 8.26 (d, ^mJ=1.5 Hz, 2H, C$H_{aromatic}$, H_c), 8.05 (t, ^mJ=1.5 Hz, 1H,C$H_{aromatic}$, H_a), 4.48 (dd, ^3J(4-3)=7.8 Hz, ^3J(4-5$_A$)=4.4 Hz, 2H, H_4), 4.28 (dd, ^3J(3-4)=7.8 Hz, ^3J(3-2)=4.4 Hz, 2H, H_3), 4.23 (s, 2H, C$H_{2\ EG}$, H_g), 3.80-

3.58 (m, 20H, C$H_{2\ EG}$), 3.55 (m, 4H, C$H_{2\ EG}$), 3.35 (m, 4H, C$H_{2\ EG}$, H_{12}), 3.21 (m, 2H, H_2), 2.91 (dd, $^3J(5_A\text{-}5_B)$=12.7, $^3J(5_A\text{-}4)$=4.9, 2H, H_{5_A}), 2.69 (d, $^3J(5_A\text{-}5_B)$=12.7 Hz, 2H, H_{5_B}), 2.17 (t, ^3J(9-8)=7.4 Hz, 4H, H_9), 1.73-1.51 (m, 8H, H_8 & H_6), 1.38 (m, 4H, H_7).

^{13}C-RMN (100 MHz, CD_3OD) δ_C (ppm): 175.0 (C_{10}), 170.0 (C_f), 167.8 (C_{21}), 164.7 ($C_{2'}$), 138.3 (C_d), 135.6 (C_b), 121.8 (C_c), 121.5 (C_a), 69.9 (6 C, C$H_{2\ EG}$, C_g, C_i, C_j, C_{15} & C_{16})), 69.2 (C$H_{2\ EG}$, C_{13}), 69.1 (C$H_{2\ EG}$, C_{18}), 62.0 (C_3), 60.2 (C_4), 55.6 (C_2), 39.7 (2 C, C_{19} & C_5), 38.9 (C_{12}), 35.3 (C_9), 28.3 (C_7), 28.1 (C_6), 25.5 (C_8).

MS (ESI): m/z (I %): 1996.9 $[M+Na]^+$ (100%)

4.3.9 *tert*-Butyl 8-amino-3,6-dioxaoctylcarbamate (**14**)

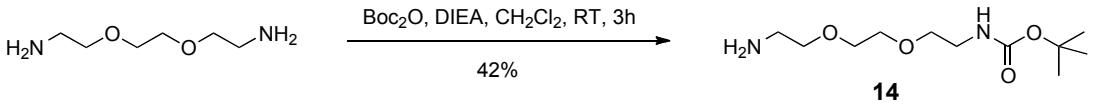

14

$C_{11}H_{24}N_2O_4$
M_w: 248.3 g·mol^{-1}

2,2-ethylenedioxy)diethylamine (12.6 g, 85 mmol, 1.5 eq.) was stirred with diisopropylethylamine (4.8 mL, 28 mmol, 0.5 eq.) in CH_2Cl_2 (50 mL), then di-*tert*-butyl dicarbonate (6.1 g, 28 mmol, 0.5 eq.) in CH_2Cl_2 (50 mL) was added drop by drop over 2 hours. The mixture was stirred during 3h at room temperature and the solvent was evaporated under vacuum. The residue was purified by chromatography (silica gel, EtOH/AcOEt/Et_3N, 5:4:1) to afford **14** as a yellowish oil (5.8 g, 42%).

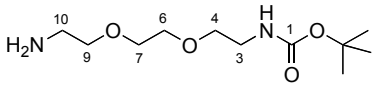

R_f (EtOH/AcOEt/Et_3N 5:4:1) = 0.31

^{1}H-RMN (400 MHz, $CDCl_3$) δ_H (ppm): 5.19 (sl, 1H, NH), 3.60 - 3.56 (m, 4H, C$H_{2\ EG}$, H_6 & H_7), 3.51 (t, 2H, C$H_{2\ EG}$, H_4), 3.49-3.47 (m, 2H, C$H_{2\ EG}$, H_9), 3.31-3.25 (m, 2H,C$H_{2\ EG}$, H_3), 2.84 (t, J = 5.2 Hz, 3H,C$H_{2\ EG}$, H_{10}), 1.66 (bs, 2H, NH_2), 1.40 (s, 9H, *t*-But).

^{13}C NMR (101 MHz, $CDCl_3$) δ_C (ppm): 156.0 (C_1), 79.1 (C_{quat} *t*-But), 73.4 (C$H_{2\ EG}$, C_9), 70.2 (C$H_{2\ EG}$, C_6 & C_7), 70.2 (C$H_{2\ EG}$, C_4), 41.7 (C_{10}), 40.3 (C_3), 28.4 (CH_3 *t*-But).

MS (ESI): m/z (I %): 249.2$[M+H]^+$ (100%), 497.1$[2M+H]^+$ (43%), 289.2 $[M+K]^+$ (15%)

4.3.10 *N,N',N''*-Tri(8-*t*-butoxycarbonylamino-3,6-dioxaoctyl)benzene-1,3,5-tricarboxamide **(15)**

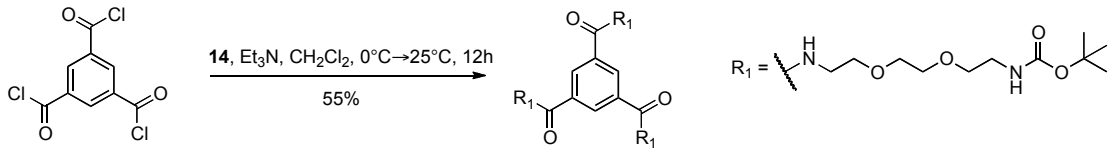

15

$C_{42}H_{72}N_6O_{15}$
M_W: 901.1 g·mol^{-1}

To a solution of trimesylchloride (1.6 g, $5.6 \cdot 10^{-3}$ mol, 1 eq.) in 70 mL CH_2Cl_2 at 0°C were added **14** (4.2 g, $17 \cdot 10^{-3}$ mol, 3 eq.) and Et_3N (8.0 g, $79 \cdot 10^{-3}$ mol, 10 eq.) in 12 mL CH_2Cl_2. After stirring for 15h at room temperature, the orange colored solution was washed with H_2O (4 x 20 mL) and dried over Na_2SO4 before removing volatiles under reduced pressure. The residue was purified by column chromatography on silica gel eluting with CH_2Cl_2 (200 mL), then CH_2Cl_2/MeOH 99:1 to yield 2.8 g (55%) of **15** as a colorless oil.

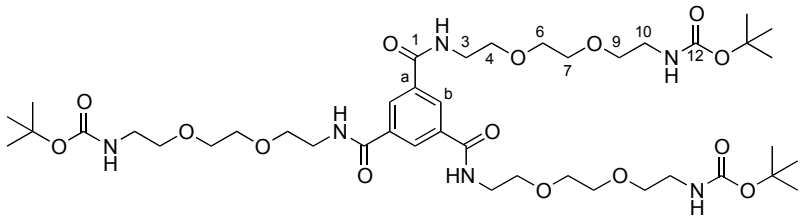

^{1}H NMR (400 MHz, MeOH-d_4) δ_H (ppm): 8.43 (s, 3H, $HC_{aromatiq}$), 3.72 – 3.56 (m, 24H, $CH_{2\ EG}$, H_3, H_4, H_6 & H_7), 3.51 (t, J = 5.6 Hz, 6H, H_9), 3.20 (t, J = 5.6 Hz, 6H, H_{10}), 1.40 (s, 27H, CH_3 *t*-But).

^{13}C NMR (126 MHz, MeOH-d_4) δ_C (ppm): 168.7 (C_1), 158.4 (C_{12}), 136.6 (C_b), 130.0 (C_a), 80.1 (C_{quat} *t*-But), 71.3 (2 x $CH_{2\ EG}$, C_6 & C_7), 71.1 (C_9), 70.5 (C_4), 41.2 (C_3), 41.1 (C_{10}), 28.8 (CH_3 *t*-But).

MS (ESI): m/z (I %): 923.4 $[M+Na^+]^+$ (100%)

4.3.11 *N,N,N"*-Tri(8-*t*-butoxycarbonylamino-3,6-dioxaoctyl)benzene-1,3,5-tricarboxamide succinic acid **(17)**

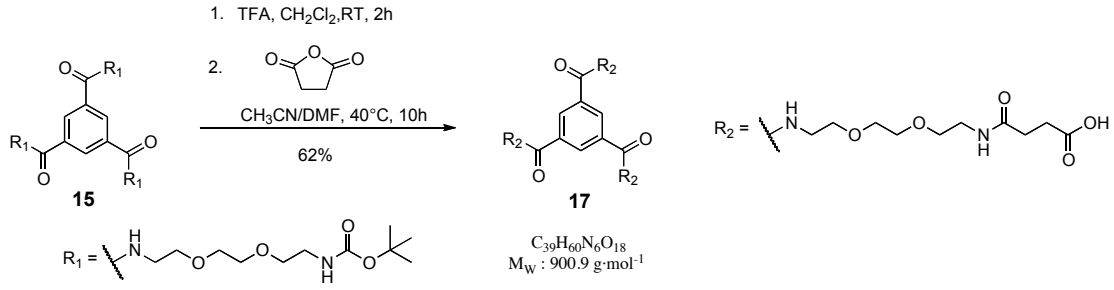

Trifluoroacetic acid (11.6 g, 0.10 mol, 40 eq.) was added to a solution of **15** (2.3 g, $2.5 \cdot 10^{-3}$ mol, 1 eq.) in 20 mL CH_2Cl_2. The mixture was stirred for 2h at room temperature and the volatile materials were removed under reduced pressure. The residue was dissolved in CH_3CN/DMF (10:1) and succinic anhydride (1.3g, $13 \cdot 10^{-3}$ mol, 5 eq.) was added. After stirring at 40°C for 14h, the solvent was evaporated under reduced pressure. The residue was purified by column chromatography on silica gel eluting with CH_2Cl_2/MeOH/NH_3 75:20:5 to yield 1.4 g (62%) of **17** as a white hygroscopic solid.

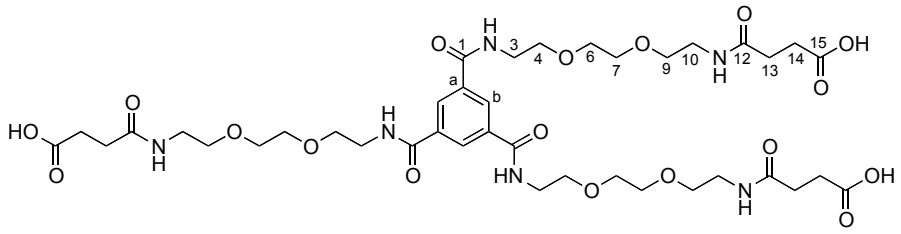

^{1}H NMR (400 MHz, MeOH-d_4) δ_H (ppm): 8.43 (s, 3H, H_a), 3.74 – 3.57 (m, 24H, CH_{EG}, H_3, H_4, H_6 & H_7), 3.53 (t, ^3J = 5.6 Hz, 6H, H_9), 3.52-3.32 (m, 6H, H_{10}), 2.53-2.48 (m, 2H, H_{14}), 2.47-2.41 (m, 2H, H_{13})

^{13}C NMR (126 MHz, MeOH-d_4) δ_C (ppm): 178.1 (C_{15}), 175.2 (C_{12}), 168.7 (C_1), 136.6 (C_b), 130.0 (C_a), 71.3 ($CH_{2\,EG}$, C_6 & C_7), 70.6 (C_9), 70.5 (C_4), 41.2 (C_3), 40.3 (C_{10}), 32.5 (C_{13}), 32.1 (C_{14})

MS (ESI): m/z (I %): 899.9 $[M\text{-}H^+]^-$ (100%)

4.3.12 2,2-dimethyl-4,15-dioxo-3,8,11-trioxa-5,14-diazaoctadecan-18-oic acid (**18**)

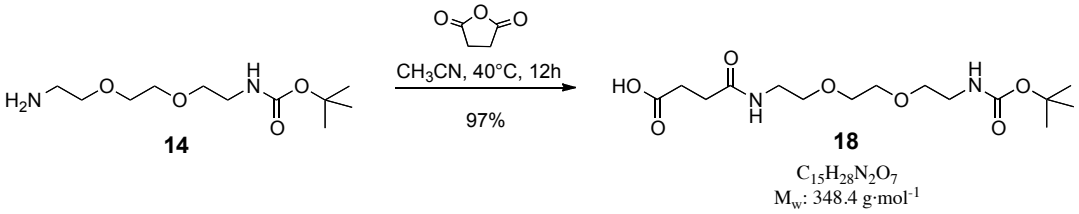

Succinic anhydride (85 mg, 0.85 mmol, 1.1 eq.) was added to a solution of **15** (0.22 g, 0.744 mmol, 1 eq.) in CH_3CN (10 mL). The mixture was stirred during 12h at 40°C and the CH_3CN was evaporated under vacuum. The remaining oil was purified by chromatography on silica gel eluting with CH_2Cl_2/MeOH 9:1 to afford 0.260 g (97%) of **19** as a yellowish oil.

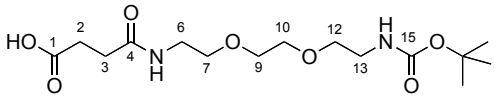

R_f (CH_2Cl_2/MeOH, 9:1) = 0.4

^{1}H NMR (400 MHz, $CDCl_3$) δ_H (ppm): 7.45 (s, 1H, N*H*), 6.91 (s, 1H, N*H*), 3.63-3.59 (m, 4H, C$H_{2\ PEG}$, H_9 & H_{10}), 3.57-3.51 (m, 4H, C$H_{2\ PEG}$, H_7 & H_{12}), 3.47-3.42 (m, 2H, CH_2NH, H_6), 3.34 – 3.29 (m, 2H, CH_2NH, H_{13}), 2.69 – 2.63 (m, 2H, O=CCH_2CH_2C=O, H_2), 2.54 – 2.46 (m, 2H, O=CCH_2CH_2C=O, H_3), 1.45 (s, 9H, CH_3 *t*-But).

^{13}C NMR (101 MHz, $CDCl_3$) δ_C (ppm): 177.5 (C_1), 173.0 (C_4), 158.0 (C_{15}), 81.1 (C_{quat} *t*-But), 70.3 (2 x $CH_{2\ EG}$, C_9 & C_{10}), 70.2 ($CH_{2\ EG}$, C_{12}), 69.6 ($CH_{2\ EG}$, C_7), 41.6 (C_{13}), 39.3 (C_6), 31.4 (C_3), 30.3 (C_2), 28.4 (CH_3 *t*-But).

MS (ESI): m/z (I %): 349.2$[M+H]^+$ (100%), 497.1$[2M+H]^+$ (43%), 289.2 $[M+K]^+$ (15%)

4.3.13 Compound (**19**)

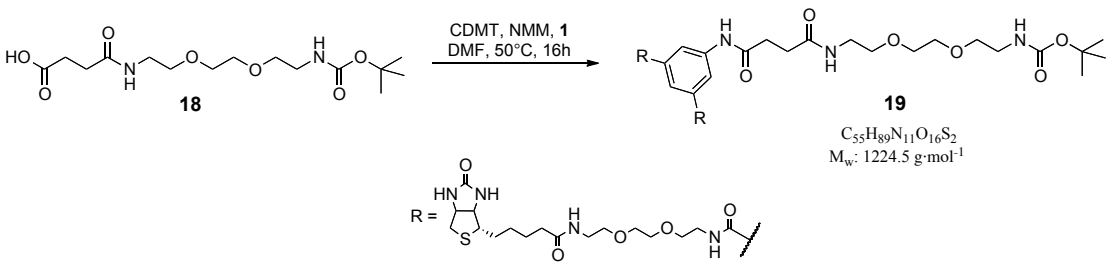

To a solution of **18** (0.177 g, $0.51 \cdot 10^{-3}$ mol, 3.25 eq.) in DMF (6 mL), CDMT (0.098 g, $0.56 \cdot 10^{-3}$ mol, 3.6 eq.) and NMM (0.17 mL, $1.5 \cdot 10^{-3}$ mol, 9.8 eq) were added. After 15 min of stirring at room temperature, amino-biotin dimer **1** (0.143 g, $0.16 \cdot 10^{-3}$ mol, 1 eq.) was added. The solution was stirred during 16h at 50°C and the DMF was evaporated under vacuum. The remaining oil was purified by chromatography (to yield 0.123 g (64%) of **19** as a white foam.

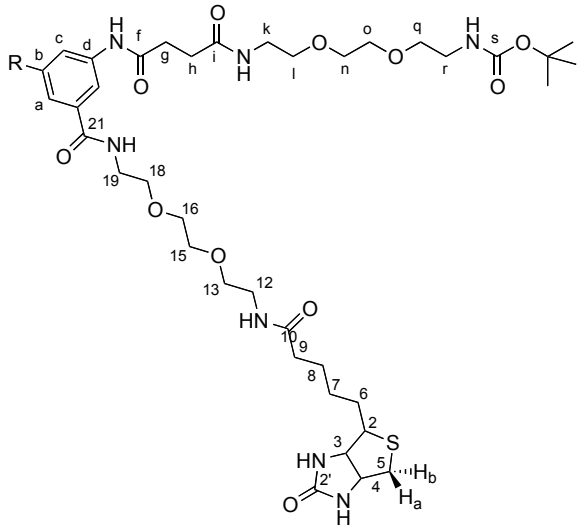

R_f (EtOH/AcOEt/ Et_3N 5:4:1) = 0.31

^{1}H NMR (400 MHz, MeOH-d_4) δ = 8.16 (d, ^mJ=1.4 Hz, 2H, C$H_{aromatic}$, H_c), 7.97 (t, ^mJ=1.4 Hz, 1H, C$H_{aromatic}$, H_a), 4.47 (dd, ^3J(4-3)=7.8 Hz, ^3J(4-5_A)=4.9 Hz, 2H, H_4), 4.27 (dd, ^3J(3-4)=7.8 Hz, ^3J(3-2)=4.4 Hz, 4H, H_3), 3.74 – 3.46 (m, 28H, C$H_{2\ EG}$), 3.40-3.32 (m, 6H, C$H_{2\ EG}$), 3.21 (m, J=5.7, 2H, H_r), 3.19 – 3.13 (m, 2H, H_2), 2.90 (dd, J=5.0, 12.7, 2H, H_{5_A}), 2.76-2.62 (m, 4H, O=CCH_2CH_2C=O and H_{5_B}), 2.61 (t, 2H,

O=CCH$_2$CH_2C=O), 2.17 (t, *J*=7.4, 2H, H_9), 1.75 – 1.49 (m, 8H, H_6 and H_8), 1.47 – 1.33 (m, 13H, H_6 and CH_{tBut})

^{13}C NMR (101 MHz, MeOH) δ = 175.04 (C_{10}), 173.61 (C_f), 172.23 (C_i), 168.17 (C_{21}), 164.43 ($C_{3'}$), 156.4 (C_t), 139.7 (C_d) , 135.9 (C_b), 121.6 (C_c), 121.2 (C_a), 79.1 (Ctert-boc), 70.4 ($CH_{2\ EG}$, C_n, C_o, C_{15} & C_{16}), 70.3 (O=CNHCH$_2$C$H_{2\ EG}$), 70.1 (O=CNHCH$_2$CH_2O), 69.7 (O=CNHCH$_2$CH_2O), 69.55 (O=CNHCH$_2$CH_2O), 62.4 (C_3), 60.6 (C_4), 56.0 (C_2), 40.3 (OCH$_2$CH_2NH), 40.1 (2 x OCH$_2$CH_2NH), 39.5 (OCH$_2$CH_2NH), 39.3 (OCH$_2$CH_2NH), 35.8 (C_9), 31.9 (CH$_2$CH_2C=O), 30.6 (CH$_2$CH_2C=O), 28.8 (C_7), 28.5 (C_6), 27.9 (CH_3 *t*-But), 25.9 (C_8).

MS (ESI): m/z (I %): 1996.9 $[M+Na]^+$ (100%)

4.3.14 BBA$_3$-1 (**3**)

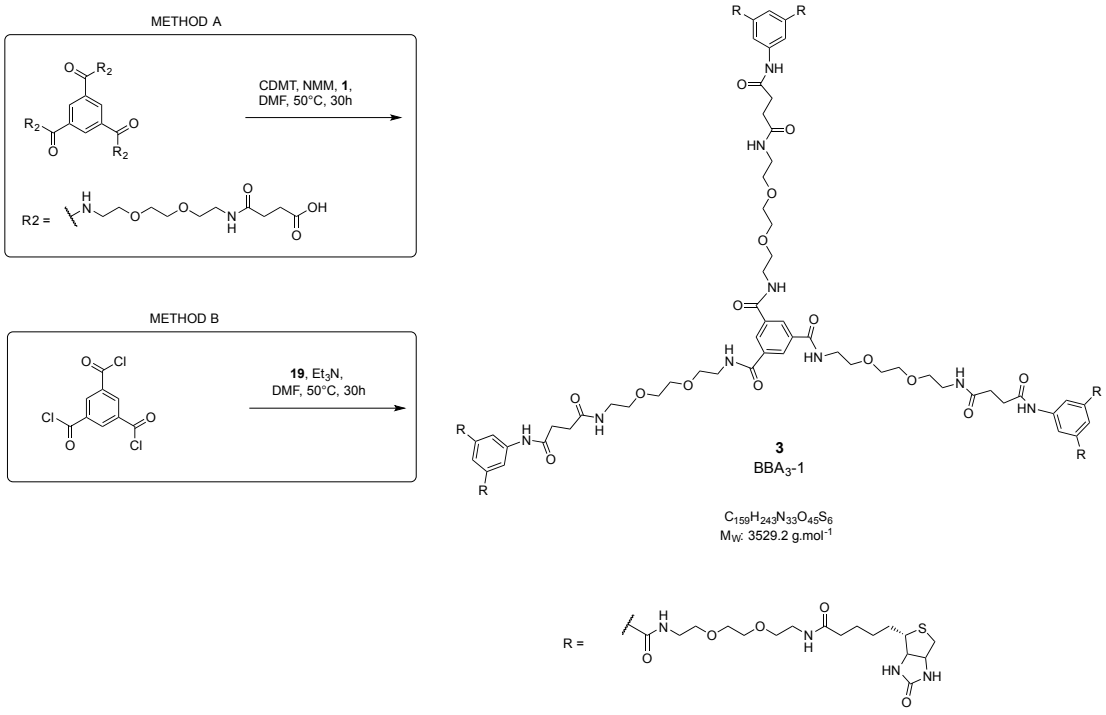

Method A

To a solution of **17** (26.8 mg, $30\cdot10^{-6}$ mol, 1 eq.) in DMF (3 mL), CDMT (18.3 mg, $0.1\cdot10^{-3}$ mol, 3.5 eq.) and NMM (29 µL, $0.26\cdot10^{-3}$ mol, 9 eq) were added. After 30 min of stirring at room temperature, amino-biotin dimer **1** (92 mg, $0.1\cdot10^{-3}$ mol, 3.5 eq.) dissolved in DMF (3 mL) was added. The mixture was stirred during 30h at 50°C and the DMF was evaporated under vacuum. The remaining oil was purified by

chromatography on silica gel eluting with CH_2Cl_2/MeOH/NH_3 75:20:5 to yield 8 mg (6%) of **3** as a brown solid.

Method B

In a 5 mL round bottom flask, **19** (0.088 g, $7.2 \cdot 10^{-6}$ mol, 3.3 eq.) was dissolved in TFA (0.16 mL, $2.16 \cdot 10^{-3}$ mol, 30 eq.) and the inner wall of the flask was rinsed with CH_2Cl_2 (1 mL). The solution was stirred at room temperature during 1h and the TFA was evaporated under reduced pressure. The deprotected amino compound was dissolved in a mixture of DMF (0.5 mL) and $CHCl_3$ (2.5 mL), Et_3N (11 µL, $7.9 \cdot 10^{-5}$ mol, 1.1 eq.) was added and the solution was cooled to 0°C. A solution of 1,3,5-tris(chlorocarbonyl)-benzene (5.7 mg, $21.6 \cdot 10^{-6}$ mol, 1 eq.) in $CHCl_3$ (0.5 mL) was added dropwise to the amine solution at 0°C, and the temperature was brought to room temperature. The solution was stirred a room temperature during 30 h and the volatiles were evaporated under reduced pressure. The residue was purified by chromatography on silica gel eluting with CH_2Cl_2/MeOH/NH_3 15:4:1 to yield 9 mg (12%) of **3** as a brown solid.

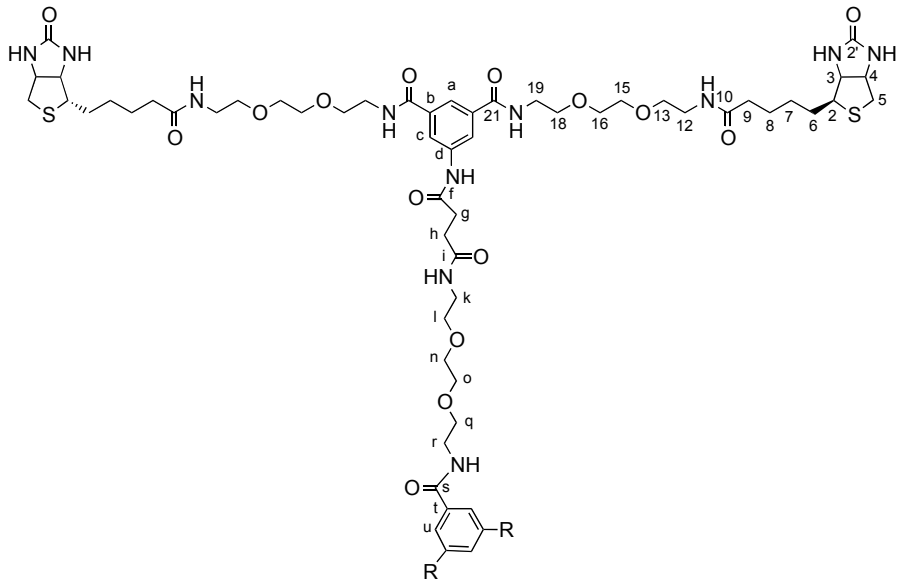

R_f (CH_2Cl_2/MeOH/ $NH_{3\ aq.}$ 15:4:1) = 0.15

^{1}H NMR (600 MHz, MeOH-d_4) δ = 8.39 (s, 1H, C$H_{aromatic}$, H_u), 8.10 (d, ^mJ=1.4 Hz, 2H, C$H_{aromatic}$, H_c), 7.94 (t, ^mJ=1.4 Hz, 1H, C$H_{aromatic}$, H_a), 4.47 (dd, 2H, H_4), 4.27 (dd, 4H, H_3), 3.70 – 3.56 (m, 24H, C$H_{2\ EG}$), 3.53 (t, 6H, C$H_{2\ EG}$), 3.33 (dt, 6H, C$H_{2\ EG}$), 3.14

(dt, J=5.7, 4H, H_2), 2.89 (dd, 2H, H_{5_A}), 2.69 (d, 2H, H_{5_B}), 2.67 (t, 2H, O=CCH_2CH$_2$C=O), 2.56 (t, 2H, O=CCH_2CH$_2$C=O), 2.16 (t, 4H, H_9), 1.73-1.50 (m, 8H, H_8 & H_6), 1.42-1.33 (m, 4H, H_7).

MS (ESI): m/z (I %): 1199.19 $[M+3Na]^{3+}$ (100%), 905.15 $[M+4Na]^{3+}$ (35%).

4.3.15 N^1,N^3,N^5-tris(2-(2-(2-(2-azidoethoxy)ethoxy)ethoxy)ethyl)benzene-1,3,5-tricarboxamide (**20**)

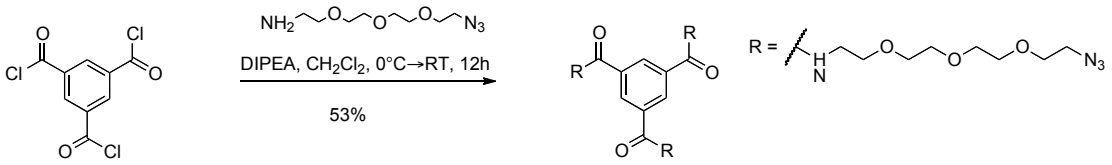

20

$C_{33}H_{54}N_{12}O_{12}$
M_W: 810.9g·mol^{-1}

A solution of trimesoyl chloride (0.200 g., 0.753 mmol) in CH_2Cl_2 (5 mL) was added to 11-azide-3,6,9-trioxaundecan-1-amine (0.8 g, 3.67 mmol) and N,N-diisopropylethylamine (0.5 g, 3.87 mmol) in CH_2Cl_2 (5 mL) under magnetic stirring at 0°C. After stirring overnight at room temperature, the mixture was washed with H_2O (30 mL x 5). The organic phase was separated and the aqueous phase was extracted with CH_2Cl_2. The organic phase was collected, dried over sodium sulfate and evaporated under reduced pressure. The residue was purified by column chromatography on silica gel eluting with CH_2Cl_2/MeOH/NH_3 75:20:5 to yield 1.4 g (62%) of **20** as a white hygroscopic solid.

R_f (CH_2Cl_2/MeOH 20:1) = 0.2

^{1}H-RMN (400 MHz, $CDCl_3$, 298 K) δ_H (ppm): 8.42 (s, 3H, $HC_{aromatiq}$), 3.81 - 3.64 (m, 14H, C$H_{2\,EG}$), 3.40-3.34 (m, 2H, C$H_{2\,EG}$).

^{13}C NMR (101 MHz, $CDCl_3$, 298 K) δ_H (ppm): 166.3 (C=O), 135.6 ($C_{aromatiq}$), 128.8 ($CH_{aromatiq}$), 71.0 (3 x $CH_{2\,EG}$), 70.7 ($CH_{2\,EG}$), 70.4 ($CH_{2\,EG}$), 70.1 ($CH_{2\,EG}$), 51.0 ($CH_{2\,EG}$), 40.6 ($CH_{2\,EG}$).

MS (ESI): m/z (I %): 833.4 $[M+Na]^+$ (100%), 811.4 $[M+H]^+$ (88%).

4.3.16 Compound **21**

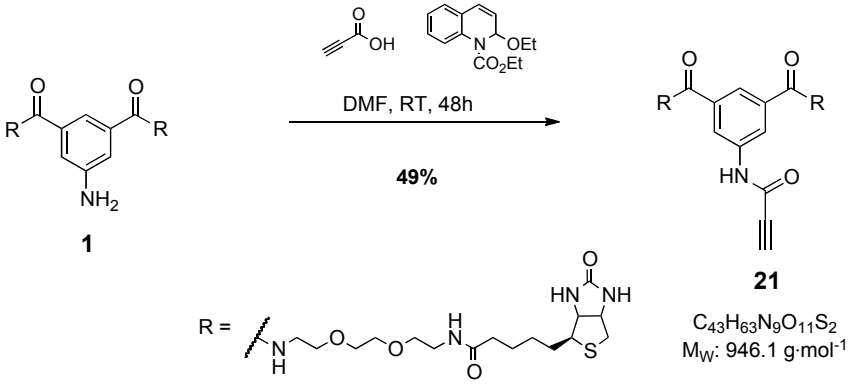

To a solution of **1** (356 mg, 0.398 mmol) in DMF (1,0 mL), propiolic acid (85.8 mg, 1.20 mmol) and EEDQ (320 mg, 1.3 mmol) dissolved in DMF (0.5 mL) were added. The mixture was left under magnetic stirring at room temperature for 2 days before removing the volatiles under reduced pressure. The residue was purified by column chromatography on silica gel eluting with CH_2Cl_2/MeOH/$NH_{3(aq.)}$ 15:4:1 to yield 184 mg (49%) of **21** as a white waxy solid.

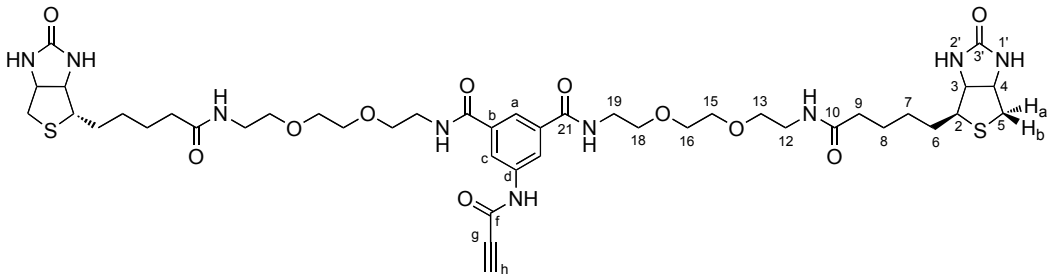

R_f (CH_2Cl_2/MeOH/$NH_{3\ (aq.)}$ 15:4:1) = 0.35

^{1}H-RMN (400 MHz, CD_3OD, 298 K): δ_H (ppm) = 8.05 (d, ^mJ=1.5 Hz, 2H, H_c), 7.92 (t, ^mJ=1.5 Hz, 1H, H_a), 4.50 (dd, ^3J(4-3)=7.9 Hz, ^3J(4-5_A)=5.0 Hz, 2H, H_4), 4.30 (dd, ^3J(3-4)=7.9 Hz, ^3J(3-2)=4.4Hz, 2H, H_3), 3.83 (s, 1H, H_h), 3.71-3.62 (m, 12H, $CH_{2(EG)}$, H_{18} & H_{15} & H_{16}), 3.60 (t,^3J=5.4, 8H, $CH_{2(EG)}$, H_{19}), 3.56 (t, ^3J=5.5, 4H, $CH_{2(EG)}$, H_{13}), 3.36 (t, 4H,^3J=5.4 Hz, $CH_{2(EG)}$, H_{12}), 3.19 (m, ^3J(2-3)=4.4 Hz, 2H, H_2), 2.93 (dd, ^3J(5_A-

5_B)=12.7, $^3J(5_A\text{-}4)$=5.0, 2H, H_{5_A}), 2.71 (d, $^3J(5_A\text{-}5_B)$=12.7 Hz, 2H, H_{5_B}), 2.19 (t, ^3J(9-8)=7.4 Hz, 4H, H_9), 1.67 (m, 8H, H_8 & H_6), 1.42 (m, 4H, H_7).

MS (ESI): m/z (I %): 968.4 $[M+Na^+]^+$ (100%), 946.4 $[M+H^+]^+$ (32%)

4.3.17 BBA_3-2 (**13**)

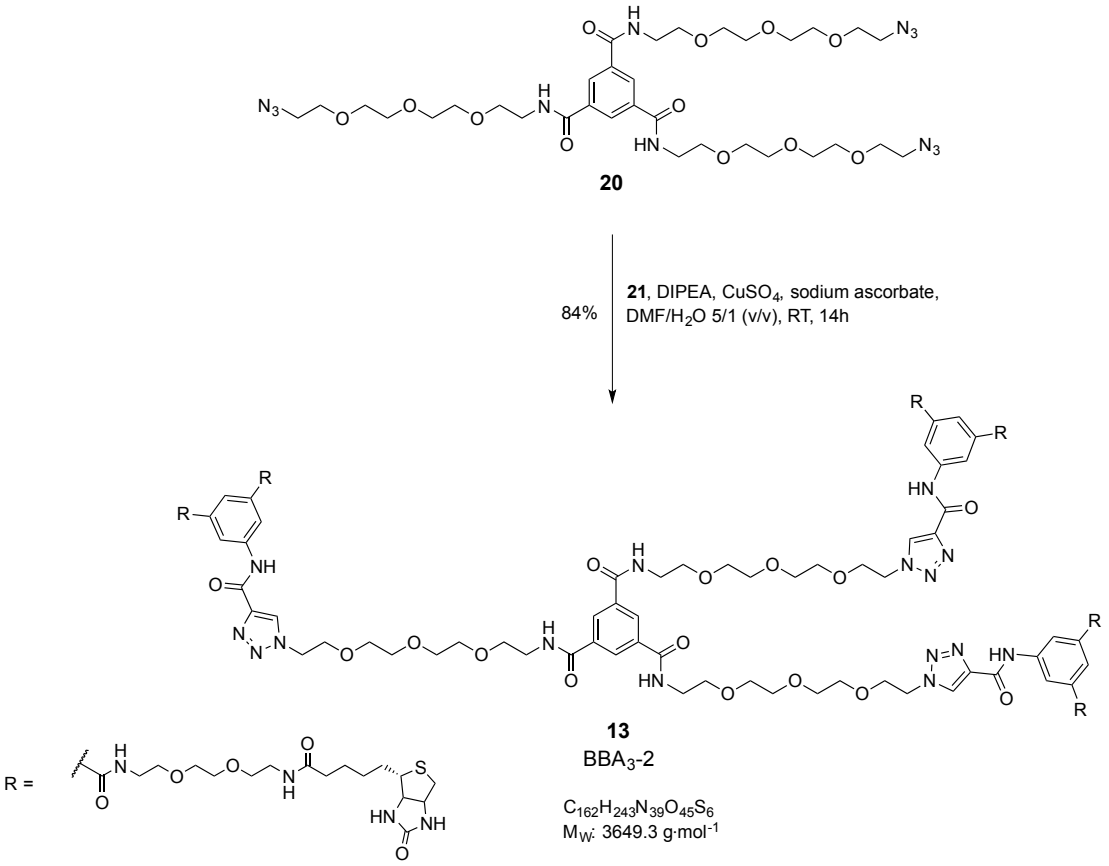

In a 5 mL round bottom flask under N_2 atmosphere, triazide (9.7 mg, 0.012 mmol), alcyne (41 mg, 0.043 mmol) and DIPEA (13 mg, 0.10 mmol) were dissolved in DMF (0.8 mL). A solution of $CuSO_4$ (1.2 mg, 7.2 mmol) and sodium ascorbate (2.9 mg, 14 mmol) in H_2O (0.2 mL) was added and the mixture was stirred at room temperature overnight. The solvent was removed under reduced pressure and the residue was purified by column chromatography on SiO2 eluting with CH_2Cl_2/MeOH/$NH_{3\ (aq.)}$ 75:20:1 to yield 37 mg (84%) of BBA_3-2 (**13**) as a brown waxy solid.

R_f (CH_2Cl_2/MeOH/$NH_{3\ (aq.)}$ 15:4:1) = 0.25

^{1}H NMR (400 MHz, methanol-d_4): 8.39 (s, 1H, $HC_{aromatiq}$), 8.24 (s, 1H, $HC_{triazole}$), 8.22 (d, 2H, $HC_{aromatiq}$, H_b), 8.07 (t, 1H, $NHC_{aromatiq}$), 7.98 (t, 1H, $HC_{aromatiq}$, H_a), 4.51 (t, 2H, O=CN*H*), 4.37 (dd, 2H, H_4), 4.18 (dd, 2H, H_3), 3.79 (t, 3H, O=CN*H*), 3.75–3.40 (m, 30 H, $CH_{2\,EG}$), 3.38-3.32 (m, 6H, $CH_{2\,EG}$,), 3.04–3.00 (m, 2H, H_2), 2.78 (dd, 2H, H_{5_A}), 2.61 (d, 2H, H_{5_B}), 2.05 (t, 4H, 7.2 Hz), 1.54–1.44 (m, 8H, H_8 & H_6), 1.30-1.25 (m, 4H, H_7).

MS (ESI): m/z (I %): 1239.2 $[M+3Na^+]^{3+}$ (100%), 1847.3 $[M+2Na^+]^{2+}$ (32%)

4.3.18 BBA-S-S-BBA (**4**)

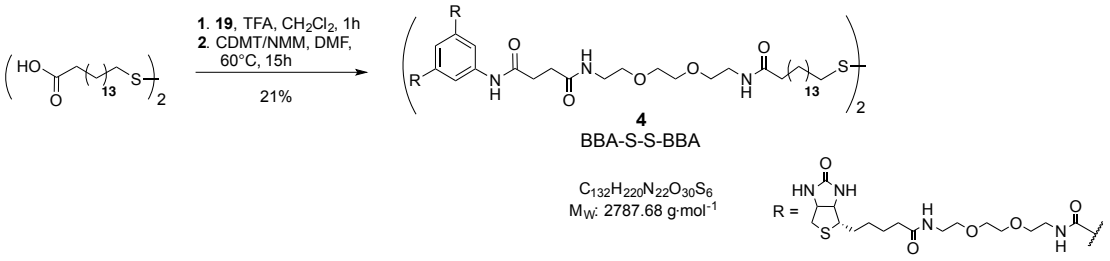

In a 5 mL round bottom flask, **19** (0.130 g, $0.11\cdot10^{-3}$ mol, 3.3 eq.) was dissolved in TFA (0.253 mL, $3.31\cdot10^{-3}$ mol, 30 eq.) and the inner wall of the flask was rinsed with CH_2Cl_2 (1 mL). The solution was stirred at room temperature during 1h and the TFA was evaporated under reduced pressure. To a solution of 16-carboxyhexadecyl disulfide (0.019 g, $33.3\cdot10^{-6}$ mol, 1 eq.) in DMF (3 mL), CDMT (0.012 g, $70\cdot10^{-6}$ mol, 2.1 eq) and NMM (8 µL, $70\cdot10^{-6}$ mol, 2.1 eq) were added. After stirring during 1h, the solution was added dropwise to a solution of the deprotected amine and NMM (13 µL, $0.11\cdot10^{-3}$ mol, 3.3 eq.) in DMF (3 mL). The orange solution was stirred during 15h at 60°C and the volatiles were evaporated under reduced pressure. The residue was purified by chromatography on silicagel eluting with CH_2Cl_2/MeOH/$NH_{3\,(aq.)}$ 75:20:1 to yield 0,016 g (17%) of BBA-S-S-BBA (**4**) as a brown solid.

R_f (CH_2Cl_2/MeOH/$NH_{3\,(aq.)}$ 15:4:1) = 0.34

^{1}H NMR (400 MHz, MeOH-d_4) δ = 10.02 (bs, 1H, O=CN*H*), 8.10 (bs, 1H, O=CN*H*), 8.11 (d, 2H, C*H*$_{aromatic}$, H_c), 7.98 (t, 1H, C*H*$_{aromatic}$, H_a), 7.48 (t, 1H, O=CN*H*), 6.99 (t, 1H, O=CN*H*), 6.29 (bs, 2H, O=CN*H*), 5.90 (bs, 2H, O=CN*H*), 4.46 (dd, 2H, H_4), 4.26 (dd, 2H, H_3), 3.65–3.47 (m, 30H, C$H_{2\ EG}$), 3.38-3.35 (m, 6H, C$H_{2\ EG}$), 3.10-3.03 (m, 2H, H_2), 2.83 (dd, 2H, H_{5_A}), 2.70-2.61 (m, 6H, SCH_2C$_{aliphatic}$, O=CCH$_2$CH_2C=O and H_{5_B}), 2.55 (m, 2H, O=CCH$_2$CH_2C=O), 2.15-2.05 (m, 6H, HNO=CCH_2C$_{aliphatic}$, H_9), 1.65-1.45 (m, 12H, H_6 and H_8), 1.47-1.33 (m, 28H, H_7 and 11 x C$H_{2\ aliphatic}$)

MS (ESI): m/z (I %): 951.9 $[M+3Na^+]^{3+}$ (100%), 1416.2 $[M+2Na^+]^{2+}$ (55%), 719.9 $[M+4Na^+]^{4+}$ (45%)

Appendices

APPENDIX 1

1) RP-HPLC analysis from crude reaction mixture and RP-HPLC/ESI-MS analysis from coumpound **9**

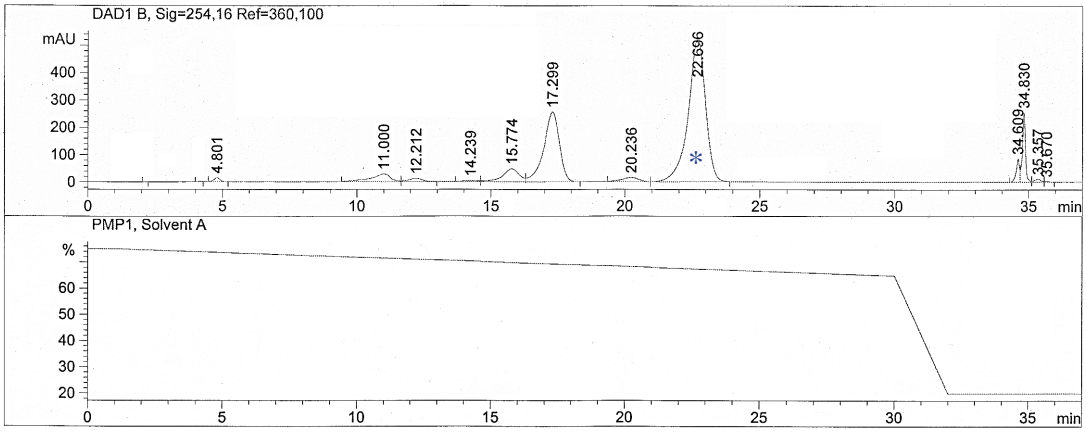

Figure 1 RP-HPLC chromatogram from reaction mixture of compound **9** (*) at 254 nm using a linear gradient elution system of ACN:H_2O 25:75 → 35:65 (flow=0.7 mL/min).

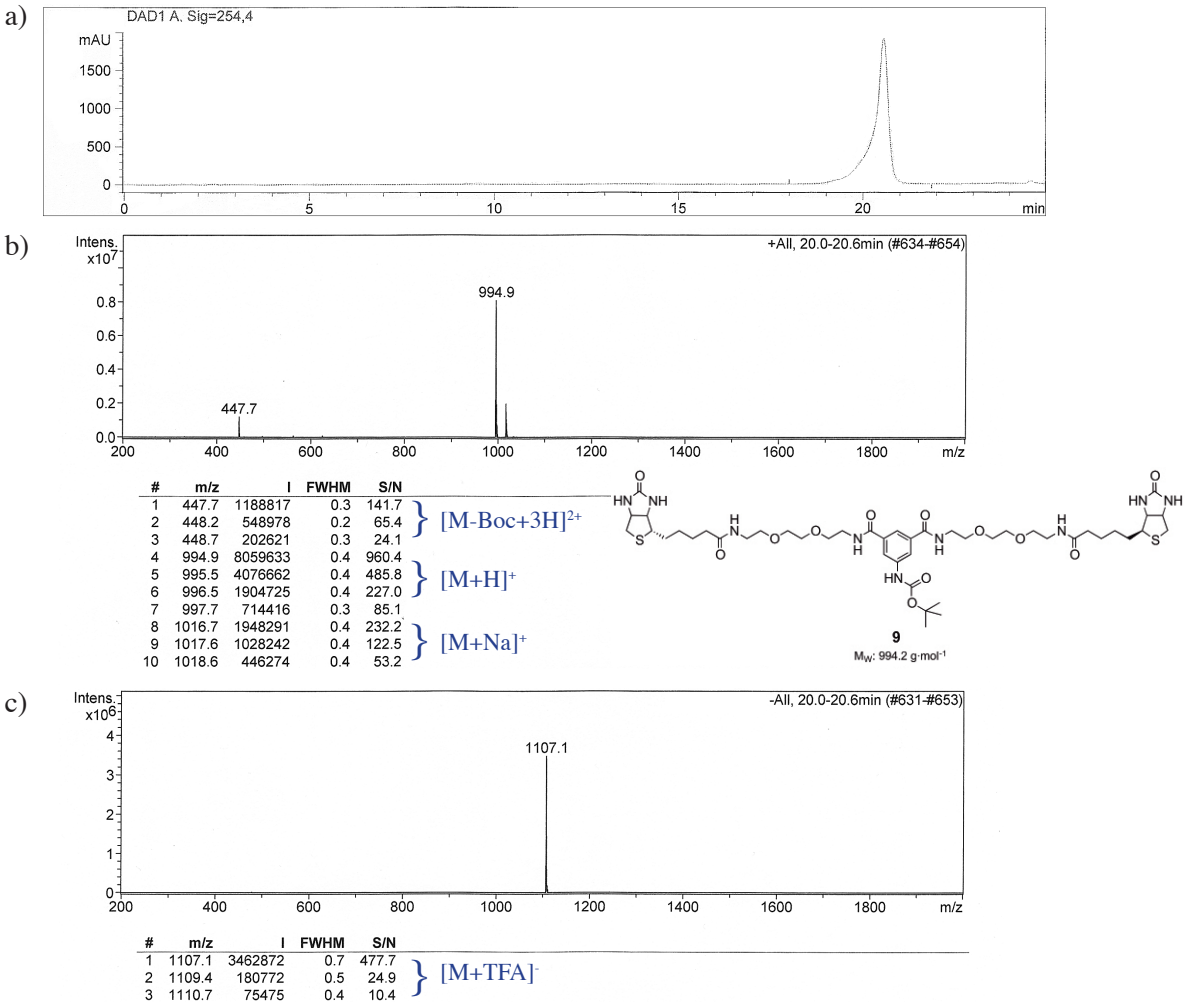

Figure 2 HPLC / ESI-MS analysis of pure compound **9** using a linear gradient elution system of ACN:H_2O (0.1% TFA) 20:80 → 35:65 (flow=0.4 mL/min) a) HPLC UV-Vis trace. b) mass spectrum (R_t: 20.5 min) recorded in b) positive and c) negative mode.

2) RP-HPLC/ ESI-MS analysis from crude reaction mixture of BBA_3-1 (**3**)

Divergent Synthetic Route

a)

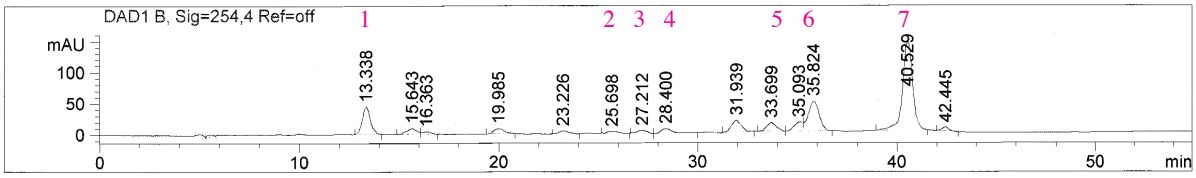

b)

Acquisition Parameter

Ion Source Type	ESI	Ion Polarity	Positive	Alternating Ion Polarity	off
Mass Range Mode	Std/Normal	Scan Begin	500 m/z	Scan End	3000 m/z
Capillary Exit	161.5 Volt	Skim 1	40.0 Volt	Trap Drive	116.6
Accumulation Time	44074 µs	Averages	5 Spectra	Auto MS/MS	off

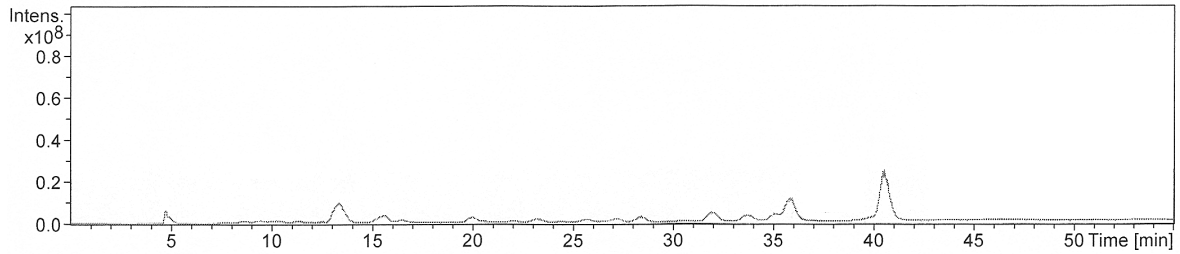

Figure 3 HPLC / ESI-MS analysis of reaction mixture of BBA3-1 (**3**) using a linear gradient elution system of MeOH:H_2O (0.1% TFA) 40:60 → 60:40 in 30 min (flow=0.5 mL/min) a) HPLC UV-Vis trace. b) mass spectrum recorded in positive and mode.

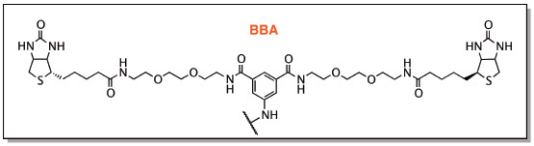

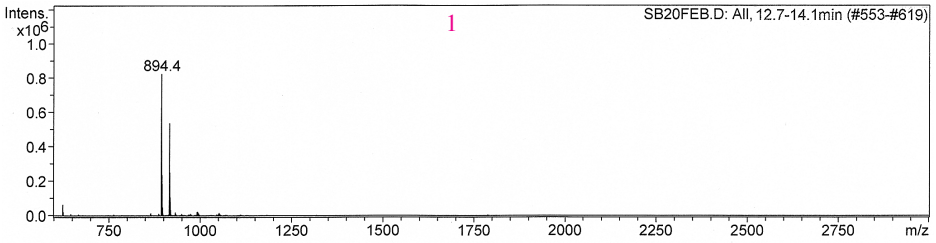

#	m/z	I	FWHM	S/N
1	625.3	62544	0.4	111.8
2	894.4	822251	0.4	1470.1
3	895.3	375564	0.4	671.5
4	896.3	181658	0.4	324.8
5	897.3	50633	0.4	90.5
6	916.3	535364	0.4	957.2
7	917.2	247842	0.4	443.1
8	918.2	105378	0.4	188.4
9	919.3	31509	0.4	56.3
10	994.1	21107	0.4	37.7

BBA-H

Mw : 894.1 g mol^{-1}

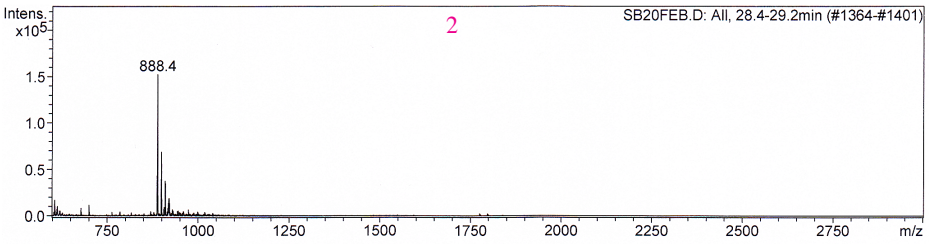

#	m/z	I	FWHM	S/N
1	888.4	152195	0.3	577.6
2	888.8	146840	0.2	557.3
3	889.3	100170	0.2	380.2
4	889.8	44100	0.2	167.4
5	899.3	64497	0.3	244.8
6	899.8	68723	0.2	260.8
7	900.3	38129	0.2	144.7
8	910.3	37427	0.3	142.0
9	910.8	35517	0.2	134.8
10	911.3	25159	0.3	95.5

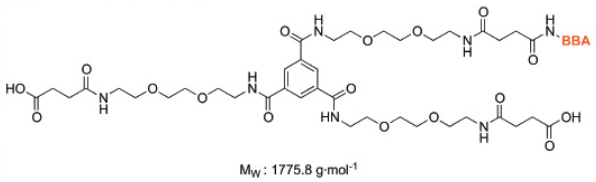

M_W : 1775.8 g·mol^{-1}

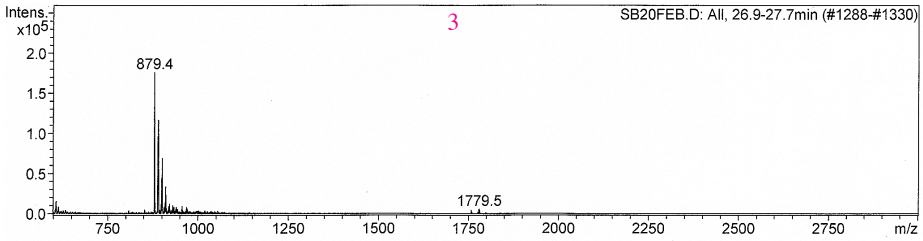

#	m/z	I	FWHM	S/N
1	879.4	175843	0.3	475.5
2	879.8	166734	0.3	450.9
3	880.3	100573	0.2	272.0
4	888.9	96110	0.3	259.9
5	889.3	86361	0.3	233.5
6	890.3	116247	0.3	314.4
7	890.8	97059	0.2	262.5
8	891.3	55544	0.3	150.2
9	901.3	69199	0.3	187.1
10	901.8	62375	0.2	168.7

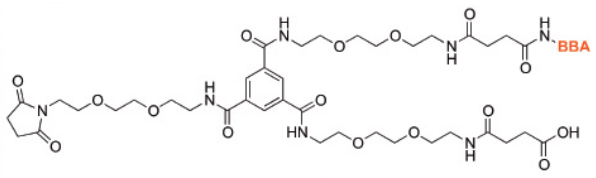

M_W : 1757.8 g·mol^{-1}

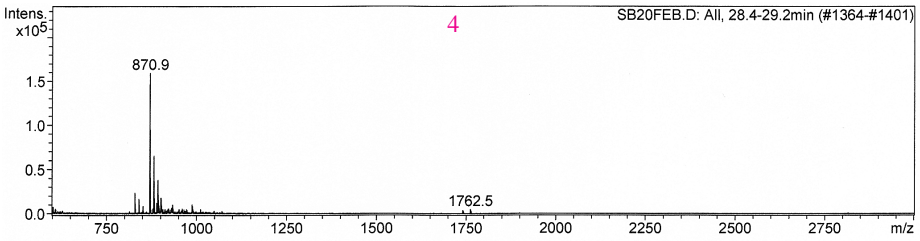

#	m/z	I	FWHM	S/N
1	829.9	23527	0.3	78.5
2	870.9	159205	0.3	531.3
3	871.3	156236	0.2	521.4
4	871.8	91300	0.2	304.7
5	872.3	40929	0.2	136.6
6	881.9	61414	0.3	204.9
7	882.3	65240	0.2	217.7
8	882.8	36808	0.2	122.8
9	892.8	37254	0.3	124.3
10	893.3	38292	0.2	127.8

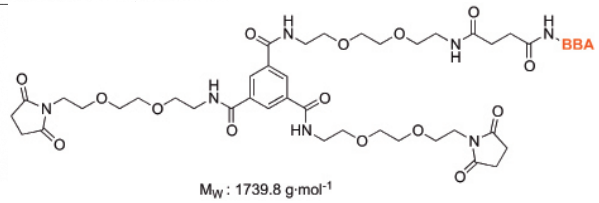

M_W : 1739.8 g·mol^{-1}

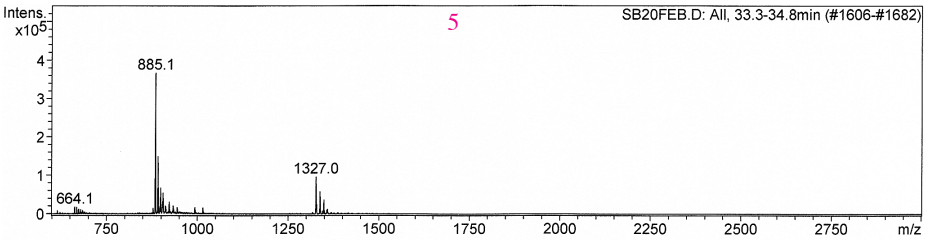

#	m/z	I	FWHM	S/N
1	885.1	366105	1.0	696.5
2	892.4	149046	1.0	283.6
3	899.7	67299	1.2	128.0
4	906.7	54289	0.2	103.3
5	907.0	52591	0.5	100.1
6	1326.5	70047	0.3	133.3
7	1327.0	95422	0.2	181.5
8	1327.4	73684	0.2	140.2
9	1327.9	48209	0.3	91.7
10	1338.0	57838	0.3	110.0

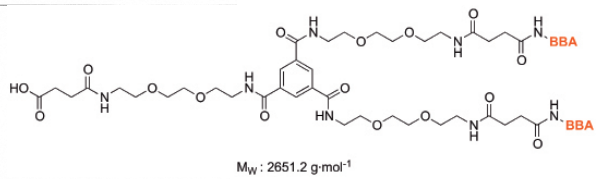

M_W : 2651.2 g·mol^{-1}

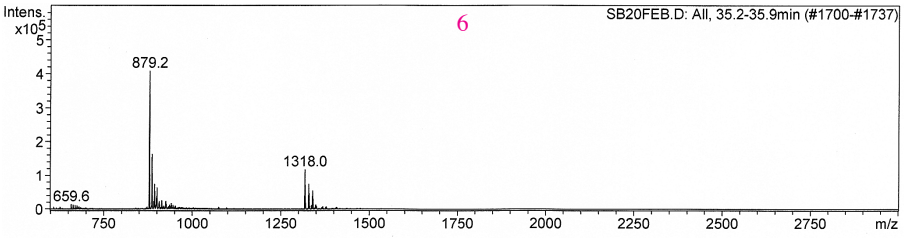

#	m/z	I	FWHM	S/N
1	879.2	407551	1.0	628.1
2	886.4	163044	1.1	251.3
3	893.7	74670	0.4	115.1
4	894.0	67811	0.2	104.5
5	1317.6	83897	0.3	129.3
6	1318.0	117277	0.2	180.8
7	1318.5	103576	0.2	159.6
8	1318.9	67255	0.2	103.7
9	1329.0	74783	0.2	115.3
10	1329.4	64248	0.3	99.0

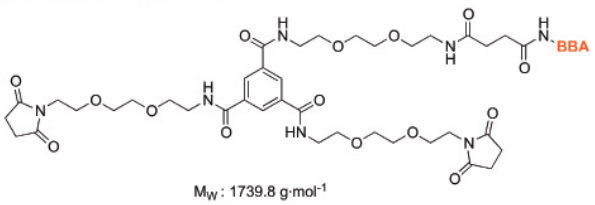

M_W : 1739.8 g·mol^{-1}

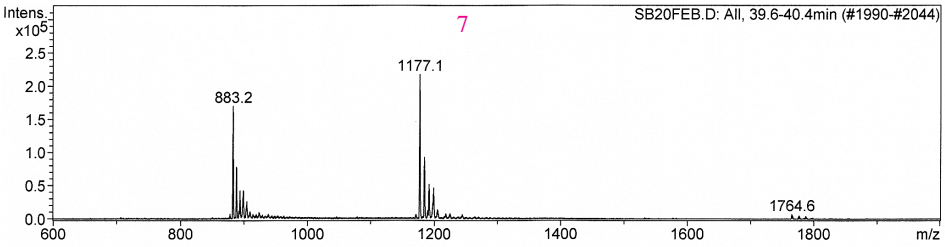

#	m/z	I	FWHM	S/N
1	883.2	170041	1.0	359.7
2	888.7	77964	1.1	164.9
3	894.2	42366	1.0	89.6
4	899.5	42283	0.8	89.4
5	1177.1	216964	1.2	458.9
6	1184.4	92532	1.3	195.7
7	1191.5	46253	0.3	97.8
8	1191.8	51793	0.8	109.6
9	1198.8	43741	0.4	92.5
10	1199.0	46562	0.2	98.5

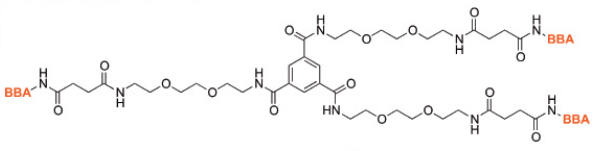

M_W : 3529.2 g·mol^{-1}

3

BBA_3-1

Convergent Synthetic Route

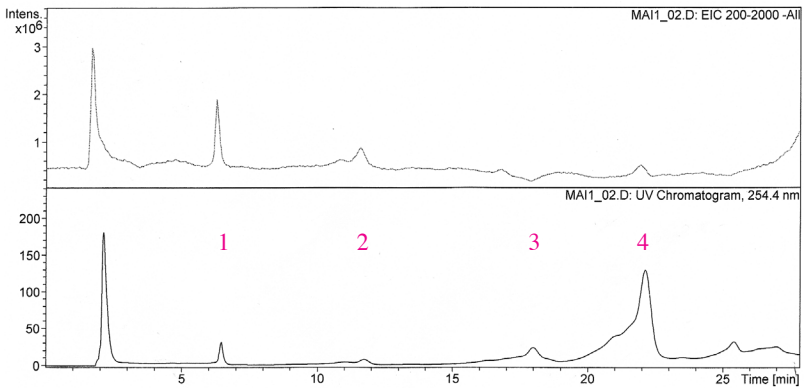

Figure 4 HPLC / ESI-MS analysis of reaction mixture of BBA3-1 (**3**) using a linear gradient elution system of MeOH:H_2O (0.1% TFA) 40:60 → 60:40 in 20 min (flow=0.5 mL/min). HPLC UV-Vis trace (254 nm) mass spectrum recorded in positive and mode.

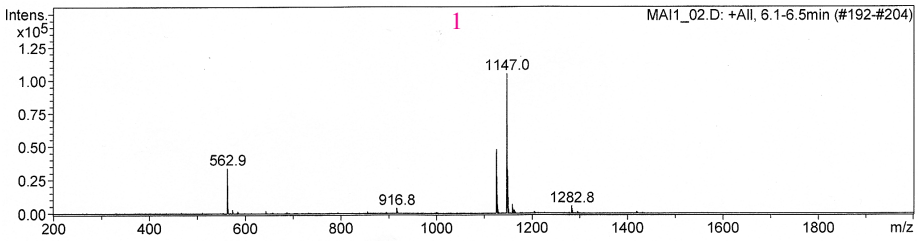

#	m/z	I	FWHM	S/N
1	562.9	33915	0.3	94.6
2	563.3	23075	0.2	64.4
3	563.7	9527	0.2	26.6
4	1125.0	47743	0.4	133.2
5	1125.9	27315	0.4	76.2
6	1126.9	13743	0.4	38.3
7	1147.0	105019	0.4	293.0
8	1147.7	66071	0.4	184.3
9	1148.7	31998	0.4	89.3
10	1149.8	11707	0.3	32.7

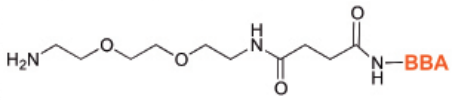

M_W: 1123.5 g·mol^{-1}

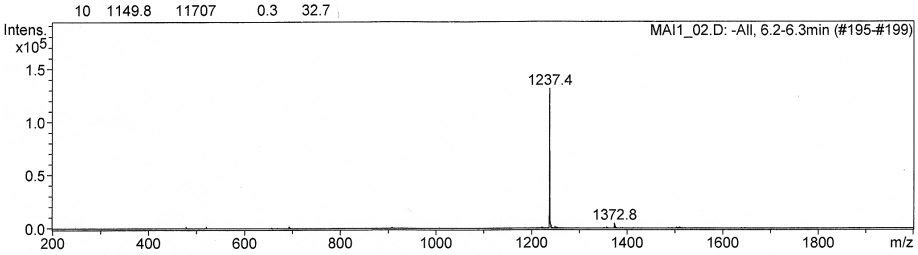

#	m/z	I	FWHM	S/N
1	1237.4	130861	0.8	144.0
2	1239.4	4568	0.5	5.0
3	1240.8	2810	0.4	3.1
4	1372.8	4596	0.4	5.1
5	1373.7	3161	0.4	3.5

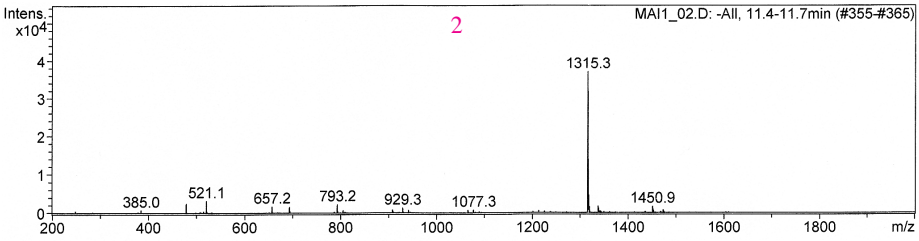

#	m/z	I	FWHM	S/N
1	479.1	2452	0.4	18.6
2	521.1	3198	0.4	24.3
3	657.2	1735	0.4	13.2
4	793.2	2257	0.4	17.2
5	1315.3	36964	0.8	281.0
6	1316.4	12295	0.4	93.5
7	1317.7	4615	0.4	35.1
8	1318.9	1593	0.3	12.1
9	1336.9	1769	0.4	13.4
10	1450.9	1699	0.4	12.9

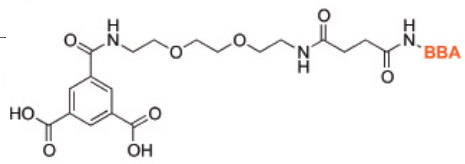

M_W : 1315.5 g·mol^{-1}

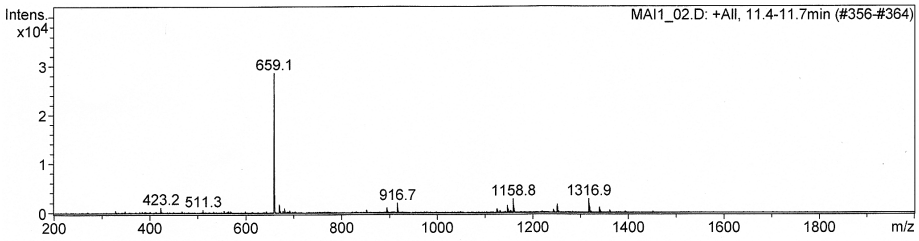

#	m/z	I	FWHM	S/N
1	659.1	28526	0.7	175.7
2	660.4	3613	0.3	22.3
3	669.9	1698	0.3	10.5
4	916.7	1918	0.4	11.8
5	1146.9	1458	0.4	9.0
6	1158.8	2745	0.4	16.9
7	1159.8	1556	0.3	9.6
8	1250.9	1642	0.4	10.1
9	1316.9	2771	0.3	17.1
10	1317.8	1759	0.4	10.8

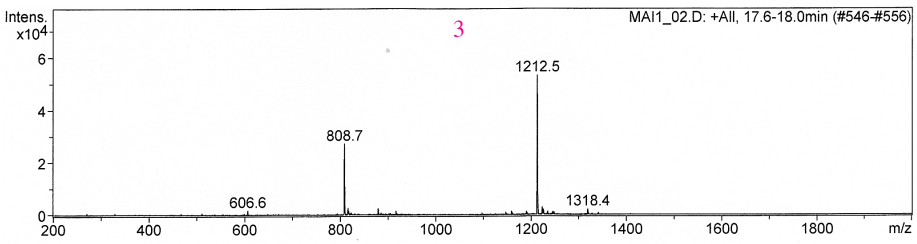

#	m/z	I	FWHM	S/N
1	808.7	27135	1.0	98.1
2	816.3	2620	0.4	9.5
3	879.4	2383	0.5	8.6
4	879.7	2082	0.3	7.5
5	1212.5	53080	1.0	191.9
6	1214.2	3744	0.3	13.5
7	1223.3	2879	0.3	10.4
8	1223.8	2183	0.3	7.9
9	1318.4	2079	0.3	7.5
10	1318.9	2056	0.2	7.4

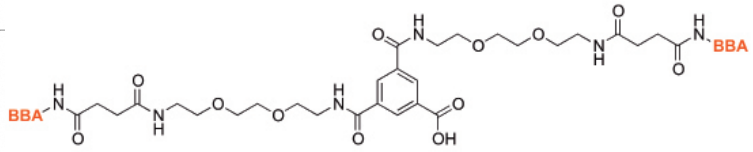

M_W : 2421.1 g·mol^{-1}

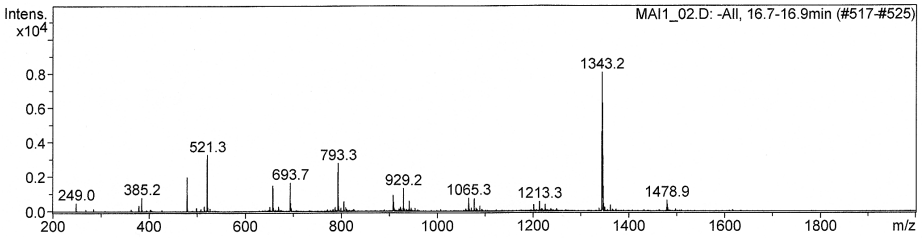

#	m/z	I	FWHM	S/N
1	479.3	1958	0.4	10.3
2	521.3	3261	0.4	17.2
3	657.4	1471	0.4	7.8
4	693.7	1637	0.4	8.6
5	793.3	2760	0.4	14.6
6	929.2	1305	0.4	6.9
7	1343.2	8043	0.4	42.5
8	1343.8	6257	0.4	33.0
9	1344.8	3567	0.4	18.8

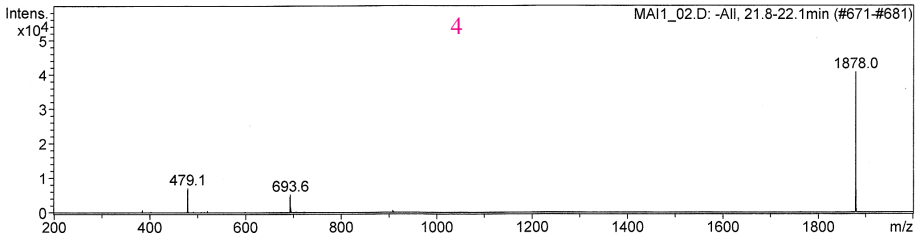

#	m/z	I	FWHM	S/N
1	479.1	6999	0.4	7.0
2	693.6	5133	0.5	5.1
3	694.5	1511	0.4	1.5
4	1878.0	40644	0.5	40.5

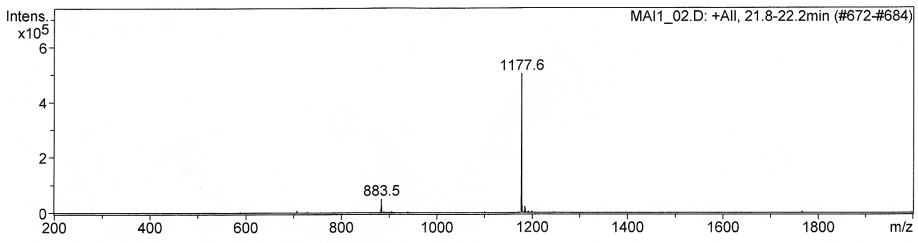

#	m/z	I	FWHM	S/N
1	883.5	49102	0.9	55.7
2	1177.6	501397	0.7	569.2
3	1184.6	21475	1.1	24.4
4	1184.7	20778	1.1	23.6

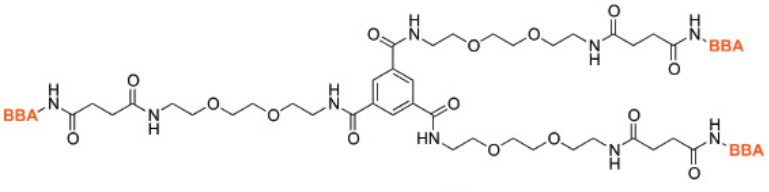

M_W : 3529.2 g·mol^{-1}

3

BBA_3-1

3) 2D NMR spectrum of BBA-S-S-BBA (**3**)

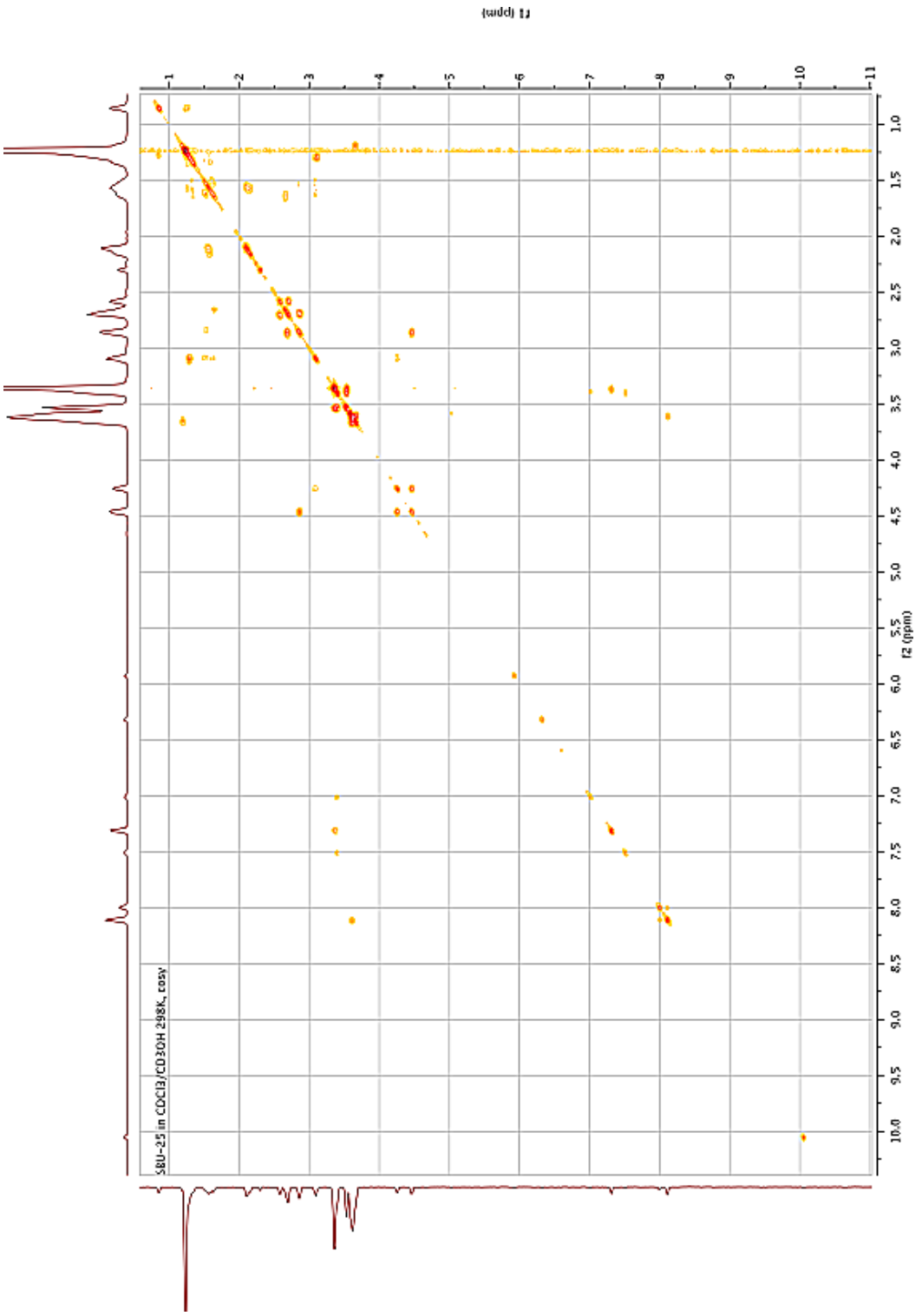

^{1}H-^{1}H COSY spectrum of BBA-S-S-BBA (**3**)

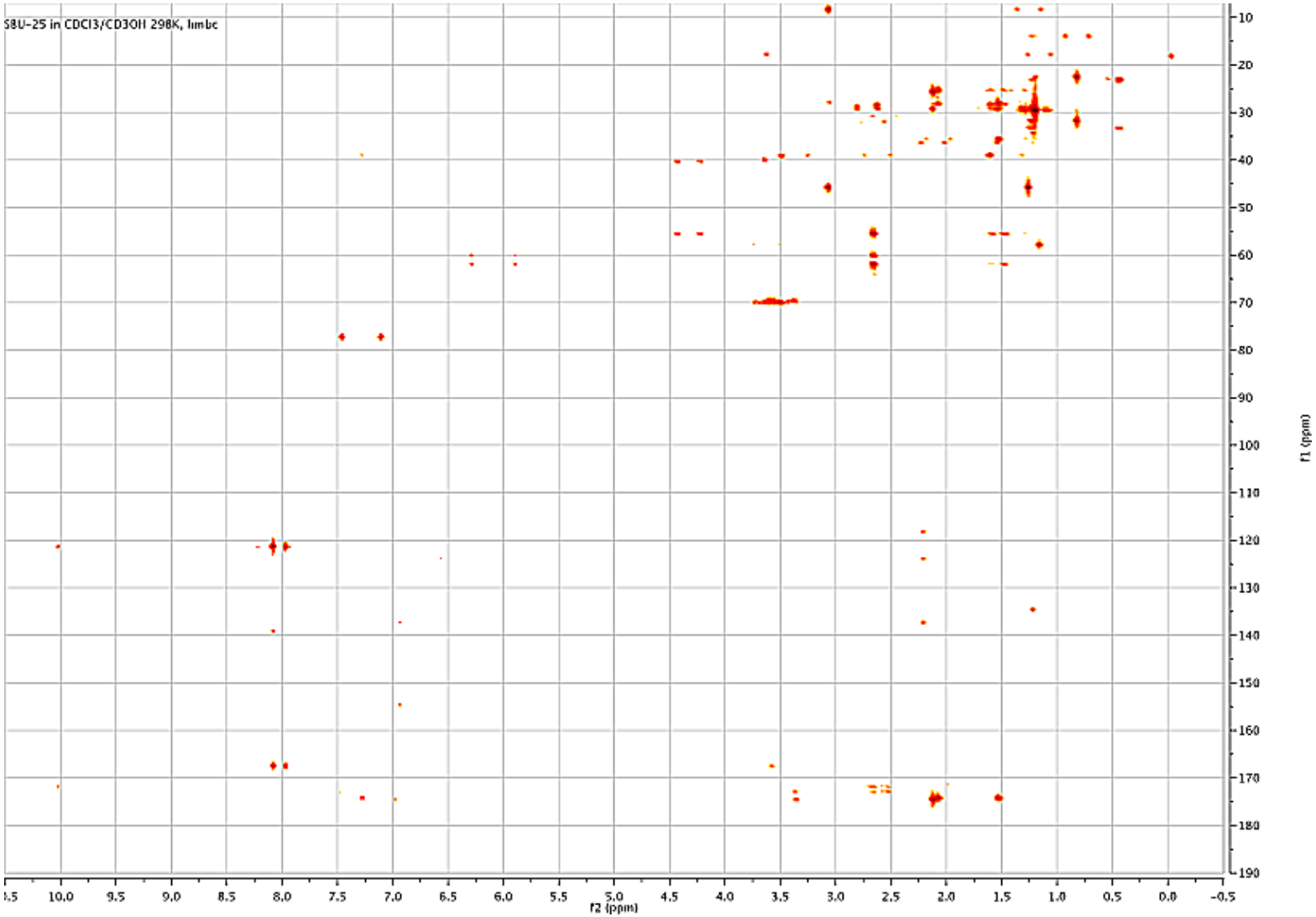

^{1}H-^{13}C HMBC spectrum of BBA-S-S-BBA (**3**)

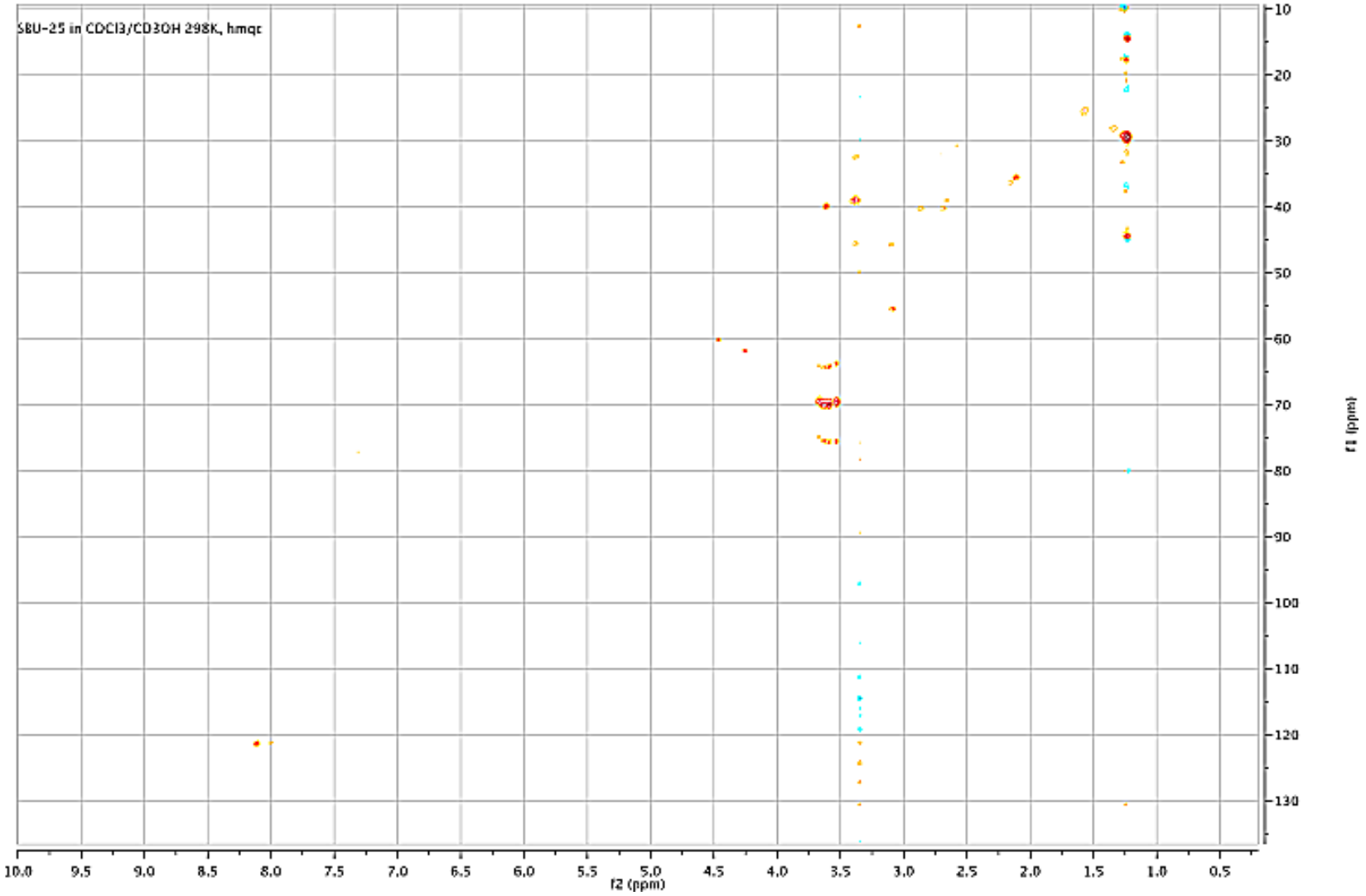

^{1}H-^{13}C HMQC spectrum of BBA-S-S-BBA (**3**)

4) NMR and ESI-MS spectrum of intermediates

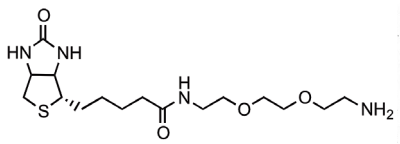

6

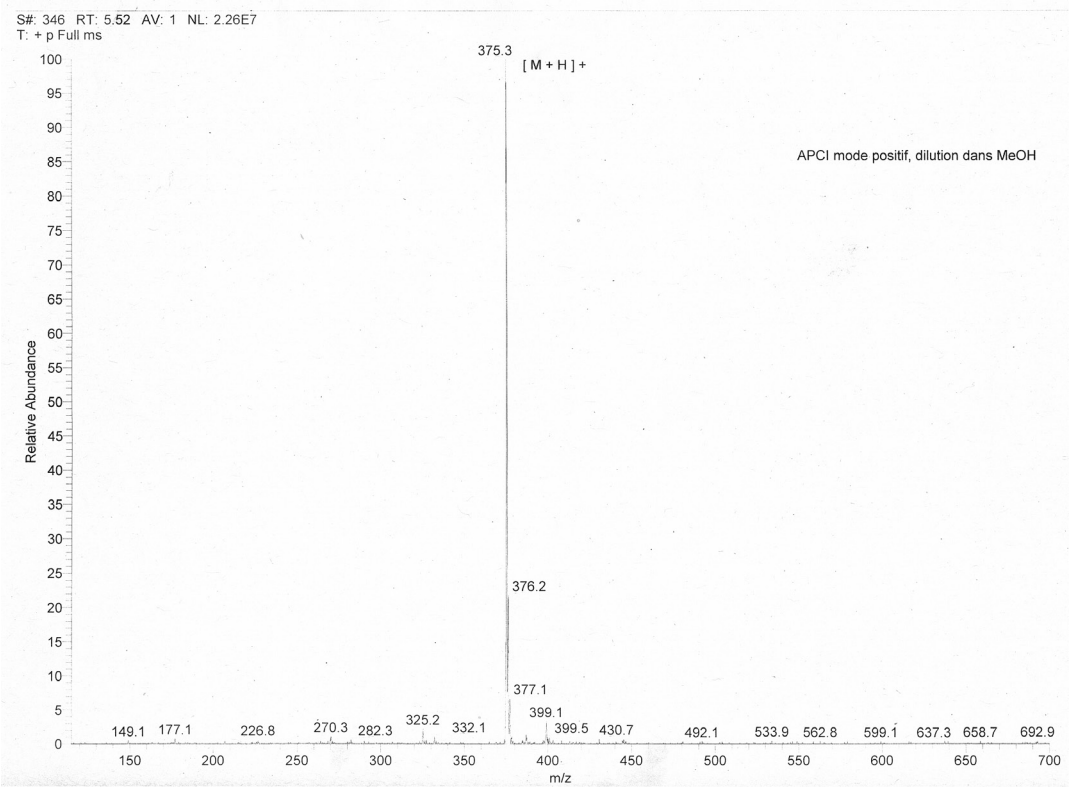
S#: 346 RT: 5.52 AV: 1 NL: 2.26E7
T: + p Full ms
375.3
[M + H] +
APCI mode positif, dilution dans MeOH
Relative Abundance
376.2
377.1
399.1
149.1 177.1 226.8 270.3 282.3 325.2 332.1 399.5 430.7 492.1 533.9 562.8 599.1 637.3 658.7 692.9
m/z

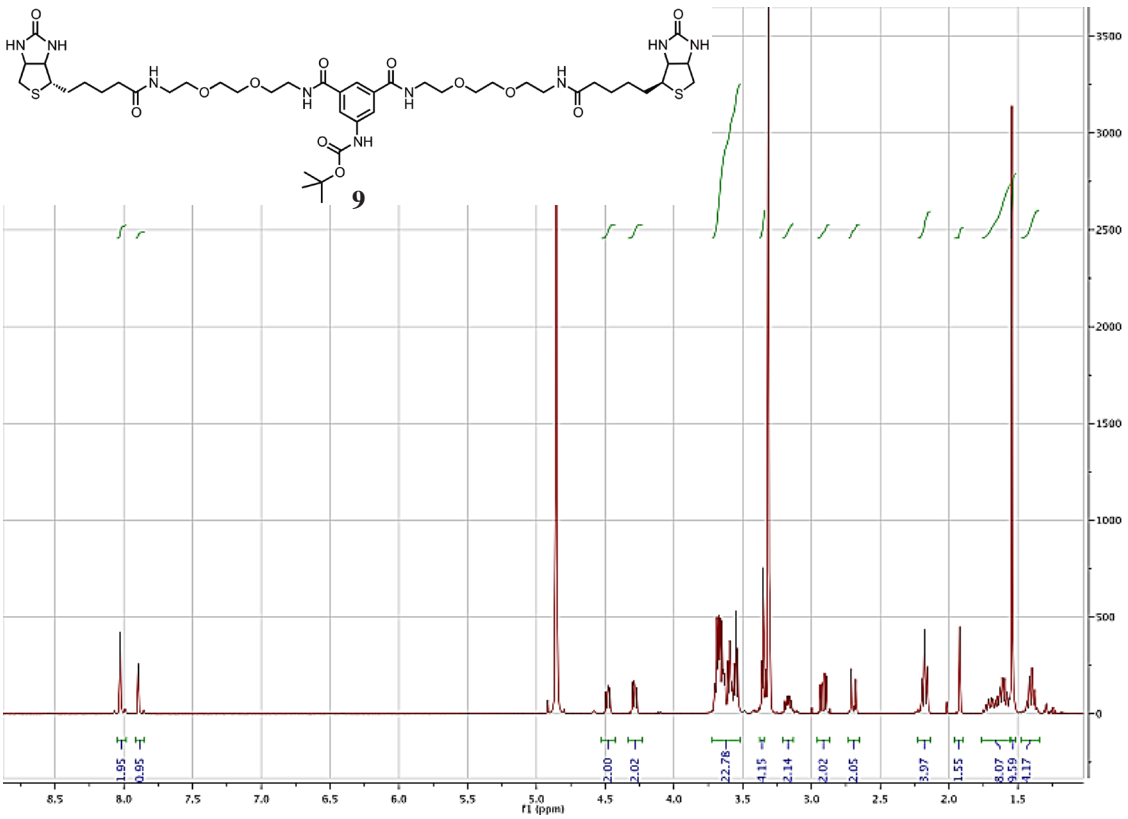
9
f1 (ppm)

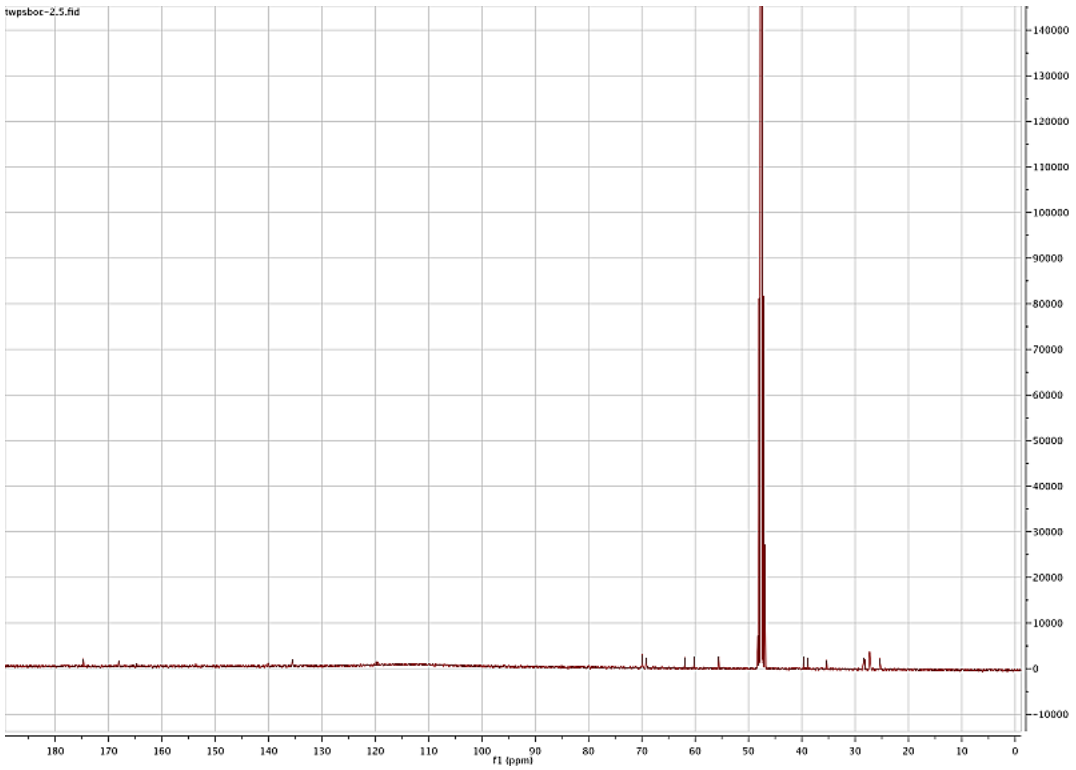

Acquisition Parameter

Ion Source Type	ESI	Ion Polarity	Positive	Alternating Ion Polarity	off
Mass Range Mode	Std/Normal	Scan Begin	50 m/z	Scan End	1200 m/z
Capillary Exit	165.6 Volt	Skim 1	40.0 Volt	Trap Drive	90.2
Accumulation Time	153 µs	Averages	5 Spectra	Auto MS/MS	off

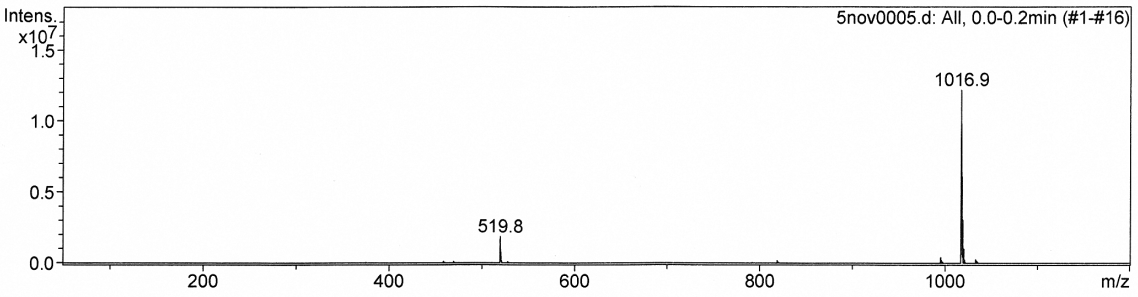

#	m/z	I	FWHM	S/N
1	519.8	1862050	0.3	217.0
2	520.2	948018	0.2	110.5
3	520.7	452613	0.2	52.8
4	994.8	402960	0.4	47.0
5	1016.9	12177938	0.4	1419.4
6	1017.5	6440710	0.4	750.7
7	1018.5	3063881	0.4	357.1
8	1019.7	1012642	0.4	118.0
9	1032.6	256932	0.4	29.9

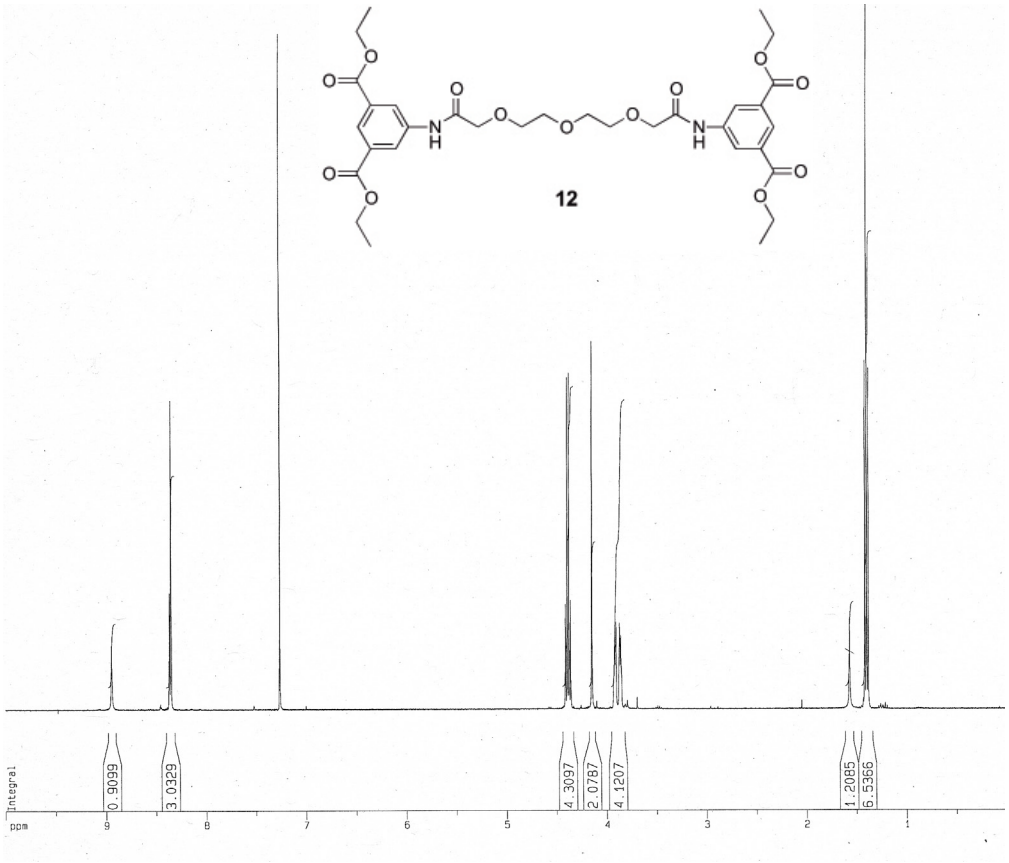
12
Integral
0.9099
3.0329
4.3097
2.0787
4.1207
1.2085
6.5366
ppm

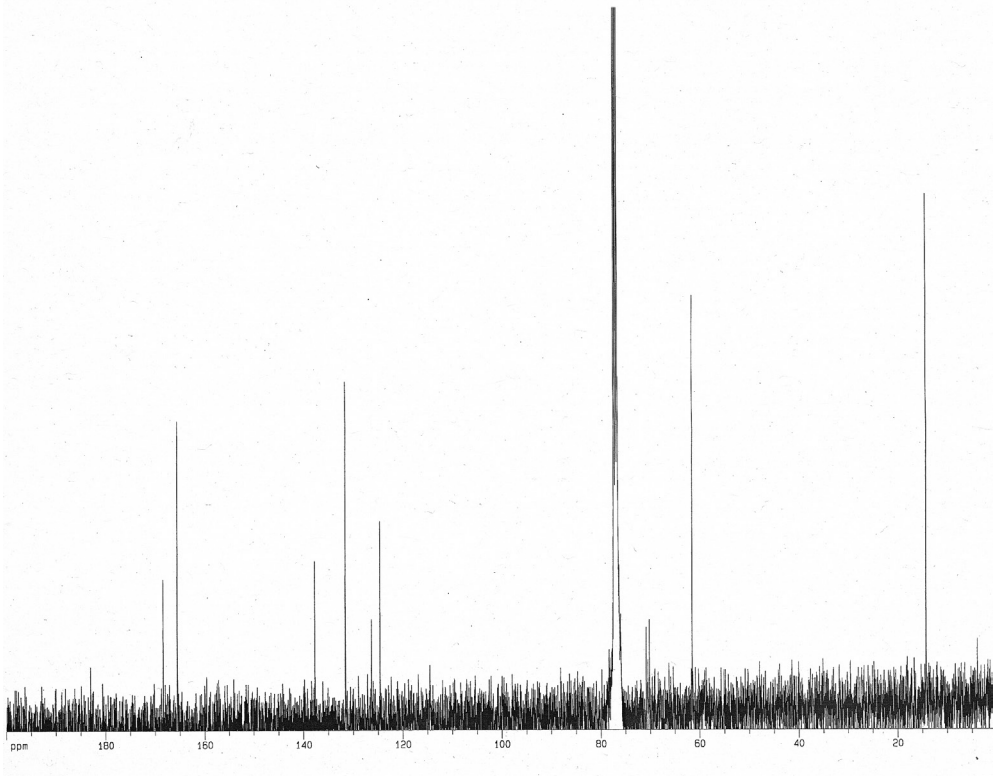
ppm

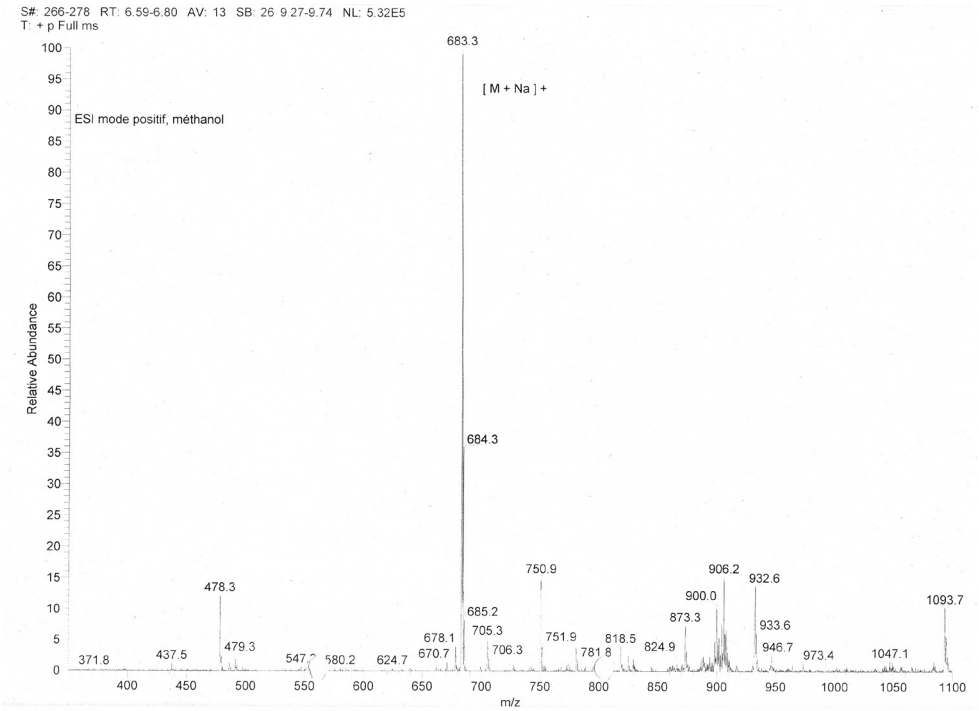
S#: 266-278 RT: 6.59-6.80 AV: 13 SB: 26 9.27-9.74 NL: 5.32E5
T: + p Full ms
ESI mode positif, méthanol
[M + Na] +
683.3
684.3
Relative Abundance
m/z

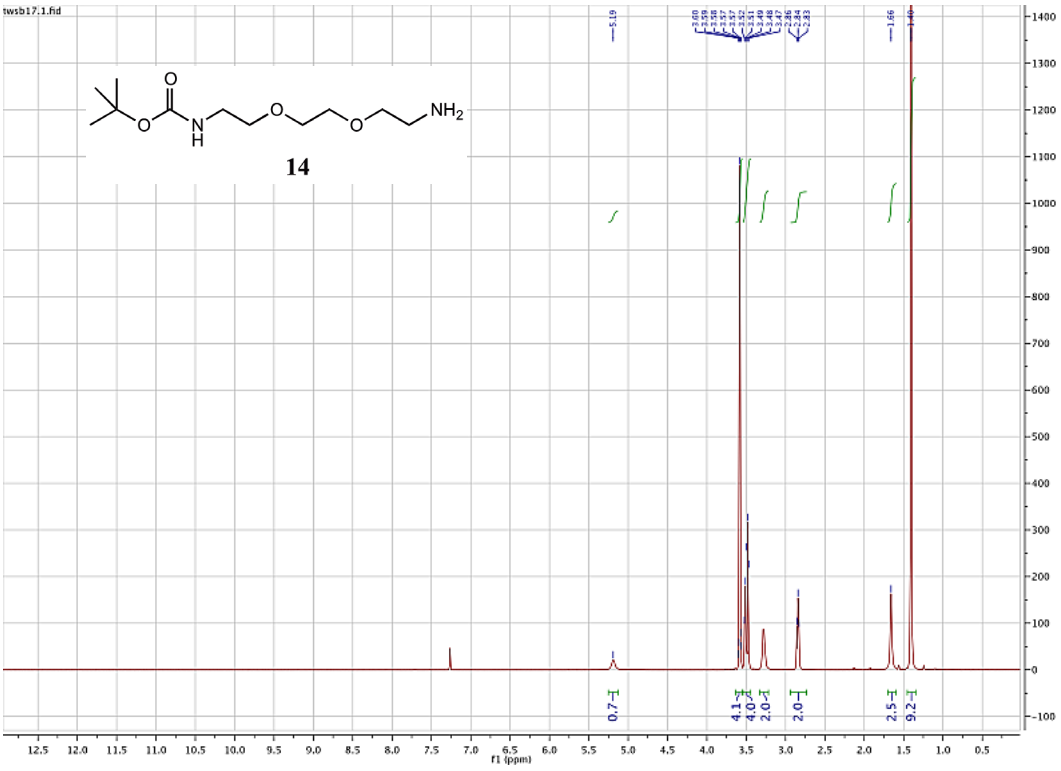
twsb17.1.fid
14
f1 (ppm)

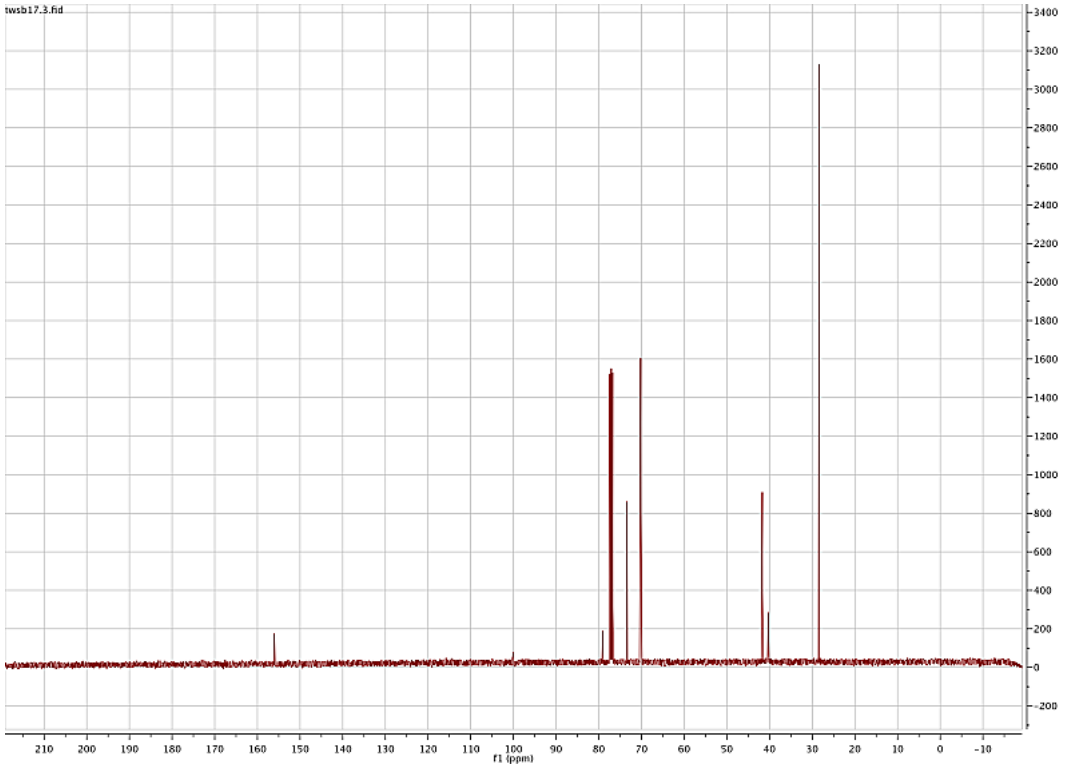

Acquisition Parameter

Ion Source Type	ESI	Ion Polarity	Positive	Alternating Ion Polarity	off
Mass Range Mode	Std/Normal	Scan Begin	100 m/z	Scan End	2800 m/z
Capillary Exit	112.3 Volt	Skim 1	40.0 Volt	Trap Drive	37.7
Accumulation Time	613 µs	Averages	5 Spectra	Auto MS/MS	off

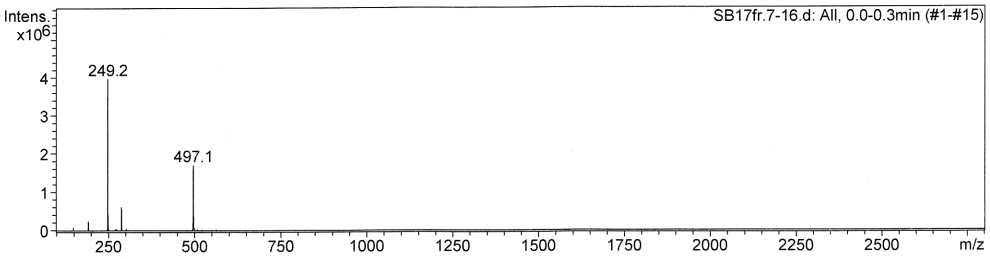

#	m/z	I	FWHM	S/N	
1	193.3	238146	0.4	86.9	
2	249.2	3957655	0.4	1444.1	$[M+H]^+$
3	249.9	412006	0.4	150.3	
4	289.2	609918	0.4	222.6	$[M+K]^+$
5	290.1	85675	0.3	31.3	
6	497.1	1701571	0.6	620.9	$[2M+H]^+$
7	497.9	377400	0.4	137.7	

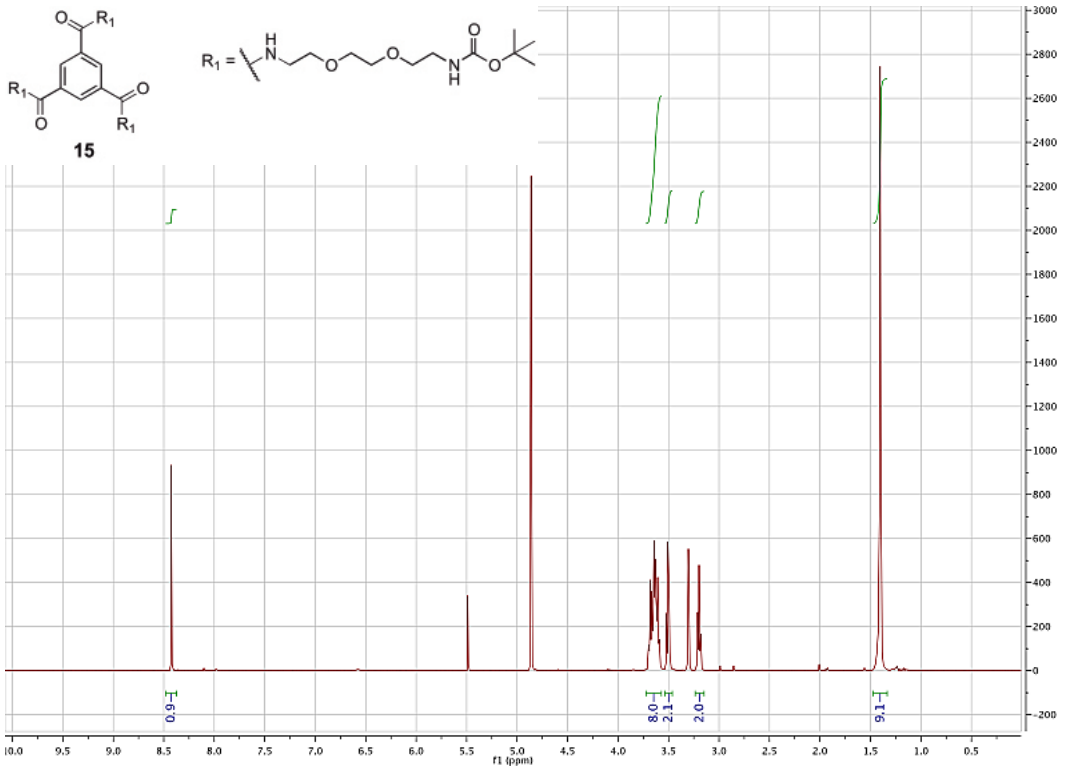
15
R1 =
0.9
8.0
2.1
2.0
9.1
f1 (ppm)

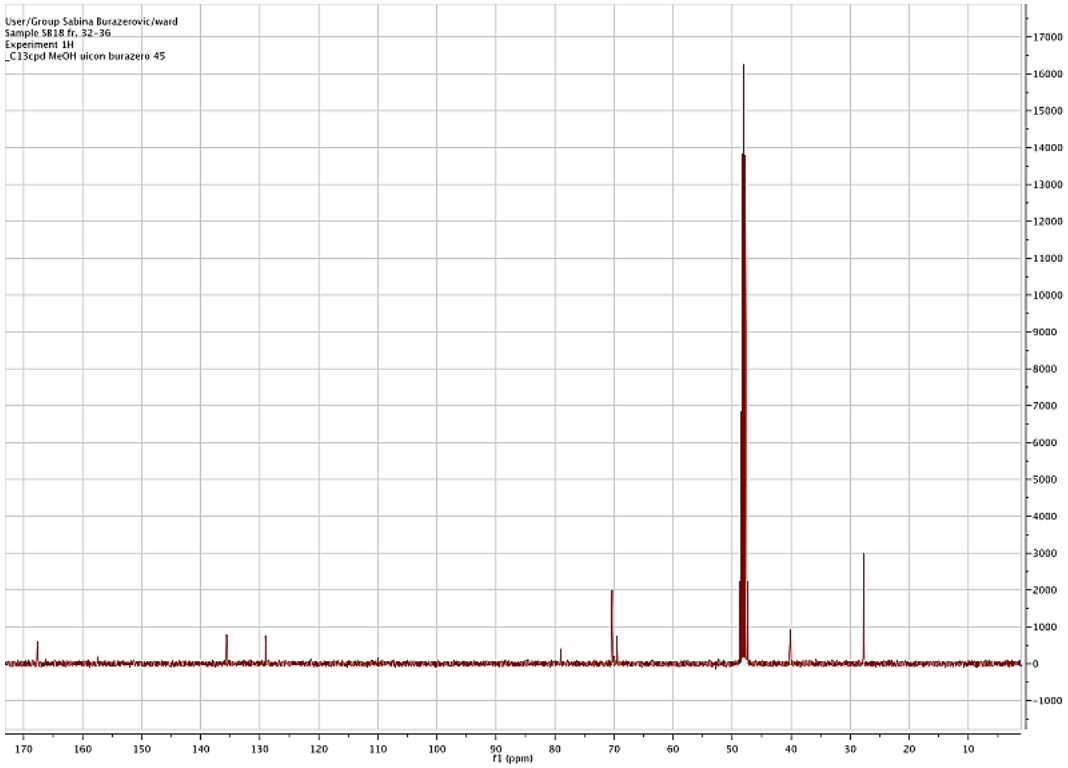
User/Group Sabina Burazerovic/ward
Sample SB18 fr. 32-36
Experiment 1H
_C13cpd MeOH uicon burazero 45
f1 (ppm)

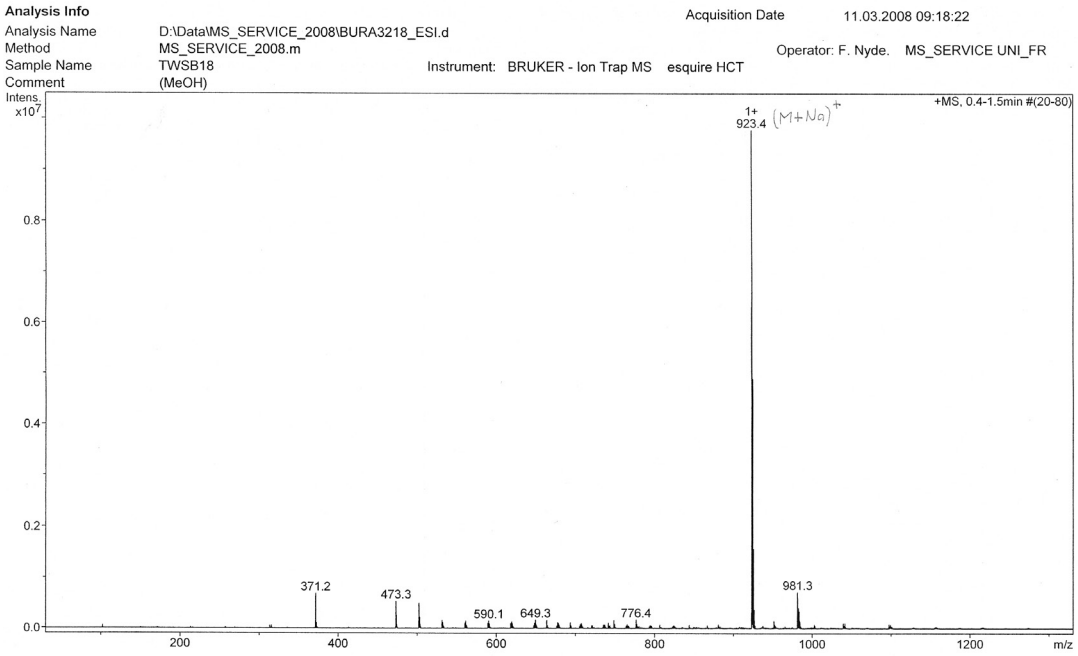
Analysis Info
Acquisition Date 11.03.2008 09:18:22
Analysis Name D:\Data\MS_SERVICE_2008\BURA3218_ESI.d
Method MS_SERVICE_2008.m
Operator: F. Nyde. MS_SERVICE UNI_FR
Sample Name TWSB18
Instrument: BRUKER - Ion Trap MS esquire HCT
Comment (MeOH)
Intens. x10^7
+MS, 0.4-1.5min #(20-80)
1+ 923.4 (M+Na)+
371.2
473.3
590.1
649.3
776.4
981.3
m/z

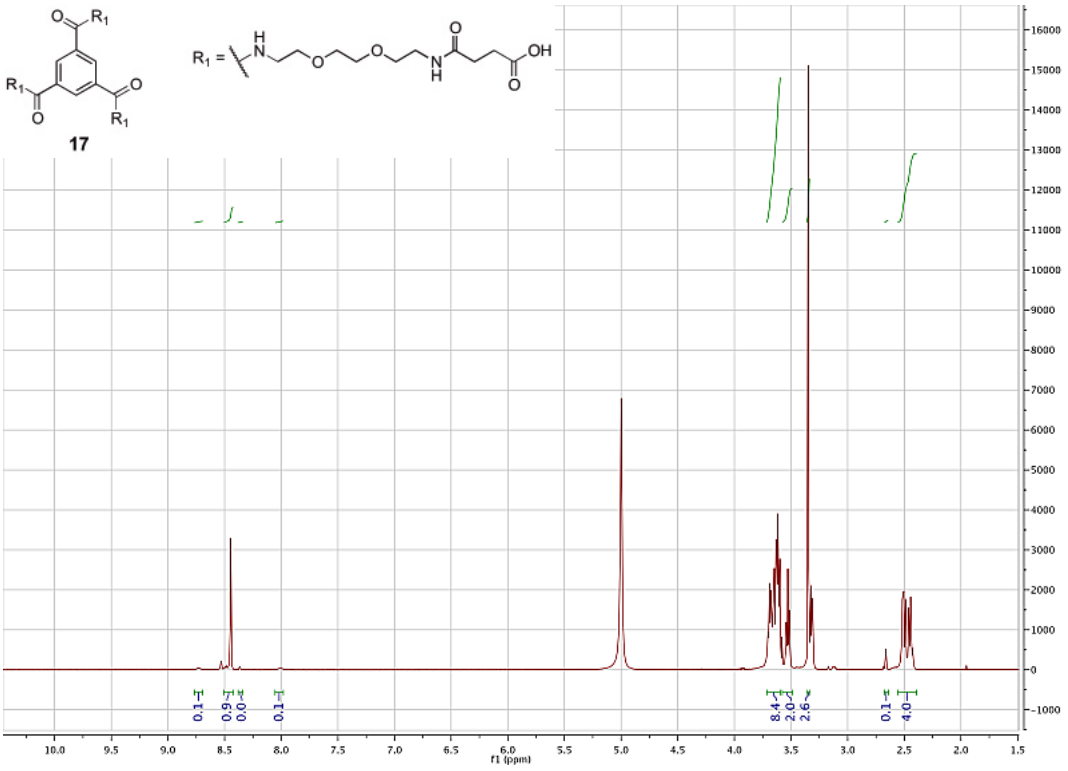
R1 =
OH
17
f1 (ppm)

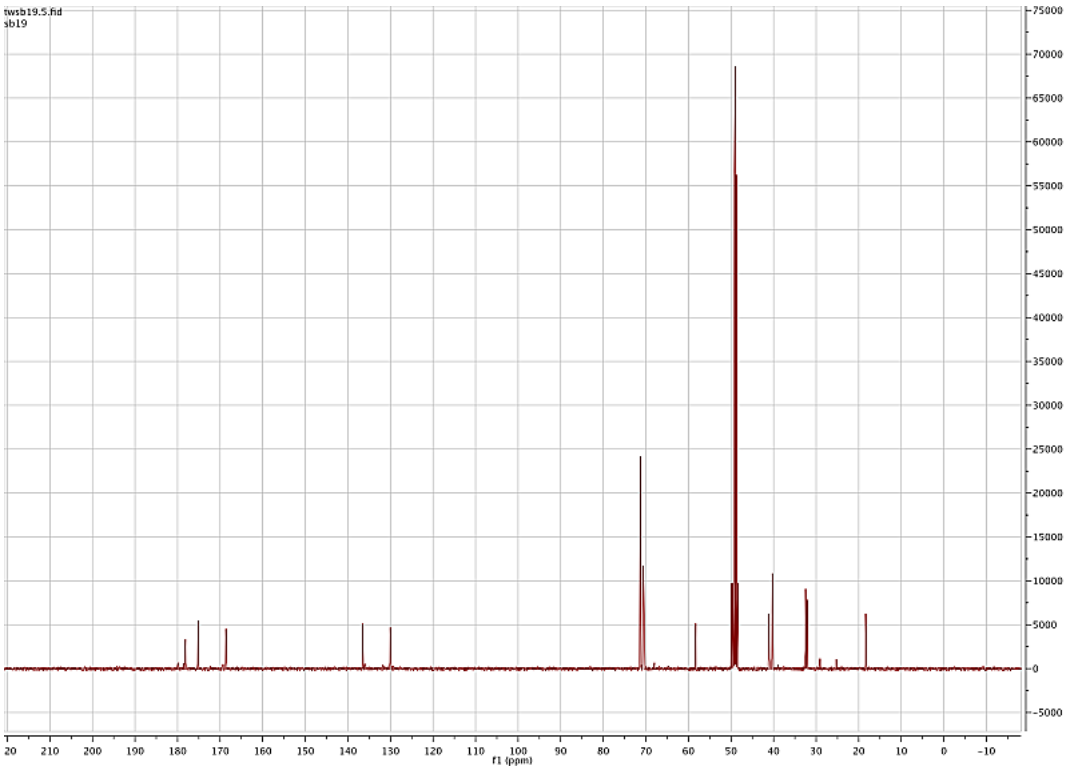
twsb19.5.fid
sb19
f1 (ppm)

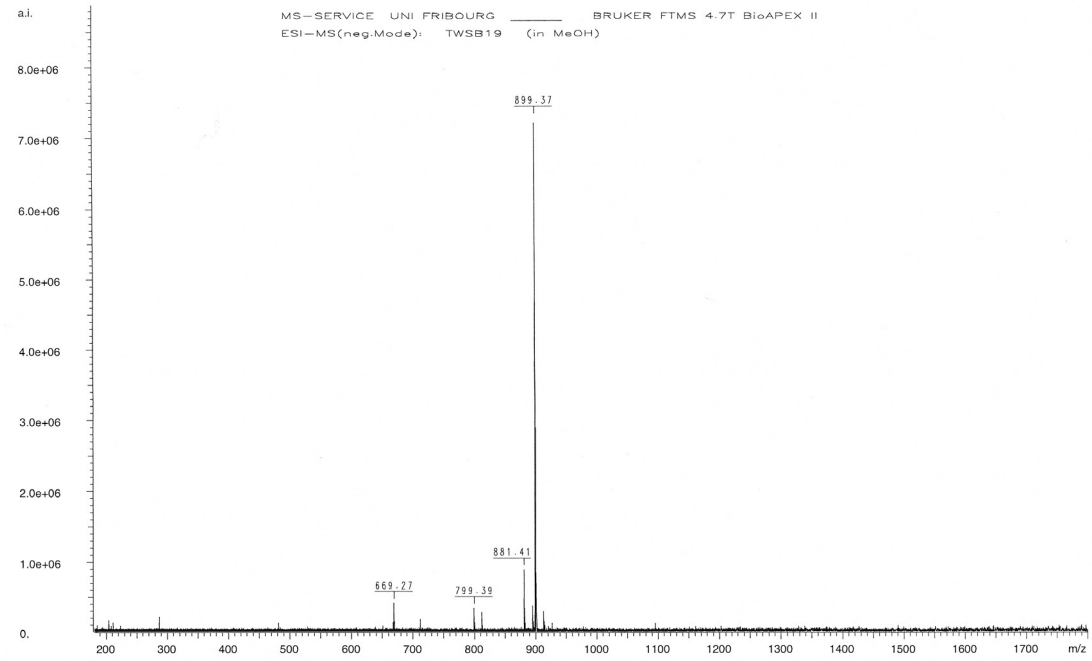
MS—SERVICE UNI FRIBOURG BRUKER FTMS 4.7T BioAPEX II
ESI—MS(neg.Mode): TWSB19 (in MeOH)
a.i.
899.37
881.41
669.27
799.39
m/z

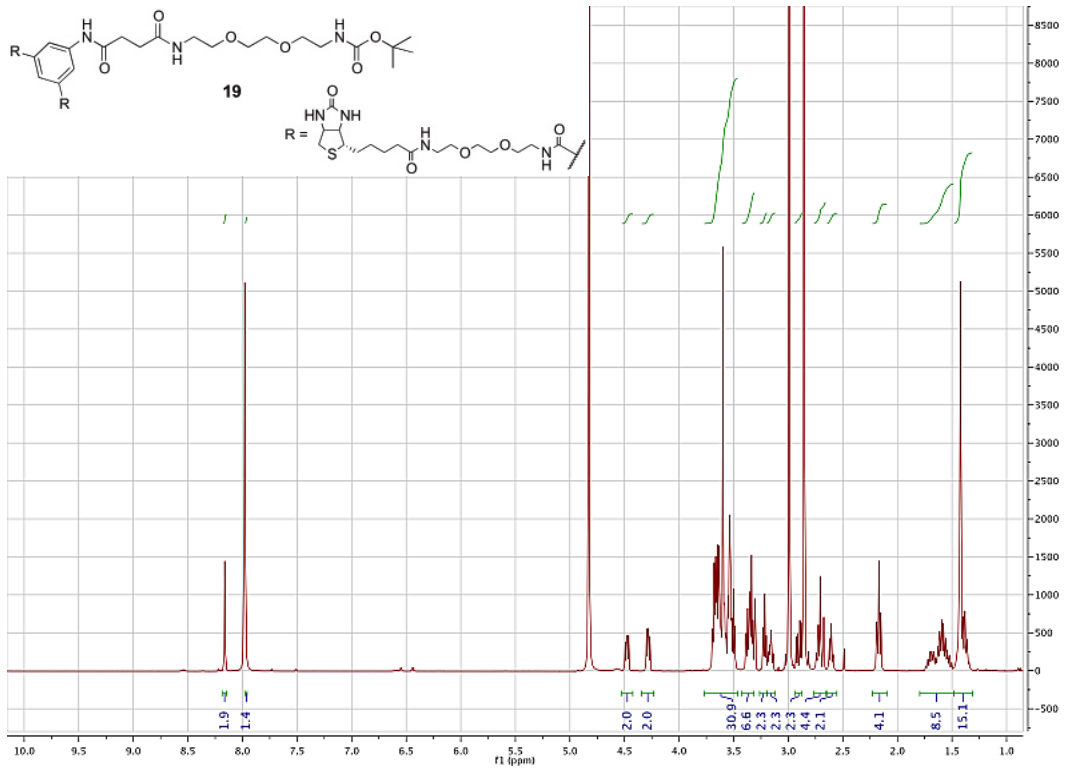
19
R =
1.9
1.4
2.0
2.0
30.9
6.6
2.3
2.3
2.3
4.4
2.1
4.1
8.5
15.1
f1 (ppm)

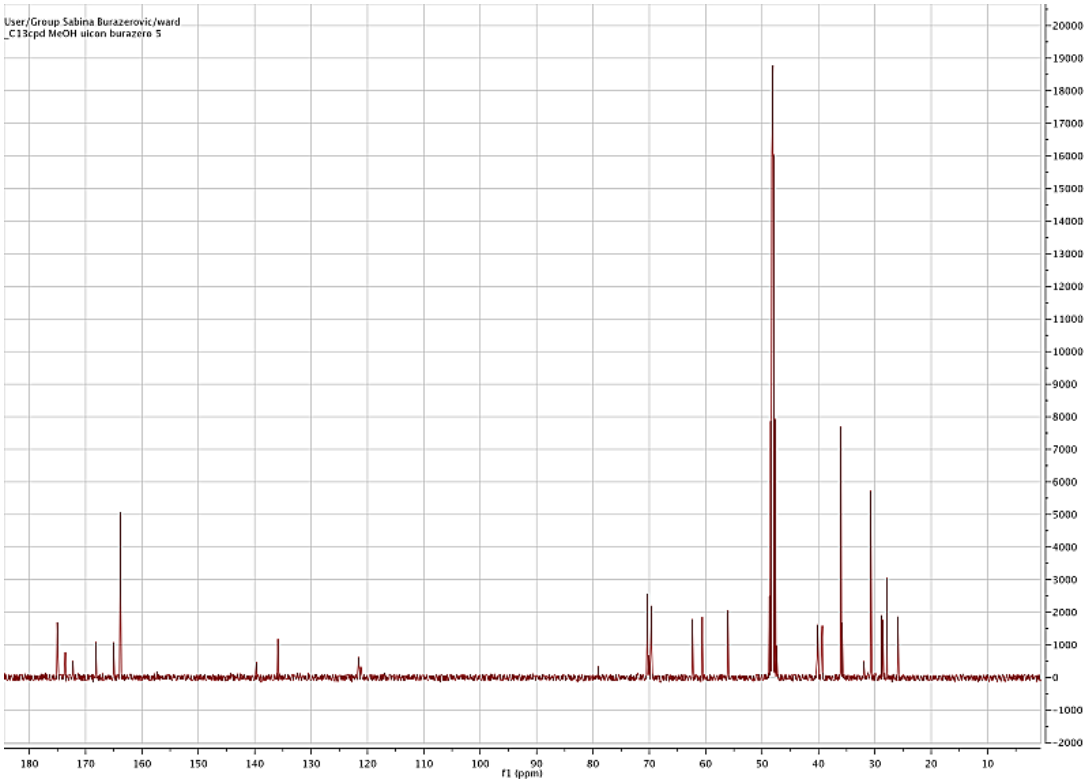
User/Group Sabina Burazerovic/ward
_C13cpd MeOH ulcon burazero 5
f1 (ppm)

All, 0.0-0.1min (#1-#6)

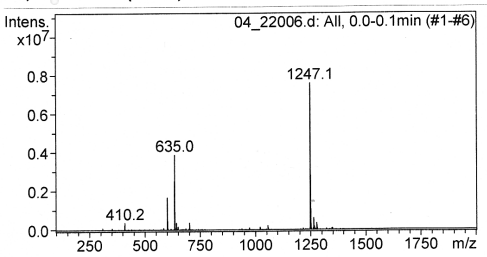

#	m/z	I	FWHM	S/N
1	601.5	1667631	0.4	61.6
2	602.4	483370	0.4	17.9
3	635.0	3859744	0.3	142.6
4	635.3	2633235	0.2	97.3
5	635.8	1219116	0.2	45.0
6	1247.1	7563616	0.4	279.4
7	1247.7	5778014	0.4	213.4
8	1248.7	2770955	0.4	102.4
9	1249.8	1046468	0.4	38.7
10	1262.8	591883	0.4	21.9

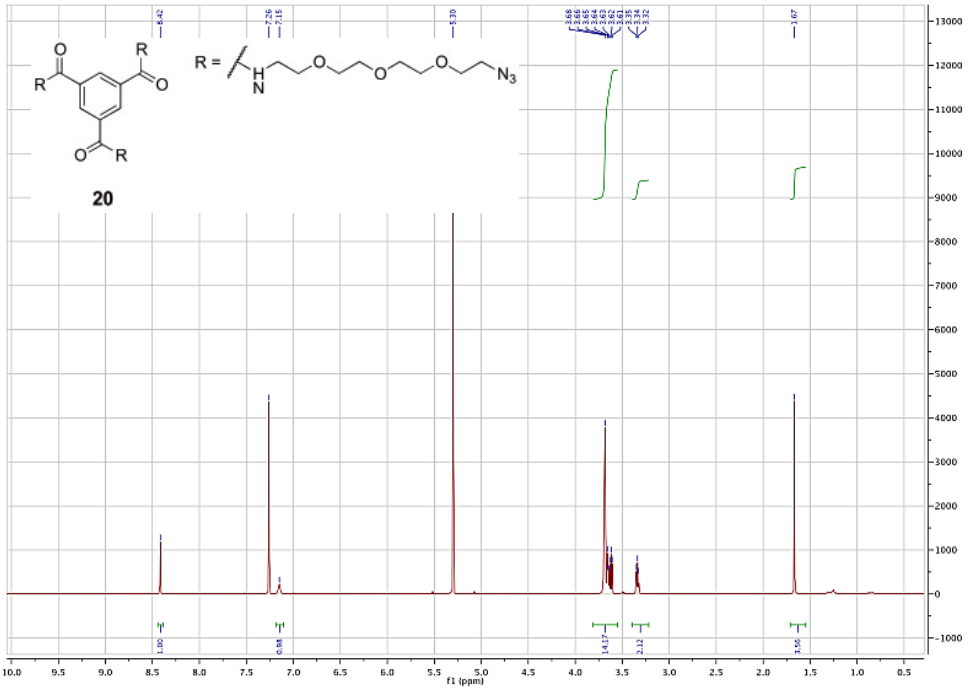

Acquisition Parameter

Source Type	ESI	Ion Polarity	Positive	Set Nebulizer	0.4 Bar
Focus	Not active			Set Dry Heater	180 °C
Scan Begin	50 m/z	Set Capillary	4500 V	Set Dry Gas	4.0 l/min
Scan End	3000 m/z	Set End Plate Offset	-500 V	Set Divert Valve	Waste

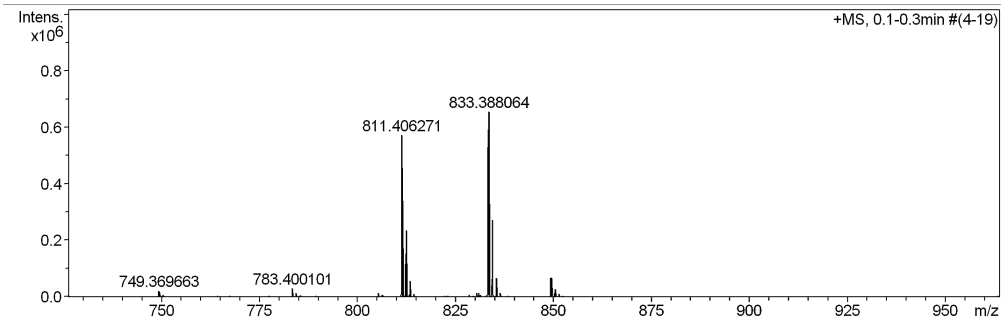

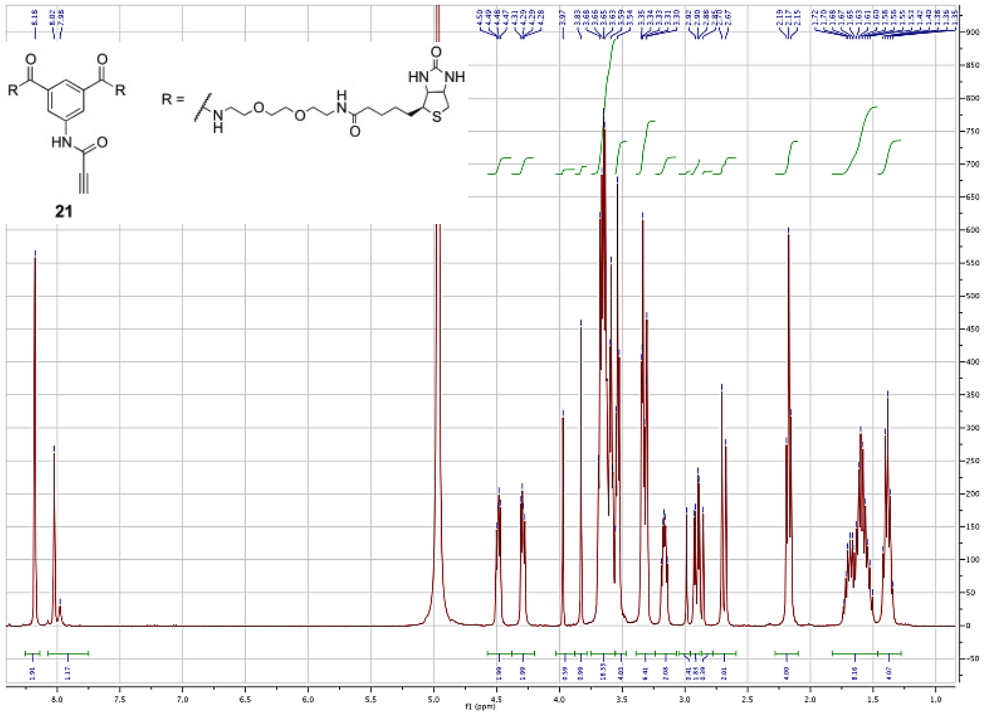

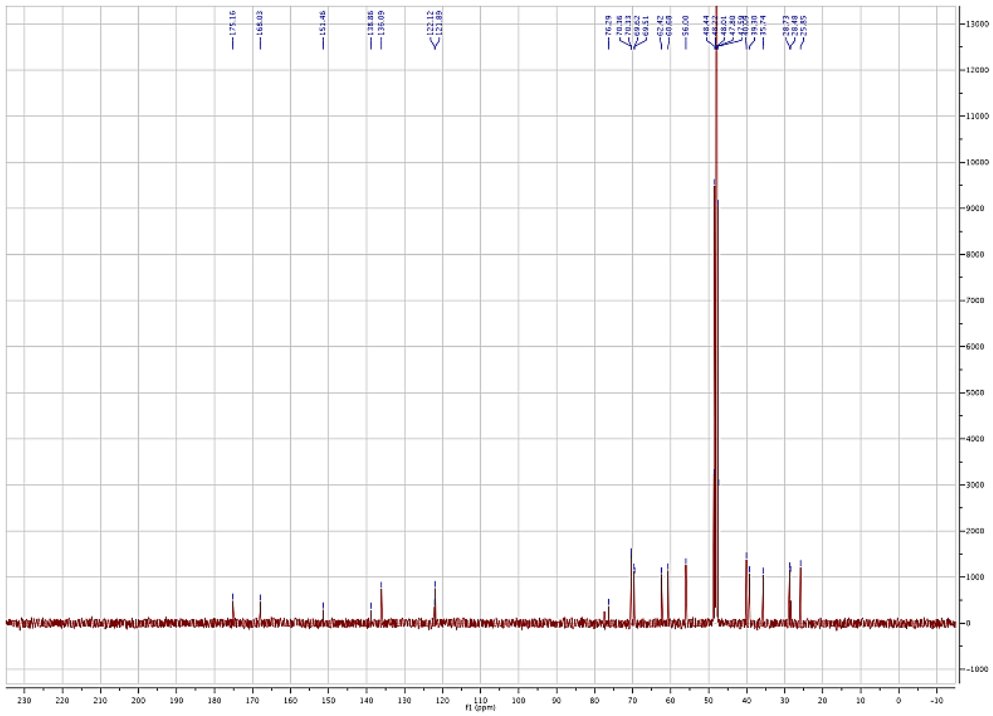

Acquisition Parameter

Source Type	ESI	Ion Polarity	Positive	Set Nebulizer	0.4 Bar
Focus	Not active			Set Dry Heater	180 °C
Scan Begin	50 m/z	Set Capillary	4500 V	Set Dry Gas	4.0 l/min
Scan End	3000 m/z	Set End Plate Offset	-500 V	Set Divert Valve	Waste

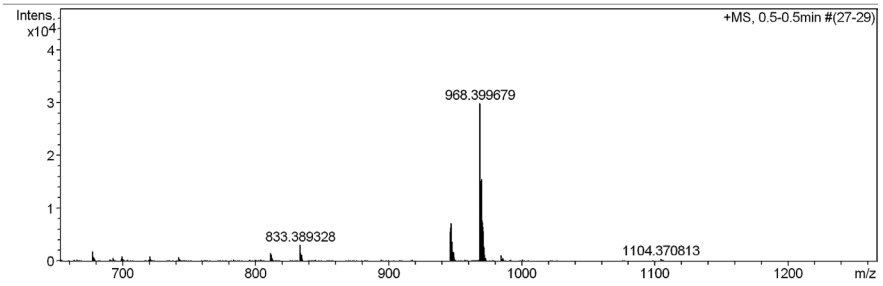

APPENDIX 2

1. SPR Datas Analysis

The SPR response shift, ΔRU, generated by each extension step was calculated as:

$$\Delta RU = RU_{n+1} - RU_n \quad (1)$$

where RU_{n-1} consisted of the absolute response before the solution of biomolecules was injected into the flow cell to the sensor surface. At the end of each injection, the surface sensor was washed (flow rate: 1 mL/min) three times, and a stable baseline was recorded during at least 5 min before proceeding to the next injection. RU_n consisted of the absolute response observed on the sensorgram ~ 1 min. before the following injection occured. The sensorgram depicted below shows the stepwise extension of SAv using BBA_2.

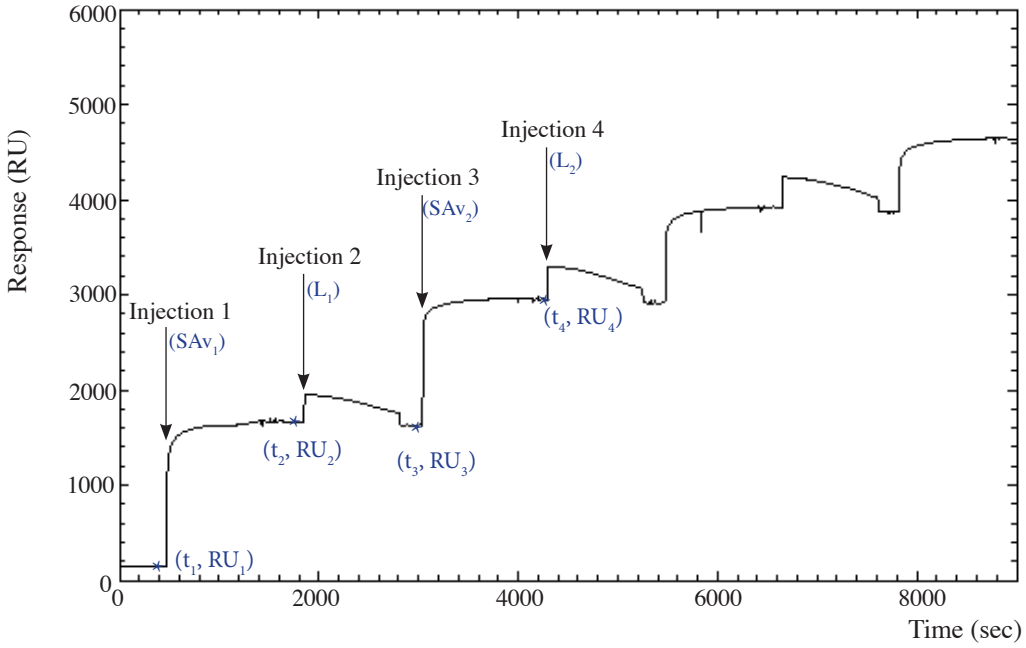

The buffer washing steps are not indicated on the sensorgram for clarity purposes. The increment of the SPR response generated by the first immobilzation step of SAv, injection 1, is $\Delta RU\,(2) = RU_2 - RU_1 = 1524$ RU. The response shift generated by the first extension step of SAv, injection 3, is $\Delta RU\,(3) = RU_4 - RU_3 = 1333$ RU. The extension efficiency (*Eff*) for each elongation step was determined by calculating the ratio of the SPR response shifts as:

$$Eff = \Delta RU_n / \Delta RU_{n-2} \quad (2)$$

The theoretical Eff values being equal to 1.0 and 2.0 when using a linear junction (as BBA_2) and a trifurcated one (as BBA_3), respectively. From the sensorgram shown above, the extension efficiency value of the first extension step of SAv is *Eff* = 0.87.

The SPR shifts were translated into mass uptake by assuming 1000 RU = 100 ng/cm^2. [1]

2. QCM-D data analysis

The same reasoning as the one explained in the previous section was applied to analyze the QCM-D datas. To translate the frequency shift into mass uptake, Sauerbrey relationship [2] was used

$$\Delta m_{QCM} = -\frac{C_{QCM}}{n}\Delta f_n \qquad (6)$$

where C_{QCM} (17.7 ng cm^{-2} Hz^{-1}) is the mass sensitivity constant, and n = (1, 3, ...) is the overtone number. This relation holds for homogeneous, thin and non-dissipative adsorbed film.

3. SPR shifts (ΔR) results

Elongation step	Response shift, ΔR (RU)	
	BBA_2	SAv
0		1523.8
1	-39.4	1332.5
2	-45.1	1009.5
3	-49.1	764.7
4	-56.0	598.3
5	-30.4	545.1
6	-41.3	520.8
7	-35.8	467.0
8	-39.9	435.3
9	-39.5	409.0
10	-40.0	411.4

Table 1 SPR response shifts recorded for the SbS assembly of SAv using BBA_2 on a 1% Biot-SH sensor (see chap 2.4, Fig. 6).

Elongation step	Response shift, ΔR (RU)	
	BBA_3	SAv
0		1393.9
1	-26.9	1280.8
2	-56.9	1166.6
3	133.8	1581.6
4	225.6	1653.2
5	170.9	1757.8

Table 2 SPR response shifts recorded for the SbS assembly of SAv using BBA_3 on a 1% Biot-SH sensor (see Fig. 7, chap 2.4).

Elongation step	Response shift, ΔR (RU)	
	BBA_2	SAv
0		40.4
1	5.9	40.1
2	1.8	37.1
3	6.5	36.8
4	4.1	34.1
5	3.2	31.8
6	3.7	30.0

Table 3 SPR response shifts recorded for the SbS assembly of SAv using BBA_2 on a 0.1‰ BBA-SH sensor (see Fig. 11, chap 2.4).

Elongation step	Response shift, ΔR (RU)	
	BBA_2	SAv
0		33.4
1	-1.1	53.7
2	-2.6	74.0
3	-1.3	95.5
4	2.6	129.4
5	5.2	162.3
6	4.4	192.5

Table 4 SPR response shifts recorded for the SbS assembly of SAv using BBA_3 on a 0.1‰ BBA-SH sensor (see Fig. 12, chap 2.4).

Elongation step	Response shift, ΔR (RU)		
	BBA_2	BBA_3	SAv
0			47.0
1	20		44.8
2		1.7	66.7
3	2.7		55.5
4		5.1	83.4
5	1.6		63.6
6		1.9	96.9

Table 5 SPR response shifts recorded for the SbS assembly of SAv using BBA_2 and BBA_3 on a 0.1‰ BBA-SH sensor (see Fig. 16, chap 2.4).

4. QCM-D Δ*D* and Δ*f* results

Elongation step	BBA_2		SAv	
	$\Delta F_{n=3}$ (Hz)	$\Delta D_{n=3}(1\cdot10^{-6})$	$\Delta F_{n=3}$ (Hz)	$\Delta D_{n=3}(1\cdot10^{-6})$
0			-27.6	0.19
1	-1.4	0.14	-14.4	0.30
2	-0.74	0.15	-10.4	0.60

Table 6 Frequency and dissipation shifts recorded for the SbS assembly of SAv using BBA_2 on a 1% Biot-SH sensor (see Chap 2.4, Fig. 4).

Elongation step	BBA_3		SAv	
	$\Delta F_{n=3}$ (Hz)	$\Delta D_{n=3}(1\cdot10^{-6})$	$\Delta F_{n=3}$ (Hz)	$\Delta D_{n=3}(1\cdot10^{-6})$
0			-29.6	0.20
1	-2.03	-0.029	-16.9	0.10
2	-1.93	0.16	-20.3	0.29
3	-1.17	0.11	-14.7	0.33
4	-1.06	0.071	-17.3	0.45

Table 7 Frequency and dissipation shifts recorded for the SbS assembly of SAv using BBA_3 on a 1% Biot-SH sensor (see Chap 2.4, Fig. 5).

Elongation step	BBA_3		SAv	
	$\Delta F_{n=3}$ (Hz)	$\Delta D_{n=3}$ ($1 \cdot 10^{-6}$)	$\Delta F_{n=3}$ (Hz)	$\Delta D_{n=3}$ ($1 \cdot 10^{-6}$)
0			-4.80	0.15
1	2.69	-0.090	-5.94	0.29
2	2.02	0.0050	-8.14	0.46
3	2.05	0.54	-10.2	1.30

Table 8 Frequency and dissipation shifts recorded for the SbS assembly of SAv using BBA_3 on a 0.1% Biot-SH sensor (see Chap 2.4, Fig. 9).

Elongation step	BBA_3		SAv	
	$\Delta F_{n=3}$ (Hz)	$\Delta D_{n=3}$ ($1 \cdot 10^{-6}$)	$\Delta F_{n=3}$ (Hz)	$\Delta D_{n=3}$ ($1 \cdot 10^{-6}$)
2			-5.84	0.34
3	-0.31	0.082	-7.17	0.71
4	-0.25	0.088	-8.96	0.90
5	-0.22	0.11	-11.5	1.1
6	-0.11	0.14	-13.6	1.2

Table 9 Frequency and dissipation shifts recorded for the SbS assembly of SAv using BBA_3 on a 0.1‰ BBA-SH sensor sensor (cf. Chap 2.4, Fig. 10).

elongation step	BBA_2		BBA_3		SAv	
	$\Delta F_{n=3}$ (Hz)	$\Delta D_{n=3}$ ($1 \cdot 10^{-6}$)	$\Delta F_{n=3}$ (Hz)	$\Delta D_{n=3}$ ($1 \cdot 10^{-6}$)	$\Delta F_{n=3}$ (Hz)	$\Delta D_{n=3}$ ($1 \cdot 10^{-6}$)
2			-0.96	0.12	-6.7	0.49
3	-0.65	0.18			-4.3	0.45
4			-0.19	0.08	-6.3	0.55
5	-0.29	0.13			-5.3	0.53
6			-0.10	0.14	-9.2	0.89

Table 10 Frequency and dissipation shifts recorded for the SbS assembly of SAv with alternate use of BBA_2 and BBA_3 on a 0.1‰ BBA-SH sensor sensor (see Chap 2.4 Fig. 15).

elongation step	BBA_2		SAv	
	$\Delta F_{n=3}$ (Hz)	$\Delta D_{n=3}$ ($1 \cdot 10^{-6}$)	$\Delta F_{n=3}$ (Hz)	$\Delta D_{n=3}$ ($1 \cdot 10^{-6}$)
0			-12.6	0.41
1	-0.32	0.20	-11.6	0.64
2	-0.73	0.095	-10.9	0.63
3	-0.96	0.27	-10.7	0.63

Table 11 Frequency and dissipation shifts recorded for the SbS assembly of SAv using BBA_2 on a 0.1% BBA-SH sensor sensor (see Chap 2.4, Fig. 19).

elongation step	Blocking step		BBA_3		SAv	
	$\Delta F_{n=3}$ (Hz)	$\Delta D_{n=3}$ ($1 \cdot 10^{-6}$)	$\Delta F_{n=3}$ (Hz)	$\Delta D_{n=3}$ ($1 \cdot 10^{-6}$)	$\Delta F_{n=3}$ (Hz)	$\Delta D_{n=3}$ ($1 \cdot 10^{-6}$)
0					-14.01	0.26
1	-2.3	0.30			-5.17	0.16
2			-0.86	0.06	-10.48	0.45
3			-0.85	0.12	-12.05	0.49
4			-0.80	0.14	-12.10	0.47

Table 20 Frequency and dissipation shifts recorded for the SbS assembly of SAv using BBA_3 on a 0.1% BBA-SH sensor (cf. Chap 2.4, Fig. 20). After the initial anchoring step of SAv, a blocking step (solution of BBA-SS-BBA / BBA : 1/4) was performed.

5. Angle-resolved photoelectron spectroscopy (ARXPS) experiment

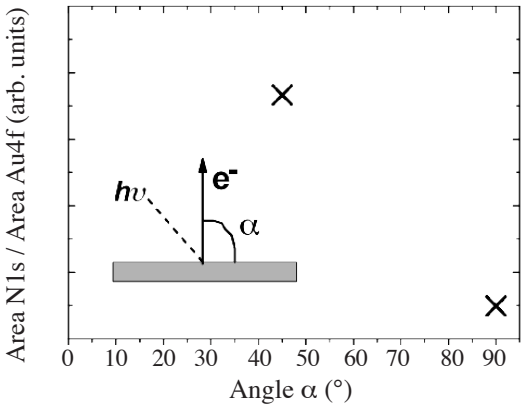

Ratio of the integrated intensities of Au 4f and N 1s as a function of the photoelectron emission angle (α), *i.e* take-off angle.

6. Additional AFM images

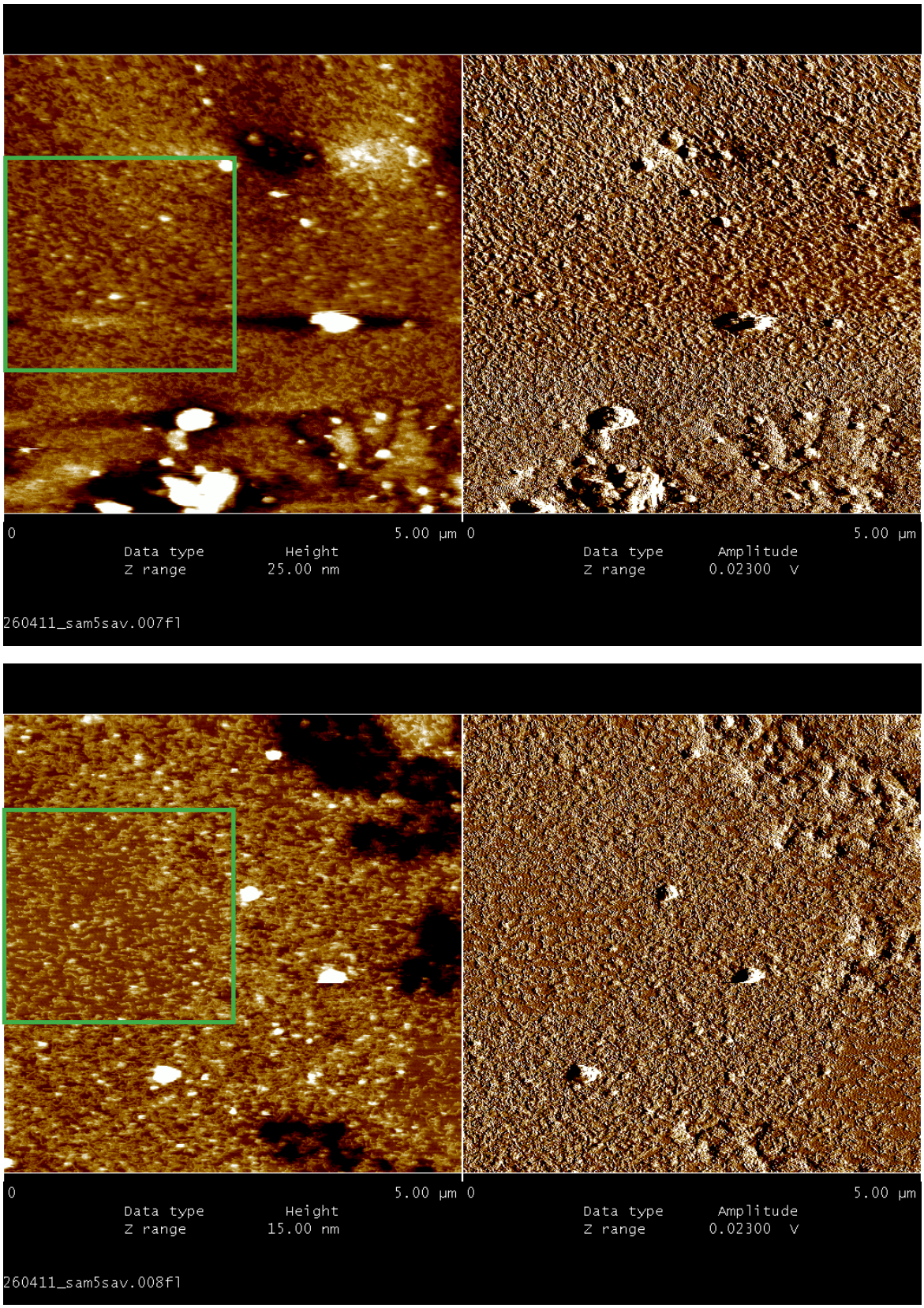

Figure 1 AFM images (in buffer) of the same area successively recorded showing disruption of the fibers occured.

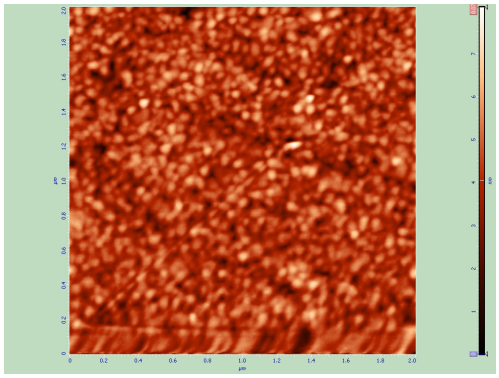

Figure 2 AFM images in air of a bare QCM sensor bare showing the gold terraces.

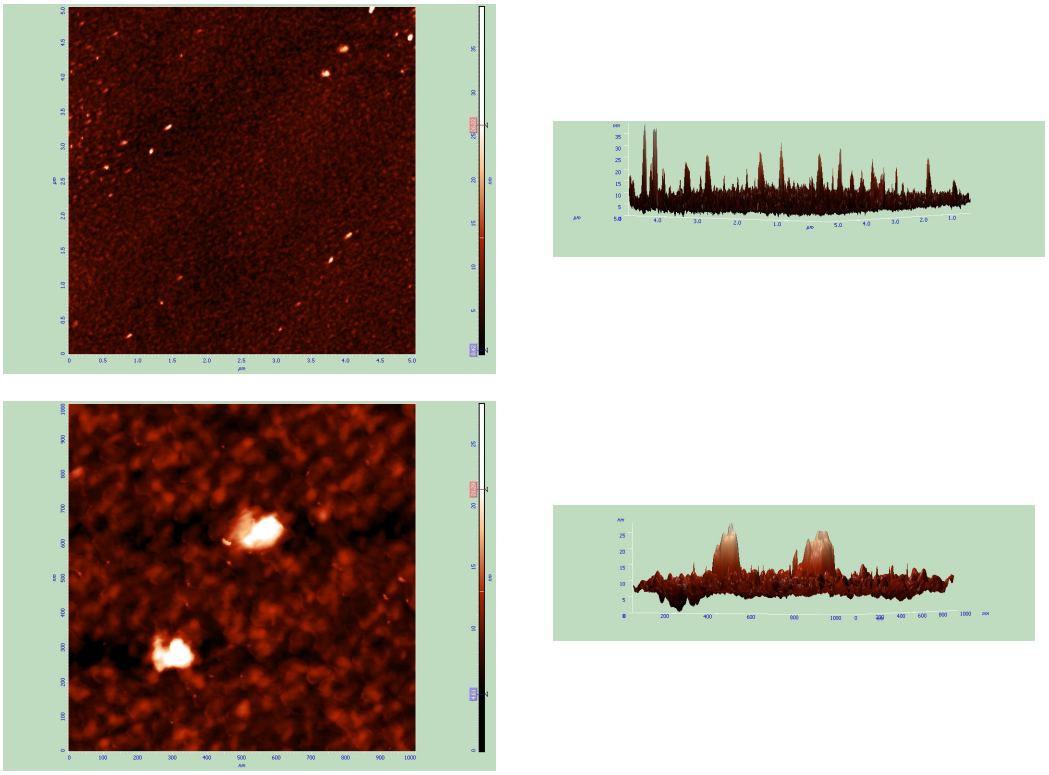

Figure 3 AFM images in air of the 0.01% BBA-SH functionalized QCM sensor onto which six elongation steps of SAv using BBA_3 were recorded (cf experiment presented in Chap 2.4, Fig. 10)

References

1. Stenberg, E.; Persson, B.; Roos, H.; Urbaniczky, C., *J. Colloid Interface Sci*. **1991**, *143* (2), 513-26.

2. Sauerbrey, G., *Z. Phys*. **1959**, *155*, 206-22.

Ackowledgements

This work would not have been possible without the support and guidance of many to whom I am grateful. I would like to thank the following people:

All the support staff of the Department of Chemistry for the administrative and technical help.

All the present and past group members who contributed to an enjoyable atmosphere in the lab.

Dr Koji Oohora (Osaka University, Japan) for synthesizing one of the trifurcated ligand and for showing true interest in this project during his short stay in Basel.

Dr Laurent Marot for performing the XPS experiments.

Dr Julieta Gradinaru for her precious help with ligands synthesis and purification.

Mireille Leboeuf and Dr Massoud Dadras (CSEM, Neuchâtel) for assistance in TEM and SEM measurements. Prof. Patrick Shahgaldian (FHNW, Muttenz) and especially Dr Susanne Wegmann (ETHZ) for guidance with the AFM. Peter Spies (FHNW, Basel) and Prof. Wolgang Meier for letting me use their lab facilities. I also thank Prof. Meier for accepting to expertise this thesis.

Elisa for all the adventures in and out of the lab.

My friends and family for always being there and believing in me.

Prof. Thomas R. Ward for giving me the opportunity to work in a very interesting interdisciplinary field of research. His refreshing enthusiasm towards science blended with a great sense of humour was greatly appreciated. I am extremely grateful for the freedom he gave me to work on a subject, which was not in alignment with the main efforts accomplished in his research group.

List of Publications

Sabina Burazerovic, Julieta Gadinaru, Julien Pierron and Thomas R. Ward. «Hierarchical Self-Assembly of One Dimensional Streptavidin Bundles as Collagen Mimetic for the Biomineralization of Calcite» *Angew. Chem. Int. Ed. Engl.* **2007**, *46*, 5510 (selected as "hot paper").

Koji Oohora, Sabina Burazerovic, Akira Onoda, Yvonne Wilson, Thomas R. Ward, and Takashi Hayashi. «Chemically Programmed Supramolecular Assembly of Hemoprotein and Streptavidin with Alternating Alignment» *Angew. Chem. Int. Ed. Engl.* **2012**, *124*, 3884.

Sabina Burazerovic

Markgräflerstr. 3, 4057 Basel
Born 29.10.1976, Swiss and Canadian

Home +41 61 331 3433
burazerovic@gmx.ch

Education

PhD in Chemistry, University of Basel (Switzerland) 2012

Title: Streptavidin-Based Nanostructures: From Bulk to Surface-Confined Assembly Studies.
Supervisor: Prof. Dr Thomas R. Ward

M.Sc. in Chemistry, University of Neuchâtel (Switzerland) 2006

Title: One-Dimensional Self-Assembly of a Block-Copolymer Composed of a Tetra-Biotin Ligand and Streptavidin.
Supervisor: Prof. Dr Thomas R. Ward

B.Sc. in Chemistry, University of Neuchâtel (Switzerland) 2001-2004
Community College (Natural Sciences), CEGEP Edouard-Montpetit (Canada) 1995-1998

Skills

Chemistry and molecular biology: Synthesis, purification and characterization of organic compounds. Lysine side-chains derivatization. protein-based polymer analysis by gel electrophoresis (SDS-PAGE).

Nanotechnology: protein-based nanostructures characterization by SEM, TEM and AFM. Gold surfaces functionalization (SAMs), monitoring protein-based polymer growth by QCM-D and SPR.

Teaching experience: supervised one MSc student and first years inorganic Practical over 2 years.

Languages skills:French (mother tongue), English (fluent spoken an written), German (basic)

Computer skills: Chemdraw, Isisdraw, Matlab, MestReNova, Scifinder, PyMol, YASARA, ImageJ, Image SXM. Word, Excel, Powerpoint, Pages, Keynote, Numbers, EndNote, Adobe CS5 on Mac and PC.

Reference

Prof. Dr. Thomas R. Ward
Department of Chemistry
University of Basel
Spitalstrasse 51
CH-4056 Basel, Switzerland
Tel: +41 (0)61 267 10 04
Fax: +41 (0)61 267 10 05
thomas.ward@unibas.ch